MULTI-WAVELENGTH OBSERVATIONS OF GALAXY CLUSTERS: POPULATION EVOLUTION AND SCALING RELATIONS FOR INTERMEDIATE-REDSHIFT CLUSTERS

By

Thomas Patrick Connor

A DISSERTATION

Submitted to
Michigan State University
in partial fulfillment of the requirements
for the degree of

Astrophysics and Astronomy - Doctor of Philosophy

2016

ABSTRACT

MULTI-WAVELENGTH OBSERVATIONS OF GALAXY CLUSTERS: POPULATION EVOLUTION AND SCALING RELATIONS FOR INTERMEDIATE-REDSHIFT CLUSTERS

$\mathbf{B}\mathbf{y}$

Thomas Patrick Connor

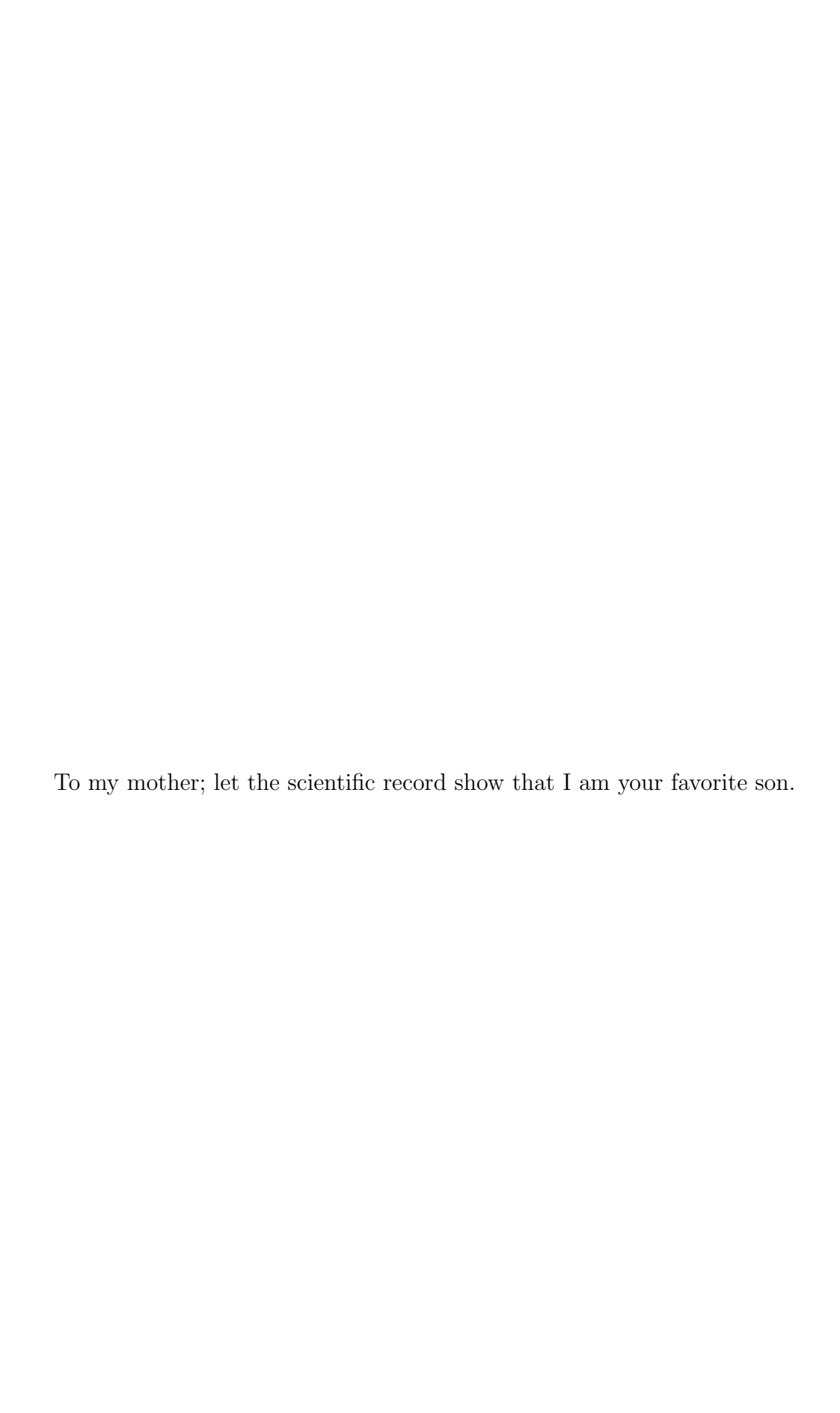
Galaxy clusters are key signatures of the formation of structure in the Universe due to their positions at the nodes of the cosmic web. However, these privileged positions feature significant amounts of activity as a consequence of frequent accretion and collisions with other galaxies and clusters of galaxies. Thus, a rigorous understanding of cluster evolution constrains not only cosmological structure formation but also galaxy dynamics in the most extreme environments. Here, we examine the evolution of clusters in two situations: how the properties of the hot intracluster gas changes with the total masses of the clusters at the observational frontiers of mass and redshift; and how cluster galaxies evolve with redshift in some of the most massive clusters in the Universe.

In Chapter 2 we examine a population of moderate-luminosity clusters at intermediate redshifts using the *XMM-Newton* telescope with well-determined masses from *Hubble Space Telescope* (HST) observations. We find that these systems do not deviate from scaling relations between mass, luminosity, and temperature derived from more massive clusters, implying that, even at the redshifts and masses probed here, gravitational energetics still dominate over supernovae.

In Chapter 3 we utilize new techniques to maximize a multi-wavelength dataset from HST of 25 massive galaxy clusters. We present new methods for detection and photometry of galaxies in the presence of inconsistent, diffuse background. Using these techniques, we construct a photometric catalog down to $M^* + 4$ -5 for clusters at redshift $z \sim 0.2$ to $z \sim 0.9$, which we validate with comparisons to spectral observations and a similar catalog. We also consider the luminosity function for these clusters; we find a drop-off in the faint-end slope when only selecting red sequence galaxies.

Finally, in Chapter 4, we exploit our new photometric catalogs to study the evolution of the red galaxies, the "red sequence of galaxies," in these massive clusters of galaxies. With the combination of resolution, depth, and spectral coverage available in this work, we are able to use spectral fitting to examine the effects of metallicity and age in shaping the photometric properties of cluster galaxies. We see evidence of a metallicity gradient along the red sequence and minimal evolution in the slope with redshift, implying it is a consequence of the mass-metallicity relation in place at $z \sim 2$. However, we also see secondary indicators that the red sequence is being steadily populated at the fainter end after its initial formation.

Copyright by THOMAS PATRICK CONNOR 2016



ACKNOWLEDGMENTS

After myself, no one has had a bigger part in the completion of this thesis than Megan Donahue. Not only did she provide the funding that let me continue to work on research, she also helped guide me through the problems of research. Furthermore, she provided me free time on SOAR and access to the CLASH collaboration, without which this dissertation would be significantly shorter.

Along with Megan, I would like to thank my other collaborators. Andisheh Mahdavi and Henk Hoekstra were instrumental in the success of my X-ray analysis. Dan Coe, Dan Kelson, and Marc Postman provided monetary, scientific, and technical support and guidance to help me shape the CLASH portion of this thesis. John Moustakas has been vital in the success of that analysis. Norbert Werner, Kevin Fogarty, and Grant Tremblay were not involved in any thesis work, but they have been excellent collaborators. Finally, Mark Voit and Ming Sun have both been exceptionally helpful and encouraging.

I would not be here were it for Chris Mihos, Veronica Strazzullo, Maurilio Pannella, Paul Harding, Colin Slater, Tim Atherton, Loránt Sjouwerman, Earle Luck, Heather Morrison, and Agnes Torontali. Their guidance and support both gave me the ability to be accepted into a graduate program and the foundation to succeed there. At MSU, Aaron Hoffer was an excellent mentor who taught me how to observe. Looking forward, I extend my thanks to John Mulchaey for giving me an immovable deadline to motivate my writing.

Five years in Lansing would not have been possible without all of the friends and col-

leagues I have shared that time with. There are too many people to name, but I would like to thank Alex Deibel, Tom Hettinger, Ryan Connolly, and Brian Crosby, in particular, for bridging the gap between coworker and friend, and Aubrey Thompson for giving me a reason to look forward to weekends.

Finally, many thanks to my family. My brothers, Andrew and Matthew, who paved the way for me to move past a four year degree, inspired me to aim for a PhD before I had even finished high school. My grandmother supported me throughout my childhood, but will not be able to see me earn one last degree. And, without debating nature vs. nurture, I am confident that I would not have accomplished half of what I have without the parents I have. Thank you.

TABLE OF CONTENTS

LIST (OF TABLES
LIST (OF FIGURES
KEY 7	ΓΟ SYMBOLS AND ABBREVIATIONS xviii
Chapte	er 1 Introduction
1.1	The Grand Dichotomy
1.2	The Red Sequence in Galaxy Clusters
1.3	CLASH: The Cluster Lensing and Supernova Survey with Hubble 8
1.4	X-ray Scaling Relations
Chapte	
0.1	ters at Intermediate Redshift
2.1	Introduction
2.2	Data and Analysis
2.3	Analysis
2.4	Results
	2.4.1 Flux
	2.4.2 X-ray Offsets
2.5	
2.5	
	ı v
	2.5.2 Comparison with Other Scaling Relations
	2.5.4 Comparison between Groups and Clusters
2.6	Conclusions
2.0	Conclusions
Chapte	er 3 Optimized Photometry of Cluster Galaxies in CLASH 61
3.1	Introduction
	3.1.1 Statistical Background Light Estimators
3.2	Data Set
	3.2.1 Detection Images
	3.2.2 Source Detection
3.3	Photometry
	3.3.1 UV Systematic Uncertainties
	3.3.2 Photometric Redshifts
2.4	Companies to Cimilar Works

3.5	Optical Scaling Relations	88
	3.5.1 Mass-Richness Relation	90
	3.5.2 Luminosity Function	91
	3.5.3 Stellar Mass	97
3.6	Summary	101
Chapte	er 4 Galaxy Properties, Membership, and Red Sequence Evolution	
	in CLASH Clusters	104
4.1	Introduction	104
4.2	Data	108
	4.2.1 SED Fitting	110
4.3	Cluster Membership	115
	4.3.1 Alternative Selections	117
4.4	Red Sequence Fitting	119
4.5	Individual Galaxies	125
4.6	Mass-to-Light Ratios	129
4.7	Discussion	131
4.8	Summary	137
Chapte	er 5 Summary	139
5.1	Revisiting the Luminosity Function	141
5.2	Which Red Sequence	143
5.3	Bring the Background to the Foreground	144
5.4	Public Release	144
APPE	NDICES	146
Appen	dix A Appendices for Chapter 2	147
		152
BEFE	RENCES	168

LIST OF TABLES

Table 1.1	Properties of CLASH Clusters	8
Table 2.1	Sample Properties	26
Table 2.2	Observations of Clusters	27
Table 2.3	Masked Sources	31
Table 2.4	Spectral Fitting Properties Within r_{2500}	37
Table 2.5	Scaling Relations	44
Table 2.6	CCCP Cluster Properties Within r_{2500}	46
Table 3.1	Source Extractor Detection Parameters	71
Table 3.2	CLASH Scaling Properties	88
Table 3.3	CLASH Luminosity Function Fit	91
Table 3.4	CLASH r_{2500} values	98
Table 4.1	CLASH Redshifted Filter Analogs	109
Table 4.2	Red Sequence Fits	122
Table B.1	ACS Data Properties – Exposure time (s), Zeropoint (AB Mag), and A_{λ} (Mag)	156
Table B.2	WFC3 (UVIS/IR) Data Properties – Exposure time (s), Zeropoint (AB Mag), and A_{λ} (Mag)	158
Table B.3	Masked Stars in CLASH fields (R $>2''$)	162

LIST OF FIGURES

Figure 1.1	g-r color-magnitude diagram for 500000 extended galaxies cataloged from the Sloan Digital Sky Survey. These galaxies are the first 500000 in the 13th Data Release with g and r magnitudes brighter than 25 and with no constraints on position. Two galaxy populations are visible: the blue cloud and the red sequence. In color-magnitude diagrams presented in this dissertation, bluer colors are lower on the y-axis, while brighter galaxies are to the left of fainter galaxies	2
Figure 1.2	Fractional throughputs of the 17 filters used by CLASH. They are, from blue to red, F225W, F275W, F336W, F390W (all UVIS); F435W, F475W, F555W F606W, F625W, F775W, F814W, F850LP (all ACS); F105W, F110W, F125W, F140W, F160W (all WFC3-IR)	9
Figure 1.3	Distribution of photometric redshifts from CLASH cluster photometry for MACS 1423. Data from the original catalogs published by (Postman et al., 2012b) is shown in orange, while data from the photometry we present in this work are shown in dark blue. The spectroscopic redshift of the cluster is indicated by the purple bar. We only consider those galaxies with F814W magnitudes brighter than 25.5.	12
Figure 1.4	X-ray scaling between X-ray temperature and X-ray luminosity for a sample of clusters (purple, Wu et al., 1999) and groups (orange, Xue & Wu, 2000). Both samples show self-similar scaling characterized by a power-law, but the different slopes of that scaling between groups and clusters is evidence of a possible break in self-similarity	14
Figure 2.1	Gaussian-smoothed X-ray emission contours overlaid on <i>Hubble Space Telescope</i> images of the four clusters we observed in this work. Contours are spaced at intervals of 10^{-6} count s ⁻¹ arcsec ⁻² , with the minimum level for each cluster described in Section 2.2	29
Figure 2.2	Comparison between our measured fluxes using XMM -Newton and those reported by Vikhlinin et al. (1998) using $ROSAT$. $ROSAT$ fluxes were adjusted to correspond to the inner 300 h_{70}^{-1} kpc of the cluster, as described in the text. The solid line is the identity line, while the shaded band indicates agreement to within 10%	39

Figure 2.3	Distribution of offsets to BCG positions measured by Hoekstra et al. (2011) from X-ray centroid measurements using XMM-Newton (this work, hashes rising to the right) and ROSAT (Vikhlinin et al., 1998, hashes lowering to the right). Data are binned to increments of 5 arcseconds	41
Figure 2.4	Plot of weak-lensing mass M_{WL} as a function of bolometric X-ray luminosity within r_{2500} . Masses and luminosities have been rescaled by $E(z)$ to account for the range of redshift covered by the samples. Data analyzed in this work are shown as circles, while cluster properties from the CCCP are shown as squares. RXJ0826.1+2625 was not included in this fit. Our best fit to Equation (2.2) for the M-L relation is shown by the solid line. Our best fit when including intrinsic scatter is shown by the dashed line. Both fits are to the combined sample of 160SD and CCCP clusters	45
Figure 2.5	Plot of X-ray temperature as a function of bolometric luminosity within r_{2500} . Luminosities have been rescaled by $E(z)$ to account for the range of redshift covered by the samples. Data analyzed in this work are shown as circles, while cluster properties from the CCCP are shown as squares. Our best fit to Equation (2.2) for the T-L relation is shown by the solid line	50
Figure 2.6	Plot of M as a function of X-ray temperature within r_{2500} . Masses have been rescaled by $E(z)$ to account for the range of redshift covered by the samples. Data analyzed in this work are shown as circles, while cluster properties from the CCCP are shown as squares; both are derived from weak lensing. RXJ0826.1+2625 was not included in this fit. We also include a sample of nearby galaxy groups from Sun et al. (2009) as diamonds, where masses are derived from hydrostatic equilibrium. Our best fit to Equation (2.2) for the M-T relation from the clusters analyzed in this work and from the CCCP is shown by the solid line. Our best fit to the M-T relation using the properties within r_{2500} of the groups from Sun et al. is shown as a dashed line.	51
Figure 3.1	The central region of Abell 383 after subtracting a local background found using the Pearson approximation for the mode. Background regions used are: left: 4 pixels (0.26"); middle: 16 pixels (1.04"); and right: 128 pixels (8.32"). Larger structures are visible when a larger background radius is used, while smaller objects are more clearly resolved with a more localized background region	69

Figure 3.2	A portion of the MACS J0717 field, seen in F125W (red), F814W (green), and F555W (blue). Detected objects are outlined in white ellipses corresponding to the region used for photometry. Also shown are objects classified as stars in this work, which are marked by blue ellipses. This image is approximately 45" wide	73
Figure 3.3	A schematic representation of the photometry technique. On the left, the galaxy of interest is shown in red, with a superimposed grid representing the pixels of the image. Starting with a pixel on the outside of the galaxy–marked here in red–we identify a circular background region. Pixels containing galaxy light (blue) are rejected, while those with only background (yellow) create our background sample. In the middle frame, we show the distribution of fluxes and uncertainties for those pixels. By convolving each flux measurement with a Gaussian kernel (sized according to the uncertainty of each point's flux) and summing, we create a histogram of flux values, such as shown on the right. The peak of that distribution is considered the mode; the width of the background distribution is found by tracing down from the peak until reaching a flux value with a frequency of ≈ 0.608 times the peak frequency	75
Figure 3.4	The effect of our background modeling and subtraction technique for Abell 209. Images are from the F814W filter: the original (left), after every galaxy has been photometered (center), and after the subtracted image has been resampled right	77
Figure 3.5	Comparison of photometric redshifts measured in this work to spectroscopic redshifts. The thin band traces the region where $ (z_p - z_s)/(1+z) < 0.05$. The full redshift coverage from z=0 to z=3.0 is shown on the left panel; a zoom-in to just z=0 to z=1.0 is shown on the right. Points are binned into hexagons, with the total density of points scaled logarithmically from 1 to 100 counts per hex, as indicated by the colorbar	80
Figure 3.6	Comparison to spectroscopic redshifts between the photometric redshifts measured in this work (orange) and those from the previously released CLASH photometric catalogs (purple). Only galaxies with spectroscopic redshifts within $ z_{\rm spec}-z_{\rm cluster} <0.05$ are shown. All outliers with $ z_{\rm phot}-z_{\rm spec} >0.2$ are shown at $ z_{\rm phot}-z_{\rm spec} =0.2$. The overlap between both histograms is shown in pink. Our technique better matches measured spectroscopic redshifts and has a significantly reduced ($\sim65\%$) fraction of outliers	81

Figure 3.7	Comparison between F814W magnitudes measured by the ASTRODEER Collaboration and this work for MACS0416. Points are binned into hexagons, with the total density of points scaled logarithmically from 1 to 30 counts per hex. Details of the fit are provided in the text. A comparison of the offsets is provided in the lower panel	84
Figure 3.8	Comparison between measured colors for MACS0416 in the ASTRODEE catalog and this work. Points are colored according to the deviation of the photometric redshift measured in this work and the cluster redshift, as indicated by the colorbar on the right	P 85
Figure 3.9	Comparison between redshifts measured by the ASTRODEEP Collaboration and this work for MACS0416. Points are binned into hexagons, with the total density of points scaled logarithmically from 1 to 30 counts per hex, as indicated by the colorbar. Details of the fit are provided in the text. A zoom-in to just matches below redshift 1.0 is provided on the right panel. The cluster redshift is indicated by the vertical and horizontal lines; the diagonal line is the identity line	87
Figure 3.10	Comparison between measured values of $E(z)$ N_{2500} and $E(z)$ M_{2500} from this work (purple) and (Hoekstra et al., 2011, orange). We also show our best-fit line in black, and a best fit to our data alone in pink. Details of the selection of N_{2500} are provided in the text	89
Figure 3.11	The k-corrected <i>i</i> -magnitude luminosity functions for all 25 CLASH clusters. Galaxies are shown binned in half-magnitude intervals. The best-fit Schechter luminosity function is shown in orange (purple) for X-ray selected (high magnification) clusters. Galaxies are plotted in order of increasing redshift. Best-fit values of α , M*, and ϕ * are provided in that order on each plot. Details of the fits are provided in the text	92
Figure 3.12	The measured slopes of the luminosity functions for all 25 CLASH clusters. We show the results for all cluster members in purple and for only those along the red sequence in orange. As a "flat slope" in magnitude-space is given by $\alpha = -1$, values greater than that show a luminosity function with fewer faint galaxies than galaxies at M*. We see a clear trend for a steepening in the faint end slope when only including red sequence members	95

Figure 3.13	The measured values of M^* for <i>i</i> -band luminosity functions of CLASH clusters. Shown in pink and orange are fits for <i>i</i> -band M^* values for all (orange) and only red (pink) galaxies, with evolution parameters from Loveday et al. (2012), although assuming the values of M^* for a double-power-law fit, as discussed in the text	95
Figure 3.14	Comparison between stellar masses and total masses within r_{2500} . Clusters are color-coded by redshift. Total masses are mostly drawn from lensing measurements by Merten et al. (2015) and Umetsu et al. (2016), but also include X-ray masses from Donahue et al. (2014). Stellar masses are derived from total cluster luminosity measurements, as described in the text, adjusted as needed to account for aperture effects. Shown are lines corresponding to $M_* = 0.01 M_{Tot}$ (solid), $M_* = 0.02 M_{Tot}$ (dot-dashed), and $M_* = 0.04 M_{Tot}$ (dotted).	100
Figure 4.1	Modeled SED fit to a galaxy in the field of MACS1423 ($z=0.545$). In this particular run, the redshift was allowed to vary. Upper limits are marked with downward pointing arrows. The empty box corresponds to the F555W filter; no data were taken using that filter for this cluster. The parameters of the shown best-fit spectrum are listed on the left	110
Figure 4.2	Best fit parameters (orange) and uncertainties (purple) from our SED fits. $t_{\rm form}$ is the age of the Universe at the cluster's redshift minus the SFR-weighted age. Only galaxies classified as cluster members are shown here. Derivation of these parameters is explained in the text	.114
Figure 4.3	The analog filter $g-r$ CMD for all 25 clusters. Shown on the left are those galaxies we call members, while those classified as non-members are plotted on the right. Hex bins are scaled logarithmically with the number of galaxies contained inside	117
Figure 4.4	The k-corrected $g-r$ CMD for all 25 clusters. Shown on the left are those galaxies we call members, while those classified as non-members are plotted on the right. A potential red sequence selection region is shown as a shaded box. Hex bins are scaled logarithmically with the number of galaxies contained inside	118
Figure 4.5	The $g-r$ vs. r color magnitude diagrams for galaxies classified as color members using analog filter magnitudes identified in Table 4.1. Clusters are plotted in increasing redshift order, starting in the upper left and finishing in the lower right; the second-lowest-redshift cluster is the second frame in the top row. Cluster names for all clusters except CLJ1226.9+3332 are displayed following the convention in Table 1.1.	120

Figure 4.6	The $g-r$ vs. r color magnitude diagrams for galaxies classified as color members using k-corrected magnitudes. The details of this plot are otherwise the same as for Figure 4.5	121
Figure 4.7	Measured red sequence slopes for the 25 CLASH clusters as a function of redshift. K-corrected values are shown in orange; observed values are in purple. The five clusters chosen for their magnification properties are marked with boxes, while the 20 X-ray selected clusters are denoted with circles. A best-fit of just the X-ray selected clusters for both sets of magnitudes is shown with solid lines; those same fits when including the strong lens sources are shown by dashed lines	123
Figure 4.8	Measured red sequence intercepts for the 25 CLASH clusters as a function of redshift. The five clusters chosen for their magnification properties are marked with orange boxes, while the 20 X-ray selected clusters are denoted with purple circles. A best fit of just the X-ray selected clusters is shown with a solid line; the same fit when including the strong lensing sources is shown by a dashed line. The expected behavior of a population with metallicity $Z\approx 0.5Z_{\odot}$ formed at $z{=}2$ is shown by the dotted black line	124
Figure 4.9	The metallicity function of cluster members, given by offset from and position along the red sequence. Hex bins are colored according to their median metallicity, as indicated by the colorbar. For legibility, only those bins with at least two counts are shown. g and r magnitudes are k-corrected. The median metallicity in one magnitude-wide bins is shown at the bottom of the plot, while the median metallicity in 0.05 magnitude-wide color bins is shown on the left	126
Figure 4.10	The SFR-weighted formation age function of cluster members. Hex bins are colored according to their median $t_{\rm form}$, which is described in the text, as indicated by the colorbar. For legibility, only those bins with at least two counts are shown. g and r magnitudes are k-corrected. The median age in 9 color bands are shown on the left of the figure and in 6 magnitude bins at the top	127
Figure 4.11	Stellar mass to <i>i</i> -band light ratios for all cluster members. In the bottom panel, we show the distribution of mass-to-light ratios with respect to overall luminosity, in Solar units. Only hex bins with at least one count are shown. In the upper panel, we show the distribution of mass-to-light ratios; purple is all galaxies, fuchsia is those galaxies $g-r$ colors within 0.1 magnitudes of the red sequence, and orange is those galaxies with $g-r$ colors within 0.05 magnitudes of the red sequence. The distribution of low mass-to-light ratio galaxies is dominated by low-luminosity galaxies off of the red sequence.	130

Figure 4.12	Measured slopes of the $g-r$ red sequence for the 25 CLASH clusters as a function of redshift. Measured slopes are shown in purple. We show two toy models: a metal-driven slope model (orange) and an age-driven slope model (pink), both of which are described in the text. Neither is able to completely model the behavior of the red sequence	134
Figure 4.13	Color-color plots showing how galaxies of different metallicities and ages occupy similar spaces in color-color plots that can be broken apart by further photometric information. In the top panel, tracks show lines of constant metallicity, while the bottom panel shows isochrones. Colors are from Johnson/Cousin filters. In the top (bottom) panel, lines are colored by increasing metallicity (age), with the bluest lines being the most metal-poor (youngest). Squares denote the youngest (most metal-poor) part of each track, while circles denote the oldest (most metal-rich). These tracks are taken from the MILES stellar library	136
Figure 5.1	Luminosity functions for the 25 CLASH cluster galaxies, taking only those within $ \Delta(g-r) < 0.2$ of the measured red sequence. This figure is otherwise the same as Figure 3.11	140
Figure 5.2	The $g-i$ vs. i color magnitude diagrams for galaxies classified as color members using k-corrected magnitudes. The details of this plot are otherwise the same as for Figure 4.6. The value of the $g-r$ slope is still shown to illustrate the change between filter sets	142

KEY TO SYMBOLS AND ABBREVIATIONS

α_{2000}
\mathring{A}
ACS Advanced Camera for Surveys, an HST instrument
AGN
BCG Brightest Cluster Galaxy
δ_{2000} Declination in J2000 Coordinates
E(z) Evolution Factor for the Hubble Expansion Parameter, E(z) = $\sqrt{\Omega_M(1+z)^3 + \Omega_\Lambda}$
$\rm H_0$ Current Value of the Hubble Constant, $\rm H_0 \sim 70~km~s^{-1}~Mpc^{-1}$
G Gravitational Constant, $G = 6.67 \times 10^{-8} \text{ erg cm g}^{-2}$
HST
ICM Intracluster Medium, hot intergalactic gas bound by gravity in a cluster
$k_{\rm B}$ Boltzmann Constant, $k_{\rm B}=1.381\times 10^{-16}~{\rm Erg~s^{-1}}$
keV Kiloelectron Volt, 1keV = 1.6×10^{-9} erg = 1.16×10^{7} K k $_{\rm B}^{-1}$
$\Lambda \mathrm{CDM}$ Cosmology with a non-zero cosmological constant and dark matter
L_{\odot} Luminosity of the Sun, $L_{\odot}=3.83\times10^{33}~{\rm erg~s^{-1}}$
M_{2500}
M_{\odot}
Ω_{Λ} Ratio of Density of Dark Energy to the Critical Density \times c^2 , $\Omega_{\Lambda} \sim 0.7$
$\Omega_{\rm M}$ Ratio of Density of Matter to the Critical Density, $\Omega_{\rm M}\sim 0.3$
pc

R_{2500}	Radius Inside Which Average Matter Density is $2500 \times \rho_c$
$ ho_c$	Critical Density of the Universe, $\rho_c \sim 10^{-29} \ \mathrm{g \ cm^{-3}}$
SED	Spectral Energy Distribution
T_X	X-Ray Temperature
WFC3	Wide Field Camera 3, an HST instrument
XMM X-ra	ay Multi-mirror Mission, XMM -Newton, an X-ray Telescope
7	Bedshift

Chapter 1

Introduction

1.1 The Grand Dichotomy

Individual galaxies, whether in a galaxy cluster or in the field, make up two separate populations, defined by color as being in either a "blue cloud" or a "red sequence" (Baldry et al., 2004; Bell et al., 2004; Wyder et al., 2007). These classifications also have morphological basis, as red sequence galaxies preferentially show early-type morphology (elliptical galaxies) while blue cloud members are dominated by late-type (spiral) morphology (Strateva et al., 2001), although color does not always act as a proxy for morphology (Lintott et al., 2008). This population bimodality extend even to large redshifts (Bell et al., 2004). We show the colors of approximately 250,000 galaxies selected from the Sloan Digital Sky Survey (SDSS) in Figure 1.1; the two populations are visible in this image.

Analysis of the physical properties of individual galaxies shows that the red sequence and blue cloud correspond to quiescent (undergoing very little to negligible star formation) and star-forming populations, respectively (Schiminovich et al., 2007). This color distinction is a consequence of ongoing star formation causing a stellar population to be blue. When it is actively forming stars, bright blue O and B stars dominate the light of a galaxy, making it appear blue. However, their short lifespans (on the order of 10's to 100's of millions of years, Hansen et al., 2004) means that, without constant replenishment of the O and B star pop-

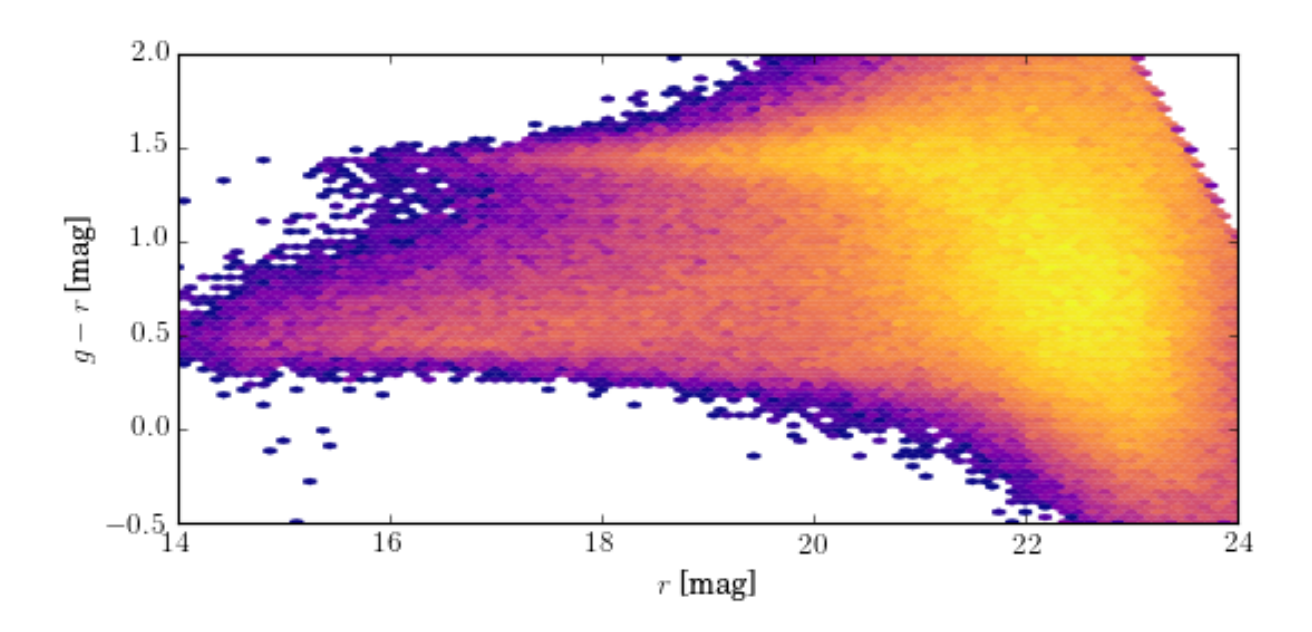


Figure 1.1 g-r color-magnitude diagram for 500000 extended galaxies cataloged from the Sloan Digital Sky Survey. These galaxies are the first 500000 in the 13th Data Release with g and r magnitudes brighter than 25 and with no constraints on position. Two galaxy populations are visible: the blue cloud and the red sequence. In color-magnitude diagrams presented in this dissertation, bluer colors are lower on the y-axis, while brighter galaxies are to the left of fainter galaxies.

ulation, galaxies will become red fairly soon after their most recent burst of star formation.

The red sequence is defined by a tight bunching in color space (Baum, 1959; Visvanathan & Sandage, 1977), yet it extends across a range of luminosity, such that it appears as a ridgeline in Figure 1.1. Red sequence galaxies have a range of luminosities, from bright to faint (e.g., Geller et al., 2012), so that the length of the red sequence implies that both large and small galaxies are having their star formation shut off.

Although the red sequence is tightly distributed in color, it is not centered on a uniform color across all luminosities; instead, the red sequence exhibits a slope, such that lower luminosity galaxies are bluer than their brighter counterparts. One possible origin for this slope is that it is caused by metallicity, whereby less massive objects are more metal-poor than brighter red sequence members (Kodama & Arimoto, 1997; Stanford et al., 1998; Ferreras et al., 1999; Gallazzi et al., 2006). Metals can make a stellar population redder in two ways: line blanketing and swelling. Metals will create absorption lines in a star; when they are at higher energies, they will absorb blue light (and then re-emit it at redder wavelengths), thereby reddening the star (Milne, 1928; Chandrasekhar, 1935; Sandage & Eggen, 1959). Also, an enhancement in metallicity causes a build up of radiation pressure, swelling a star and thereby reducing its effective temperature and making it redder (Conroy, 2013).

Due to how metallicity affects the colors of a stellar population, a metal-rich galaxy will be redder than a metal-poor galaxy (Faber, 1973; Worthey, 1994; Bruzual & Charlot, 2003; Maraston, 2005). If the red sequence slope is caused by metallicity differences, then the massive galaxies are therefore more metal-rich than less massive galaxies. A qualitative

origin for this relation is that supernovae-driven wind eject metals from galaxies, and the effectiveness of this process is inversely correlated with the depth of the potential well of the galaxy (Larson, 1974; Arimoto & Yoshii, 1987; Matteucci & Tornambe, 1987; Lilly et al., 2013; Voit et al., 2015). Because they have less gravitational pull, less massive galaxies may have had more metals ejected, and are therefore less metal-enriched than massive galaxies, which can retain metals in spite of supernova winds. Matching this behavior with simulations, however, has proven to be a difficult task (De Lucia et al., 2004a; de Rossi et al., 2007; Mouhcine et al., 2008).

A different origin of the red sequence slope could come from fainter galaxies having their star formation quenched at a later time. Even after several billion years, older galaxies are still somewhat redder than their younger counterparts with similar metallicity. As age and metallicity both affect observed colors of galaxies (this effect is called the "age-metallicity degeneracy," Worthey, 1994, 1999), disentangling the origin of the slope cannot be done by color alone. The origin can be easily tested, however, by investigating the redshift evolution of the red sequence; were it caused by age, the slope would become more pronounced as the relative age discrepancy between massive and less massive galaxies became more significant. Observations of the red sequence existing beyond even moderate redshifts ($z \approx 0.3$) shows that the trend must be driven by metallicity (Kodama & Arimoto, 1997; Kauffmann & Charlot, 1998; Kodama et al., 1998). Nevertheless, while metallicity appears to be the primary component to the red sequence slope, age variations can still have an effect (Ferreras et al., 1999; Terlevich et al., 1999; Trager et al., 2000; Poggianti et al., 2001; Rakos & Schombert, 2004).

One further clue about the origin of the red sequence comes from the intrinsic scatter, the dispersion about the nominal red sequence line beyond that caused by photometric measurement uncertainties. Zero scatter means that all galaxies of a given luminosity stopped forming stars at the same time, while a large scatter means that star-formation ceased over a range of times for galaxies of the same size. While early works on the red sequence found a tight scatter (Bower et al., 1992; Ellis et al., 1997; Stanford et al., 1998; Bower et al., 1998; Andreon, 2003; McIntosh et al., 2005), which implies that the shut-off time was consistent for galaxies of a given size, recent studies have seen that the measured scatter grows and evolves with redshift (Hilton et al., 2009; Papovich et al., 2010; Foltz et al., 2015). As the color offsets between two stellar populations of different ages decrease with time, relative to the size of their age gap, the measurement of scatter and its evolution constrains both when and over how long galaxies of a certain size stopped forming stars. Other works have shown that the intrinsic scatter is larger at the faint end of the red sequence (Conselice et al., 2002; Gallazzi et al., 2006), implying that fainter galaxies are either quenching (ceasing star formation) later or over a larger distribution of time.

1.2 The Red Sequence in Galaxy Clusters

While red galaxies – and the red sequence – occur in the field, they are significantly more common in dense environments such as galaxy clusters (Balogh et al., 2004; Sánchez-Janssen et al., 2008). Clusters are therefore the best way to study the formation mechanisms of the red sequence; not only is a cluster galaxy more likely to be red, but the enhanced galaxy density means we can observe more galaxies.

Hubble & Humason (1931) first noted the tendency for elliptical galaxies to be more common in clusters than in the field (see also Morgan, 1961), which was statistically confirmed by Dressler (1980). Spitzer & Baade (1951) considered the implication of this discrepancy and its relation to cluster formation and evolution; a cluster environment is prone to galaxy collisions, which would convert spirals to ellipticals.

One complicating factor is that clusters are not static objects, but grow and merge over time. Infalling galaxies experience a burst of star formation as they cross the cluster's virial radius (Porter et al., 2008), which appears to be sustained for $\approx 0.5-2.0$ billion years (Haines et al., 2015). Bahé et al. (2013) showed that galaxies falling through filaments are showing signs of hot gas stripping out to around five times the virial radius, as opposed to those equidistant from cluster centers but falling in through voids. As clusters are continually accreting galaxies throughout cosmic history (Berrier et al., 2009), these effects will have a major impact on the observable properties of the bulk population of cluster galaxies.

Despite these concerns, galaxy clusters still act as a fantastic laboratory for studying the red sequence. Hogg et al. (2004) found that for bright elliptical galaxies (with *i*-band absolute magnitudes $M_i < -20$), galaxy colors were mostly independent of the density of their environments. However, Tanaka et al. (2005) showed that the faint end of the red sequence is not as distinct for field galaxies as it is for cluster galaxies, implying a "downsizing" scenario in which more massive galaxies and galaxies in denser regions quench their star formation earlier.

If fainter galaxies are moving onto the red sequence at a later time, but the overall slope of the red sequence is caused by metallicity, then, to study the red sequence, we will need a way to measure the ages and metallicities of individual galaxies. The previously-mentioned age-metallicity degeneracy means that individual colors alone cannot constrain one property without assuming the other. However, while older populations and more metal-enriched galaxies are both redder than their younger or metal-poor counterparts, they do not redden in the same way. By sampling multiple colors, we can break the age-metallicity degeneracy for individual galaxies. In the astronomical context, colors are the difference in magnitudes measured in two filters. Since magnitudes are logarithmic measure of flux, the difference in magnitudes is a flux ratio. Conventionally, the bluer filter is placed first in the difference, so the larger the color, the redder the object.

Additionally, to study the faint galaxy population, we require a sample with both excellent angular resolution (to resolve galaxies smaller in size) and sufficient depth to observe faint galaxies. To obtain such observations, previous studies have mostly used nearby clusters, which are accessible to ground-based observations (e.g., Edwards & Fadda, 2011; Liu et al., 2011; Zhang et al., 2011; Tian et al., 2012; Ferrarese et al., 2016). However, to study the evolution of the red sequence, we also need temporal coverage. Based on these constraints, the ideal survey is a high resolution survey of multiple clusters spanning a large range of redshifts with sufficient filter coverage to break the age-metallicity degeneracy. We describe such a survey in the next section.

Table 1.1. Properties of CLASH Clusters

Full Name	Cluster	$lpha_{2000}{}^1$	$\delta_{2000}{}^2$	z^3	T_X^4 (keV)	$L_X^{4,5}$ (10 ⁴⁴ erg s ⁻¹)	${M_{2500}}^6 \\ (10^{14} h_{70}^{-1} M_{\odot})$
X-ray Selected:							
Abell 209	A209	01:31:52.54	-13:36:40.4	0.206	7.3 ± 0.54	12.7 ± 0.3	2.49 ± 0.36
Abell 383	A383	02:48:03.40	-03:31:44.9	0.187	6.5 ± 0.24	6.7 ± 0.2	1.42 ± 0.07
MACSJ0329.6-0211	m0329	03:29:41.56	-02:11:46.1	0.450	8.0 ± 0.50	17.0 ± 0.6	2.24 ± 0.24
MACSJ0429.6 - 0253	m0429	04:29:36.05	-02:53:06.1	0.399	6.0 ± 0.44	11.2 ± 0.5	2.49 ± 0.57
MACSJ0744.9+3927	m0744	07:44:52.82	+39:27:26.9	0.686	8.9 ± 0.80	29.1 ± 1.2	2.34 ± 0.24
Abell 611	A611	08:00:56.82	+36:03:23.6	0.288	7.9 ± 0.35	11.7 ± 0.2	3.20 ± 0.35
MACSJ1115.8+0129	m1115	11:15:51.90	+01:29:55.1	0.355	8.0 ± 0.40	21.1 ± 0.4	3.30 ± 0.42
Abell 1423	A1423	11:57:17.36	+33:36:37.5	0.213	7.1 ± 0.65	7.8 ± 0.2	1.82 ± 0.17
MACSJ1206.2-0847	m1206	12:06:12.09	-08:48:04.4	0.439	10.8 ± 0.60	43.0 ± 1.0	4.59 ± 0.68
WARP 1226.9+3332	c1226	12:26:58.25	+33:32:48.6	0.890	13.8 ± 2.80	34.4 ± 3.0	13.6 ± 2.90
MACSJ1311.0-0311	m1311	13:11:01.80	-03:10:39.8	0.494	5.9 ± 0.40	9.4 ± 0.4	1.80 ± 0.30
RXJ1347.5-1145	r1347	13:47:30.62	-11:45:09.4	0.451	15.5 ± 0.60	90.8 ± 1.0	9.14 ± 0.45
MACSJ1423.8+2404	m1423	14:23:47.88	+24:04:42.5	0.545	6.5 ± 0.24	14.5 ± 0.4	2.70 ± 0.50
MACSJ1532.8+3021	r1532	15:32:53.78	+30:20:59.4	0.362	5.5 ± 0.40	20.5 ± 0.9	3.00 ± 0.15
MACSJ1720.2+3536	m1720	17:20:16.78	+35:36:26.5	0.387	6.6 ± 0.40	13.3 ± 0.5	2.40 ± 0.29
Abell 2261	A2261	17:22:27.18	+32:07:57.3	0.224	7.6 ± 0.30	18.0 ± 0.2	3.24 ± 0.23
MACSJ1931.8-2635	m1931	19:31:49.62	-26:34:32.9	0.352	6.7 ± 0.40	20.9 ± 0.6	2.74 ± 0.12
RXJ2129.6+0005	r2129	21:29:39.96	+00:05:21.2	0.234	5.8 ± 0.40	11.4 ± 2.0	2.67 ± 0.25
MS 2137.3-2353	ms2137	21:40:15.17	-23:39:40.2	0.313	5.9 ± 0.30	9.9 ± 0.3	1.78 ± 0.12
Abell S1063	r2248	22:48:43.96	-44:31:51.3	0.348	12.4 ± 0.60	69.5 ± 0.1	7.19 ± 0.79
High Magnif.:							
MACSJ0416.1-2403	m0416	04:16:08.38	-24:04:20.8	0.397	7.5 ± 0.80	16.0 ± 0.9	3.8 ± 1.4
MACSJ0647.8+7015	m0647	06:47:50.27	+70:14:55.0	0.584	13.3 ± 1.80	32.5 ± 2.1	6.5 ± 3.2
MACSJ0717+3745	m0717	07:17:32.63	+37:44:59.7	0.548	12.5 ± 0.70	55.8 ± 1.1	5.4 ± 0.5
MACSJ1149.6+2223	m1149	11:49:35.69	+22:23:54.6	0.544	8.7 ± 0.90	30.2 ± 1.2	3.1 ± 0.8
MACSJ2129-0741	m2129	21:29:26.06	-07:41:28.8	0.570	9.0 ± 1.20	22.6 ± 1.5	4.7 ± 1.7

¹Right ascension.

1.3 CLASH: The Cluster Lensing and Supernova Survey with Hubble

Much of this work is based on observations conducted as part of the Cluster Lensing and Supernova survey with Hubble (CLASH), a *Hubble Space Telescope* (HST) Multi-Cycle Treasury program (for an overview of the survey, see Postman et al., 2012b). The CLASH sample consists of 25 galaxy clusters: 20 (16 from Allen et al., 2008) selected due to their dynami-

²Declination.

³Redshifts are from Postman et al. (2012b), except m0416, which was updated by Ebeling et al. (2014).

 $^{^4}$ From Postman et al. (2012b).

⁵Bolometric luminosity (from 0.1 - 100 keV).

⁶Chandra HSE masses from Donahue et al. (2014).

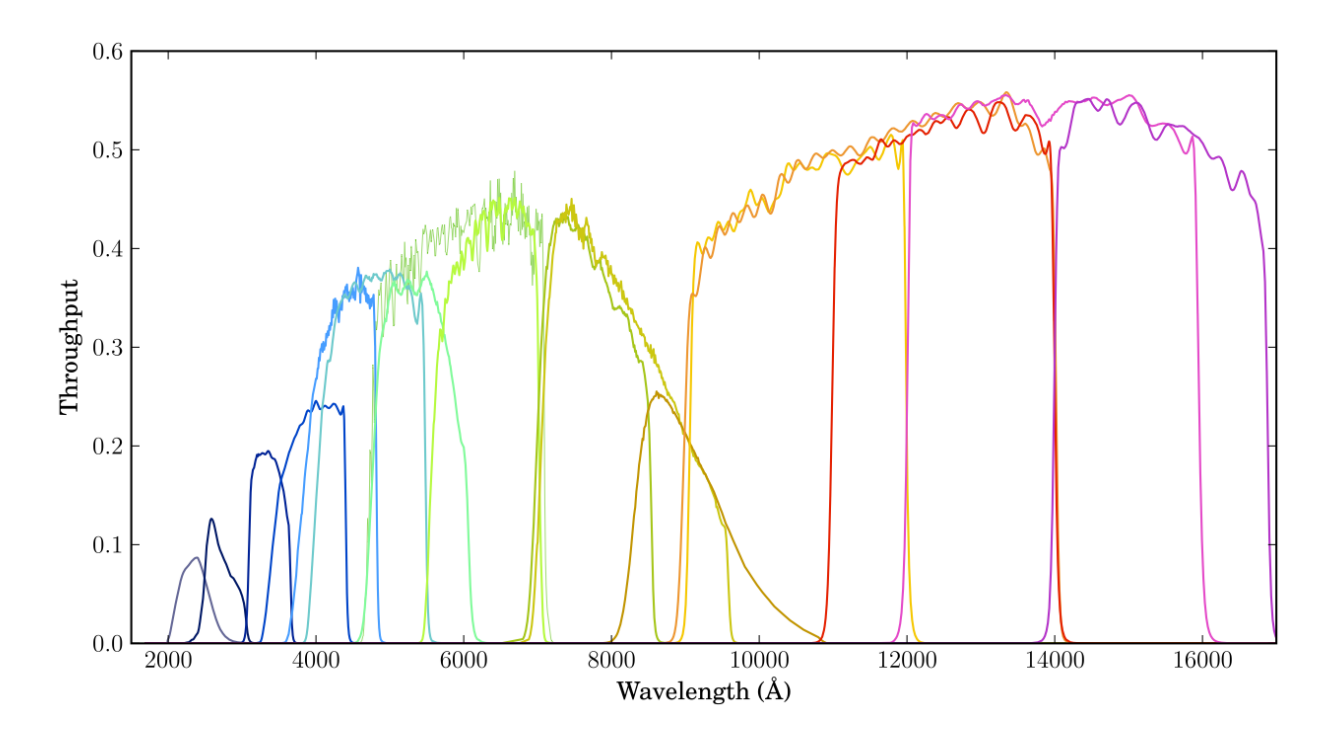


Figure 1.2 Fractional throughputs of the 17 filters used by CLASH. They are, from blue to red, F225W, F275W, F336W, F390W (all UVIS); F435W, F475W, F555W F606W, F625W, F775W, F814W, F850LP (all ACS); F105W, F110W, F125W, F140W, F160W (all WFC3-IR).

cally relaxed X-ray morphology, in order to quantify the distribution of dark matter within clusters, and 5 selected due to their strength as strong gravitational lenses, for exploring the high redshift Universe. These 25 systems were chosen from the Massive Cluster Survey (MACS, Ebeling et al., 2001, 2007, 2010) and the Abell catalog (Abell, 1958; Abell et al., 1989). All CLASH clusters have X-ray temperatures $kT \geq 5.0$ keV. Coordinates and observed properties of the 25 clusters are provided in Table 1.1.

CLASH observations consist of 524 orbits of Hubble time divided among the 25 clusters using 16 filters (with an additional filter used in archival observations). These filters, shown in Figure 1.2, span ≈ 2000 Å to ≈ 1.7 microns and the WFC3/UVIS, ACS, and WFC3/IR instruments. Filters were chosen to maximize photometric redshift results, based on the

results of a simulated re-observation of spectral energy distribution (SED) templates with the HST filter set. This selection was made so that 80% of objects with AB Mag < 26 in the F775W band would have accurate photometric redshifts ($\Delta z < 0.02(1+z)$). In addition, for all ACS and WFC3/IR filters, the 5 σ detection threshold was as faint or fainter than AB Mag = 26.7 for a circular aperture 0.4" in diameter.

For each filter, each cluster was observed for ≈ 1 to ≈ 2 orbits, with the total observations for each cluster totaling 20 orbits. Only 476 orbits of new observations were required for this, as archival images were also used. As an additional reserve, 50 orbits of followup observations were allotted to supernovae searches, drawn from a pool of 200 additional orbits shared with the Cosmic Assembly Near-IR Deep Extragalactic Legacy Survey (CANDELS; Grogin et al., 2011; Koekemoer et al., 2011).

Combining three different instruments presents the problem of differing fields of view. The largest detector, ACS, has 2 2048 \times 4096 pixel detectors, providing a coverage area of $202'' \times 202''$. WFC3/IR, however, has only a 1014×1014 pixel detector and an angular coverage of $136'' \times 123''$. Finally, WFC3/UVIS has 2 2051×4096 CCDs and a field of view of $162'' \times 162''$. These areas are expanded by the two separate pointings being turned 30° apart, but this comes at reduced depth for objects only in the field of view for one pointing.

Observations are first reduced by the MosaicDrizzle pipeline (Koekemoer et al. 2011, based on Fruchter & Hook 2002; Koekemoer et al. 2003). ACS/WFC data are first corrected for bias striping and charge transfer efficiency degradation (Anderson & Bedin, 2010). The pipeline then aligns every visit and every filter onto the same grid, providing astrometric

accuracy on the order of one milliarcsecond. Bad pixels and cosmic rays are rejected, which, along with read noise, statistical uncertainty, and accumulated dark current, are used to produce an inverse variance map for each filter and cluster. The output images are binned to several scales, but throughout this work we only use those images binned to 0.065" per pixel.

Since observations began, the CLASH data have been widely studied. Coe et al. (2013), Bradley et al. (2014), Bouwens et al. (2014), and McLeod et al. (2016) have found extremely-high redshift galaxies in the lensed backgrounds of these clusters. Numerous studies have been made of the lensing profiles of galaxy clusters (Zitrin et al., 2011; Limousin et al., 2012; Umetsu et al., 2012; Zitrin et al., 2012b; Gruen et al., 2013; Medezinski et al., 2013; Zitrin et al., 2013; Umetsu et al., 2014; Zitrin et al., 2015; Umetsu et al., 2016). Meneghetti et al. (2014), Merten et al. (2015), and Sereno et al. (2015) have used the CLASH data to refine the concentration-mass relation for galaxy clusters. Individual galaxies have been studied at a photometric (Jouvel et al., 2014) and spectroscopic (Biviano et al., 2013; Annunziatella et al., 2014; Girardi et al., 2015; Fogarty et al., 2015) level. Donahue et al. (2014) and Donahue et al. (2016) explored the X-ray properties of the 25 clusters. CLASH clusters are being further studied by the Hubble Frontier Fields (Coe et al., 2015) and the Grism Lens-Amplified Survey from Space (Schmidt et al., 2014).

Photometric catalogs of the CLASH cluster galaxies were published by Postman et al. (2012b), but these were not suitable to study the cluster populations. We show the distribution of photometric redshifts derived from this catalog for one of the clusters, MACS 1423, in orange in Figure 1.3. Not only is the cluster not apparent in the distribution, but much of the detected galaxy population appears to not be associated with the cluster, contrary to

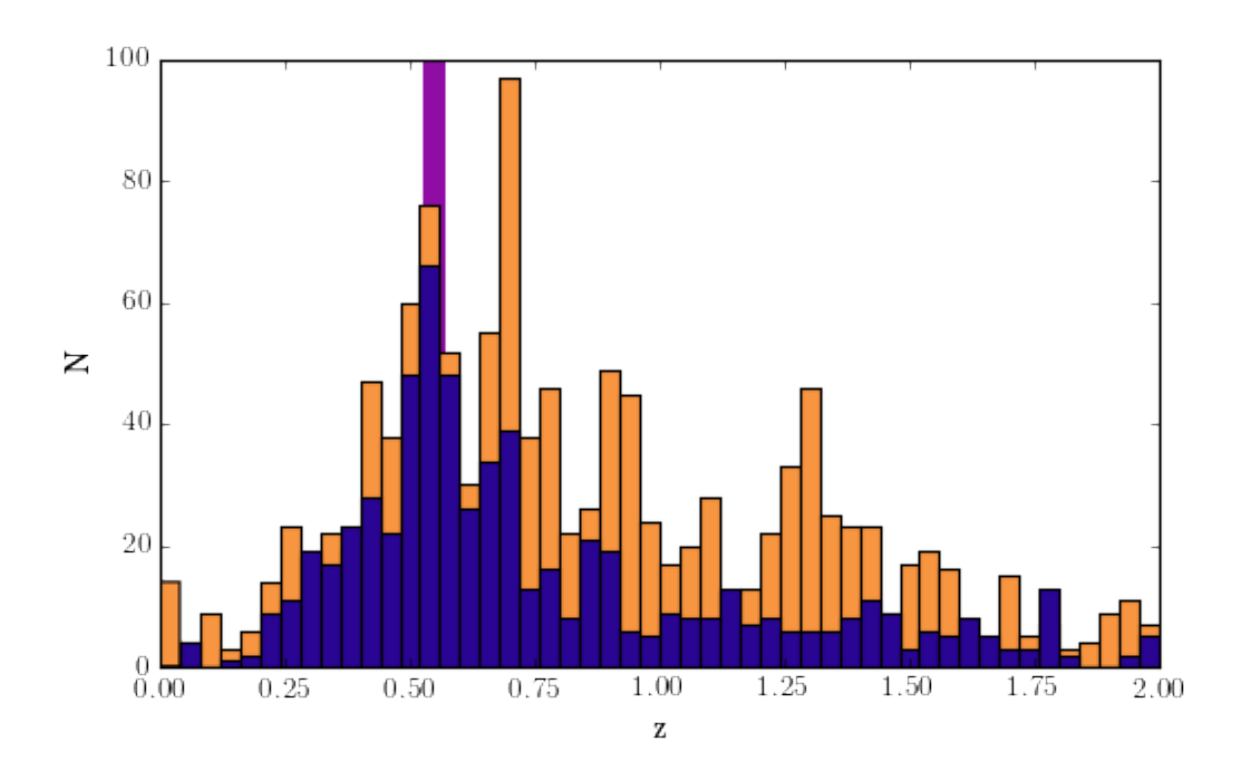


Figure 1.3 Distribution of photometric redshifts from CLASH cluster photometry for MACS 1423. Data from the original catalogs published by (Postman et al., 2012b) is shown in orange, while data from the photometry we present in this work are shown in dark blue. The spectroscopic redshift of the cluster is indicated by the purple bar. We only consider those galaxies with F814W magnitudes brighter than 25.5.

what a visual inspection of the Hubble image would indicate. To study the CLASH cluster population, we therefore needed to perform our own detection and photometry in a way that avoids the issues of the original catalog.

As the CLASH clusters are crowded fields, we use mode-based background subtraction to detect galaxies of all sizes with only a minimal amount of source decomposition; using a similar technique, we estimate the backgrounds of all the galaxies to photometer them individually. This technique, as well as our photometric results, are presented in Chapter 3. The improvement in photometry is seen in Figure 1.3, where the new data are shown in dark blue. We characterize our detection limit as at least $M^* + 5$ for most of the clusters.

In Chapter 4, we use our measured photometry to investigate the red sequence. Starting with SED fitting to measure ages and metallicities for each galaxy, we observe a metallicity gradient along the red sequence. Further investigation, however, shows evidence for a population evolving onto the red sequence at faint magnitudes.

1.4 X-ray Scaling Relations

Galaxy clusters are assumed, at least to first-order, to be self-similar; that is, smaller clusters are just scaled-down versions of larger clusters. Statistically, this means that the relationship between mass and other parameters is often represented by power-laws (Giodini et al., 2013), which, in turn, means those other parameters have their own self-similar scaling. We show an example of self-similar scaling for cluster X-ray properties in purple in Figure 1.4; the

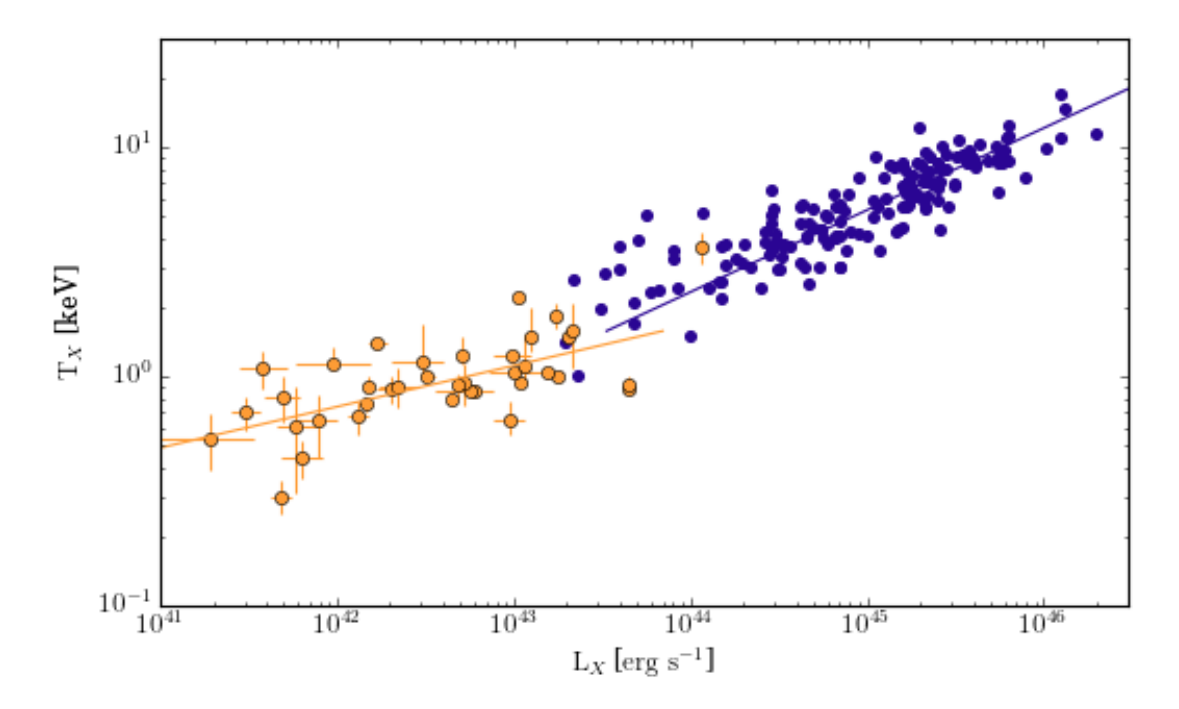


Figure 1.4 X-ray scaling between X-ray temperature and X-ray luminosity for a sample of clusters (purple, Wu et al., 1999) and groups (orange, Xue & Wu, 2000). Both samples show self-similar scaling characterized by a power-law, but the different slopes of that scaling between groups and clusters is evidence of a possible break in self-similarity.

data for this part of the figure are from Wu et al. (1999).

In science, we seek to compare nature with our models for nature. For clusters, the fundamental properties predicted by our cosmological models are total gravitating masses (otherwise known as virial masses), or, less commonly, velocity dispersion (which is related to the depth of the gravitational potential M/R). In the era of large surveys, well-calibrated scaling relations are a vital link in connecting easily-observed quantities (such as L_X or Y_{SZ}) with more easily-predicted but tougher-to-measure parameters such as virial mass.

Cluster of galaxies are extended astronomical sources, made up of an aggregate of individual galaxies, or, in the X-ray regime, a giant diffuse cloud of hot gas with no well-defined edge. Even assigning something as simple as a luminosity requires careful definition of the size of the region over which the measurement is made. Scaling relations can assist in defining such regions (usually some fraction of a virial radius or a radius inside which the total mass represents some scaled overdensity compared to the critical density) by allowing an estimate of the virial mass and the virial radius without directly measuring either. A number of studies use scaling relations to maximize the utility of their datasets, even when the derived parameters are not the end goal. Böhringer et al. (2013) used the X-ray luminosity-mass scaling relation to iteratively refine luminosity measurements by correcting for flux deficits in derived r_{500} apertures. Böhringer & Chon (2015) used scaling relations to convert a matter density fluctuation-derived cluster mass function into an X-ray luminosity function. To rule out a statistical fluctuation in Sunyaev-Zeldovich effect (SZE) data from a catalog of detected clusters, van der Burg et al. (2016) used a scaling relation. For these reasons, a more thorough understanding of scaling relations allows for more accurate estimation of these parameters.

Another use for studying scaling relations is to see where they deviate from expectations. Deviations from behavior predicted by a simple model can be used to adjust that model (e.g., Kaiser, 1991), and, by extension, further understand the behavior of galaxy clusters. Additionally, breaks from scaling relations at the extremes of cluster environments (particularly at the transition between cluster and group, e.g., Ponman et al., 1996; Helsdon & Ponman, 2000; Mulchaey, 2000; Osmond & Ponman, 2004; Sun et al., 2009; Eckmiller et al., 2011; Kettula et al., 2013; Connor et al., 2014) reveal the scale at which different processes – such as AGN heating (Puchwein et al., 2008; Fabjan et al., 2010; McCarthy et al., 2010; Gaspari et al., 2014) and supernova feedback (Balogh et al., 1999; Loewenstein, 2000; Kay, 2004) –

dominate in a cluster; how properties scale below this threshold is also used to quantify the effects of these events.

While a simple model predicts that $L_X \propto T^2 E(z)$, where E(z) is a correction for cosmological evolution, numerous studies have observed a luminosity-temperature (L-T) relationship better fit by $L_X \propto T^3 E(z)$ (Mushotzky, 1984; Edge & Stewart, 1991; David et al., 1993; Maughan et al., 2012). The implication of this discrepancy is that something other than gravitational collapse alone is heating cluster baryons. One mechanism to produce the observed L-T scaling is to increase the central gas entropy of clusters (Evrard & Henry, 1991; Kaiser, 1991; Ponman et al., 1999; Tozzi & Norman, 2001), which can be accomplished through energetic events, heating, and, indirectly, through cooling (and therefore the removal of low-entropy gas to make stars or non-X-ray emitting "cold" gas; Balogh et al., 1999; Bryan, 2000; Bower et al., 2001; Voit & Bryan, 2001; Voit et al., 2002; Muanwong et al., 2006). This central entropy floor makes it tougher to compress gas, thereby imposing an upper limit on central density. As X-ray luminosity is proportional to density squared (see Equation 1.8), this density limit reduces the cluster luminosity, such that the higher the baseline entropy floor, the lower the X-ray luminosity.

Along with the luminosity-temperature relation, we also consider the mass-temperature (M-T) and luminosity-mass (L-M) relations. The M-T relation steepens slightly for low-mass clusters and groups (Arnaud et al., 2005), but otherwise displays small intrinsic scatter (e.g., Mantz et al., 2010a), which is believed to appear as a consequence of substructure (O'Hara et al., 2006; Yang et al., 2009). Much like the L-T relation, the L-M relation is steeper than that predicted by gravity alone (e.g., Reiprich & Böhringer, 2002; Eckmiller et al., 2011),

and previous studies have seen large intrinsic scatter (Pratt et al., 2009; Vikhlinin et al., 2009).

Not only do cluster scaling relations follow a slope different from what is expected by predictions based solely on gravity, but a number of previous studies have found evidence for "breaks" in the power law relations, such that low-mass groups follow a different power law than massive clusters (Ponman et al., 1996; Xue & Wu, 2000; Eckmiller et al., 2011; Stott et al., 2012). We show an example of such a break in Figure 1.4; group observations (orange) from Xue & Wu (2000) are best-fit by a different power-law than cluster observations (purple) from Wu et al. (1999). These breaks in self-similarity can be tied to the mechanism that raises the cluster entropy; if, e.g., supernovae and active galactic nuclei (AGN) are raising the cluster entropy, these events will have a larger effect on groups, which have shallower gravitational potential wells. Characterizing the location and magnitude of breaks from self-similarity, as well as the deviation from gravity-only scaling, is important to constrain the astrophysics of clusters. Breaks can also be caused by inconsistent choices for the regions over which luminosity, temperature, and mass are measured. Finally, breaks can also be caused by biases in the sample selection and changes in the intrinsic scatter as a function of cluster size (so a "break" in a power-law relation might not be a break at all). Therefore, in this work we have to be careful in our definitions of "luminosity," "temperature," and "mass," in the sense that the volume over which those quantities are measured must be specified and consistent from cluster to cluster.

To find the predicted behavior of scaling relations, we begin with a way to relate mass

to radius. If r_{Δ}^{-1} (such as r_{2500}) is defined to be the radius in which the average density of a system is $\Delta \times \rho_c$, where ρ_c is the critical density, then

$$M_{\Delta} = \frac{4\pi}{3} \Delta \rho_c r_{\Delta}^3. \tag{1.1}$$

We can then substitute the critical density with E(z) using

$$\rho_c = \frac{3 (H_0 E(z))^2}{8\pi G} \propto E(z)^2, \tag{1.2}$$

where H_0 is the Hubble constant and G is the gravitational constant. Rearranging Equations 1.1 and 1.2, we have an expression for the radius

$$R \propto E(z)^{-2/3} M^{1/3}$$
. (1.3)

With this expression, we can substitute the radius out of any expression and replace it with observable quantities.

Next, we consider the equation of hydrostatic equilibrium,

$$\frac{dP}{dr} = -GM(r)\rho(r)r^{-2}. (1.4)$$

We assume that the mass in hydrostatic equilibrium can be represented by an ideal gas, so that the pressure is given by

$$P = \frac{\rho}{m} k_{\rm B} T,\tag{1.5}$$

 $^{^{1}}$ Throughout this work, we denote values with subscripts "2500" and "500"; these correspond to values measured within radii given by this formula, or to the radii themselves.

where m is the mass of a particle, not of the system. By multiplying Equation 1.4 by r/P, using Equation 1.3 to set $M/r \propto (ME(z))^{2/3}$, and using Equation 1.5 to set $\rho/P \propto T^{-1}$, we find

$$\frac{d\ln P}{d\ln r} = -G (M(r)/r) (\rho(r)/P) \propto (ME(z))^{2/3} T^{-1}.$$
 (1.6)

We therefore come upon a scaling relation between mass and temperature:

$$M \propto T^{3/2}/E(z). \tag{1.7}$$

Under the assumption that the hot cluster gas is in hydrostatic equilibrium and follows the ideal gas law, this model allows us to convert observed gas temperatures to masses and vice versa.

To extend these relations to X-ray luminosity, we assume that all of the emission of the hot gas comes from bremsstrahlung. In that case, we use a simplified version of the equation of bremsstrahlung emission,

$$L_X \propto M \ \rho \ T_X^{1/2}. \tag{1.8}$$

We convert the density term to an evolution term with Equation 1.2 and reduce this expression to temperature alone using our conversion from mass to temperature, Equation 1.7. This leaves us with a scaling relation between the X-ray luminosity and gas temperature,

$$L_X \propto T^2 E(z). \tag{1.9}$$

By completing the triangle created by Equations 1.7 and 1.9, we have

$$L_X/E(z) \propto M^{2/3} E^{2/3}(z),$$
 (1.10)

a way to connect easily-obtained redshift and luminosity measurements of clusters to estimates of their mass.

One of the important predictions of the gravity-only model is that these relationships have a dependence on redshift, caused by the evolution of the critical density of the Universe (Equation 1.2). In contrast, non-gravitational effects should have a more significant redshift dependence if they depend on the evolution of the astrophysical processes, such as the AGN luminosity function (Georgakakis et al., 2015; Fotopoulou et al., 2016). Due to the difficulty in obtaining good measurements for higher-redshift clusters, previous studies have been inconclusive about the characterization of evolution (e.g., Ettori et al., 2004; Kotov & Vikhlinin, 2005; O'Hara et al., 2006; Pacaud et al., 2007; Reichert et al., 2011).

In Chapter 2 we investigate a sample of 15 galaxy clusters with weak-lensing masses derived from HST data; we use new and archival observations from XMM-Newton to measure X-ray luminosities and temperatures for these systems. Due to how these clusters were randomly selected for snapshot HST observations from a complete, X-ray flux-limited sample of clusters of galaxies (Vikhlinin et al., 1998; Mullis et al., 2003), they are effectively an X-ray flux-limited sample, with X-ray properties consistent with being at the boundary between groups and clusters and with redshifts covering 0.3 < z < 0.6.

To maximize the utility of our sample, we also include 50 more massive galaxy clusters in the same redshift regime from Mahdavi et al. (2013, 2014) as well as a sample of low-redshift groups from Sun et al. (2009). Both samples were selected based on their X-ray characteristics. We find no evidence for a break in the three scaling relations between luminosity, temperature, and mass for these samples. In comparison with the low-redshift groups, we also find a weak statistical preference for the expected self-similar evolution.

Chapter 2

X-Ray Scaling Relations for Moderate

Luminosity Galaxy Clusters at

${\bf Intermediate} \ {\bf Redshift}^1$

We present new X-ray temperatures and improved X-ray luminosity estimates for 15 new and archival XMM-Newton observations of galaxy clusters at intermediate redshift with mass and luminosities near the galaxy group/cluster division ($M_{2500} < 2.4 \times 10^{14} \, h_{70}^{-1} \, \mathrm{M}_{\odot}$, $L < 2 \times 10^{44} \, \mathrm{erg \, s^{-1}}$, 0.3 < z < 0.6). These clusters have weak-lensing mass measurements based on $Hubble \, Space \, Telescope$ observations of clusters representative of an X-ray selected sample (the $ROSAT \, 160\mathrm{SD} \, \mathrm{survey}$). The angular resolution of XMM-Newton allows us to disentangle the emission of these galaxy clusters from nearby point sources, which significantly contaminated previous X-ray luminosity estimates for six of the fifteen clusters. We extend cluster scaling relations between X-ray luminosity, temperature, and weak-lensing mass for low-mass, X-ray-selected clusters out to redshift ~ 0.45 . These relations are important for cosmology and the astrophysics of feedback in galaxy groups and clusters. Our joint analysis with a sample of 50 clusters in a similar redshift range but with larger masses $(M_{500} < 21.9 \times 10^{14} \, \mathrm{M}_{\odot}, \, 0.15 \leq z \leq 0.55)$ from the Canadian Cluster Comparison Project

¹This chapter is taken mostly word-for-word from Connor et al. (2014), as published in the Astrophysical Journal

finds that within r_{2500} , $M \propto L^{0.44\pm0.05}$, $T \propto L^{0.23\pm0.02}$, and $M \propto T^{1.9\pm0.2}$. The estimated intrinsic scatter in the M-L relation for the combined sample is reduced to $\sigma_{\log(M|L)} = 0.10$, from $\sigma_{\log(M|L)} = 0.26$ with the original ROSAT measurements. We also find an intrinsic scatter for the T-L relation, $\sigma_{\log(T|L)} = 0.07 \pm 0.01$.

2.1 Introduction

Simulations of cosmological structure formation show clusters and filaments of dark matter growing from a set of random initial perturbations into a cosmic web (e.g., Springel et al., 2005; Boylan-Kolchin et al., 2009; Klypin et al., 2011). The statistical properties of this cosmic web are extremely sensitive to the values of certain cosmological parameters, particularly Ω_M and σ_8 , the amplitude of the initial perturbation spectrum (e.g., Eke et al., 1996; Bahcall & Fan, 1998; Holder et al., 2001; Allen et al., 2011).

This cosmic web of dark matter is easiest to investigate by studying its most massive systems, which are clusters of galaxies. About 85% of a cluster's mass is composed of dark matter, while nearly all of the rest is intergalactic hot gas, with a trace amount contributed by stars (Rosati et al., 2002; Voit, 2005; LaRoque et al., 2006). The hot gas is confined by the cluster's gravitational potential and radiates X-rays, providing powerful diagnostics for properties of the host cluster, including its mass, baryonic content, and dynamic status.

Accurate measurements of galaxy cluster masses are useful for more than just describing individual systems; galaxy cluster masses are needed to verify models of large-scale structure formation (Jenkins et al., 2001; Grossi et al., 2007; Vikhlinin et al., 2009) and to constrain

cosmological parameters (Tinker et al., 2008; Rozo et al., 2010; Mantz et al., 2010b; Bhattacharya et al., 2011). One way to accurately measure the projected mass of a cluster is through measurements of gravitational lensing (Hoekstra et al., 2013). However, performing such measurements is prohibitively expensive for large samples of clusters and difficult for low redshift clusters. To this end, scaling relations have been empirically calibrated to connect observed properties to masses. Examples of this include $L_X - M_X$, $M_X - T_X$, and $M_X - Y_X$ relations.

Early work by Kaiser (1986) showed that these relations can be cast analytically for the case where cold gas falls into preexisting dark matter structures. Those early relations predicted clusters that were overluminous for a given temperature compared to observations. So Kaiser (1991) and Evrard & Henry (1991) showed that preheating could increase the entropy of intergalactic gas. Such a "preheating" model elevates the entropy of the gas, preventing the gas from getting too dense. These predicted $L_X - M_X$ and $T_X - M_X$ relations were roughly consistent with observations. This expectation that clusters would follow such laws over a large range of M_X , with standard evolutionary factors, is known as self-similarity (Navarro et al., 1997; Bower, 1997; Bryan & Norman, 1998). The scale-free nature of this behavior arises because the gravitational potential dominates over other energy sources, and gravity is scale-free.

Previous work has shown possible deviations from self-similarity at masses approaching those of galaxy groups (e.g., Ponman et al., 1996; Xue & Wu, 2000; Eckmiller et al., 2011; Stott et al., 2012), possibly due to the increasing fractional contribution of local feedback processes to the cluster energy budget compared to the gravitational potential. The exact

magnitude and behavior of this deviation is not yet defined, but it has been qualitatively reproduced in numerical work (Puchwein et al., 2008; Fabjan et al., 2010).

A full understanding of the deviation from self-similarity can only come through a thorough exploration of the cluster parameter space – across cluster mass ranges and redshifts. One under-sampled regime is at moderate redshift and low mass. Clusters with these properties offer us the ability to answer the questions of how scaling relations change from high redshift to low redshift and whether there is any evolution in the low-mass behavior of these relations.

Recent work by Hoekstra et al. (2011) provided weak lensing mass measurements from the *Hubble Space Telescope* (HST) of 25 galaxy clusters occupying this redshift regime. That work lacked high-quality X-ray observations for most of the objects, however. We use observations with the *XMM-Newton* satellite to study the X-ray characteristics of this sample and to constrain X-ray property and mass scaling relations for this redshift and mass regime.

The structure of this chapter is as follows. In Section 2.2, we describe the properties of our sample, while our analysis techniques are described in Section 2.3. The results of our analysis are presented in Section 2.4. In particular, we discuss our fits of three scaling relations involving X-ray luminosity, temperature, and weak lensing mass. Finally, we compare our results to other published works in Section 2.5 and Appendix A. Throughout this paper, we assume a flat Λ CDM cosmology with $\Omega_M = 0.3$, and $H_0 = 70 \,\mathrm{km\,s^{-1}\,Mpc^{-1}}$.

Table 2.1. Sample Properties

Cluster Name	$\alpha_{2000}^{\mathrm{a}}$	$\delta_{2000}{}^{\mathrm{a}}$	$lpha_{2000}{}^{ m b}$	$\delta_{2000}{}^{ m b}$	z^c	$^{N_{H}^{\rm d}}_{10^{20}~{\rm cm}^{-2}}$	$\frac{r_{2500}^{\mathrm{a}}}{h_{70}^{-1}\;\mathrm{Mpc}}$
RXJ0056.9-2740	$00^{\rm h}56^{\rm m}56.98^{\rm s}$	$-27^{\circ}40^{\mathrm{m}}29.9^{\mathrm{s}}$	$00^{\rm h}56^{\rm m}57.9^{\rm s}$	$-27^{\circ}40^{\mathrm{m}}29.3^{\mathrm{s}}$	0.563	1.79	0.270
RXJ0110.3+1938	$01^{\rm h}10^{\rm m}18.22^{\rm s}$	$+19^{\circ}38^{\mathrm{m}}19.4^{\mathrm{s}}$	$01^{\rm h}10^{\rm m}18.2^{\rm s}$	$+19^{\circ}38^{\mathrm{m}}18.7^{\mathrm{s}}$	0.317	3.82	0.293
RXJ0522.2 - 3625	$05^{\rm h}22^{\rm m}15.48^{\rm s}$	$-36^{\circ}24^{\mathrm{m}}56.1^{\mathrm{s}}$	$05^{\rm h}22^{\rm m}15.4^{\rm s}$	$-36^{\circ}24^{\mathrm{m}}55.7^{\mathrm{s}}$	0.472	3.63	0.313
RXJ0826.1 + 2625			$08^{\rm h}26^{\rm m}08.03^{\rm s}$	$+26^{\circ}25^{\mathrm{m}}16.7^{\mathrm{s}}$	0.351	3.39	0.157
RXJ0847.1+3449	$08^{\rm h}47^{\rm m}11.79^{\rm s}$	$+34^{\circ}48^{\mathrm{m}}51.8^{\mathrm{s}}$	$08^{\rm h}47^{\rm m}11.7^{\rm s}$	$+34^{\circ}48^{\mathrm{m}}51.9^{\mathrm{s}}$	0.560	2.92	0.452
RXJ0957.8+6534	$09^{\rm h}57^{\rm m}51.22^{\rm s}$	$+65^{\circ}34^{\mathrm{m}}25.1^{\mathrm{s}}$	$09^{\rm h}57^{\rm m}51.1^{\rm s}$	$+65^{\circ}34^{\mathrm{m}}26.1^{\mathrm{s}}$	0.530	5.32	0.257
RXJ1117.4+0743	$11^{\rm h}17^{\rm m}26.04^{\rm s}$	$+07^{\circ}43^{\mathrm{m}}38.3^{\mathrm{s}}$	$11^{\rm h}17^{\rm m}26.1^{\rm s}$	$+07^{\circ}43^{\mathrm{m}}41.0^{\mathrm{s}}$	0.477	3.59	0.280
RXJ1354.2 - 0221	$13^{ m h}54^{ m m}17.19^{ m s}$	$-02^{\circ}21^{\mathrm{m}}59.0^{\mathrm{s}}$	$13^{\rm h}54^{\rm m}17.2^{\rm s}$	$-02^{\circ}21^{\mathrm{m}}59.4^{\mathrm{s}}$	0.546	3.22	0.428
RXJ1642.6+3935	$16^{\rm h}42^{\rm m}38.35^{\rm s}$	$+39^{\circ}36^{\mathrm{m}}10.4^{\mathrm{s}}$	$16^{\rm h}42^{\rm m}38.4^{\rm s}$	$+39^{\circ}36^{\mathrm{m}}07.9^{\mathrm{s}}$	0.355	1.20	0.239
RXJ2059.9 - 4245	$20^{\rm h}59^{\rm m}54.92^{\rm s}$	$-42^{\circ}45^{\mathrm{m}}32.1^{\mathrm{s}}$	$20^{\rm h}59^{\rm m}54.9^{\rm s}$	$-42^{\circ}45^{\mathrm{m}}34.8^{\mathrm{s}}$	0.323	3.13	0.280
RXJ2108.8 - 0516	$21^{\rm h}08^{\rm m}51.17^{\rm s}$	$-05^{\circ}16^{\mathrm{m}}58.4^{\mathrm{s}}$	$21^{\rm h}08^{\rm m}51.2^{\rm s}$	$-05^{\circ}16^{\mathrm{m}}57.6^{\mathrm{s}}$	0.319	6.30	0.210
RXJ2139.9 - 4305	$21^{\rm h}39^{\rm m}58.22^{\rm s}$	$-43^{\circ}05^{\mathrm{m}}13.9^{\mathrm{s}}$	$21^{\rm h}39^{\rm m}58.3^{\rm s}$	$-43^{\circ}05^{\mathrm{m}}14.2^{\mathrm{s}}$	0.376	1.63	0.292
RXJ2146.0+0423	$21^{\rm h}46^{\rm m}05.52^{\rm s}$	$+04^{\circ}23^{\mathrm{m}}14.3^{\mathrm{s}}$	$21^{\rm h}46^{\rm m}05.6^{\rm s}$	$+04^{\circ}23^{\mathrm{m}}02.6^{\mathrm{s}}$	0.531	4.82	0.436
RXJ2202.7 - 1902	$22^{\rm h}02^{\rm m}45.50^{\rm s}$	$-19^{\circ}02^{\mathrm{m}}21.1^{\mathrm{s}}$	$22^{\rm h}02^{\rm m}45.5^{\rm s}$	$-19^{\circ}02^{\mathrm{m}}20.1^{\mathrm{s}}$	0.438	2.44	0.152
RXJ2328.8 + 1453	$23^{\rm h}28^{\rm m}52.27^{\rm s}$	$+14^{\circ}52^{\mathrm{m}}42.8^{\mathrm{s}}$	$23^{\rm h}28^{\rm m}52.3^{\rm s}$	$+14^{\circ}52^{\mathrm{m}}42.7^{\mathrm{s}}$	0.497	3.88	0.254

^aCoordinates and r_{2500} from Hoekstra et al. (2011).

^bCoordinates from XMM centroid (see Section 2.4.2).

^cCluster redshift from Mullis et al. (2003).

^dColumn density from Kalberla et al. (2005).

Table 2.2. Observations of Clusters

Cluster Name	OBSID	Exposure Time (s)	Usable MOS1	Exposure MOS2	Time pn
RXJ0056.9-2740	0111282001	8876	8190	8017	4135
RXJ0110.3+1938	0500940101	32818	18883	18497	6973
RXJ0522.2 - 3625	0065760201	31919	31333	31317	26904
	0302580901	31110	20077	20284	16481
RXJ0826.1+2625	0691670201^{a}	48742	31516	31419	23135
	0603500301^{a}	40509	19967	20463	
RXJ0847.1+3449	0107860501	91419	58708	58333	
RXJ0957.8+6534	0502430201	72070	44762	45062	30090
RXJ1117.4+0743	0203560401	86515	81073		56293
	0203560201	81913	71366		57255
	0082340101	63206	60889		43232
RXJ1354.2 - 0221	0112250101	33646	24584	24000	
RXJ1642.6+3935	0603500701^{a}	23917	17108	17133	11099
RXJ2059.9 - 4245	0691670101^{a}	57915	56794	56571	41238
RXJ2108.8 - 0516	0110860101	38116	34637	34668	
RXJ2139.9-4305	0603501001^{a}	41916	36715	36875	19382
RXJ2146.0+0423	0302580701	47120	24091	24081	18316
RXJ2202.7 - 1902	0203450201	64117	27842	26081	6919
RXJ2328.8+1453	0502430301	104910	94004	94249	70516

^aNew data.

2.2 Data and Analysis

Our sample is based on 25 galaxy clusters first detected in the *ROSAT* 160 Square Degree Survey. Vikhlinin et al. (1998) describe the initial survey, and a reanalysis with spectroscopic redshifts comes from Mullis et al. (2003). These 25 clusters were further studied with an HST snapshot program (PI: Donahue) of one orbit per cluster with the F814W filter. Due to the nature of the snapshot program, the clusters were randomly selected from a master list of 72 clusters. Hoekstra et al. (2011) used those images to estimate weak-lensing masses for these clusters. The focus of this work is to improve and augment the X-ray measurements of these clusters with observations with *XMM-Newton*. Along with new observations, we used archival data to supplement the cluster sample with new uniform measurements of X-ray properties.

We searched the archive of XMM-Newton observations with the XMM-Newton Science Archive (XSA) v7.2 within a 15' radius of the cluster positions given in Hoekstra et al. (2011). As of June 28, 2013, we found 27 observations that included one of the clusters. We excluded 9 because they were too short and excluded 4 that were unusable due to excessive particle contamination from flares, leaving 14 observations of 11 clusters. We supplemented these with five new observations of four clusters. All observations were taken with the European Photon Imaging Camera (EPIC), which consists of two MOS cameras (Turner et al., 2001) and the pn camera (Strüder et al., 2001). Cluster properties drawn from earlier works are provided in Table 2.1. Hydrogen column density, N_H, is taken from the compilation by Kalberla et al. (2005). The datasets used in this work are listed in Table 2.2.

Our new observations are presented in Figure 2.1. Our data are shown as smoothed X-ray contours from combined EPIC images overlaid on HST images of the cluster using the Advanced Camera for Surveys / Wide Field Channel F814W filter. Combined X-ray products were created using the XMM-Newton Science Analysis System (SAS) images script binning to 2" and smoothing with a Gaussian FWHM of 15" in the energy range of 0.4 - 8.0 keV. Contours are levels of 10^{-6} count s⁻¹ arcsec⁻², with the lowest displayed contour corresponding to 10^{-6} count s⁻¹ arcsec⁻² for RXJ0826.1+2625 and RXJ2059.9-4245 and 2×10^{-6} count s⁻¹ arcsec⁻² for RXJ1642.6+3935 and RXJ2139.9-4305.

Observations were reduced using the XMM-Newton SAS version $12.0.1.^2$ Bad time intervals were defined based on the count rate of high energy events (>10 keV) in 100-second bins; time periods where those exceeded 0.35 count s⁻¹ (MOS) or 0.40 count s⁻¹ (pn)

²http://xmm.esac.esa.int/sas/

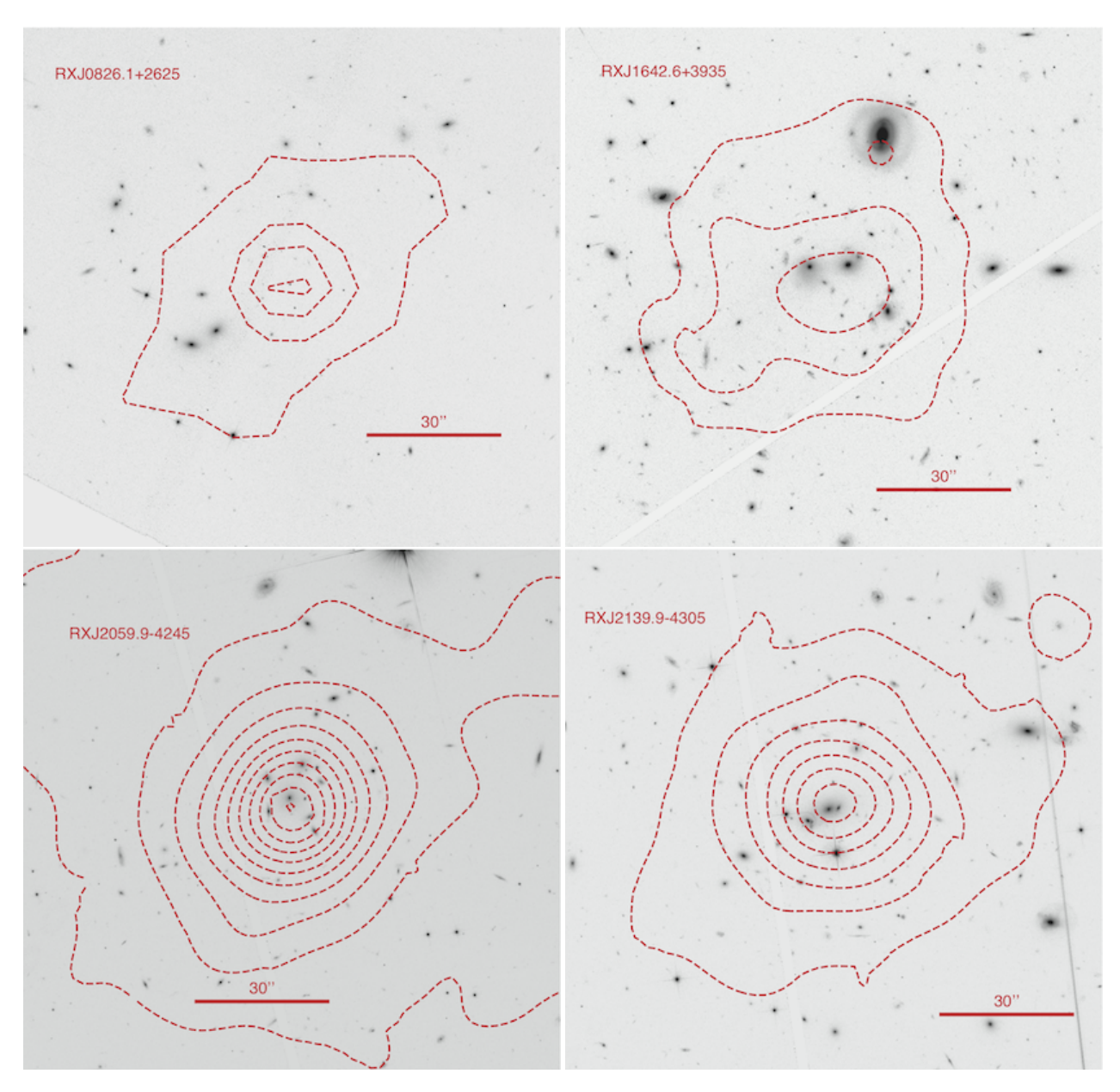


Figure 2.1 Gaussian-smoothed X-ray emission contours overlaid on *Hubble Space Telescope* images of the four clusters we observed in this work. Contours are spaced at intervals of $10^{-6} \, \mathrm{count} \, \mathrm{s}^{-1} \, \mathrm{arcsec}^{-2}$, with the minimum level for each cluster described in Section 2.2.

were excluded. One exception to this was the observation of RXJ1354.2–0221, 0112250101, which had an abnormally high high-energy background. To avoid overfiltering the data, we increased the count rate limits to 0.5 count s⁻¹ (MOS) and 0.65 counts s⁻¹ (pn) for this observation only. For all observations the filtering levels were scrutinized to ensure that periods of significant flaring were entirely removed. When necessary, we made the high-energy count rate thresholds more stringent.

Point sources were detected using the individual tasks that make up edetect_chain. This task uses eboxdetect to perform a sliding box detection of sources with a local background, then has esplinemap generate a source-corrected global background, which a second run of eboxdetect uses to find sources again. Sources were selected from these detections by hand after a visual inspection. Table 2.3 lists the coordinates and radii of our masks. All identified sources were excluded from the spectral extraction regions.

We then extracted spectra from the observations in three different apertures using standard options ("#XMMEA_EM" for MOS data and "#XMMEA_EP" for pn). For all cameras we selected single and double events, filtering with "PATTERN <12" for MOS and "PATTERN <4" for pn. Our first aperture was $300 \ h_{70}^{-1}$ kpc, which was chosen to compare our measured fluxes against those of Vikhlinin et al. (1998). Our second aperture was a circle with radius equal to the value of r_{2500} given in Table 2 of Hoekstra et al. (2011). r_{2500} is the radius inside which the estimated mean mass density is 2500 times the critical density at the redshift of the cluster ³. Weak lensing mass measurements used in this work were derived for r_{2500} for

 $^{^3}$ Similarly, r_{500} is the radius where average density is 500 times the critical density. Throughout this work, we use the subscripts 2500 and 500 to denote that quantities are measured inside these radii.

Table 2.3: Masked Sources

α_{2000}	δ_{2000}	radius	
		()	
$0^{\mathrm{h}}57^{\mathrm{m}}04.704^{\mathrm{s}}$	$-27^{\circ}40^{\mathrm{m}}23.52^{\mathrm{s}}$	21.46210	
$0^{\mathrm{h}}57^{\mathrm{m}}04.103^{\mathrm{s}}$	$-27^{\circ}41^{\mathrm{m}}11.52^{\mathrm{s}}$	21.46210	
$0^{\mathrm{h}}57^{\mathrm{m}}09.219^{\mathrm{s}}$	$-27^{\circ}39^{\mathrm{m}}39.49^{\mathrm{s}}$	20.51370	
$0^{\mathrm{h}}56^{\mathrm{m}}49.649^{\mathrm{s}}$	$-27^{\circ}40^{\mathrm{m}}07.55^{\mathrm{s}}$	25.76800	
$0^{\mathrm{h}}56^{\mathrm{m}}48.444^{\mathrm{s}}$	$-27^{\circ}40^{\mathrm{m}}59.54^{\mathrm{s}}$	12.87300	
$1^{\rm h}10^{\rm m}11.496^{\rm s}$	$19^{\circ}38^{\mathrm{m}}56.76^{\mathrm{s}}$	26.30820	
$1^{\rm h}10^{\rm m}11.448^{\rm s}$	19°40 ^m 27.12 ^s	22.24570	
$1^{\rm h}10^{\rm m}28.704^{\rm s}$	$19^{\circ}38^{\mathrm{m}}41.64^{\mathrm{s}}$	23.60290	
$1^{\rm h}10^{\rm m}22.008^{\rm s}$	$19^{\circ}39^{\mathrm{m}}32.40^{\mathrm{s}}$	21.23640	
$1^{\rm h}10^{\rm m}09.960^{\rm s}$	$19^{\circ}36^{\mathrm{m}}50.76^{\mathrm{s}}$	23.41770	
$1^{\rm h}10^{\rm m}09.048^{\rm s}$	19°38 ^m 22.92 ^s	23.37580	
$1^{\rm h}10^{\rm m}08.640^{\rm s}$	$19^{\circ}38^{\mathrm{m}}55.68^{\mathrm{s}}$	27.93620	
$1^{\rm h}10^{\rm m}14.287^{\rm s}$	$19^{\circ}35^{\mathrm{m}}16.84^{\mathrm{s}}$	19.30940	
$1^{\rm h}10^{\rm m}13.831^{\rm s}$	19°36 ^m 17.04 ^s	19.30940	
$5^{\rm h}22^{\rm m}23.736^{\rm s}$	$-36^{\circ}25^{\mathrm{m}}22.08^{\mathrm{s}}$	26.33210	
$5^{\mathrm{h}}22^{\mathrm{m}}14.424^{\mathrm{s}}$	$-36^{\circ}24^{\mathrm{m}}33.48^{\mathrm{s}}$	19.66380	
$5^{\rm h}22^{\rm m}20.328^{\rm s}$	$-36^{\circ}22^{\mathrm{m}}15.24^{\mathrm{s}}$	24.54040	
$5^{\mathrm{h}}22^{\mathrm{m}}12.792^{\mathrm{s}}$	$-36^{\circ}23^{\mathrm{m}}14.28^{\mathrm{s}}$	23.98020	
$5^{\rm h}22^{\rm m}12.168^{\rm s}$	$-36^{\circ}21^{\mathrm{m}}46.44^{\mathrm{s}}$	21.62000	

Table 2.3 (cont'd)

α_{2000}	δ_{2000}	radius
		(")
$5^{\rm h}22^{\rm m}15.216^{\rm s}$	$-36^{\circ}23^{\mathrm{m}}37.68^{\mathrm{s}}$	22.72560
$5^{\rm h}22^{\rm m}12.978^{\rm s}$	$-36^{\circ}25^{\mathrm{m}}42.22^{\mathrm{s}}$	10.15460
$8^{\rm h}26^{\rm m}05.760^{\rm s}$	$26^{\circ}27^{\mathrm{m}}40.32^{\mathrm{s}}$	24.86200
$8^{\rm h}26^{\rm m}13.920^{\rm s}$	$26^{\circ}26^{\mathrm{m}}16.44^{\mathrm{s}}$	20.45040
$8^{\rm h}26^{\rm m}10.320^{\rm s}$	$26^{\circ}26^{\mathrm{m}}27.60^{\mathrm{s}}$	20.61220
$8^{\rm h}26^{\rm m}04.080^{\rm s}$	$26^{\circ}26^{\mathrm{m}}33.00^{\mathrm{s}}$	21.48950
$8^{\rm h}26^{\rm m}15.120^{\rm s}$	$26^{\circ}25^{\mathrm{m}}18.12^{\mathrm{s}}$	22.79060
$8^{\rm h}26^{\rm m}03.360^{\rm s}$	$26^{\circ}22^{\mathrm{m}}56.64^{\mathrm{s}}$	19.13610
$8^{\rm h}26^{\rm m}18.823^{\rm s}$	$26^{\circ}24^{\mathrm{m}}48.31^{\mathrm{s}}$	16.96330
$8^{\rm h}26^{\rm m}13.824^{\rm s}$	$26^{\circ}27^{\mathrm{m}}41.13^{\mathrm{s}}$	16.96330
$8^{\rm h}26^{\rm m}00.960^{\rm s}$	$26^{\circ}23^{\mathrm{m}}28.32^{\mathrm{s}}$	16.96330
$8^{\rm h}46^{\rm m}59.280^{\rm s}$	$34^{\circ}48^{\mathrm{m}}24.12^{\mathrm{s}}$	22.65160
$8^{\rm h}47^{\rm m}09.840^{\rm s}$	34°49 ^m 18.84 ^s	17.03520
$8^{\rm h}47^{\rm m}11.520^{\rm s}$	$34^{\circ}47^{\mathrm{m}}16.44^{\mathrm{s}}$	23.74660
$8^{\rm h}47^{\rm m}07.622^{\rm s}$	$34^{\circ}49^{\mathrm{m}}46.84^{\mathrm{s}}$	14.86670
$8^{\rm h}47^{\rm m}14.376^{\rm s}$	$34^{\circ}46^{\mathrm{m}}54.03^{\mathrm{s}}$	14.86670
$8^{\rm h}47^{\rm m}03.209^{\rm s}$	$34^{\circ}47^{\mathrm{m}}03.63^{\mathrm{s}}$	21.50600
$8^{\rm h}47^{\rm m}07.622^{\rm s}$	$34^{\circ}47^{\mathrm{m}}38.84^{\mathrm{s}}$	19.70790
$9^{\rm h}57^{\rm m}57.360^{\rm s}$	$65^{\circ}35^{\mathrm{m}}25.08^{\mathrm{s}}$	17.89060

Table 2.3 (cont'd)

α_{2000}	δ_{2000}	radius	
		(")	
$11^{\rm h}17^{\rm m}40.080^{\rm s}$	$07^{\circ}44^{\mathrm{m}}11.22^{\mathrm{s}}$	24.45140	
$11^{\rm h}17^{\rm m}35.040^{\rm s}$	$07^{\circ}43^{\mathrm{m}}35.04^{\mathrm{s}}$	28.20480	
$11^{\rm h}17^{\rm m}32.880^{\rm s}$	$07^{\circ}41^{\mathrm{m}}46.57^{\mathrm{s}}$	24.72820	
$11^{\rm h}17^{\rm m}29.280^{\rm s}$	$07^{\circ}46^{\mathrm{m}}31.84^{\mathrm{s}}$	25.12260	
$11^{\rm h}17^{\rm m}37.200^{\rm s}$	$07^{\circ}42^{\mathrm{m}}44.96^{\mathrm{s}}$	24.51630	
$13^{\mathrm{h}}54^{\mathrm{m}}14.751^{\mathrm{s}}$	$-02^{\circ}20^{\mathrm{m}}28.26^{\mathrm{s}}$	16.09790	
$16^{\rm h}42^{\rm m}32.640^{\rm s}$	$39^{\circ}34^{\mathrm{m}}50.52^{\mathrm{s}}$	18.55730	
$20^{\rm h}59^{\rm m}44.880^{\rm s}$	$-42^{\circ}44^{\mathrm{m}}57.84^{\mathrm{s}}$	47.34360	
$20^{\rm h}59^{\rm m}57.840^{\rm s}$	$-42^{\circ}42^{\mathrm{m}}24.12^{\mathrm{s}}$	22.99390	
$20^{\rm h}59^{\rm m}57.600^{\rm s}$	$-42^{\circ}42^{\mathrm{m}}57.96^{\mathrm{s}}$	18.61880	
$20^{\rm h}59^{\rm m}49.920^{\rm s}$	$-42^{\circ}44^{\mathrm{m}}53.88^{\mathrm{s}}$	15.60080	
$21^{\rm h}08^{\rm m}40.800^{\rm s}$	$-05^{\circ}18^{\mathrm{m}}10.51^{\mathrm{s}}$	21.59710	
$21^{\rm h}39^{\rm m}51.286^{\rm s}$	$-43^{\circ}07^{\mathrm{m}}57.00^{\mathrm{s}}$	19.15510	
$21^{\rm h}40^{\rm m}14.022^{\rm s}$	$-43^{\circ}05^{\mathrm{m}}11.40^{\mathrm{s}}$	21.86930	
$21^{\rm h}46^{\rm m}08.880^{\rm s}$	$04^{\circ}24^{\mathrm{m}}03.92^{\mathrm{s}}$	19.97970	
$21^{\rm h}46^{\rm m}08.160^{\rm s}$	$04^{\circ}24^{\mathrm{m}}42.95^{\mathrm{s}}$	19.24580	
$21^{\rm h}46^{\rm m}05.280^{\rm s}$	$04^{\circ}20^{\mathrm{m}}22.74^{\mathrm{s}}$	16.28820	
$22^{\rm h}02^{\rm m}39.120^{\rm s}$	$-19^{\circ}03^{\mathrm{m}}17.28^{\mathrm{s}}$	15.91970	
$22^{\rm h}02^{\rm m}48.240^{\rm s}$	$-19^{\circ}03^{\mathrm{m}}47.52^{\mathrm{s}}$	21.83670	

Table 2.3 (cont'd)

α_{2000}	δ_{2000}	radius (")
22 ^h 02 ^m 39.600 ^s 22 ^h 02 ^m 43.200 ^s 22 ^h 02 ^m 48.480 ^s 22 ^h 02 ^m 36.720 ^s 22 ^h 02 ^m 42.960 ^s 22 ^h 02 ^m 52.268 ^s 23 ^h 28 ^m 43.680 ^s 23 ^h 28 ^m 52.800 ^s	$-19^{\circ}00^{\mathrm{m}}05.76^{\mathrm{s}}$ $-19^{\circ}04^{\mathrm{m}}33.96^{\mathrm{s}}$ $-19^{\circ}04^{\mathrm{m}}27.84^{\mathrm{s}}$ $-19^{\circ}03^{\mathrm{m}}32.04^{\mathrm{s}}$ $-19^{\circ}00^{\mathrm{m}}28.08^{\mathrm{s}}$ $-19^{\circ}01^{\mathrm{m}}08.05^{\mathrm{s}}$ $14^{\circ}53^{\mathrm{m}}35.16^{\mathrm{s}}$ $14^{\circ}50^{\mathrm{m}}02.76^{\mathrm{s}}$	22.49370 22.53220 20.52570 26.10110 21.26010 14.62140 18.70160 21.44180
23 ^h 29 ^m 03.360 ^s 23 ^h 28 ^m 48.372 ^s	14°52 ^m 01.20 ^s 14°54 ^m 11.16 ^s	36.00000 18.70160

each cluster. This radius was typically between 40-60''. For background regions, we used annuli centered on the cluster with inner radii of 1.2' and outer radii of 1.8'. We chose to use this size to obtain as local a background on the detector as possible without any detectable cluster emission present. For typical ranges of beta-profile parameters (Vikhlinin et al., 1998) we estimate that our choice of background annuli may slightly over-subtract the flux at < 1% level, well below our statistical uncertainties. This estimate is conservative because a single

beta-model tends to over-predict the X-ray surface brightness when extrapolated to large radii (e.g., Ettori & Brighenti, 2008).

With one exception, when choosing a center for our apertures, we used the Brightest Cluster Galaxy (BCG) coordinates presented in Hoekstra et al. (2011). This position is the center around which they estimate r_{2500} and M_{2500} , and a direct comparison between the mass and X-ray properties of a cluster should be within the same area. The exception, RXJ0826.1+2625, we will show in Section 2.4.1, is an example where the ROSAT center is in error due to point source contamination. Hoekstra et al. (2011) identified a BCG with a reported "quality" of the BCG detection of 0, implying an ambiguous identification. Furthermore, their reported value of $M_{2500} = 0.8^{+2.1}_{-2.1}$ implies a poor determination of the cluster mass around that location. As the center of the X-ray emission detected in XMM-Newton is barely within r_{2500} of the reported BCG position, we instead repositioned our aperture around the center of the X-ray emission. The coordinates around which we located our apertures are provided in Table 2.1. Because of the centering issues, RXJ0826.1+2625 was not included in fits of weak-lensing mass scaling relations.

Spectra were extracted using the SAS task evselect, while redistribution matrix files (RMF) and ancillary response files (ARF) were generated with SAS tasks rmfgen and arfgen, respectively. The task backscale was used to determine the usable area (correcting for bad pixels and CCD edges) for each spectrum. Photon spectra, RMF, and ARF were all binned from 0.4 to 8.0 keV with bins of size 0.038 keV.

2.3 Analysis

Our extracted spectra were analyzed using XSPEC version 12.8.0 and PyXspec version 1.0.1. For each cluster, three independent spectra from MOS1, MOS2, and pn were fit simultaneously with the same model. In all three observations of RXJ1117.4+0743, the cluster aperture we chose extended outside of the field of view for the MOS2 camera. As this would bias our results toward the properties of the center of the cluster, we did not use those MOS2 data for any of the three observations. Aside from the spectral binning performed in the spectral generation, no binning was performed. Because of that – and the low number of counts for our objects – we used the modified C-statistic (a maximum likelihood function; Cash, 1979; Wachter et al., 1979) for determining the best fit and uncertainties for our model parameters.

Our spectra were modeled with a combination of emission (APEC, a diffuse gas emission spectrum) and absorption (phabs, a photoelectric absorption model) components from 0.7-8.0 keV. APEC uses the ATOMDB v2.0.2 ⁴ code to compare the observed data to models of collisionally ionized diffuse gas emission spectra. It requires the redshift (from Mullis et al., 2003) and metal abundances to fit a normalization and plasma temperature. We used the angr abundance table, which comes from Anders & Grevesse (1989). For all model fits, we used XSPEC to derive flux values from 0.5-2.0 keV, the same range used by Mullis et al. (2003). We also calculated luminosities from 0.1-2.4 keV (the range presented in Hoekstra et al., 2011), 0.5-2.0 keV (to match Mullis et al., 2003), and 0.1-50 keV (a "bolometric" luminosity).

⁴http://atomdb.org/

Table 2.4. Spectral Fitting Properties Within r₂₅₀₀

70	$h_{70}^{-4} = 10^{-14} $ $h_{70}^{-2} = 10^{44} $ $h_{70}^{-2} = 10^{$
$\begin{array}{cccccccccccccccccccccccccccccccccccc$	$\begin{array}{cccccccccccccccccccccccccccccccccccc$

^aWeak lensing masses from Hoekstra et al. (2011).

 $^{^{\}rm b}0.5$ - 2.0 keV.

 $^{^{\}rm c}0.1$ - $2.4~{\rm keV}.$

 $^{^{\}rm d}$ Bolometric.

e $10^{-14} \left(4\pi [\mathcal{D}_{\mathcal{A}}(1+z)]^2\right)^{-1} \int n_e n_H dV$. $\mathcal{D}_{\mathcal{A}}$ has units cm. n_e and n_H have units cm⁻³.

 $^{^{\}mathrm{f}}3\sigma$ upper limit.

2.4 Results

The results of our spectral fitting are summarized in Table 2.4. Mass estimates based on weak-lensing analyses are those reported in Hoekstra et al. (2011). Our reported luminosities are the unabsorbed luminosities. For all measurements, the reported errors are at the 1σ level.

2.4.1 Flux

One of our aims was to investigate how improved *XMM-Newton* imaging would affect the measurements of these faint clusters. Along with improved spectral response and calibrations, the improved resolution allowed us to identify and mask out contaminating point sources. To this end, we compare our measured fluxes to those reported in the initial 160SD paper of Vikhlinin et al. (1998), V98 hereafter.

In the original work, V98 were unable to use a wide aperture to integrate flux due to the large statistical uncertainty introduced by the ROSAT background. Instead, they estimated the flux from the normalization of a β -model (Cavaliere & Fusco-Femiano, 1976),

$$I(r, r_c) = I_0(1 + r^2/r_c^2)^{-3\beta + 0.5}.$$
(2.1)

They estimated core radii by fitting a $\beta = 0.67$ model to their surface brightness profiles; then, they extrapolated to obtain the flux based on the normalization and shape of the best-fit β -model. Their final reported flux was actually $(f_{0.6} + f_{0.7})/2$, where $f_{0.6}$ and $f_{0.7}$

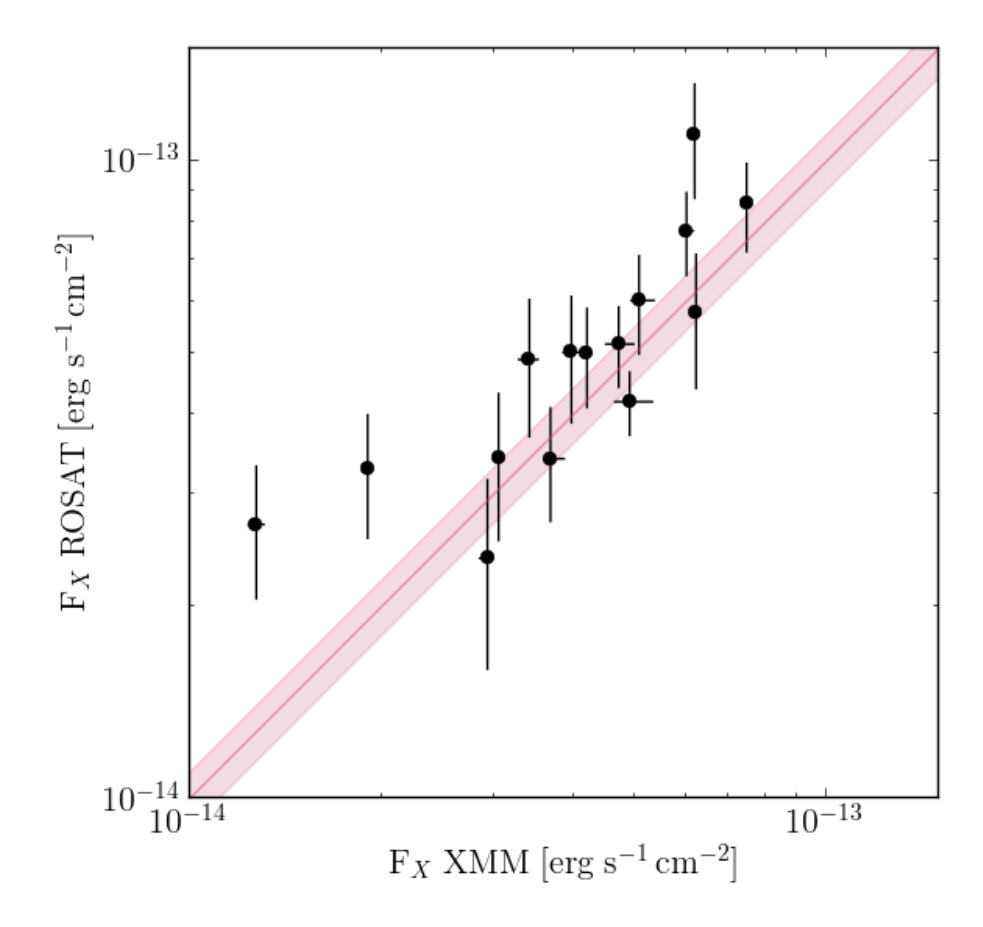


Figure 2.2 Comparison between our measured fluxes using XMM-Newton and those reported by Vikhlinin et al. (1998) using ROSAT. ROSAT fluxes were adjusted to correspond to the inner 300 ${\rm h}_{70}^{-1}$ kpc of the cluster, as described in the text. The solid line is the identity line, while the shaded band indicates agreement to within 10%.

are the fluxes obtained assuming $\beta = 0.6$ and $\beta = 0.7$, respectively.

For direct comparison with these results, we integrated counts inside a fixed aperture. In order to avoid biasing these results by our somewhat uncertain estimation of r_{2500} , we adopted a metric aperture of radius 300 h_{70}^{-1} kpc. For the equivalent flux, we used the β -model parameters from V98 to infer the estimated ROSAT fluxes inside 300 h_{70}^{-1} kpc. The errors on these fluxes were kept at the same percent as the originally reported values. Details of this procedure are given in Appendix A. The comparison between our results and V98 is shown in Figure 2.2.

Our measured fluxes agree to within 1σ with the modified fluxes of V98 in all but six cases. For RXJ0847.1+3449, including an XMM-Newton point source blended with the cluster causes the measured fluxes to agree within their combined 1σ errors. To match our flux measurement of RXJ0056.9-2740 with that of V98, we only needed to center our aperture on the same position. RXJ2146.0+0423, which we find to be slightly lower in flux than allowed by V98's uncertainty, matches perfectly when we shift to the V98 coordinates and expand the aperture to include a nearby XMM-Newton point source. To account for our expanded aperture, we rederived a new, corrected V98 flux to compare in this case. Similarly, repositioning our aperture around RXJ0522.2-3625 and using a larger aperture brings the two measurements into agreement. Finally, RXJ0826.1+2625 and RXJ2328.8+1453 were originally measured at a significant positional offset from V98 ($\approx 37''$ and 45'', respectively). In both cases, it appears as if the ROSAT images blended in nearby point sources. By recentering our aperture around the V98 coordinates and expanding the region to include the neighboring objects, we find agreement between the two sets of flux measurements.

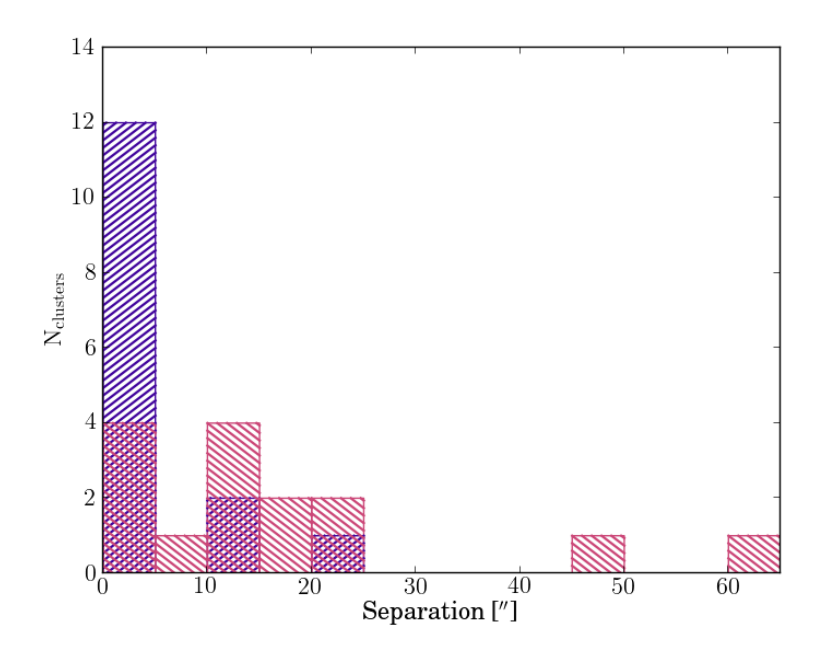


Figure 2.3 Distribution of offsets to BCG positions measured by Hoekstra et al. (2011) from X-ray centroid measurements using *XMM-Newton* (this work, hashes rising to the right) and *ROSAT* (Vikhlinin et al., 1998, hashes lowering to the right). Data are binned to increments of 5 arcseconds.

We have reproduced the *ROSAT* X-ray flux estimates from V98 and demonstrated that blended point sources and off-center apertures affected the flux estimates of these clusters over and above the uncertainty based on counting statistics and background subtraction alone.

2.4.2 X-ray Offsets

In Table 2.1 we list coordinates for each cluster twice. The coordinates from Hoekstra et al. (2011) are their best estimate of the position of each cluster's BCG. The new coordinates are of an X-ray centroid performed on data from the MOS1 camera around each cluster's

X-ray emission. Centroids were computed in five iterations of centroiding an aperture with radius 16", of images binned to 1.6" per pixel. Twelve of the X-ray-determined positions are within 5" of the BCG position, and the only position more than 12" from the BCG is for RXJ0826.1+2625, where the BCG identification may be questionable. We plot our results, along with the offsets using X-ray positions from ROSAT, in Figure 2.3. These XMM-Newton observations provide a significant improvement in the ability to properly detect the cluster position over the original ROSAT detection positions.

2.4.3 Scaling Relations

We fit our measurements of bolometric luminosity, temperature, and mass inside r_{2500} to the relation

$$\log\left(\frac{\mathbf{Y}}{\mathbf{Y}_0}\right) = \alpha \log\left(\frac{\mathbf{X}}{\mathbf{X}_0}\right) + \mathbf{C}_X. \tag{2.2}$$

 X_0 and Y_0 are pivot values, which were $10^{44}\,\mathrm{erg\,s^{-1}}$, 4 keV, and $10^{14}\,\mathrm{M}_\odot$ for luminosity, temperature, and mass, respectively. Luminosity and mass were corrected for redshift evolution by including the factor E(z); fits were therefore of L/E(z) and ME(z). To extend the dynamic range of our sample and to compare our low mass sample with a higher mass sample at similar redshift, we also included data from the Canadian Cluster Comparison Project (Hoekstra et al., 2012; Mahdavi et al., 2013, hereafter CCCP). This sample of 50 galaxy clusters spans redshifts 0.15 < z < 0.55, and all clusters were required to have a temperature $k_B T_X > 3$ keV. CCCP data was acquired through the online database⁵. In an erratum (Mahdavi et al., 2014) these data have been updated since original publication to

⁵http://sfstar.sfsu.edu/cccp

fix an error in the bolometric luminosity correction factor. We therefore present all of the cluster properties used for fitting in Table 2.6.

Individual fits are discussed below, but the results are given in Table 2.5. Fits including data in this work are labeled "160SD," while those including CCCP data are marked as such. Except where noted, uncertainties in fit values were derived through 50,000 bootstrap resamplings. Fits were performed using the WLS and BCES methods described by Akritas & Bershady (1996). Where luminosity was serving as the X variable, we used the WLS and BCES (Y|X) methods, which minimized the residuals in the other parameter. Conversely, when luminosity was the Y variable, we used the BCES (X|Y) method. When fitting the mass-temperature relation, we used the BCES Bisector and Orthogonal methods, which considers the residuals in both variables. To account for asymmetric error bars, we estimated a single, logarithmic error for a value X_{-d}^{+u} to be

$$\sigma = 0.4343 \frac{0.5(u+d)}{X}.$$
 (2.3)

For clarity, when describing a relation fit by Equation (2.2), we call it the Y-X relation, where X is the independent variable.

Our first fit was of the luminosity-mass relation within r_{2500} . When fitting this relation, we did not include RXJ0826.1+2625, as its mass was not well determined (as discussed in Section 2.2). We first fit this relationship without assuming intrinsic scatter; the resulting best-fit slope was $\alpha = 0.435 \pm 0.047$. This result shows no significant difference from the result for the 50 CCCP clusters alone, but it does not agree with the result for a fit

Table 2.5. Scaling Relations

X	Y	Sample	Log Slope	Log Intercept	Bootstrapped	Notes
L/E(z)	ME(z)	CCCP+160SD	0.305 ± 0.042	0.134 ± 0.043	NO	WLS, $\sigma_{\log(M L)} = 0.100$
L/E(z)	ME(z)	CCCP+160SD	0.435 ± 0.047	-0.039 ± 0.049	YES	BCES(Y X)
L/E(z)	ME(z)	CCCP	0.291 ± 0.075	0.135 ± 0.082	YES	WLS, $\sigma_{\log(M L)} = 0.137 \pm 0.028$
L/E(z)	ME(z)	CCCP	0.379 ± 0.081	0.005 ± 0.091	YES	BCES(Y X)
L/E(z)	ME(z)	160SD	1.02 ± 0.17	0.195 ± 0.076	YES	BCES(Y X)
ME(z)	L/E(z)	CCCP+160SD	2.33 ± 0.27	0.079 ± 0.111	YES	BCES(X Y)
ME(z)	L/E(z)	CCCP	2.78 ± 0.73	-0.071 ± 0.311	YES	BCES(X Y)
ME(z)	L/E(z)	160SD	1.01 ± 0.225	-0.186 ± 0.066	YES	BCES(X Y)
L/E(z)	$^{\mathrm{T}}$	CCCP+160SD	0.229 ± 0.016	0.005 ± 0.015	YES	WLS, $\sigma_{\log(T L)} = 0.073 \pm 0.009$
L/E(z)	${ m T}$	CCCP+160SD	0.225 ± 0.016	0.012 ± 0.015	YES	BCES(Y X)
L/E(z)	${f T}$	CCCP	0.257 ± 0.029	-0.026 ± 0.029	YES	WLS, $\sigma_{\log(T L)} = 0.070 \pm 0.009$
L/E(z)	${ m T}$	CCCP	0.261 ± 0.029	-0.028 ± 0.028	YES	BCES(Y X)
L/E(z)	${ m T}$	160SD	0.300 ± 0.055	0.052 ± 0.030	NO	WLS, $\sigma_{\log(T L)} = 0.066$
L/E(z)	${ m T}$	160SD	0.293 ± 0.064	0.063 ± 0.039	YES	BCES(Y X)
$^{\mathrm{T}}$	L/E(z)	CCCP+160SD	4.47 ± 0.33	-0.057 ± 0.072	YES	BCES(X Y)
${ m T}$	L/E(z)	CCCP	3.88 ± 0.45	0.098 ± 0.100	YES	BCES(X Y)
${ m T}$	L/E(z)	160SD	3.29 ± 0.57	-0.225 ± 0.090	NO	BCES(X Y)
${ m T}$	ME(z)	CCCP+160SD	1.88 ± 0.21	-0.058 ± 0.049	YES	BCES Bisector
${ m T}$	ME(z)	CCCP+160SD	1.93 ± 0.24	-0.066 ± 0.053	YES	BCES Orthogonal
$^{\mathrm{T}}$	ME(z)	CCCP	1.65 ± 0.24	-0.005 ± 0.061	YES	BCES Bisector
$^{\mathrm{T}}$	ME(z)	CCCP	1.80 ± 0.33	-0.029 ± 0.077	YES	BCES Orthogonal
$^{\mathrm{T}}$	ME(z)	160SD	1.98 ± 0.92	-0.096 ± 0.100	NO	BCES Bisector
${ m T}$	ME(z)	160SD	1.79 ± 0.96	-0.103 ± 0.101	NO	BCES Orthogonal
ME(z)	${ m T}$	CCCP+160SD	0.537 ± 0.059	0.029 ± 0.024	YES	BCES Bisector
ME(z)	T	CCCP+160SD	0.525 ± 0.065	0.032 ± 0.024	YES	BCES Orthogonal
ME(z)	T	CCCP	0.622 ± 0.097	-0.008 ± 0.040	YES	BCES Bisector
ME(z)	${ m T}$	CCCP	0.574 ± 0.111	0.009 ± 0.044	YES	BCES Orthogonal
ME(z)	T	160SD	0.506 ± 0.235	0.049 ± 0.066	NO	BCES Bisector
ME(z)	Т	160SD	0.559 ± 0.300	0.058 ± 0.079	NO	BCES Orthogonal

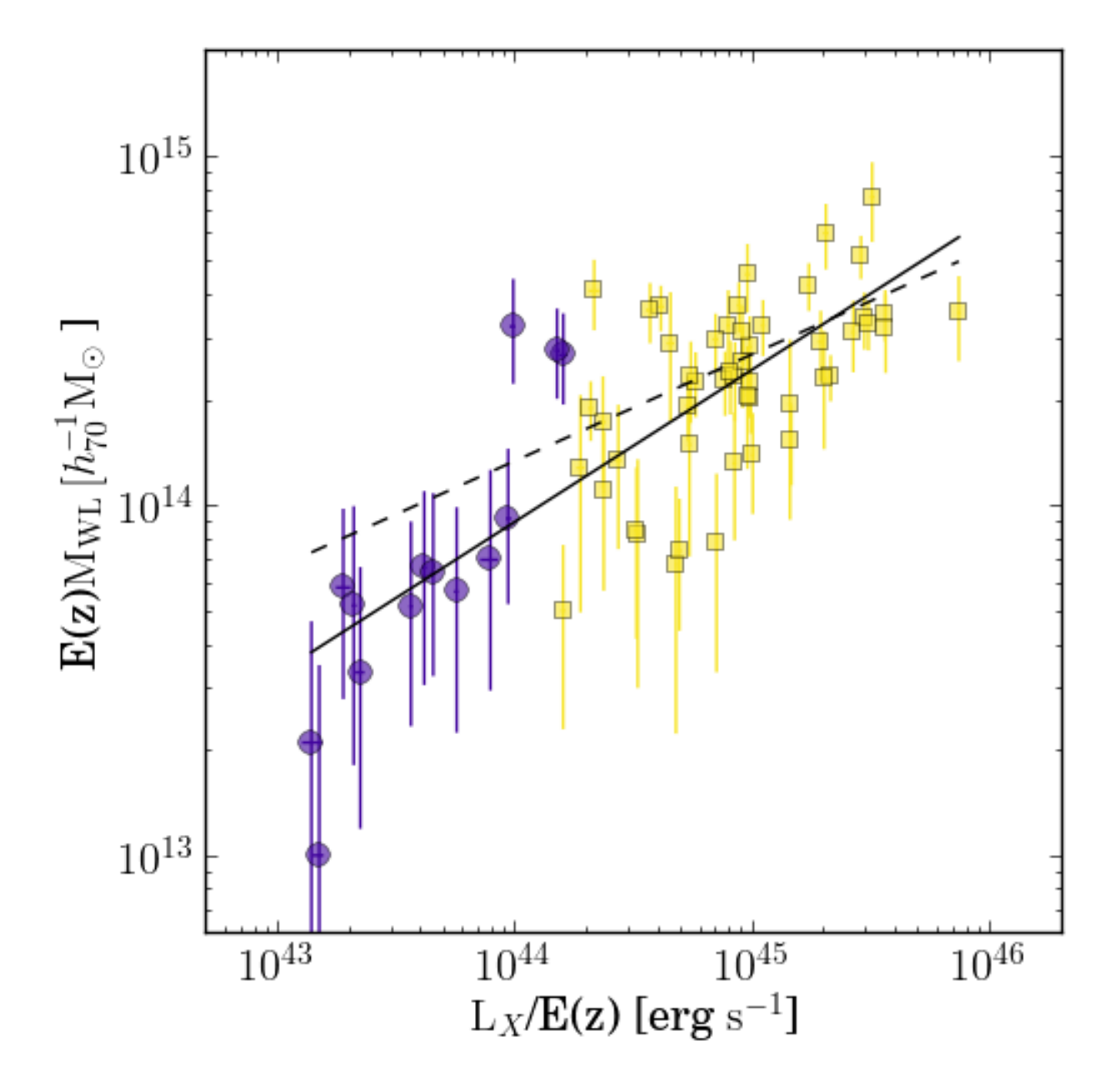


Figure 2.4 Plot of weak-lensing mass M_{WL} as a function of bolometric X-ray luminosity within r_{2500} . Masses and luminosities have been rescaled by E(z) to account for the range of redshift covered by the samples. Data analyzed in this work are shown as circles, while cluster properties from the CCCP are shown as squares. RXJ0826.1+2625 was not included in this fit. Our best fit to Equation (2.2) for the M-L relation is shown by the solid line. Our best fit when including intrinsic scatter is shown by the dashed line. Both fits are to the combined sample of 160SD and CCCP clusters.

Table 2.6: CCCP Cluster Properties Within ${\bf r}_{2500}$

NT.	Mana V E()	I /E/)	1 m	D - 1-1-10
Name	$Mass \times E(z)$, , ,	k_BT	Redshift
	$h_{70}^{-1}10^{14}\mathrm{M}_{\odot}$	$h_{70}^{-2} 10^{45} \mathrm{erg}\mathrm{s}^{-1}$	keV	
3C295	3.30 ± 0.860	0.78 ± 0.01	6.43 ± 0.35	0.464
Abell0068	2.87 ± 0.645	0.96 ± 0.02	7.25 ± 0.34	0.255
Abell0115N	0.68 ± 0.460	0.47 ± 0.01	4.84 ± 0.10	0.197
Abell0115S	0.84 ± 0.530	0.32 ± 0.01	5.60 ± 0.24	0.197
Abell0209	2.05 ± 0.430	0.97 ± 0.01	7.14 ± 0.34	0.206
Abell0222	1.75 ± 0.620	0.23 ± 0.01	4.35 ± 0.27	0.207
Abell0223S	1.11 ± 0.530	0.23 ± 0.01	5.55 ± 0.18	0.207
Abell0267	2.30 ± 0.480	0.76 ± 0.01	6.90 ± 0.25	0.231
Abell0370	4.62 ± 1.030	0.94 ± 0.02	7.60 ± 0.46	0.375
Abell0383	0.79 ± 0.450	0.70 ± 0.01	4.24 ± 0.06	0.187
Abell0520	2.27 ± 0.470	0.96 ± 0.01	8.19 ± 0.21	0.199
Abell0521	1.51 ± 0.780	0.53 ± 0.01	6.00 ± 0.35	0.253
Abell0586	1.33 ± 0.530	0.83 ± 0.02	5.70 ± 0.37	0.171
Abell0611	2.08 ± 0.800	0.94 ± 0.02	6.36 ± 0.38	0.288
Abell0697	2.97 ± 0.670	1.91 ± 0.05	10.60 ± 0.67	0.282
Abell0851	3.73 ± 0.560	0.41 ± 0.01	6.05 ± 0.36	0.407
Abell0959	3.65 ± 0.720	0.37 ± 0.01	6.98 ± 0.79	0.286
Abell0963	1.41 ± 0.450	0.99 ± 0.01	6.42 ± 0.12	0.206
Abell1689	5.22 ± 0.740	2.83 ± 0.01	8.88 ± 0.14	0.183

Table 2.6 (cont'd)

Name	$Mass \times E(z)$	L/E(z)	$\mathbf{k}_{B}\mathrm{T}$	Redshift
	$h_{70}^{-1}10^{14}\mathrm{M}_{\odot}$	$h_{70}^{-2} 10^{45} \mathrm{erg}\mathrm{s}^{-1}$	keV	
Abell1758E	3.17 ± 0.600	0.89 ± 0.02	7.78 ± 0.37	0.279
Abell1758W	3.02 ± 0.550	0.69 ± 0.02	8.21 ± 0.53	0.279
Abell1763	3.30 ± 0.600	1.09 ± 0.02	7.59 ± 0.23	0.223
Abell1835	3.57 ± 0.600	3.58 ± 0.01	7.04 ± 0.07	0.253
Abell1914	2.36 ± 0.360	2.11 ± 0.03	9.41 ± 0.16	0.171
Abell1942	1.92 ± 0.370	0.21 ± 0.01	4.87 ± 0.28	0.224
Abell2104	2.36 ± 0.600	0.83 ± 0.01	6.14 ± 0.23	0.153
Abell2111	2.29 ± 0.480	0.57 ± 0.02	6.63 ± 0.57	0.229
Abell2163	3.23 ± 0.820	3.59 ± 0.01	10.80 ± 0.16	0.203
Abell2204	3.46 ± 0.640	2.92 ± 0.01	6.53 ± 0.06	0.152
Abell2218	2.60 ± 0.680	0.90 ± 0.01	6.96 ± 0.19	0.176
Abell2219	3.16 ± 0.730	2.62 ± 0.05	9.19 ± 0.39	0.226
Abell2259	0.75 ± 0.310	0.49 ± 0.01	4.69 ± 0.54	0.164
Abell2261	4.31 ± 0.670	1.70 ± 0.02	7.28 ± 0.29	0.224
Abell2390	3.35 ± 0.540	3.04 ± 0.04	8.60 ± 0.21	0.228
Abell2537	3.77 ± 0.620	0.87 ± 0.02	6.42 ± 0.44	0.295
CL0024.0+1652	4.15 ± 0.940	0.21 ± 0.01	4.84 ± 0.51	0.390
MACSJ0717.5+3745	7.70 ± 1.980	3.15 ± 0.06	11.50 ± 0.77	0.548
MACSJ0913.7+4056	1.97 ± 1.050	1.42 ± 0.03	6.35 ± 0.18	0.442

Table 2.6 (cont'd)

		- (-)		5
Name	$Mass \times E(z)$	L/E(z)	k_BT	Redshift
	$h_{70}^{-1}10^{14}\mathrm{M}_{\odot}$	$h_{70}^{-2} 10^{45} \mathrm{erg}\mathrm{s}^{-1}$	keV	
MS0015.9 + 1609	6.07 ± 1.290	2.01 ± 0.05	8.87 ± 0.53	0.541
MS0440.5+0204	1.36 ± 0.600	0.27 ± 0.01	3.94 ± 0.28	0.190
MS0451.6 - 0305	2.33 ± 0.860	1.98 ± 0.06	10.20 ± 0.93	0.550
MS0906.5+1110	1.95 ± 0.410	0.53 ± 0.01	5.59 ± 0.23	0.174
MS1008.1 - 1224	2.35 ± 0.620	0.54 ± 0.02	6.52 ± 0.51	0.301
MS1231.3+1542	0.51 ± 0.270	0.16 ± 0.01	4.98 ± 0.26	0.233
MS1358.1+6245	2.41 ± 0.570	0.80 ± 0.01	6.34 ± 0.29	0.328
MS1455.0+2232	1.55 ± 0.400	1.44 ± 0.01	4.58 ± 0.06	0.258
MS1512.4 + 3647	0.86 ± 0.440	0.32 ± 0.01	3.27 ± 0.16	0.372
MS1621.5 + 2640	2.94 ± 1.180	0.45 ± 0.02	4.96 ± 0.64	0.426
RXJ1347.5-1145	3.59 ± 0.980	7.30 ± 0.12	12.20 ± 0.41	0.451
RXJ1524.6+0957	1.29 ± 0.800	0.19 ± 0.01	4.00 ± 0.39	0.520

only of the low-mass sample presented here. We caution that this discrepancy is not necessarily indicative of a break in the scaling relation, for reasons we will discuss in Section 2.5.

When allowing for intrinsic scatter, the best-fit value of α is 0.305 ± 0.042 , with an intrinsic scatter of $\sigma_{\log(M|L)} = 0.100$. Figure 2.4 shows both fits along with the cluster properties

for both samples. For a direct comparison of the reduced scatter, we fit the M-L relation using luminosities from the original work by Hoekstra et al. (2011). With these, the intrinsic scatter was $\sigma_{\log(M|L)} = 0.262$.

Next we fit the temperature-luminosity relation within r_{2500} , this time using all fifteen clusters studied here. We found that the best fit for the entire sample was $\alpha = 0.229 \pm 0.016$ with an intrinsic scatter of $\sigma_{\log(T|L)} = 0.073 \pm 0.009$, consistent with the fits for the two individual samples. This fit is shown along with the data in Figure 2.5. When we did not allow for intrinsic scatter, we found the best-fit slope was relatively unchanged, becoming $\alpha = 0.225 \pm 0.016$.

We also investigated the scaling between mass and temperature within r_{2500} . Again, RXJ0826.1+2625 was excluded from this fit. For the combined sample, the best-fit with the BCES Bisector was $\alpha = 1.88 \pm 0.21$, which was consistent with fits for the sub-samples alone. This fit is shown in Figure 2.6. In addition, we include data taken from Sun et al. (2009). Masses from that study are not based on weak lensing measurements, but were instead derived from an assumption of hydrostatic equilibrium. These data were not included in our fits, however.

In order to more easily compare our work to other studies, we also fit the inverse of these three relations. Using BCES(X|Y), the L-M relation fit for the CCCP+160SD sample is $\alpha = 2.33 \pm 0.27$. In contrast, for BCES(Y|X), the inverse of the M-L relation is $\alpha^{-1} = 2.30$. Our BCES(Y|X) fit of L-T is $\alpha = 4.47 \pm 0.33$, while the corresponding fit from the T-L relation is $\alpha^{-1} = 4.36$. When fitting T-M, the best fit from BCES Bisector was

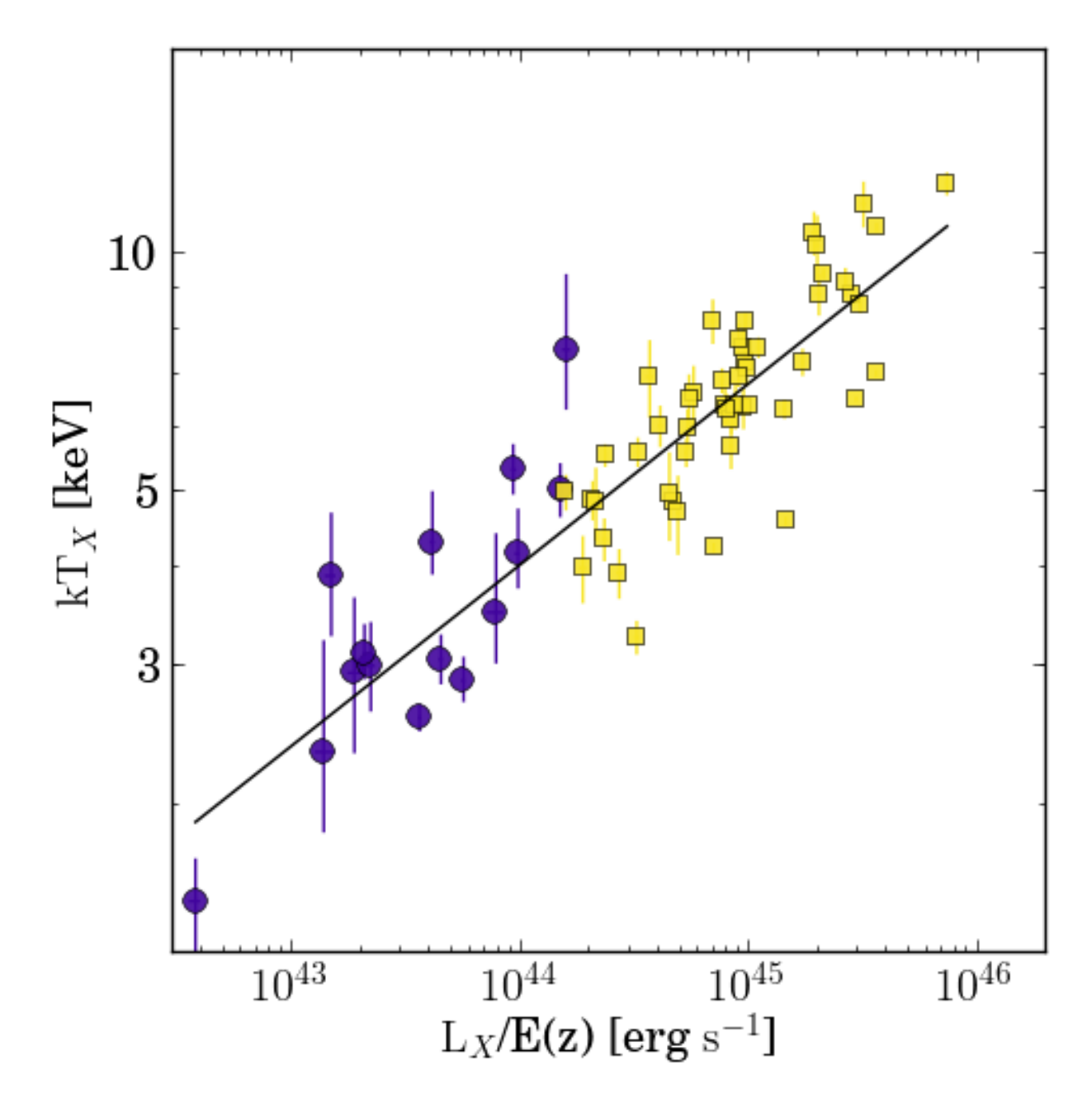


Figure 2.5 Plot of X-ray temperature as a function of bolometric luminosity within r_{2500} . Luminosities have been rescaled by E(z) to account for the range of redshift covered by the samples. Data analyzed in this work are shown as circles, while cluster properties from the CCCP are shown as squares. Our best fit to Equation (2.2) for the T-L relation is shown by the solid line.

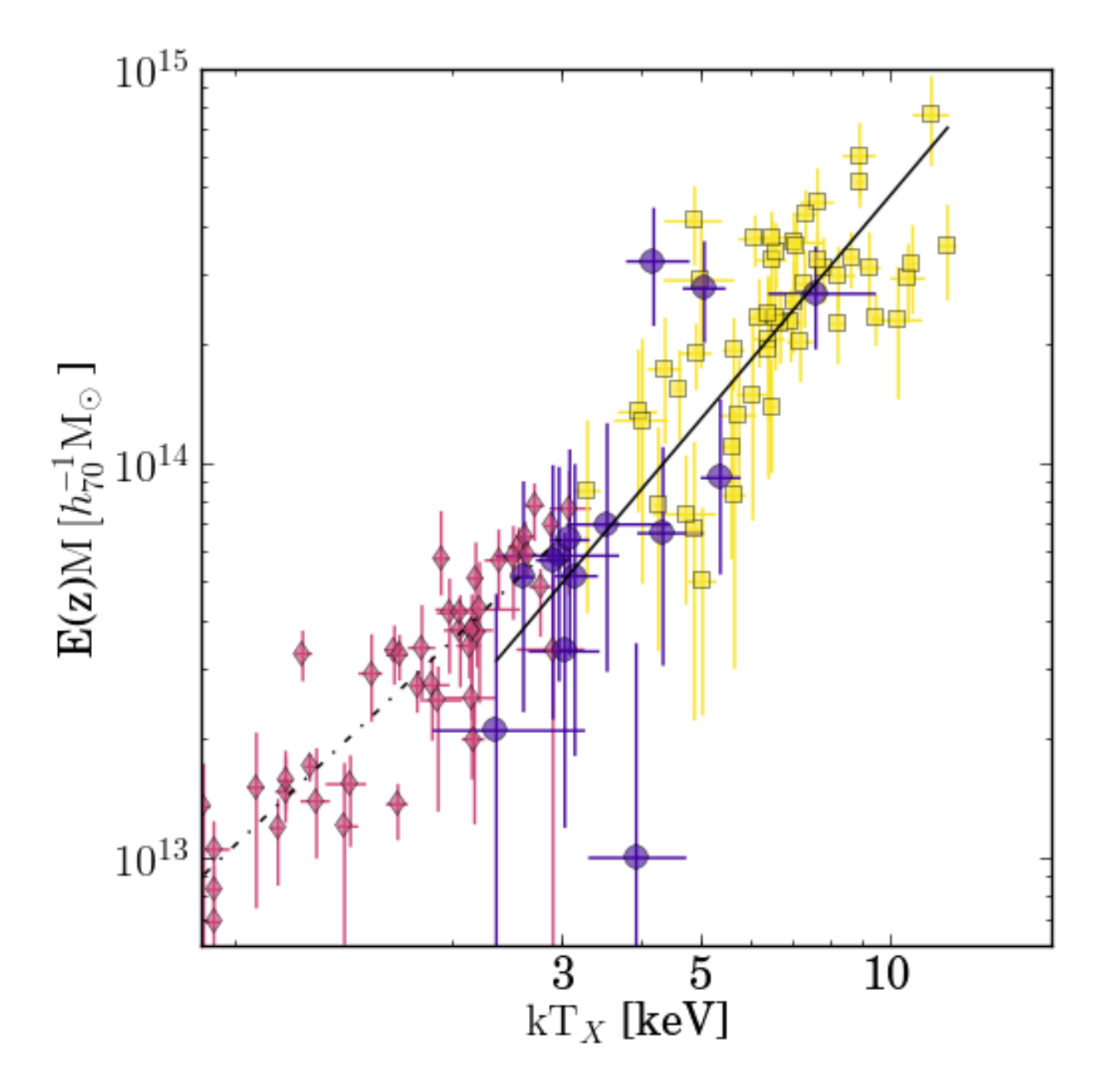


Figure 2.6 Plot of M as a function of X-ray temperature within r_{2500} . Masses have been rescaled by E(z) to account for the range of redshift covered by the samples. Data analyzed in this work are shown as circles, while cluster properties from the CCCP are shown as squares; both are derived from weak lensing. RXJ0826.1+2625 was not included in this fit. We also include a sample of nearby galaxy groups from Sun et al. (2009) as diamonds, where masses are derived from hydrostatic equilibrium. Our best fit to Equation (2.2) for the M-T relation from the clusters analyzed in this work and from the CCCP is shown by the solid line. Our best fit to the M-T relation using the properties within r_{2500} of the groups from Sun et al. is shown as a dashed line.

 $\alpha = 0.537 \pm 0.059$, which agrees with the BCES Bisector of M-T, $\alpha^{-1} = 0.532$.

2.5 Discussion

2.5.1 Comparison with Previous X-ray Observations

We compared our results to previously published individual XMM-Newton results for four clusters (RXJ0110.3+1938, RXJ0847.1+3449, RXJ1117.4+0743, and RXJ1354.2-0221). To investigate the differences, we replicated the analysis of previous observations, including their aperture sizes and cosmology. We were able to reasonably reproduce previous results. The discrepancies arising from systematics such as differences in background choices or particle background screening criteria are smaller than the statistical uncertainty. We find that any apparent differences between our results for these clusters with previous results arise because of differences in aperture sizes, and rarely, choice of aperture centers. The details of this comparison are reported in Appendix A.

Our most obvious source of possible discrepancy with previous works is our choice of apertures, which have a radius r_{2500} motivated by weak-lensing estimates from Hoekstra et al. (2011) that were unavailable to most of the other studies. Another potential source of X-ray temperature discrepancy is the choice of binning spectral data. Some previous works binned spectral data to as few as 12 counts per spectral bin. We leave our spectra unbinned and fit with the C-statistic. As this work is focusing on faint clusters, we are limited by low photon counts. If data are binned such that only a few counts are in each bin, each bin will have non-Gaussian behavior. Since the χ^2 statistic is defined for Gaussian-distributed

data, it will not be a valid fitting statistic in this case. Alternatively, data can be binned, but doing so potentially degrades spectral resolution. Along with producing better fits for low counts (Nousek & Shue, 1989; Tozzi et al., 2006), use of the C-statistic can also avoid biases in the high-count regime (Humphrey et al., 2009). Use of different thermal models for fitting spectra did not cause major deviations in our results. As we were able to reproduce the earlier results while still using an APEC model, this should not therefore bias our results significantly (see also Belsole et al., 2005; Matsushita et al., 2007).

We demonstrated in detail (see Appendix A) that we can recover results of previous works, which verifies their results and ours. However we caution that the choice of aperture and center affect the estimate of L, T, and M for any cluster, and that results from different analyses cannot be blindly combined.

2.5.2 Comparison with Other Scaling Relations

We have measured scaling relations between weak lensing mass, X-ray luminosity, and temperature for a sample of clusters with mass and luminosity around the cluster/group boundary and at redshifts 0.3 < z < 0.6. As we used weak lensing masses and bolometric luminosities and because we only investigated X-ray properties within r_{2500} , no exact comparisons are available for our results. However, we can compare our results to other similar studies, both those focused on local groups and those that include clusters at redshifts similar to what was studied here but more massive than our sample.

Our best fit of the M-L relation within r₂₅₀₀ was, when neglecting intrinsic scatter,

 $\alpha=0.435\pm0.047$. Hoekstra et al. (2011) fit this relation using almost the same clusters studied here, with ROSAT luminosities taken from the ROSAT measurements, and a higher mass sample, reporting $\alpha=0.68\pm0.07$. Other works (Maughan, 2007; Rykoff et al., 2008; Eckmiller et al., 2011; Reichert et al., 2011) find values in the range $0.5\lesssim\alpha\lesssim0.75$, consistent with but somewhat steeper than ours.

For the L-T relation within r_{2500} , we found a best fit of $\alpha = 4.47 \pm 0.33$, although the 160SD groups and the CCCP clusters each had shallower slopes when fit independently. Previous results (Maughan, 2007; Pratt et al., 2009; Bruch et al., 2010; Eckmiller et al., 2011; Reichert et al., 2011; Nastasi et al., 2014) have reported slopes from $2.5 \lesssim \alpha \lesssim 4.5$. Our results, particularly for the two sub-samples fit individually, are consistent with this range, albeit on the high end.

In this work, we reported the best fit slope of the M-T relation within r_{2500} was $\alpha = 1.88 \pm 0.21$. Previous works (Sun et al., 2009; Eckmiller et al., 2011; Reichert et al., 2011; Kettula et al., 2013) have reported slopes in the range $1.45 \lesssim \alpha \lesssim 1.85$. As was the case with the T-L relation, our slope for the combined sample is slightly higher than this range, but the group and cluster samples, when fit independently, are both in agreement with these studies.

While comparing our scaling relationships to others is worthwhile, we caution that there are a handful of issues that make direct comparison problematic. As mentioned earlier in this discussion, other works used different radii within which to measure cluster properties. Our choice of r_{2500} was motivated by the requirements imposed from our weak lensing masses, but it means we are analyzing X-ray properties in different apertures from other studies.

Another issue that arises when comparing to other studies is the definition of luminosity. In this work, we used bolometric luminosities. However, in the three works that looked at groups that we discuss in this section (Rykoff et al., 2008; Hoekstra et al., 2011; Eckmiller et al., 2011), all fit scaling relations with a luminosity only within the energy band of 0.1 - 2.4 keV. The importance of energy bands was shown by Markevitch (1998), who found that when switching from luminosities within 0.1-2.4 keV to bolometric luminosites the measured slope of the L-T relation steepened from $\alpha = 2.10 \pm 0.24$ to $\alpha = 2.64 \pm 0.27$. Such a large change in the fit means that we should be careful comparing scaling relations for luminosities derived from different energy bands. As a test of this effect, we fit the M-L and T-L relations using luminosities measured in the 0.1 - 2.4 keV energy band for the 160SD clusters. The power law indices increased when using the energy limited luminosities from 1.02 \pm 0.17 to $\alpha = 1.19 \pm 0.22$ and from 0.293 \pm 0.064 to $\alpha = 0.334 \pm 0.101$ for M-L and T-L, respectively. The 160SD sample here has too small a dynamical range to be seriously considered for a scaling relation, but the effect of choosing to fit bolometric luminosities over band-limited luminosities is clear.

Also, while our sample is a subset of a randomly selected survey, it is originally based on X-ray selected clusters. Hicks et al. (2013) suggest that X-ray selection preferentially picks centrally concentrated systems; these systems populate the high L_X side of the T-L relation. Similarly, since our data were drawn from the faint end of a flux-limited sample, we would expect preferentially over-luminous clusters for their mass to be selected.

2.5.3 Comparison to Low-Redshift Groups

One of the issues with comparing the difference between the groups examined in this paper and those at low redshift is the ubiquity of masses derived from hydrostatic equilibrium. Hydrostatic masses may somewhat underestimate the mass of galaxy clusters when compared to weak lensing measurements (Arnaud et al., 2007; Mahdavi et al., 2008, 2013). However, in order to allow a comparison with work on low redshift groups and poor clusters using hydrostatic masses, we make the assumption that both mass estimates are identical.

Looking at Figure 2.6, we can see that our moderate redshift clusters ($\bar{z}=0.444$) are almost all hotter and/or less massive than what would be predicted by the lower redshift scaling relations for groups presented in Sun et al. (2009) ($\bar{z}=0.042$), although five low-temperature clusters agree very well. If we test the hypothesis whether our data are fit by the Sun2009 relationship between mass and temperature, we find a χ^2 value of 19.09 for 14 clusters (p=0.089). Therefore, to within $2-\sigma$ we see no difference between our sample and the low-redshift sample. If we limit this analysis to only those clusters with temperature kT <4 keV, our value of χ^2 is 3.15 for 9 clusters (p=0.87). If we do not scale the mass by E(z), χ^2 becomes 29.53 for 14 clusters (p=0.0033). This significance is just below 3σ , constituting very weak evidence for the expected self-similar evolution in the temperature-mass relation for groups.

2.5.4 Comparison between Groups and Clusters

A direct comparison between the CCCP sample and our sample, which affords a comparison between low-mass and high-mass clusters at a similar redshift range, is difficult due to the limited number of clusters in both sets. So to provide some quantification of whether the two populations differ, we utilize Fisher's exact test, which looks at how two properties are distributed in two populations. In this case, we look at how our sample and the CCCP sample compare to the scaling relations. We choose to use Fisher's exact test due to how few objects we have; in this domain, Fisher's exact test is the best, if not the only, test to use (Wall & Jenkins, 2012).

For both samples, we count how many clusters lie above the lines of best fit for each scaling relation and how many lie below. Our null hypothesis is that the samples are similar and so the number of clusters above the relation should equal the number below, statistically. We compute p-values for the T-L, M-L, and M-T relations of p = 0.13, p = 0.19, and p = 0.19, respectively. We therefore cannot reject the hypothesis that groups and clusters at intermediate redshift behave identically with respect to the scaling relations derived in this work, so our measurements are consistent with the hypothesis that $z\sim0.3-0.5$ X-ray selected clusters and groups/poor clusters follow similar X-ray scaling laws.

2.6 Conclusions

We have presented new and revised X-ray properties for a sample of 15 galaxy clusters originally drawn from a random sample of the 160 Square Degree Survey. Covering a range of

redshifts from 0.3 < z < 0.6 and limited in mass to $M_{2500} \lesssim 2 \times 10^{15} \,\mathrm{M}_{\odot}$, our new X-ray data together with previously published HST weak lensing measurements probe a largely-unexplored parameter space in cluster mass and redshift. By using a rigorous analysis to match cluster properties measured within the same radius as existing weak-lensing masses, we investigate scaling relations between mass, luminosity, and temperature. Our primary conclusions are summarized below.

- 1. We measure fainter fluxes than reported from earlier ROSAT measurements (Vikhlinin et al., 1998) for five of the fifteen clusters studied here (RXJ0522.2–3625, RXJ0826.1+2625, RXJ0847.1+3449, RXJ2146.0+0423, RXJ2328.8+1453). Due to a combination of fainter sources blending into the extended cluster light profile and multiple sources blending into one, we also found that reported X-ray positions for these clusters were not accurate. Due to the original positional inaccuracy, RXJ0056.9–2740 was originally reported to be fainter than we measured. Use of detections near the flux threshold of objects subject to blending because of the angular resolution, such as ROSAT cluster surveys, can therefore lead to errors in both position and flux that can be larger than the quoted statistical flux uncertainty.
- 2. Inside r_{2500} , for the mass and redshift range studied here, the fourteen clusters with reasonable mass measurements and 50 clusters from the CCCP are best fit by the relation

$$\frac{\text{ME(z)}}{10^{14} \,\text{M}_{\odot}} = 10^{-0.04 \pm 0.05} \times \left(\frac{\text{LE(z)}^{-1}}{10^{44} \,\text{erg s}^{-1}}\right)^{0.44 \pm 0.05}.$$
 (2.4)

When we allow for intrinsic scatter, the exponent of the best fit becomes 0.31 ± 0.04 . Our results indicate neither a break in the scaling relation among groups nor increased scatter

at low mass.

- 3. Using uncontaminated luminosity measurements and uniformly-defined r_{2500} values from weak lensing, the intrinsic scatter in the L-M relation reduced from $\sigma_{\log(M|L)} = 0.26$ to $\sigma_{\log(M|L)} = 0.10$.
- 4. Similarly, when determining the scaling relation between luminosity and temperature within r_{2500} , we find that

$$\frac{k_{\rm B}T}{4\,{\rm keV}} = 10^{0.005 \pm 0.015} \times \left(\frac{LE(z)^{-1}}{10^{44}\,{\rm erg\,s}^{-1}}\right)^{0.23 \pm 0.02}.$$
(2.5)

We find a small intrinsic scatter of $\sigma_{\log(T|L)} = 0.07 \pm 0.01$. When the high- and low-mass samples are fit separately, the 50 clusters from the CCCP sample and the 15 clusters from the 160SD sample scaling relations each have steeper slopes, 0.26 ± 0.03 and 0.30 ± 0.06 , respectively. Again, we find no evidence of a break in this relation among groups.

5. For scaling between weak-lensing masses and X-ray temperatures within r_{2500} , the combined sample of 14 clusters from this work with reasonable mass measurements and 50 from the CCCP are best fit by the relation

$$\frac{\text{ME(z)}}{10^{14} \,\text{M}_{\odot}} = 10^{-0.06 \pm 0.05} \times \left(\frac{\text{k}_{\text{B}}\text{T}}{4 \,\text{keV}}\right)^{1.9 \pm 0.2}.$$
(2.6)

When fitting high and low mass subsamples independently, the slope becomes 1.7 ± 0.2 and 1.8 ± 1.0 , respectively. These results agree with other results for both nearby groups and

intermediate-redshift clusters, along with the self-similar prediction that $M \propto T^{3/2}$.

6. To the statistical limits of our data, the intermediate redshift groups are within 2σ of the M-T relation extrapolated from a low-redshift group sample from Sun et al. (2009). Without self-similar evolution, there is a deviation just below the level of 3σ , indicating a weak statistical preference for the expected self-similar evolution.

The authors wish to thank Seth Bruch for his work planning this project. Megan Donahue and Thomas Connor acknowledge partial support from a NASA ADAP award NNX11AJ60G. Anidisheh Mahdavi acknowledges support from NASA grant NNX12AE45G. This work is based on observations obtained with *XMM-Newton*, an ESA science mission with instruments and contributions directly funded by ESA Member States and NASA.

Chapter 3

Optimized Photometry of Cluster

Galaxies in CLASH

We present a new method for measuring the photometry of objects around galaxy clusters, employing a novel mode-filtering technique for both detection and photometry. With this, we are able to investigate the galaxy populations inside the 25 massive clusters observed by the Cluster Lensing and Supernova survey with Hubble (CLASH). We produce multi-wavelength catalogs covering 16 bandpasses from ultraviolet ($\sim 2360 \text{ Å}$) to infrared ($\sim 1.54 \mu\text{m}$) including photometric redshifts. A comparison with spectroscopic values from the literature finds that $\sim 82\%$ of our reported photometric redshifts lie within $|z_p-z_s|/(1+z_s)<0.05$. This improvement in redshift accuracy, in combination with a detection scheme designed to maximize purity, yields a substantial upgrade in cluster member identification over the previous CLASH galaxy catalog. We find consistency between the galaxy magnitudes, colors, and photometric redshifts obtained here and from previous studies, including a deeper observation of one of the CLASH clusters. Evaluating the luminosity functions for these clusters, we find that we are able to observe galaxies down to $M \sim M^* + 5$, and the values of M^* we derive are consistent with that expected from published cluster galaxy luminosity functions. These clusters follow a consistent trend in mass-richness that agrees with low-mass cluster observations. We measure luminosity functions for these clusters, which we use to derive total luminosity, and, from that, stellar masses. We find stellar mass fractions of $1.8 \pm 0.7\%$ of the total halo mass, in agreement with previous studies. Not only will this catalog enable new studies of the properties of CLASH clusters, but the photometric techniques we use set the stage for future surveys of galaxy clusters.

3.1 Introduction

Galaxy clusters are the largest virialized structures in the Universe, although most of that mass is in dark matter and hot intracluster gas. Galaxies themselves only contribute a small ($\approx 1\%$) amount to the cluster mass budget (e.g. Gonzalez et al., 2013). Despite this fact, individual galaxies play a critical role in understanding the nature of cluster growth and formation of massive galaxies and of galaxies in a dense environment. Not only are individual galaxies tracer particles for the gravitational potential of their hosts, their evolution is sensitive to the conditions of their environment (Cerulo et al., 2016).

Having formed out of the same overdensity as the cluster itself (see Kravtsov & Borgani, 2012, for a review), the initial conditions of cluster galaxies are probes of their host's beginnings (Voit, 2005). As galaxies accrete onto the cluster, they sample the physical properties of inner and outer regions of the system. Variations between more- and less-massive galaxies can be used to investigate the energetic scale of events such as active galactic nucleus (AGN) feedback and supernovae (e.g., Larson, 1974; Arimoto & Yoshii, 1987; Matteucci & Tornambe, 1987).

Detailed studies of cluster members are mostly conducted at low redshift (e.g., Edwards

& Fadda, 2011; Liu et al., 2011; Zhang et al., 2011; Tian et al., 2012; Ferrarese et al., 2016), as these clusters are brighter and more accessible to ground-based observations. Distant clusters offer the ability to study the evolution of cluster populations, however, by providing temporal constraints (e.g., Hilton et al., 2009; Papovich et al., 2010; Foltz et al., 2015). Due to the difficulty in observing these clusters, previous works have had limited spatial resolution, filter coverage, and/or depth (e.g. Muzzin et al., 2013).

In particular, the study of galaxy cluster luminosity functions requires precise photometry of redshifted cluster members to draw meaningful conclusions. A number of works have observed a steepening of the faint-end slope (Rudnick et al., 2009; Lan et al., 2016), but evidence for evolution is inconclusive (Crawford et al., 2009; Lu et al., 2009). Even inside a single cluster, the parameters of the luminosity function are sensitive to the galaxies included (Agulli et al., 2016), meaning that accurate membership determination is necessary to draw meaningful conclusions about any slope evolution.

In this work, we present a photometric catalog of 25 massive galaxy clusters, using mode-based filtering to select and photometer galaxies down to $M-M^*\sim 5$ (where M^* is the characteristic magnitude of each cluster's luminosity function) across 16 filters using the Hubble Space Telescope (HST). We verify the accuracy of these results with checks to spectroscopic measurements and an overlap with a cluster in the Hubble Frontier Fields. Finally, we present fits to the observed luminosity functions for these 25 clusters in rest frame i bandpass. Throughout this work, we assume a Λ CDM cosmology, with $\Omega_{\rm M}=0.3$, $\Omega_{\Lambda}=0.7$, and $H_0=70~{\rm km~s^{-1}~Mpc^{-1}}$.

3.1.1 Statistical Background Light Estimators

Obtaining accurate photometry – particularly color photometry – for galaxies in clusters is a longstanding problem (e.g Butcher & Oemler, 1978). Clusters are filled with intracluster light (ICL, Vílchez-Gómez, 1999; Mihos et al., 2005; DeMaio et al., 2015), which can impact the observed colors of galaxies (Zibetti et al., 2005; Da Rocha & Mendes de Oliveira, 2005; Williams et al., 2007; Rudick et al., 2010). In particular, it is difficult to disentangle the contributions of ICL from galaxy emission near the center of clusters (Krick et al., 2006). Along with the ICL, the estimate of light from a given galaxy may be affected by projected overlaps between galaxies and fore- and background contamination. While previous work has modeled and subtracted the surface brightness profiles of major galaxies such as the brightest cluster galaxy (BCG, Postman et al., 2012a), this result does not scale well to measurements of the hundreds of objects visible even in the narrow WFC3 field of view. And any method to account for light contamination needs to be filter dependent – ICL, galaxy brightness, and PSF size all change with color. Here, we present a technique to determine background properties by statistically modeling the light of nearby pixels.

One of the fundamental assumptions of this work is that, for a pixel containing the light from a galaxy, the observed flux in that pixel is the sum of light from the galaxy and from the background light drawn from some unknown distribution. Lacking a complete understanding of the background light due to the limitations of our telescope's optics and the finite observation time, our best solution is to model the background light distribution from nearby pixels.

There are three challenges that must be contended with to accurately describe the back-

ground: determining a nominal measure of the expected value of the background light, determining the range of that distribution, and performing this characterization with a limited sample of pixels, some of which may be outliers from a separate distribution (such as from the wings of a nearby galaxy). The easiest statistic to compute from a background sample, the mean, is biased by outliers. A common choice is to instead use the median, which is swayed less by skew. However, the median is still sensitive to outliers; additionally, it will always be the value of one of the measurements in the background sample (or the midpoint of two values when there is an even number of sampling points), which introduces an extra level of error in the background measurement. To avoid these issues, we instead consider the mode.

For a given probability distribution, we define the mode as the point at which the frequency is greatest. For a well-sampled distribution, this will converge with the classical definition of the mode, which is the sample value that appears most often. The mode is extremely useful as a background measure as, for a sampling of background pixels wherein two distinctly-resolved background distributions can be detected, the mode will find the central value of the dominant background distribution. In the context of this work, we use two determinations of the mode: a less-rigorous yet more computationally efficient estimator to detect galaxies and a more robust yet computationally intensive method for accurate measurements of flux and flux ratios. We first describe the former.

Pearson (1895) first noted that the mode of a distribution can be approximated through the relation

$$M = 3m - 2\mu,\tag{3.1}$$

where M is the mode, m is the median, and μ is the mean. This relation, which we will refer to as the Pearson approximation in this work, has an important caveat: this is an empirically-derived relation, and it does not always find the correct mode, particularly in the case of complex backgrounds. Indeed, in the case of a background region containing light from two distributions (such as for a region consisting mostly of ICL, but with a small sub-region containing e.g. the emission of a nearby galaxy), this expression will not give an accurate representation of the mode. Due to these concerns, we will use this method for computational expediency in estimating the background for purposes of identification and detection of sources, but not for flux estimation. Since our science does not depend on teasing out detections of the faintest, smallest background sources, small errors in the mode for individual pixels do not affect detection and source definition for our scientific purposes here.

One additional input to consider when determining the background is the contribution of measurement uncertainty. A sample point with uncertain flux should not be weighted as highly as a point with more accuracy, yet it should also support background determination over a larger range. To account for all of these issues, we instead compute the mode using a kernel density estimation to derive accurate colors within fixed apertures.

Each background pixel is defined by two values: f_i and σ_i , the flux and uncertainty, respectively. By convolving the flux in each pixel with a Gaussian kernel of width σ_i , we create a probability distribution for the entire flux of the background region. The mode is

then found as the peak of this distribution, which is given by

$$P(x) = \sum_{i} \frac{1}{\sigma_i} \exp^{-(x - f_i)^2 / (2\sigma_i^2)}.$$
 (3.2)

To find the maximum of this function in a computationally expedient manner over a large number of points, we identify the zeroes of its derivative, given by

$$dP(x)/dx = \sum_{i} \frac{(x - f_i)}{\sigma_i^3} \exp^{-(x - f_i)^2/(2\sigma_i^2)}.$$
 (3.3)

A full description of the application of this technique is provided below. Due to the limits of computational efficiency, we only employ the more accurate kernel density estimation using Equations 3.2 and 3.3 for measuring flux.

3.2 Data Set

Imaging data in this work comes from the Cluster Lensing and Supernova survey with Hubble (CLASH, Postman et al., 2012b). This HST Multi-cycle Treasury Program imaged 25 galaxy cluster in 16 filters, covering the ultraviolet to the infrared. With an average of 20 orbits per cluster, the HST component of CLASH provides us with an unprecedented look into the environments of galaxy clusters. To create this catalog, we utilized all sixteen filters for each cluster; however, due to differing fields of view between HST instruments, many objects away from the cluster center lack IR coverage. HST filters used in this work have the naming convention that a filter of central wavelength nnn is labeled as either "FNNNW" or "FNNNLP," depending on if it is a wide or long-pass filter, respectively (long-pass filters are

slightly broader in their spectral coverage; see Figure 1.2 for the filters used in this work). For central wavelengths longer than 1 micron, nnn is listed in μ m; below 1 micron, nnn is in nm (for these filters, nnn is always greater than 200). For some clusters we also used archival F555W images.

Observations are first reduced by the MosaicDrizzle pipeline (Koekemoer et al. 2011, based on Fruchter & Hook 2002; Koekemoer et al. 2003). ACS/WFC data are first corrected for bias striping and charge transfer efficiency degradation (Anderson & Bedin, 2010). The pipeline then aligns every visit and every filter onto the same grid, providing astrometric accuracy on the order of one milliarcsecond. Bad pixels and cosmic rays are rejected, which, along with read noise, accumulated dark current, and statistical uncertainty in each pixel, are used to produce an inverse variance map for each filter and cluster. The output images available in the public CLASH data distribution are binned to several scales, but throughout this work we only use those images binned to 0.065" per pixel.

Photometric properties of these observations are provided in Table B.1 (ACS) and B.2 (WFC3) in Appendix B. As each processed image was reduced to a count rate, exposure times double as gain values. Zeropoints are in AB Magnitudes. Assumed Galactic extinction values are taken from the NASA/IPAC Extragalactic Database (NED)¹, which uses the Schlafly & Finkbeiner (2011) recalibration of the Schlegel et al. (1998) infrared-based dust maps utilizing a Fitzpatrick (1999) reddening law with $R_{\rm v}=3.1$.

¹NED is operated by the Jet Propulsion Laboratory, California Institute of Technology, under contract with the National Aeronautics and Space Administration.

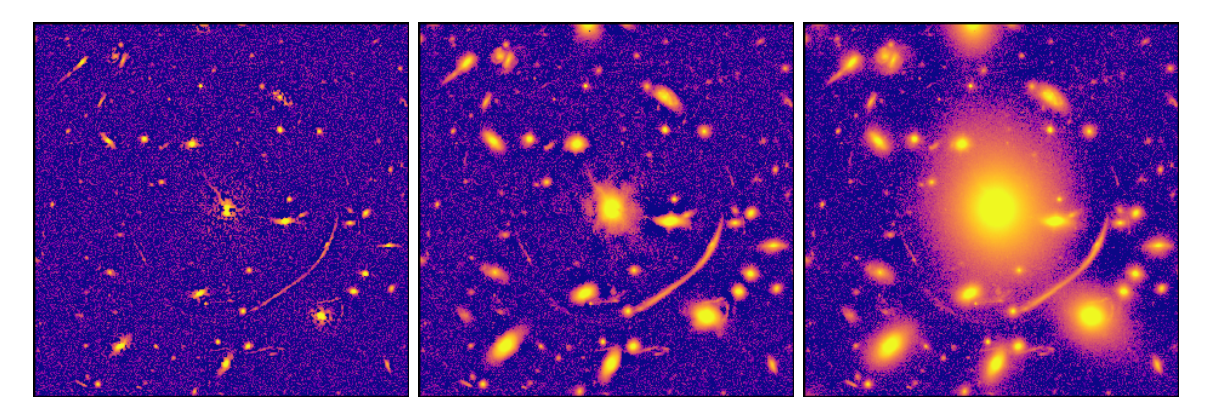


Figure 3.1 The central region of Abell 383 after subtracting a local background found using the Pearson approximation for the mode. Background regions used are: left: 4 pixels (0.26"); middle: 16 pixels (1.04"); and right: 128 pixels (8.32"). Larger structures are visible when a larger background radius is used, while smaller objects are more clearly resolved with a more localized background region.

3.2.1 Detection Images

To facilitate the detection of smaller objects embedded in massive structure, we created special detection images for each cluster and filter, with the exception of the four UVIS filters. For each pixel in each image, we subtracted the mode of nearby pixels in a surrounding region. For speed of processing, we used the Pearson approximation of the mode. We generated 7 background-subtracted images, with background regions logarithmically spaced in sizes from 4 to 256 pixels. Three of these for Abell 383 are shown in Figure 3.1. As this technique destroys structure that does not vary within the filtering box, a range of filtering scales reveals both large and small galaxies.

One issue that hampers detection of objects in cluster fields is source confusion, whereby two nearby galaxies are detected as one, creating a pseudo object that includes both of them but is concentric with neither. To mitigate this issue, we produced a separate suite of paired-scale background-subtracted difference images; here, background-subtracted images produced at each background scale were subtracted from the background-subtracted image with the next-smallest background scale (e.g., the image with an 8 pixel background scale was subtracted from the image with a 16 pixel background scale). This strategy removes smaller sources from the detection areas of larger galaxies.

Our method of determining the mode is potentially biased by its use of the median and the mean, both of which can be skewed by outliers. Indeed, some non-physical blotting in the innermost regions of galaxies is seen on the left panel of Figure 3.1. Here, background estimation is limited by the complexity of more robust mode determinants; to generate seven scales of background-subtracted images for 12 filters for each of 25 galaxy clusters, a root-finding method for mode-based estimation would have been prohibitively expensive in terms of computer time. Because of this potential systematic uncertainty, however, these detection images are used only for detection and not for photometry.

3.2.2 Source Detection

To detect objects, we ran Source Extractor (Bertin & Arnouts, 1996) on all six paired-scale background-subtracted difference images and the smallest scale (4 pixels) background-subtracted image for each non-UVIS filter for each cluster. Parameters used for each detection are given in Table 3.1.We used an RMS map based on the weight map produced by MosaicDrizzle for each filter and cluster combination. For each detection, Source Extractor output geometric properties of the detection ellipse, specifically WCS and pixel coordinates, semi-major and -minor axes, position angle, and the KRON_RADIUS².

²The Kron radius (Kron, 1980) is a radius selected to capture more than 90% of a galaxy's flux. See Graham & Driver (2005) for a discussion of its usage in Source Extractor.

Table 3.1. Source Extractor Detection Parameters

Detection ^a	CLEAN_PARAM ^b	DEBLEND_MINCONT ^b	${\tt DEBLEND_NTHRESH^b}$	$\begin{array}{c} {\tt DETECT_MINAREA^b} \\ {\rm (pix)} \end{array}$	Max Offset (pix)
004	0.2	0.40	50	15	
008 - 004	0.2	0.20	60	16	0.5
016 - 008	0.3	0.10	60	18	0.8
032 - 016	0.4	0.10	60	20	1.5
064 - 032	0.5	0.10	60	20	1.5
128 - 064	0.6	0.10	60	20	1.5
256 - 128	0.2	0.10	60	20	1.5
Stars	0.4	0.10	60	20	

^aNumerical detection images are either the background size of mode filtering (004) or the backgound sizes of the subtracted images (e.g., 008-004)

We combined the detections across each individual filter by working from the larger background region images and working to the smallest. For every object detected in one catalog,
we checked to see if there was a match in the next-smallest detection catalog within a small
offset specified in Table 3.1. Those that had matches, as well as unmatched objects from the
smaller catalog, were passed on to the next step. For all but the last image in each filter,
the actual detection was performed on a subtraction image; because of this, our technique
has the result of detecting the full extent of all but the very largest galaxies and propagating
them down to the small-background images.

After collecting all the detections from each filter into one catalog, we then created a master source list for each cluster field based on the multi-wavelength detection suite. Master-list creation was done in a similar fashion: we started with the sources detected in F160W and

bCLEAN_PARAM is the efficiency of cleaning artifacts of bright sources from the detection list; a lower value of CLEAN_PARAM fits more extended structure to bright sources, resulting in a more aggressive cleaning. DEBLEND_MINCONT and DEBLEND_NTHRESH determine whether Source Extractor separates detections into multiple objects. For DEBLEND_MINCONT of the flux of their combined flux measure. DETECT_MINAREA is the minimum required number of pixels above the detection threshold for a galaxy to be detected by Source Extractor.

worked blueward filter-by-filter, combining objects with centers within 2 pixels of each other. As more detections defined an object, the center was taken as a running average of those coordinates. After working through all filters, we reduced the geometric parameters of each object to those of a detection of that object in one filter. The filter was chosen to be where the sum of semi-major and semi-minor axes was at its median for that object (for an even number of detections, the object with the larger of the two values straddling the median was used). We trimmed this catalog to only those objects detected in at least four filters. To avoid detecting diffraction spikes from stars, we also only included those objects with semi-major axis no more than 8 times the length of the semi-minor axis or with a semi-minor axis of at least 5 pixels.

To remove stars from our catalog, we ran Source Extractor on the original images for each filter, using the parameters given in Table 3.1. Detections in each filter were combined in the same manner as before; to only include stars, we excluded any object with a CLASS_STAR value below 0.9. We matched this star catalog with our previous detection catalog, and those objects included in both were marked as stars. We generated a mask aperture using the geometric parameters from our original detection image for each star.

After creating the master detection images for each cluster, we inspected them by hand. We verified the accuracy of our star masks, reclassifying easily-identifiable objects that our pipeline had identified as stars. To ensure repeatability, we provide the coordinates and radii of the star masks used in this work with mask radii of r > 2'' in Table B.3. Second, we identified any catastrophic errors in our detections; these consisted of double detections of the same object or of over-detection of spiral galaxies, particularly of spiral arms. This last

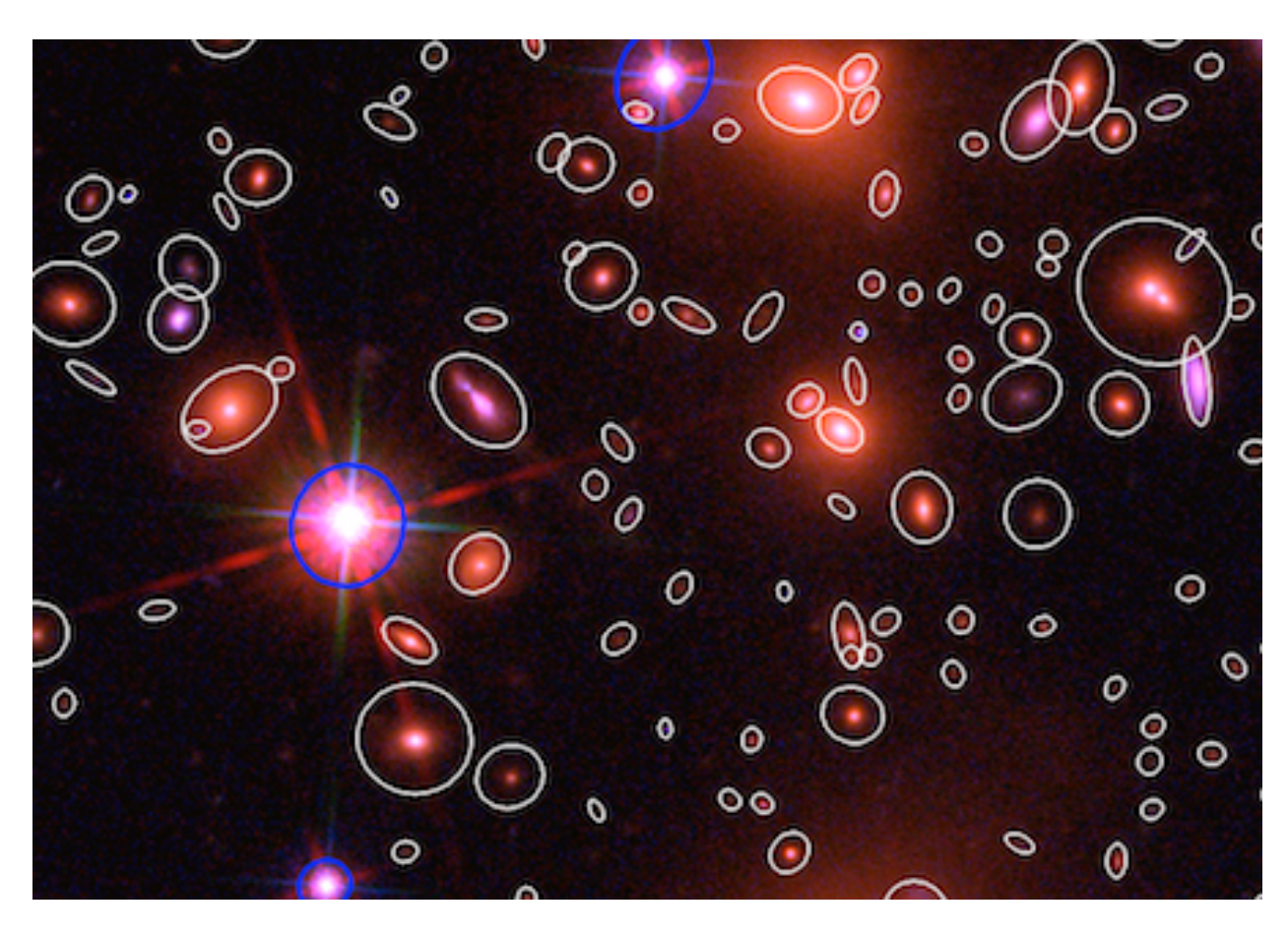


Figure 3.2 A portion of the MACS J0717 field, seen in F125W (red), F814W (green), and F555W (blue). Detected objects are outlined in white ellipses corresponding to the region used for photometry. Also shown are objects classified as stars in this work, which are marked by blue ellipses. This image is approximately 45'' wide.

step was on the order of a handful of sources excised for each cluster. The detection regions for a section of MACS J0717 are shown in Figure 3.2.

While this technique was successful in detecting galaxies of all sizes across the CLASH fields, it has two characteristics that need to be considered before applying it to future works. As can be seen in Figure 3.2, large galaxies are not detected to their full extent; this is noticeable in this work due to the combination of IR and optical imaging. Additionally, due to this technique's ability to detect small structure embedded in larger galaxies, low-redshift spiral galaxies with large angular size can be over-divided into non-physical regions. Therefore, to use these measurements to estimate the total amount of light from larger galaxies or to study resolved spirals in this field, additional careful work is necessary.

3.3 Photometry

For each filter, we worked through each detected galaxy, beginning with the smallest and working to the largest (as ranked by semi-major axis). Each galaxy was photometered on a pixel-by-pixel basis, starting from the outer edges and working in. Backgrounds were found locally, and, once photometered, pixels were replaced with the measured flux of their backgrounds. Note that for a small galaxy being photometered against the projected light from a larger galaxy, this procedure replaces the smaller galaxy's image with light estimates that are dominated by the larger galaxy. This process is shown schematically in Figure 3.3 and explained below.

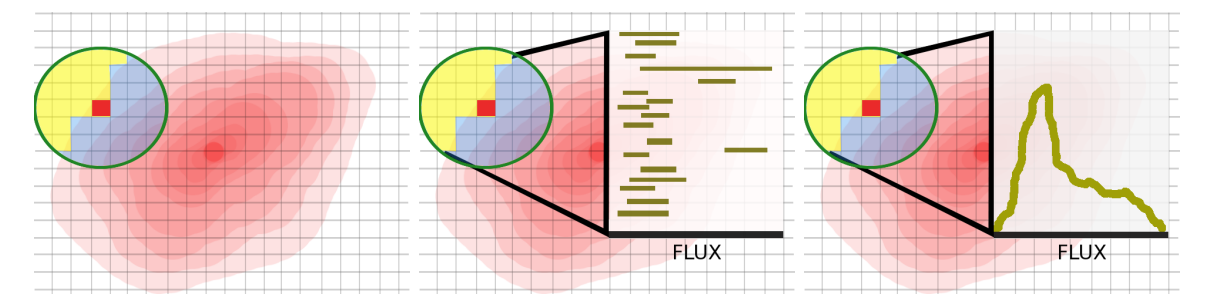


Figure 3.3 A schematic representation of the photometry technique. On the left, the galaxy of interest is shown in red, with a superimposed grid representing the pixels of the image. Starting with a pixel on the outside of the galaxy–marked here in red—we identify a circular background region. Pixels containing galaxy light (blue) are rejected, while those with only background (yellow) create our background sample. In the middle frame, we show the distribution of fluxes and uncertainties for those pixels. By convolving each flux measurement with a Gaussian kernel (sized according to the uncertainty of each point's flux) and summing, we create a histogram of flux values, such as shown on the right. The peak of that distribution is considered the mode; the width of the background distribution is found by tracing down from the peak until reaching a flux value with a frequency of ≈ 0.608 times the peak frequency.

When photometering each galaxy, we create an elliptical aperture based on the Source Extractor detection parameters. This region is blocky; pixels are either in the aperture or out of it, with no partial associations. We then assign an order of photometry by taking a one-pixel-wide annulus with outer radius equal to the galaxy's semi-major axis, and finding all of the galaxy pixels inside that ring. We shrink the annular radius pixel-by-pixel, noting the order of galaxy pixels to fall within it, until we have reached the center-most pixel. We then photometer the galaxy following that order.

To measure the flux of a pixel, we must first compute the background value. We consider a circular aperture around that pixel, with radius equal to $1.5 \times b$, where b is the semi-minor axis of the galaxy. This value is constrained to lie within 3 and 12 pixels (0.195'') and 0.78'', respectively; the former to ensure enough background pixels can be found and the latter to keep the background local to the galaxy. We exclude from this aperture any pixels

contained within the galaxy itself that have not yet been photometered. For the remaining pixels, we pass their measured fluxes and uncertainties to our background measuring routine.

This routine convolves each flux measurement with a Gaussian kernel that has a standard deviation given by that flux measurement's uncertainty (initially drawn from the variance map of the image, but increased for pixels that have already had a background replacement performed). These distributions are then summed to create a single probability frequency curve for the background flux (as given in Equation 3.2). The nominal location of the background intensity is determined by finding the peak of this distribution; to do this, we employ a root finder on the derivative (given in Equation 3.3) to find all maxima. As these distributions can be multi-modal, it is important to find all maxima. We therefore step through the ordered range of flux measurements. If the sign of the derivative changes from positive to negative, we use these bounds to find a root. If the derivative is zero at any flux measurement, we add it to the list of roots. We ignore any changes from negative derivative to positive, as those mark minima. One implicit assumption is that maxima cannot occur bounded by two flux measurements at which the derivatives are the same sign – these would not be found by our root finder, which requires boundary values of opposite sign to function.

As we have bounds of the maxima, we used the brentq algorithm in the scipy package, which finds a root using the Brent (1973) interval bisection method. We required the root detector to find a root to within a flux value of 10^{-6} counts s⁻¹ (the precision of our images). In the event of an error in this process, our code will find the mode using the Newton-Raphson method; as this method is unbounded, we seeded it with an initial guess of the median of the background flux distribution. In both cases, the uncertainty on the back-

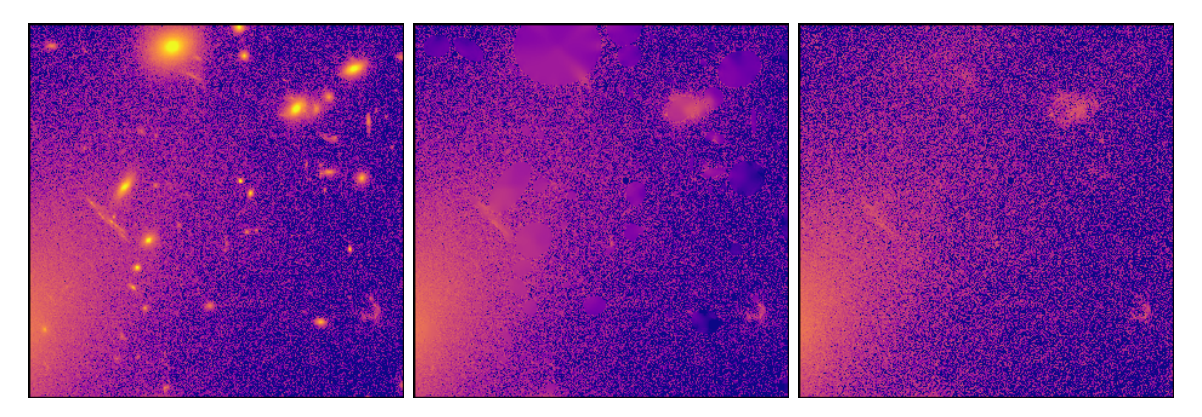


Figure 3.4 The effect of our background modeling and subtraction technique for Abell 209. Images are from the F814W filter: the original (left), after every galaxy has been photometered (center), and after the subtracted image has been resampled right.

ground value is found by finding the flux value in both directions at which the probability distribution given by Equation 3.2 is equal to $0.606531 \times \mu$, where μ is the measured mode. This value is the relative height of a Gaussian distribution at 1σ at the precision of our images.

Having determined the background value for a pixel, the excess flux is assigned to the galaxy, while the pixel value is replaced with the background value and the width of the background probability distribution is included into the weight map. We work from the outside of the galaxy in, so that the conditions at the outside of the galaxy are propagated inward. After the entire field has been photometered, we also produce resampled images using the weight maps; this step maintains the noise properties of the galaxy-subtracted image. We show the before, after, and resampled images of a section of Abell 209 in Figure 3.4.

3.3.1 UV Systematic Uncertainties

UVIS photometry, at least within the CLASH sample, is both noisy and sensitive to scattered light. Since the count rate of the UV images is so low, the systematic noise across the image often exceeds the statistical noise from aperture photometry. In order to properly determine detection thresholds, we first had to account for the systematic uncertainties of each image.

Donahue et al. (2015) measured systematic uncertainties of UV photometry for CLASH BCGs by measuring the flux in seemingly-blank sky areas around the image and computing the deviation in those measurements. However, those measurements were limited to apertures with the same radius and annular background size as the aperture used to photometer the BCG. In this work, we measure galaxies of a range of sizes, which will all have their own systematic uncertainty, so our technique must account for the area of the aperture.

We first made a mask image of each cluster, blanking out areas not covered by the CCD (such as chip gaps and off-frame pixels) and areas with detected sources (as determined by running Source Extractor on the F390W image). We then randomly distributed 1,000 points across the image, and measured the photometry of circular apertures centered on each of them, with radii increasing from 0.195" to 5.20". Photometry was corrected for the amount of each aperture covering masked off pixels.

For each filter and cluster pair, we fit the measured standard deviation as a function of radius to an equation of the form $F(r) = k_0 \times r^2 + k_1$, where k_0 and k_1 are best-fit polynomial coefficients. For each object, when determining its UV photometry, we included a systematic error based on this result. Since the objects were all parameterized as an ellipse, we used a pseudo-radius, $p = \sqrt{a \times b}$. When this was greater than 20 pixels, the systematic uncertainty was computed from the fit. When the pseudo-radius was less than 20 pixels,

we used a linear interpolation between the two nearest measurements, as the fit was less accurate at small radii.

3.3.2 Photometric Redshifts

We used BPZ³ (Benítez, 2000; Benítez et al., 2004; Coe et al., 2006) to estimate redshift probabilities for each galaxy in our catalog. BPZ determines redshift probabilities for every galaxy using χ^2 minimization and template-fitting. This code has been used previously for the CLASH clusters (Postman et al., 2012b; Jouvel et al., 2014), and is the default redshift estimation tool used in the CLASH pipeline.

Our determination of redshift probabilities covers the range of redshifts from z = 0.01 to z = 12.0 in steps of $\Delta_z = 0.001$. We use 11 template spectra, including both elliptical and spiral galaxies. From these, we interpolate 9 additional templates for every interval between original templates, for a total of 101 templates. To account for variations between galaxies and zero-point uncertainties, we enforce a minimum photometric error of 0.03 magnitudes.

To characterize the accuracy of our redshifts, we compare a sample of galaxies with spectroscopically-derived redshifts to our values. These values come from the CLASH-VLT collaboration (Biviano et al., 2013; Balestra et al., 2016; Monna et al., 2016) as well as works by Cohen & Kneib (2002), Mercurio et al. (2008), Guzzo et al. (2009), Holden et al. (2009), Richard et al. (2010), Stern et al. (2010), Coe et al. (2012), Gómez et al. (2012), Rines et al. (2013), and Ebeling et al. (2014). Additionally, we use a sample of unpublished VLT-VIMOS

 $^{^3}$ http://www.stsci.edu/ dcoe/BPZ/

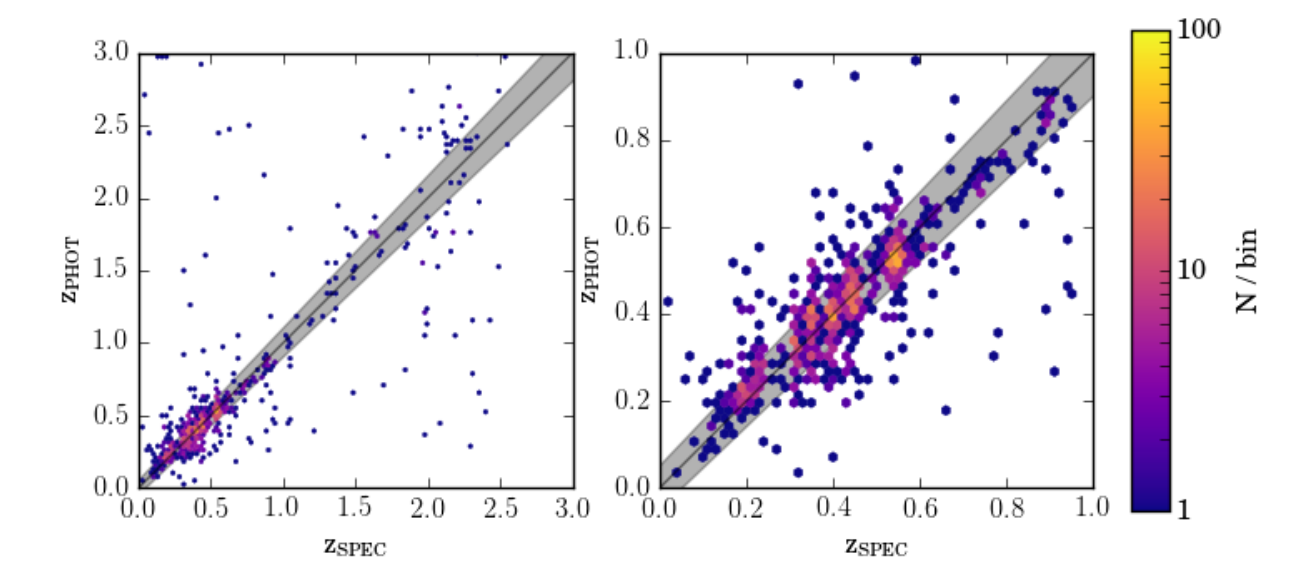


Figure 3.5 Comparison of photometric redshifts measured in this work to spectroscopic redshifts. The thin band traces the region where $|(z_p - z_s)/(1+z)| < 0.05$. The full redshift coverage from z=0 to z=3.0 is shown on the left panel; a zoom-in to just z=0 to z=1.0 is shown on the right. Points are binned into hexagons, with the total density of points scaled logarithmically from 1 to 100 counts per hex, as indicated by the colorbar.

redshifts for four cluster fields (Piero Rosati and Mario Nonino, private communication).

After combining the spectral redshift catalogs and removing duplicates (any two objects with positions within 1" of each other), we cross-matched this catalog with our own catalog of detected objects. For each spectroscopic redshift, we matched it with any object within 1.5" of the reported coordinates. In the event of multiple objects within this region, we matched with the brightest object; if multiple objects were within 0.5 magnitudes of this object, we matched to the object closest to the spectroscopic position. From this matched catalog, we report 1306 objects with spectroscopic counterparts. 54 (4.13%) are catastrophic outliers ($|(z_p - z_s)|/(1 + z_s) > 0.5$), 41 (3.14%) are substantial outliers (0.5 $\geq |(z_p - z_s)|/(1 + z_s) > 0.15$), 145 (11.10%) are minor outliers (0.15 $\geq |(z_p - z_s)|/(1 + z_s) > 0.05$), and the remaining 1066 (81.62%) are well-matched ($|(z_p - z_s)|/(1 + z_s) \leq 0.05$). A comparison between our

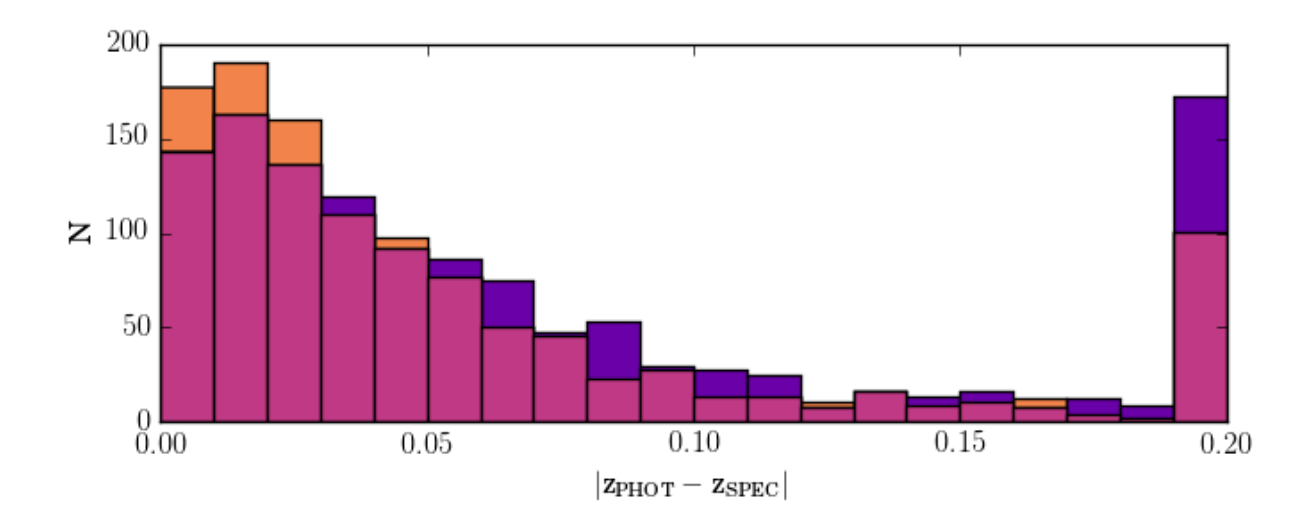


Figure 3.6 Comparison to spectroscopic redshifts between the photometric redshifts measured in this work (orange) and those from the previously released CLASH photometric catalogs (purple). Only galaxies with spectroscopic redshifts within $|z_{\rm spec}-z_{\rm cluster}|<0.05$ are shown. All outliers with $|z_{\rm phot}-z_{\rm spec}|>0.2$ are shown at $|z_{\rm phot}-z_{\rm spec}|=0.2$. The overlap between both histograms is shown in pink. Our technique better matches measured spectroscopic redshifts and has a significantly reduced ($\sim 65\%$) fraction of outliers.

photometric redshifts and spectroscopically-derived measurements is provided in Figure 3.5.

3.4 Comparison to Similar Works

One way to verify our technique is to compare our results to other photometric studies of these clusters. However, the only previous study using CLASH photometry (Postman et al., 2012b) was not tailored for optimizing cluster galaxy photometry; rather it was a general-purpose attempt to measure everything in the field, including background galaxies. Nevertheless, it provides an important first check of our results.

We match the publicly available photometric redshift $catalogs^4$ to spectroscopic redshifts

⁴https://archive.stsci.edu/prepds/clash/

following the same technique as we used to match our new results. Using the same standards as in Section 3.3.2, of the 1398 total matches, 77 (5.51%) are catastrophic outliers, 59 (4.22%) are substantial outliers, 186 (13.30%) are minor outliers, and the remaining 1076 (76.97%) are well-matched, an almost-5% decrease from our work. For galaxies with spectroscopic redshifts $z_{\rm s} \leq 1.0$ and weighted offset $\Delta_{\rm z} = |(z_{\rm p} - z_{\rm s})|/(1 + z_{\rm s}) < 0.2$, the standard deviation of the weighted offset is $\sigma_{\Delta} = 0.0531$ in this work and $\sigma_{\Delta} = 0.0612$ in the original catalogs. In the well-matched case where $\Delta_{\rm z} < 0.05$, $\sigma_{\Delta} = 0.0438$ in this work and $\sigma_{\Delta} = 0.0513$ in the original catalog. A comparison of redshift offsets for those galaxies within $|z_{\rm spec} - z_{\rm cluster}| < 0.05$ of their associated cluster is shown in Figure 3.6. As well as more accurately fitting the redshifts of those galaxies in clusters, we also greatly reduce the outlier rate for cluster galaxies.

In comparison to the earlier catalog, our improved detection routine combined with more accurate photometric redshifts should produce a more pure sample for cluster identification. To test this, we consider the photometric redshifts of every object in these 25 fields. Considering only those objects with $m_{\rm F814W} \leq 22$, 2008 of 3484 (57.6%) objects in this catalog compared to 2129 of 6608 (32.2%) in the old catalog have $|(z_{\rm p}-z_{\rm c})|/(1+z_{\rm c}) \leq 0.05$. These numbers move to 3772 out of 10302 (36.6%) and 3866 out of 17051 (22.7%) for $m_{\rm F814W} \leq 24$ and to 5217 out of 27694 (18.8%) and 6287 out of 46157 (13.6%) for $m_{\rm F814W} \leq 26$.

Another comparison for our work is that of the Hubble Frontier Fields (HFF) catalogs produced by the ASTRODEEP collaboration (Merlin et al., 2016; Castellano et al., 2016). They analyzed HST imaging of MACS-J0416 (as well as Abell 2744, which is outside the scope of the CLASH observations) using HFF HST data as well as ground-based K and

Spitzer IRAC observations. HFF observations achieve a substantial depth, nominally ≈ 2 magnitudes fainter than CLASH data. The ASTRODEEP catalogs are created through a series of steps involving masking bright objects, fitting the ICL, and fitting bright galaxies, with intermediate steps involving subtraction of either ICL or galaxies. They make an excellent comparison sample for our work; their observations are deeper, their results have been referred, and their catalog is compiled under different assumptions (galaxy and ICL model-based vs. model-agnostic).

To compare our results for MACS 0416 with those of ASTRODEEP, we first match our catalogs galaxy-by-galaxy. After sorting our catalog from brightest to faintest (using F814W magnitudes), we find a best match for each galaxy using the following process: if only one galaxy in the ASTRODEEP catalog is within 0.65'' (10 pixels) of our target, that galaxy is matched with ours. If more than one possible match is within that angular radius, we consider only those galaxies with F814W magnitudes $m \le m_b + 0.5$, where m_b is the brightest galaxy in that angular range. We take the galaxy with smallest angular offset to the target in that subset to be the match.

As a first check, we compare our measured F814W magnitudes to those measured for the same galaxies by ASTRODEEP in Figure 3.7. This verification is particularly important, as it is sensitive to whether our apertures are able to well-sample the entire flux of galaxies. We find that we report fainter fluxes than ASTRODEEP for the brightest galaxies, but otherwise are able to reproduce their results for almost all of the galaxies in the combined sample.

Our next verification step is to compare our measured colors to those of ASTRODEEP.

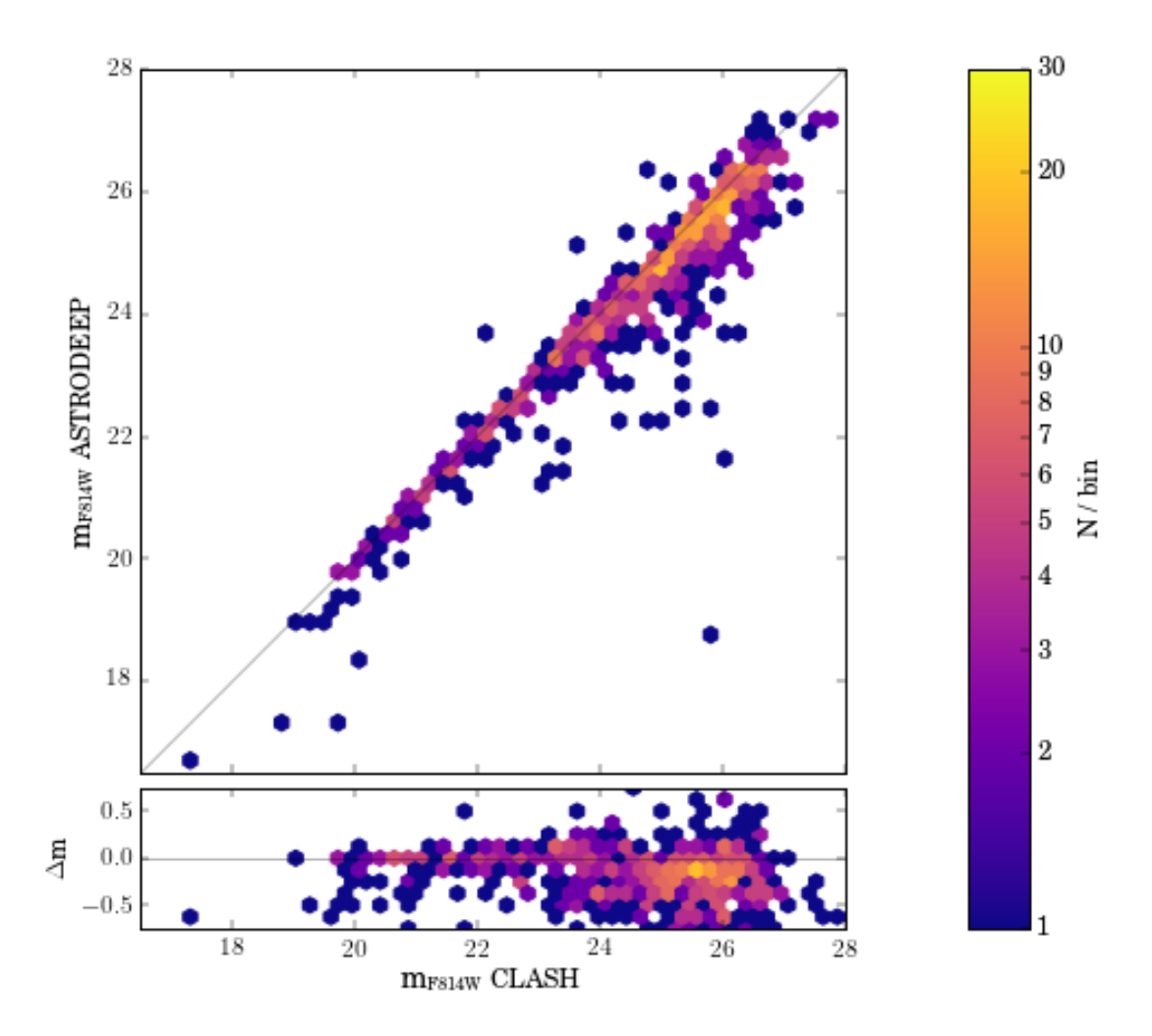


Figure 3.7 Comparison between F814W magnitudes measured by the ASTRODEEP Collaboration and this work for MACS0416. Points are binned into hexagons, with the total density of points scaled logarithmically from 1 to 30 counts per hex. Details of the fit are provided in the text. A comparison of the offsets is provided in the lower panel.

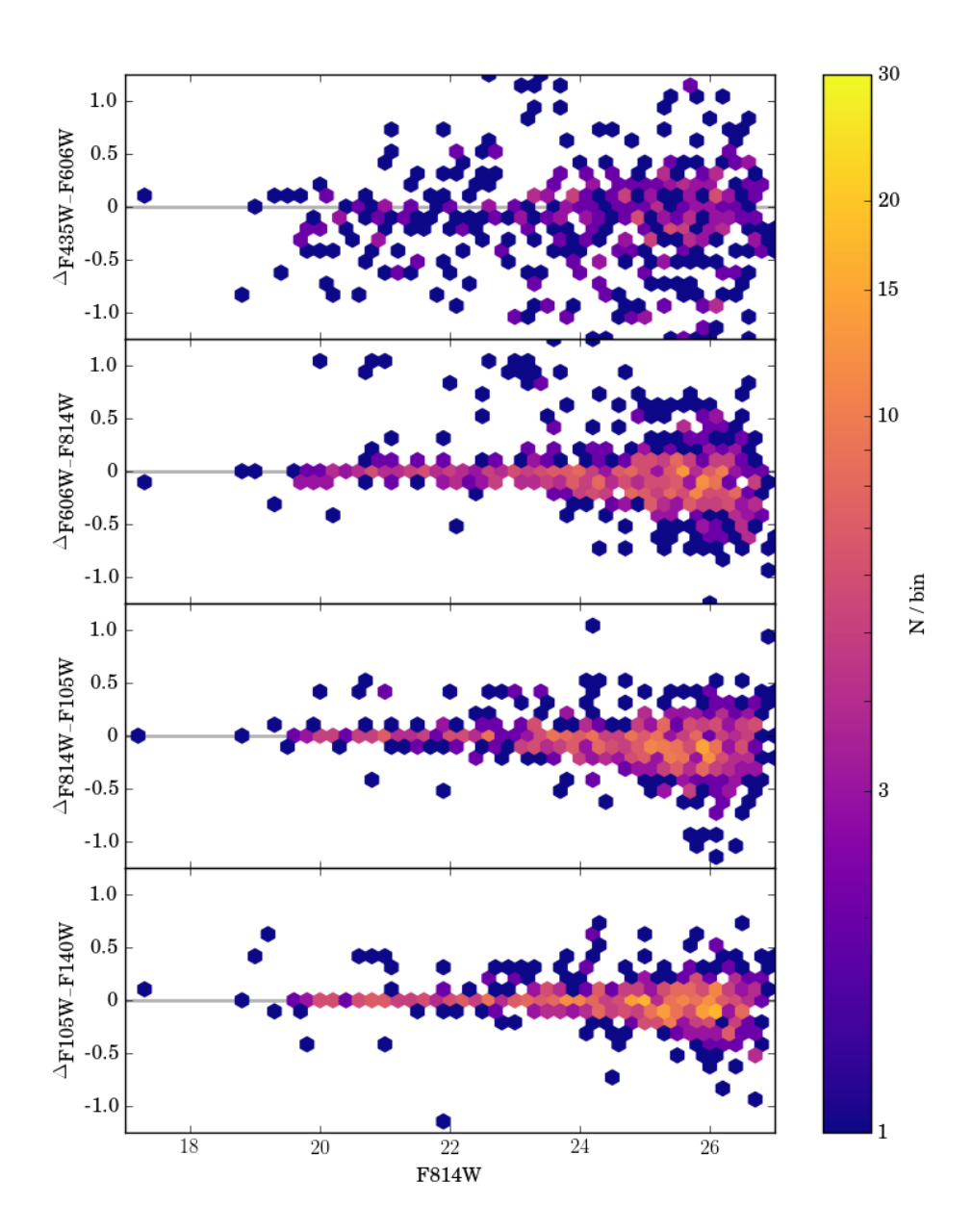


Figure 3.8 Comparison between measured colors for MACS0416 in the ASTRODEEP catalog and this work. Points are colored according to the deviation of the photometric redshift measured in this work and the cluster redshift, as indicated by the colorbar on the right.

While the HFF observations are deeper than those of CLASH, they only have 7 HST filters, so our color comparison is limited. The comparison is shown in Figure 3.8. We see a slight trend for galaxies in our sample to be bluer in F435W than in the ASTRODEEP catalog, but that color discrepancy is diminished for all of the redder filters. Numerically, the median offset between colors is -0.043 ± 0.233 (F435W - F606W), -0.049 ± 0.182 (F606W - F814W), -0.044 ± 0.178 (F814W - F105W), and -0.013 ± 0.150 (F105W - F140W), where the reported uncertainties are the standard deviation of offsets. For galaxies with $|z_p-z_c|<0.1$ and red filter magnitude <25, these values are -0.111 ± 0.235 , -0.013 ± 0.107 , -0.004 ± 0.160 , and 0.002 ± 0.139 , respectively. For the same redshift and magnitude limited subsample, we also compare the median offset between colors measured in this work and by ASTRODEEP to the median color uncertainty for our photometry alone; in the same color order as before, we find color offset to color uncertainty ratios of -0.111 (offset) to 0.127 (uncertainty), -0.013 to 0.028, -0.004 to 0.017, and 0.002 to 0.011, where all values are in magnitudes. The slight offset for blue colors is therefore within the uncertainties of our photometry. As MACS 0416 is at redshift z = 0.397, F435W is well below the 4,000 Å break for cluster galaxies, while F606W straddles the break; we therefore do not expect the color term to cause significant variations in SED fitting between the two results.

One way to check that is to compare our measured photometric redshifts. Here, AS-TRODEEP used multiple methods for redshift estimation and combined them all for a final answer, while we only consider our redshift estimates from BPZ. We show in Figure 3.9 a comparison between our reported photometric redshifts and the photometric and spectroscopic redshifts reported by the ASTRODEEP collaboration. When considering the uncertainties on these measurements, we find good agreement between our reported redshifts and the com-

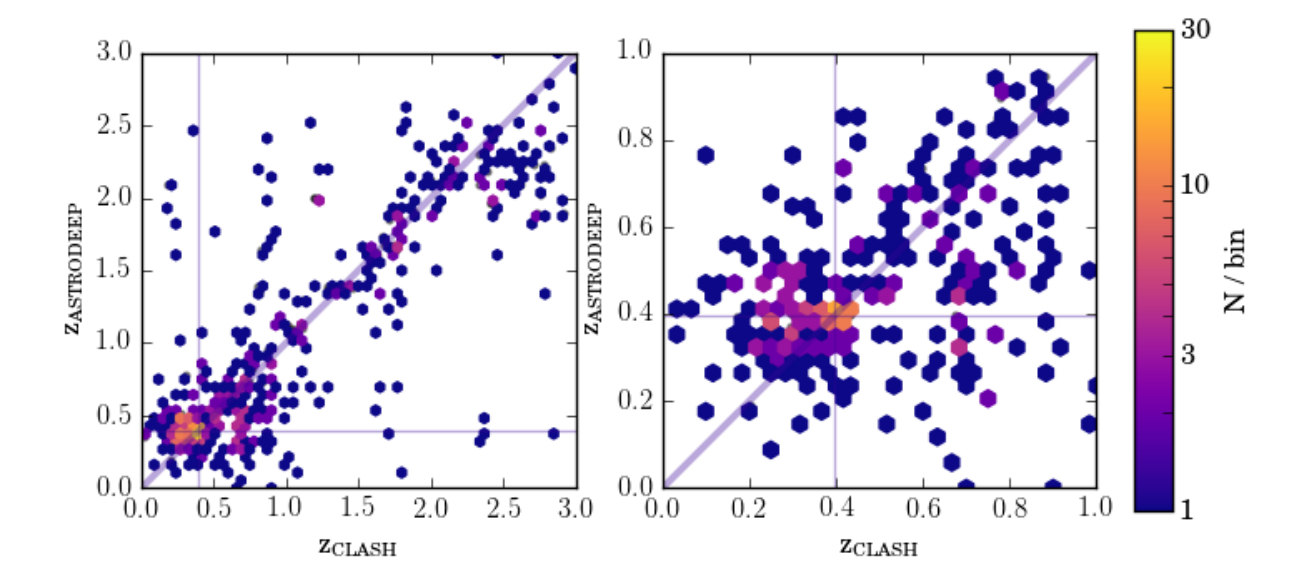


Figure 3.9 Comparison between redshifts measured by the ASTRODEEP Collaboration and this work for MACS0416. Points are binned into hexagons, with the total density of points scaled logarithmically from 1 to 30 counts per hex, as indicated by the colorbar. Details of the fit are provided in the text. A zoom-in to just matches below redshift 1.0 is provided on the right panel. The cluster redshift is indicated by the vertical and horizontal lines; the diagonal line is the identity line.

parison sample. For galaxies with photometric redshifts $z_p < 0.8$ in either of our samples, the median redshift offset between our catalogs is -0.007, while the median absolute redshift offset is 0.099.

This comparison serves to validate both our results and those of the ASTRODEEP collaboration. Both techniques – iterative background modeling and statistical background decomposition – produce similar results for the same cluster of galaxies, and, depending on the time constraints and purposes of future studies, can both be used to measure cluster galaxy populations. Nevertheless, as our technique only makes basic assumptions about background light distributions, we would recommend its use for determining the properties of clusters with only minimal priors.

Table 3.2. CLASH Scaling Properties

Cluster Name	$h_{70}^{r_{\rm s}}$ Mpc)	$^{\mathrm{M}_{2500}}_{(h_{70}^{-1}10^{14}\mathrm{M}_{\odot})}$	$(h_{70}^{-1} \text{ Mpc})$	N_{2500}	Source
Abell 209	0.660 ± 0.100	3.140 ± 0.710	0.590 ± 0.210	58 ± 8	a
Abell 383	0.470 ± 0.060	3.710 ± 0.710	0.610 ± 0.150	50 ± 7	a
Abell 611	0.590 ± 0.090	3.000 ± 0.570	0.530 ± 0.180	93 ± 10	a
Abell 1423	0.280 ± 0.050	1.820 ± 0.170	0.470 ± 0.010	51 ± 7	c
Abell 2261	0.730 ± 0.160	4.860 ± 1.710	0.660 ± 0.310	90 ± 10	a
CLJ 1226	0.500 ± 0.070	6.140 ± 1.000	0.550 ± 0.160	181 ± 17	a
MACS~0329	0.470 ± 0.110	2.860 ± 0.860	0.520 ± 0.200	148 ± 13	a
MACS 0416	0.650 ± 0.180	2.210 ± 0.530	0.410 ± 0.030	92 ± 10	b
MACS 0429	0.590 ± 0.110	2.710 ± 1.570	0.530 ± 0.240	80 ± 9	a
MACS~0647	0.480 ± 0.210	3.720 ± 0.980	0.420 ± 0.040	112 ± 12	ь
MACS 0717	1.310 ± 0.310	3.420 ± 0.870	0.420 ± 0.040	199 ± 16	b
MACS 0744	0.400 ± 0.060	2.860 ± 0.430	0.480 ± 0.120	160 ± 15	a
MACS 1115	0.890 ± 0.160	2.140 ± 0.710	0.440 ± 0.190	74 ± 9	a
MACS 1149	1.120 ± 0.350	3.730 ± 1.110	0.430 ± 0.040	167 ± 15	b
MACS 1206	0.440 ± 0.090	3.570 ± 1.140	0.530 ± 0.230	155 ± 14	a
MACS 1311	0.340 ± 0.040	2.000 ± 0.290	0.450 ± 0.100	89 ± 10	a
MACS 1423	0.340 ± 0.090	2.570 ± 1.140	0.480 ± 0.280	102 ± 11	a
MACS 1720	0.440 ± 0.090	3.140 ± 0.860	0.530 ± 0.230	104 ± 11	a
MACS 1931	0.590 ± 0.100	2.290 ± 0.430	0.470 ± 0.130	57 ± 8	a
MACS 2129	0.650 ± 0.350	4.700 ± 1.700	0.560 ± 0.060	162 ± 14	d
MS 2137	0.690 ± 0.070	3.290 ± 0.570	0.550 ± 0.140	59 ± 8	a
RXJ 1347	0.540 ± 0.110	4.430 ± 1.860	0.600 ± 0.280	152 ± 13	a
RXJ 1532	0.560 ± 0.140	1.570 ± 0.710	0.450 ± 0.230	60 ± 8	a
RXJ 2129	0.430 ± 0.070	2.570 ± 0.430	0.510 ± 0.180	52 ± 7	a
RXJ 2248	0.690 ± 0.100	3.860 ± 1.000	0.550 ± 0.210	143 ± 13	a

 $^{^{\}mathrm{a}}\mathrm{r_{s}},\,\mathrm{R}_{2500},\,\mathrm{and}\,\,\mathrm{M}_{2500}$ from Merten et al. (2015).

3.5 Optical Scaling Relations

As well as studying the individual cluster galaxies (see Chapter 4), our catalog and output photometric results enable us to better understand the scaling relations of these CLASH clusters, particularly the amount of intrinsic scatter present. To facilitate these analysis, we utilize previous observations of r_s , R_{2500} , and M_{2500} from previous CLASH studies, where r_s is the scale radius of the cluster density profile. For 19 of these clusters, we use the values

 $^{^{\}rm b}$ r_s, R₂₅₀₀, and M₂₅₀₀ from Umetsu et al. (2016).

 $^{^{\}mathrm{c}}\mathrm{r_{s}},\ \mathrm{R}_{2500},\ \mathrm{and}\ \mathrm{M}_{2500}$ from Donahue et al. (2014).

 $^{^{\}rm d}R_{2500},$ and M_{2500} from Donahue et al. (2014).

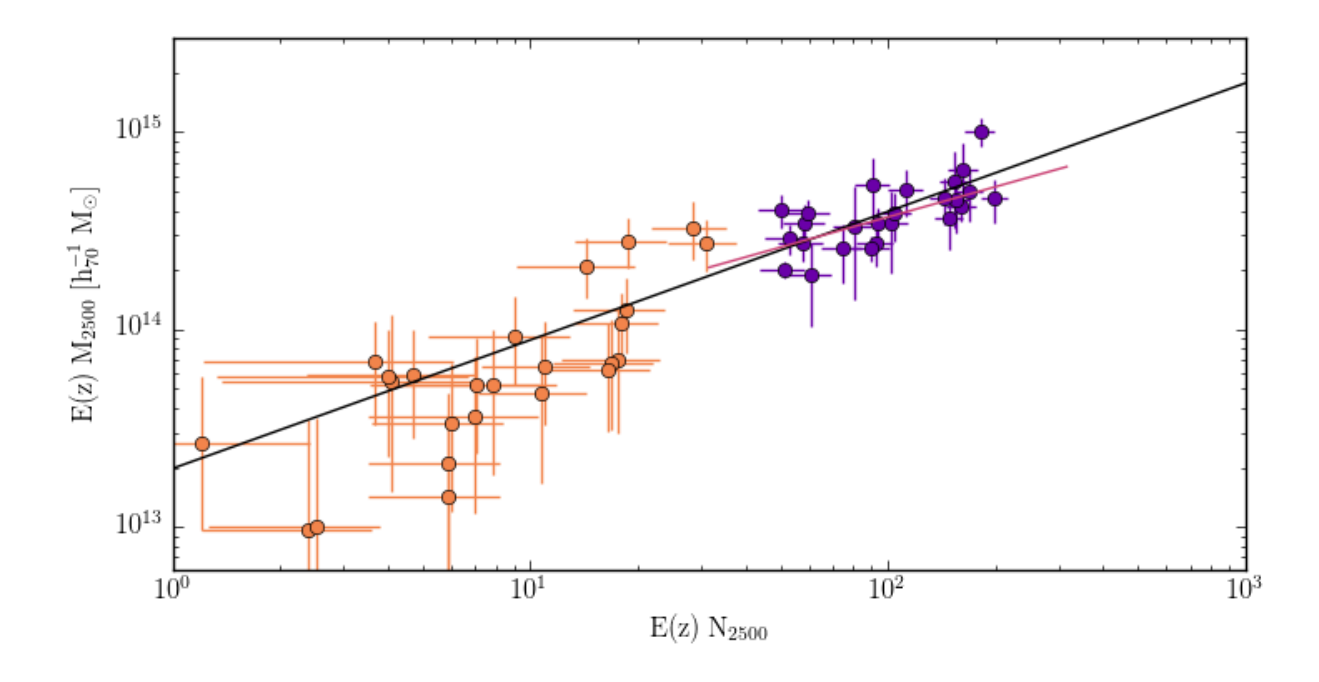


Figure 3.10 Comparison between measured values of E(z) N_{2500} and E(z) M_{2500} from this work (purple) and (Hoekstra et al., 2011, orange). We also show our best-fit line in black, and a best fit to our data alone in pink. Details of the selection of N_{2500} are provided in the text.

presented in Merten et al. (2015). For four of the strong magnification clusters, we use the properties from Umetsu et al. (2016), assuming $\gamma_c = 1$, as defined in that work. Two clusters, Abell 1423 and MACS 2129, did not have measurements reported in either of those works; we instead use values from Donahue et al. (2014). As MACS 2129 did not have any value of r_s in any literature, we set it to $r_s = 0.65 \pm 0.35$ Mpc, which is consistent with clusters of similar mass and R_{2500} values. The properties for each cluster are given in Table 3.2. To minimize bias in these relations, we only consider cluster members; the process we use to select members is described in Section 4.3.

3.5.1 Mass-Richness Relation

We first consider the relation between mass and cluster member counts. We consider the same cluster sample discussed in Chapter 2, 25 moderate-luminosity clusters with weak lensing measurements from Hoekstra et al. (2011). That work also reported measurements of N_{2500} , the overdensity of galaxies with rest frame B-band absolute magnitude $-22 < M_B < -18.5$ within r_{2500} . We find a similar value by counting the number of cluster members with k-corrected *i*-band absolute magnitude $-22 < M_g < -18.5$ within r_{2500} ; details on the k-correction⁵ which, if inaccurate, can bias slope measurements and member selection are given in Chapter 4. Our values of N_{2500} are reported in Table 3.2.

The sample of clusters from Hoekstra et al. (2011) provides an excellent comparison sample to our own, as both have r_{2500} masses derived from HST observations (weak-lensing mass measurements were presented in Hoekstra et al., 2011), both are X-ray selected (the selection of CLASH clusters is presented in Postman et al., 2012b), and both samples cover similar redshift ranges. This cluster sample is also the basis sample for our study of X-ray scaling relations in Chapter 2 (Connor et al., 2014). Here, we use the WLS routine (Akritas & Bershady, 1996) to fit a power-law scaling relation to the combined sample; we find a best fit of

$$\frac{E(z)M}{10^{14} \times M_{\odot}} = 10^{-0.70 \pm 0.04} \times (E(z) N_{2500})^{0.651}. \tag{3.4}$$

Due to the large measurement errors of the Hoekstra et al. (2011) sample, the intrinsic

⁵A k-correction is a correction from observed magnitudes to rest frame magnitudes, accounting for the dual effects of filters sampling bluer regions of the rest frame spectrum at higher redshift and of the relative spectral width of the rest frame spectrum being sampled in smaller increments with increasing redshift. K-corrections are informed by assumed spectral properties of a galaxy; this is why it is important we sample the spectra of our galaxies continuously across a wide range of wavelengths in this work.

Table 3.3. CLASH Luminosity Function Fit

Cluster Name	α	M_i^* (mag)	ϕ^*	Det. Limit (mag)	$lpha_{ m RS}$
		(-0)		(-0)	
Abell 383	$-0.86^{+0.05}_{-0.04}$	$-21.54^{+0.36}_{-0.40}$	$32.9_{-5.0}^{+5.6}$	$M^* + 6.79$	$-0.65^{+0.07}_{-0.06}$
Abell 209	$-0.79_{-0.04}^{+0.04}$	$-21.36^{+0.30}_{-0.33}$	$49.1_{-7.0}^{+7.6}$	$M^* + 6.61$	$-0.72^{+0.06}_{-0.06}$
Abell 1423	$-0.83^{+0.05}_{-0.05}$	$-20.93^{+0.32}_{-0.35}$	$43.5^{+7.2}_{-6.5}$	$M^* + 6.18$	$-0.63^{+0.08}_{-0.07}$
Abell 2261	$-0.83^{+0.04}_{-0.03}$	$-21.20^{+0.25}_{-0.27}$	$73.2^{+9.1}_{-8.3}$	$M^* + 5.95$	$-0.68^{+0.05}_{-0.05}$
RXJ 2129	$-0.82^{+0.05}_{-0.04}$	$-21.15^{+0.29}_{-0.32}$	$51.1_{-7.0}^{+7.8}$	$M^* + 4.90$	$-0.67^{+0.07}_{-0.05}$
Abell 611	$-0.68^{+0.06}_{-0.06}$	$-21.22_{-0.26}^{+0.24}$	$79.8^{+11.9}_{-10.8}$	$M^* + 4.97$	$-0.53^{+0.09}_{-0.06}$
$MS\ 2137$	$-0.84^{+0.06}_{-0.06}$	$-21.31^{+0.32}_{-0.35}$	$43.0^{+7.3}_{-6.6}$	$M^* + 5.56$	$-0.61^{+0.09}_{-0.08}$
RXJ 1532	$-0.72_{-0.05}^{+0.05}$	$-21.33^{+0.24}_{-0.26}$	$81.7^{+11.4}_{-10.5}$	$M^* + 5.08$	$-0.50^{+0.10}_{-0.06}$
RXJ 2248	$-0.76_{-0.04}^{+0.04}$	$-21.38^{+0.20}_{-0.22}$	$112.5^{+12.8}_{-12.1}$	$M^* + 5.13$	$-0.59^{+0.06}_{-0.05}$
MACS 1931	$-0.98^{+0.04}_{-0.04}$	$-21.13^{+0.26}_{-0.28}$	$59.9^{+7.4}_{-6.7}$	$M^* + 4.88$	$-0.77^{+0.06}_{-0.06}$
MACS 1115	$-0.82^{+0.05}_{-0.05}$	$-21.66^{+0.25}_{-0.28}$	$70.1_{-8.7}^{+9.6}$	$M^* + 4.41$	$-0.62^{+0.07}_{-0.07}$
MACS~1720	$-0.87^{+0.04}_{-0.04}$	$-21.80^{+0.25}_{-0.27}$	$70.6^{+8.8}_{-8.2}$	$M^* + 5.05$	$-0.66^{+0.06}_{-0.06}$
MACS 0416	$-0.72^{+0.05}_{-0.04}$	$-21.72_{-0.23}^{+0.22}$	$98.2^{+12.5}_{-11.5}$	$M^* + 4.97$	$-0.56^{+0.07}_{-0.06}$
MACS 0429	$-0.79^{+0.06}_{-0.05}$	$-21.20^{+0.25}_{-0.27}$	$73.0^{+10.3}_{-9.5}$	$M^* + 4.95$	$-0.54^{+0.09}_{-0.09}$
MACS~1206	$-0.80^{+0.04}_{-0.04}$	$-22.02^{+0.21}_{-0.22}$	$109.9^{+11.8}_{-11.1}$	$M^* + 5.27$	$-0.62^{+0.06}_{-0.05}$
MACS 0329	$-0.81^{+0.04}_{-0.04}$	$-22.07^{+0.22}_{-0.24}$	$96.9^{+11.0}_{-10.3}$	$M^* + 5.32$	$-0.61^{+0.05}_{-0.05}$
RXJ 1347	$-0.76^{+0.04}_{-0.04}$	$-21.69^{+0.20}_{-0.22}$	$113.0^{+13.0}_{-11.9}$	$M^* + 4.94$	$-0.60^{+0.06}_{-0.06}$
MACS 1311	$-1.09^{+0.04}_{-0.03}$	$-22.58^{+0.33}_{-0.36}$	$31.7^{+4.2}_{-3.9}$	$M^* + 5.33$	$-0.65^{+0.08}_{-0.07}$
MACS 1149	$-0.76^{+0.04}_{-0.04}$	$-21.96^{+0.17}_{-0.19}$	$155.6^{+15.4}_{-14.3}$	$M^* + 4.71$	$-0.53^{+0.09}_{-0.04}$
MACS 1423	$-0.89^{+0.04}_{-0.04}$	$-22.16^{+0.25}_{-0.28}$	$70.1^{+8.8}_{-8.1}$	$M^* + 4.91$	$-0.51^{+0.08}_{-0.08}$
MACS 0717	$-0.75^{+0.04}_{-0.03}$	$-21.92^{+0.16}_{-0.17}$	$189.9^{+17.0}_{-16.2}$	$M^* + 4.67$	$-0.50^{+0.08}_{-0.04}$
MACS 2129	$-0.87^{+0.04}_{-0.04}$	$-21.88^{+0.22}_{-0.23}$	$97.0^{+10.8}_{-10.2}$	$M^* + 4.63$	$-0.53^{+0.09}_{-0.08}$
MACS 0647	$-0.83^{+0.04}_{-0.04}$	$-21.94^{+0.22}_{-0.23}$	$97.2^{+11.1}_{-10.1}$	$M^* + 4.69$	$-0.63^{+0.07}_{-0.06}$
MACS~0744	$-0.90^{+0.04}_{-0.04}$	$-22.20^{+0.21}_{-0.24}$	$97.8^{+10.7}_{-10.0}$	$M^* + 4.45$	$-0.50^{+0.10}_{-0.06}$
CLJ 1226	$-0.96^{+0.05}_{-0.04}$	$-22.21^{+0.23}_{-0.24}$	$82.9_{-9.1}^{+9.8}$	$M^* + 3.96$	$-0.50^{+0.20}_{-0.10}$

scatter is consistent with 0. By fitting just our data, we find a slightly different slope, $E(z)M \propto E(z)N^{0.510}.$ These data, as well as both fits, are shown in Figure 3.10.

3.5.2 Luminosity Function

One way to characterize the quality of our photometric pipeline is to measure the luminosity function of cluster galaxies; this also serves as a way to characterize the cluster population

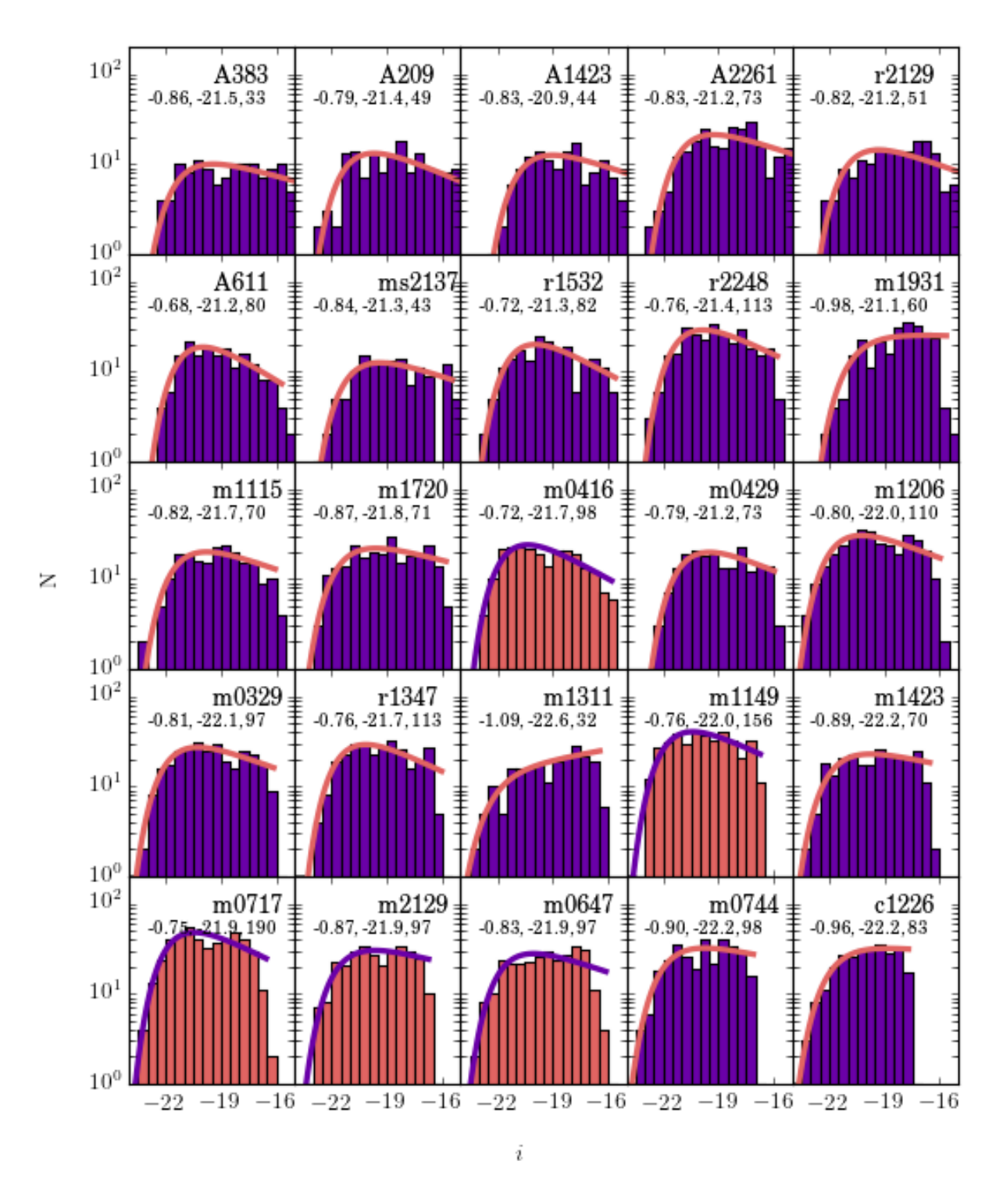


Figure 3.11 The k-corrected *i*-magnitude luminosity functions for all 25 CLASH clusters. Galaxies are shown binned in half-magnitude intervals. The best-fit Schechter luminosity function is shown in orange (purple) for X-ray selected (high magnification) clusters. Galaxies are plotted in order of increasing redshift. Best-fit values of α , M*, and ϕ * are provided in that order on each plot. Details of the fits are provided in the text.

with respect to previous cluster studies. To do this, we consider a Schechter luminosity function (Schechter, 1976), of the form

$$\phi(M) \ dM = 0.4 \ \phi^* \ln(10) \times 10^{0.4(M^* - M) \times (1 + \alpha)} \times \exp(-10^{0.4(M^* - M)}) \ dM, \tag{3.5}$$

where ϕ^* is the density of galaxies, M* is the characteristic magnitude of the function, M is the absolute magnitude of a galaxy, and α is the faint-end slope. We caution the reader that, in this form, a "flat slope" occurs at $\alpha = -1$. For each cluster, we determined the parameters of the Schechter function using unbinned luminosity data, by following the maximum likelihood technique described in Marshall et al. (1983) and Donahue & Voit (1999). Using *i*-band k-corrected magnitudes, we found the minimum of a likelihood function defined such that

$$S = -2\ln(\mathcal{L}) = -2\sum_{i}^{N} \ln(\phi(M_i)) + 2\int_{M_{faint}} \phi(M) dM$$
 (3.6)

in a grid of values for α , M*, and ϕ^* . Defined this way, the increments in S are similar to the increments in χ^2 for the determination of uncertainties. This statistical method does not by itself give a goodness of fit, however. M_{faint} is set for each cluster to be the faintest object classified as a member. We used a 50x50x25 grid covering $\alpha = [-1.3, -0.5]$, $M^* = [-23, -18]$, and $\phi^* = [10^{-1}, 10^4]$, where ϕ^* is in units of galaxies per magnitude per cluster field (within the observed field of view). After finding the best value, we examined a sub-grid covering the 9x9x9 box centered on the best parameters. We repeated the sub-sampling step a second time, for a total of three resolution levels for the three luminosity function parameters of interest. To determine the $1-\sigma$ uncertainties we held two parameters fixed and iterated the

third until $\Delta(S) \geq 3.53$ (The $\Delta \chi^2$ value = 3.53 for 1σ constraints for three free parameters, e.g. Lampton et al., 1976).

We present our best-fit values for each of the CLASH clusters in Table 3.3. Uncertainties listed are 1σ values. We also plot our luminosity functions, as well as histograms of cluster members, in Figure 3.11. ϕ^* has been divided by 2 in this figure to match the half-magnitude-wide bins.

For our sample, we find best-fit α values in the range $-1.0 \lesssim \alpha \lesssim -0.7$ and M* values in the range $-22 \lesssim \mathrm{M}^* \lesssim -21$. We compare these values to those derived by Rudnick et al. (2009). They fit SDSS clusters drawn from the sample presented in von der Linden et al. (2007) to a maximum redshift of $z \leqslant 0.06$. For *i*-band observations, their best fit was $\mathrm{M}_i^* = -21.46^{+0.03}_{-0.04}, \ \alpha = -0.75^{+0.02}_{-0.01}$. That work also examined the luminosity function of 16 clusters in the ESO Distant Cluster Survey (EDisCS) spanning redshifts 0.4 < z < 0.8. When only including red sequence members, the EDisCS clusters together were best fit by an *i*-band luminosity function of $\mathrm{M}_i^* = -21.80^{+0.22}_{-0.17}$ and $\alpha = -0.34^{+0.16}_{-0.10}$.

De Propris et al. (2013) studied 11 merging clusters at $0.2 \lesssim z \lesssim 0.6$, finding best fit Schechter slopes of $\alpha \approx -1$. Stott et al. (2007) derived values of $\alpha = -0.91 \pm 0.02$, $M_V = -21.39 \pm 0.05$ for 10 MACS (Ebeling et al., 2001) clusters at $z \sim 0.5$, including several considered in this work. Martinet et al. (2015) presented measurements of luminosity functions for $0.4 \leq z < 0.9$ at rest-frame I and R; their red-sequence selected results are $\alpha_R = -0.80 \pm 0.14$, $M_R^* = -22.4 \pm 0.2$ and $\alpha_I = -0.37 \pm 0.18$, $M_I^* = -22.0 \pm 0.2$.

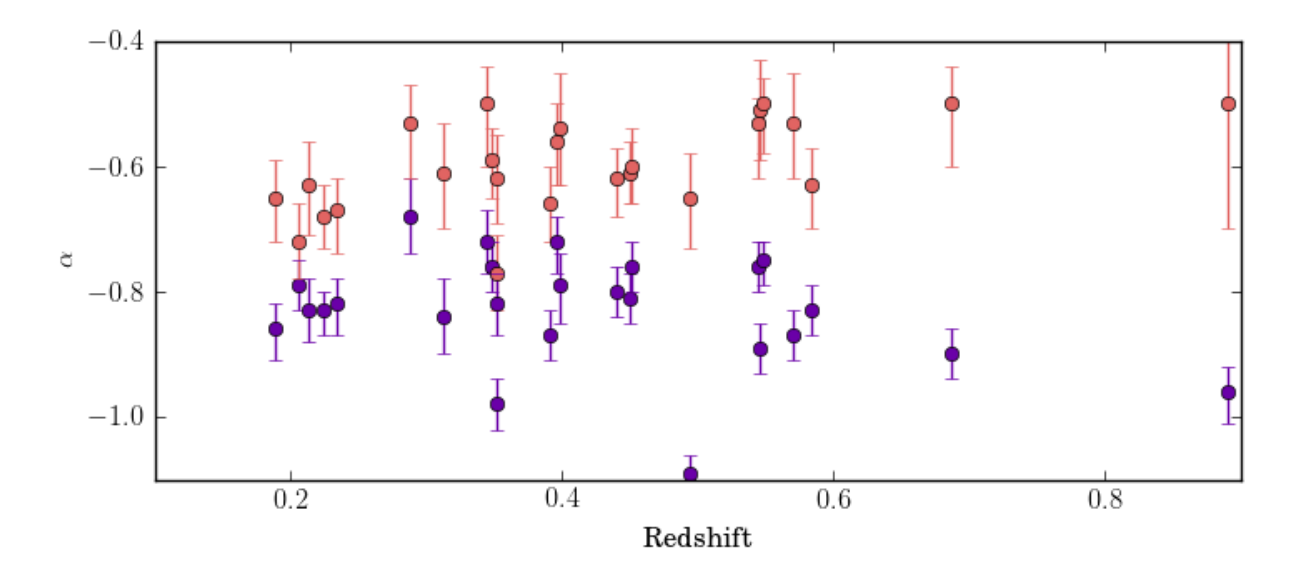


Figure 3.12 The measured slopes of the luminosity functions for all 25 CLASH clusters. We show the results for all cluster members in purple and for only those along the red sequence in orange. As a "flat slope" in magnitude-space is given by $\alpha = -1$, values greater than that show a luminosity function with fewer faint galaxies than galaxies at M*. We see a clear trend for a steepening in the faint end slope when only including red sequence members.

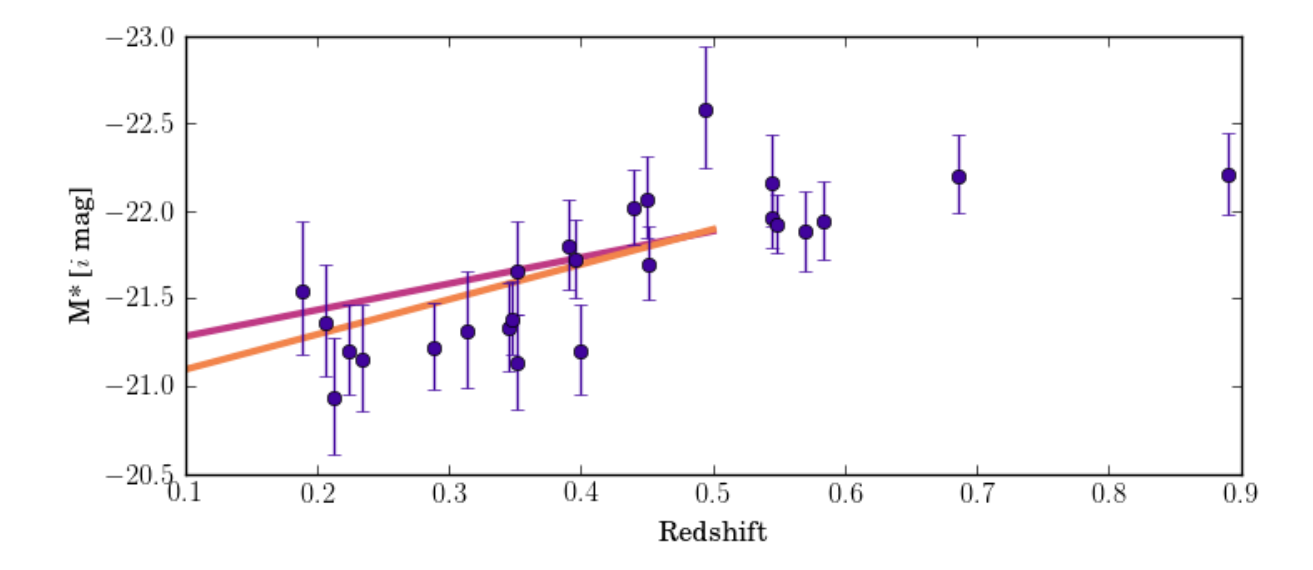


Figure 3.13 The measured values of M^* for *i*-band luminosity functions of CLASH clusters. Shown in pink and orange are fits for *i*-band M^* values for all (orange) and only red (pink) galaxies, with evolution parameters from Loveday et al. (2012), although assuming the values of M^* for a double-power-law fit, as discussed in the text.

The results presented in this work are consistent with those described above. The values of M* we report are in agreement with other studies, which supports our determination of photometry for relatively bright cluster galaxies. Several works report a much steeper slope (lower value of α), namely Martinet et al. (2015) and Rudnick et al. (2009); these fits only considered red sequence galaxies. While several other studies have found steeper faint-end slopes for red sequence-only samples (e.g., De Lucia et al., 2004b), works that do not select only red sequence members find α values more consistent with what we present here (Strazzullo et al., 2010; Mancone et al., 2012). As a comparison, we used galaxies with g-r colors within $|\Delta(g-r)| < 0.1$ of our red sequence slopes (discussed in Section 4.4) to compute a red sequence-only luminosity function for each cluster. Faint end slopes, denoted as α_{RS} , for each cluster are shown in Table 3.3. We see a consistent steepening of the faint-end slope by only considering red sequence objects, which we show in Figure 3.12.

We also consider our measured evolution in M*. In Figure 3.13 we plot our measured values of M* in *i*-band for all cluster members. We see a trend for increasing M* brightness with increasing redshift, which is not unexpected (e.g. Xia et al., 2006). We also plot the best-fit evolutionary parameters from the Galaxy and Mass Assembly (GAMA) k-corrected *i*-band luminosity fuctions presented by Loveday et al. (2012). While the linear slope they fit to the redshift evolution of M* is based on the best-fit values from a single-component fit, they found that double-power-law fits provided significantly better fits for *i*-band. Because of that, the plotted result from Loveday et al. (2012) is normalized to the best-fit M* at z=0.1 from the double-power-law fit but evolves with the slope derived from single-component fits. GAMA observations cover relatively large areas of sky, as opposed to centering on galaxy clusters, so they provide a field galaxy comparison. We see a similar evolution in M* with the

GAMA sample in the redshift range they sampled, albeit with preferentially fainter values of M*.

Having confirmed the validity of our luminosity function measurements, we use our measured galaxy counts to infer a detection limit for each cluster in terms of $M-M^*$. To do this, we consider each half-magnitude bin shown in Table 3.11; we find the faintest bin for which the total galaxy count is within 90% of that predicted by our best-fit Schechter function. We report those values in Table 3.3. We find that, even out to $z \sim 0.5$, we detect galaxies down to $M-M^* \sim 5$. As this measurement of our detection limit may be biased by a lack of detected galaxies pulling the slope down, we also find a limiting magnitude by finding the faintest bin that is within 80% of that expected by a Schechter function with the same values of M^* and ϕ^* but $\alpha = -1$; these limits are exactly the same. Obtaining robust detections of galaxies this deep into the cluster luminosity function validates our assertion that we can use mode-filtered detection and photometry to extract faint cluster members from the CLASH field.

3.5.3 Stellar Mass

We examine the total stellar mass of the 25 CLASH clusters by integrating their luminosity functions and utilizing a mass-to-light ratio to convert from luminosity to stellar mass. To provide a uniform measure across the entire sample, we limit ourselves to the luminosity within r_{2500} . We re-fit luminosity functions for the galaxies contained inside this radius for all 25 clusters; the results of this are given in Table 3.4.

Table 3.4. CLASH r_{2500} values

Classian Name		N. (*	1*	т	D + 8	М
Cluster Name	α	M_i^* (mag)	ϕ^*	$(10^{12} L_{\odot})$	Boost ^a	$^{\rm M_*}_{(10^{12}~{ m M}_\odot)}$
	10.05		150			
Abell 383	$-0.86^{+0.05}_{-0.04}$	$-21.54^{+0.36}_{-0.40}$	$32.9_{-5.0}^{+5.6}$	$1.40^{+0.70}_{-0.48}$	1.64	$4.24^{+1.68}_{-2.75}$
Abell 209	$-0.79_{-0.04}^{+0.04}$	$-21.36^{+0.30}_{-0.33}$	$49.1_{-7.0}^{+7.6}$	$1.56^{+0.62}_{-0.46}$	1.48	$4.72^{+1.68}_{-2.58}$
Abell 1423	$-0.82^{+0.05}_{-0.05}$	$-20.93^{+0.32}_{-0.35}$	$43.4^{+7.2}_{-6.6}$	$0.66^{+0.29}_{-0.20}$	1.04	$1.99^{+0.74}_{-1.16}$
Abell 2261	$-0.83^{+0.04}_{-0.03}$	$-21.20^{+0.25}_{-0.27}$	$73.2^{+9.1}_{-8.3}$	$2.18^{+0.68}_{-0.53}$	1.58	$6.58^{+2.17}_{-3.10}$
RXJ 2129	$-0.82^{+0.05}_{-0.04}$	$-21.18^{+0.30}_{-0.33}$	$49.2^{+7.6}_{-6.8}$	$0.95^{+0.39}_{-0.28}$	1.05	$2.87^{+1.01}_{-1.57}$
Abell 611	$-0.67^{+0.06}_{-0.06}$	$-21.16^{+0.24}_{-0.26}$	$80.0^{+12.0}_{-11.0}$	$1.40^{+0.45}_{-0.35}$	1.00	$4.23^{+1.39}_{-2.04}$
MS 2137	$-0.85^{+0.06}_{-0.05}$	$-21.40^{+0.34}_{-0.37}$	$38.8^{+6.8}_{-6.2}$	$0.88^{+0.40}_{-0.29}$	1.00	$2.67^{+1.01}_{-1.58}$
RXJ 1532	$-0.73^{+0.07}_{-0.06}$	$-21.30^{+0.30}_{-0.33}$	$51.4^{+9.1}_{-8.1}$	$1.03^{+0.43}_{-0.31}$	1.00	$3.12^{+1.15}_{-1.73}$
RXJ 2248	$-0.77^{+0.05}_{-0.04}$	$-21.43^{+0.22}_{-0.23}$	$98.0^{+11.9}_{-11.1}$	$2.24^{+0.63}_{-0.49}$	1.00	$6.77^{+2.14}_{-2.98}$
MACS 1931	$-0.99^{+0.05}_{-0.04}$	$-21.17^{+0.30}_{-0.32}$	$43.7^{+6.2}_{-5.7}$	$0.86^{+0.33}_{-0.24}$	1.00	$2.59^{+0.90}_{-1.39}$
MACS 1115	$-0.84^{+0.06}_{-0.06}$	$-21.84^{+0.32}_{-0.36}$	$42.0_{-6.5}^{+7.2}$	$1.43^{+0.65}_{-0.46}$	1.00	$4.32^{+1.63}_{-2.63}$
MACS 1720	$-0.89^{+0.05}_{-0.04}$	$-21.89^{+0.29}_{-0.32}$	$51.1^{+7.3}_{-6.7}$	$1.86^{+0.71}_{-0.52}$	1.00	$5.61^{+1.99}_{-2.96}$
MACS 0416	$-0.69^{+0.06}_{-0.06}$	$-21.72^{+0.28}_{-0.30}$	$59.7^{+10.1}_{-9.0}$	$1.76^{+0.65}_{-0.50}$	1.00	$5.30^{+1.86}_{-2.79}$
MACS 0429	$-0.81^{+0.06}_{-0.06}$	$-21.17_{-0.33}^{+0.30}$	$51.2^{+8.5}_{-7.7}$	$0.93^{+0.38}_{-0.27}$	1.00	$2.81^{+1.01}_{-1.55}$
MACS~1206	$-0.84^{+0.04}_{-0.04}$	$-22.15^{+0.26}_{-0.28}$	$69.7^{+9.0}_{-8.4}$	$3.16^{+1.04}_{-0.79}$	1.00	$9.54^{+3.18}_{-4.62}$
MACS 0329	$-0.83^{+0.04}_{-0.04}$	$-22.13^{+0.25}_{-0.28}$	$70.1_{-8.5}^{+9.3}$	$3.11^{+1.02}_{-0.80}$	1.00	$9.39^{+3.14}_{-4.56}$
RXJ 1347	$-0.75^{+0.05}_{-0.05}$	$-21.63^{+0.22}_{-0.24}$	$96.7^{+12.1}_{-11.2}$	$2.65^{+0.76}_{-0.60}$	1.00	$7.99^{+2.52}_{-3.57}$
MACS 1311	$-1.04^{+0.05}_{-0.04}$	$-22.70^{+0.41}_{-0.49}$	$23.0^{+3.9}_{-3.5}$	$1.91^{+1.19}_{-0.74}$	1.00	$5.76^{+2.49}_{-4.28}$
MACS 1149	$-0.61^{+0.07}_{-0.06}$	$-21.81^{+0.22}_{-0.24}$	$97.2^{+14.1}_{-13.0}$	$3.08^{+0.92}_{-0.73}$	1.00	$9.29^{+2.98}_{-4.21}$
MACS 1423	$-0.95^{+0.05}_{-0.05}$	$-22.33^{+0.34}_{-0.39}$	$37.0^{+6.1}_{-5.5}$	$2.07^{+1.02}_{-0.68}$	1.00	$6.26^{+2.43}_{-3.83}$
MACS 0717	$-0.73^{+0.06}_{-0.05}$	$-22.06^{+0.22}_{-0.24}$	$97.8^{+12.8}_{-11.8}$	$3.96^{+1.14}_{-0.92}$	1.00	$11.96^{+3.83}_{-5.55}$
MACS 2129	$-0.76^{+0.05}_{-0.06}$	$-21.79_{-0.26}^{+0.24}$	$81.4^{+11.4}_{-10.4}$	$2.59^{+0.84}_{-0.63}$	1.00	$7.82^{+2.59}_{-3.74}$
MACS 0647	$-0.80^{+0.07}_{-0.06}$	$-21.86^{+0.29}_{-0.32}$	$53.0^{+8.8}_{-7.9}$	$1.82^{+0.73}_{-0.54}$	1.00	$5.49^{+2.00}_{-3.01}$
MACS 0744	$-0.71^{+0.07}_{-0.07}$	$-21.83^{+0.24}_{-0.26}$	$82.1_{-11.2}^{+12.5}$	$2.68^{+0.83}_{-0.69}$	1.00	$8.09^{+2.71}_{-3.96}$
CLJ 1226	$-0.94^{+0.07}_{-0.06}$	$-22.32^{+0.29}_{-0.33}$	$51.2^{+8.2}_{-7.4}$	$2.83^{+1.16}_{-0.86}$	1.00	$8.54^{+3.09}_{-4.64}$

 $^{^{\}rm a}{\rm Factor}$ by which luminosity was scaled to account for incomplete aperture effects.

A Schechter luminosity function has the property that the integrated luminosity can be found analytically,

$$L = \int_0^\infty L \ \phi(L) \ dL = \phi^* \ L^* \ \Gamma(\alpha + 2), \tag{3.7}$$

where $\phi(L)$ is the luminosity function in terms of luminosity and Γ is the Gamma function. α and ϕ^* are the same for a luminosity function characterized by magnitudes or luminosity, while L^* is the luminosity that M^* corresponds to. To account for the fact that several clusters do not have full photometric coverage out to r_{2500} , we calculate a correction factor based on the radius at which the total cluster coverage in the F814W filter drops below 60%. Assuming an NFW profile (Navarro et al., 1997), the total mass inside a radius r can be found as

$$M(r) \propto r_s^3 \left(\log(r_s + r) - \log(r_s) - \frac{r}{r_s + r} \right). \tag{3.8}$$

The scale radius r_s for each cluster, as well as r_{2500} , is given in Table 3.2. For those galaxies without full coverage out to r_{2500} , we calculate the NFW mass at r_{2500} and at the radius at which coverage drops below 60%; the ratio between those two values is the coefficient we use to scale up our luminosity measurements. This value is given for each cluster in Table 3.4.

In Section 4.6 we find that the *i*-band stellar mass-to-light ratio is $\log \left((\frac{M_*}{M_{\odot}})/(\frac{L}{L_{\odot}}) \right) = 0.48 \pm 0.12$ for luminous red sequence cluster members. As these galaxies make up the majority of the light in our sample, we use this value of the stellar mass-to-light ratio, as opposed to the value computed for all cluster members, which has larger uncertainty due to the population of blue cloud galaxies. We convert integrated luminosities into stellar masses; the results of this are given in Table 3.4. To determine the errors on the luminosities and stellar masses, we randomly draw 10,000 samples from the uncertainty distributions of α ,

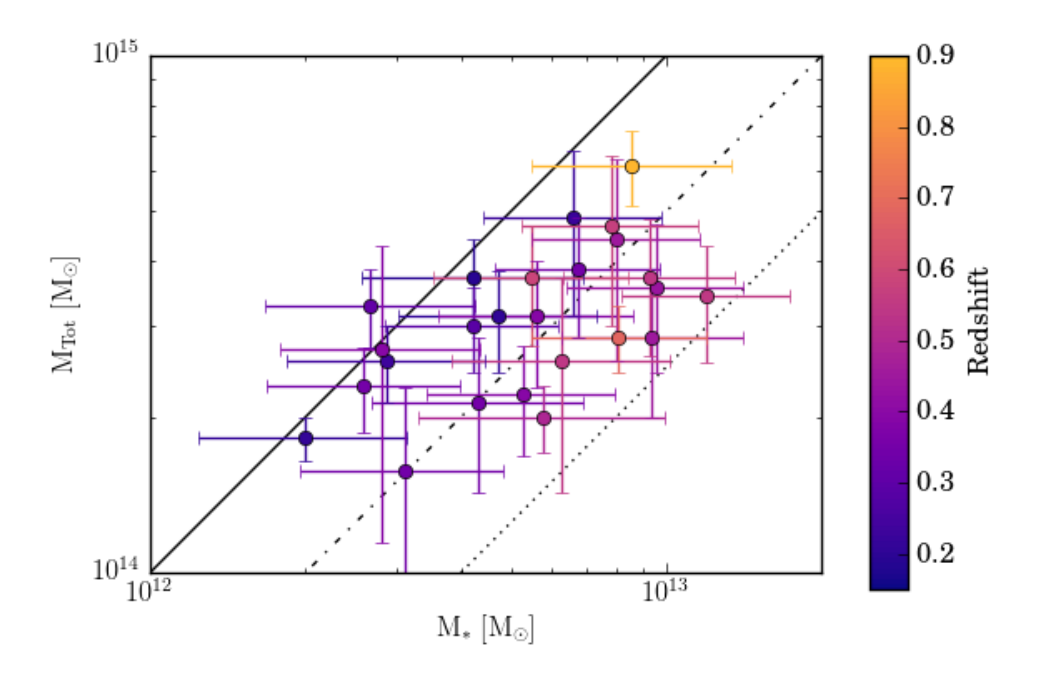


Figure 3.14 Comparison between stellar masses and total masses within r_{2500} . Clusters are color-coded by redshift. Total masses are mostly drawn from lensing measurements by Merten et al. (2015) and Umetsu et al. (2016), but also include X-ray masses from Donahue et al. (2014). Stellar masses are derived from total cluster luminosity measurements, as described in the text, adjusted as needed to account for aperture effects. Shown are lines corresponding to $M_* = 0.01 M_{Tot}$ (solid), $M_* = 0.02 M_{Tot}$ (dot-dashed), and $M_* = 0.04 M_{Tot}$ (dotted).

 M^* , ϕ^* , and the stellar mass-to-light ratio; upper and lower limits correspond to the 68.27 percentiles (1 σ) above and below the nominal value.

We plot our results for M_* against the lensing masses derived by Merten et al. (2015) and Umetsu et al. (2016), as well as two HSE mass estimates from Donahue et al. (2014), in Figure 3.14. These results show a median stellar mass fraction of 1.8%, with a scatter of 0.7%. Measurement uncertainties are too large for us to calculate an intrinsic scatter of this sample, however. While the sample lacks the dynamic range to consider scaling relations, these clusters show consistency with each other. As our measurement of stellar mass is based directly on measurements of luminosity, the internal consistency is further evidence that we

are well-sampling the luminosity of the cluster population.

Lin et al. (2012) measured the stellar mass fraction for 96 massive clusters between redshifts 0.0 < z < 0.6. They found that, for a halo of mass $M_{500} = 10^{14} h_{71}^{-1} M_{\odot}$, the stellar mass fraction is $M_*/M_{500} = 0.018 \pm 0.001$, with a scatter of 31% (our measured scatter is 41%). Lin et al. (2012) also took mass scaling into account. Gonzalez et al. (2013) measured a stellar mass ratio of $M_*/M_{500} = 0.039 \pm 0.002$, but with a steep slope such that at $M_{500} = 4 \times 10^{14} M_{\odot}$ (a halo mass characteristic of what we study here, although within r_{500}) that ratio is $M_*/M_{500} \approx 0.021$.

3.6 Summary

In this chapter, we presented a new photometric catalog of CLASH cluster sources, with photometric redshifts. Objects in this catalog were detected using multiple scales of mode-based background subtraction to best identify small objects embedded in the complex light profile of these massive clusters. We used local background modeling and annular degradation to photometer galaxies while leaving behind the large-scale light structure. Highlights of this work include:

1. We detect and photometer 22,557 objects in the fields of 25 massive galaxy clusters, with a median of 683 objects per cluster field brighter than AB Mag in F814W = 25. A median of 459 of these per cluster are well detected in at least 8 filters; 318 in 12, and 154 in 14, spanning the ultraviolet to the near infrared. Such complete photometry will allow us to model the physical properties of these objects, as is discussed in Chapter 4.

- 2. Thanks to the optimized background measurement, source detection, and photometry techniques described in this paper, we obtain accurate measurements of photometric redshifts for $\approx 82\%$ of objects with spectroscopic redshift confirmation, with $\sigma(\Delta_z) = 0.0438$. Additionally, our catalog is able to obtain comparable numbers of detected objects with photometric redshifts consistent with clusters as was reported in the original attempt for the CLASH clusters, yet has a significantly reduced amount of excess detections.
- 3. We validate our photometry and that of the ASTRODEEP collaboration by cross-comparing results for MACS J0416, a galaxy cluster also observed as part of the Hubble Frontier Fields. We find minimal differences in measured photometric redshifts and photometry between our two techniques.
- 4. We characterize our detection limits for these clusters with a Schechter luminosity function. For k-corrected *i*-band values, 17 clusters are detected out to $M_i \gtrsim M^* + 5$ and all 25 are detected to $M_i \sim M^* + 4$. These luminosity functions also provide measures of the cluster populations across a range of redshifts. We find evidence for a decrease in the faint-end slope caused by selecting only red sequence members.
- 5. In conjunction with observations of moderate-luminosity clusters by Hoekstra et al. (2011), we find a relationship between the optical luminosity of a cluster and its mass, where both properties are for within r_{2500} . We find $E(z)M \propto (E(z) N_{2500})^{0.651}$.
 - 6. Using Schechter luminosity functions to derive total integrated luminosities for the 25

CLASH clusters within r_{2500} , in combination with a mass-to-light conversion described in

Chapter 4, we compare the stellar mass to total (mostly lensing-measured) masses. We find

that these clusters have stellar mass fractions of around $1.8 \pm 0.7\%$ relative to the total mass.

The internal consistency of our sample, in combination with the measured consistency from

the richness-mass scaling relation, is further evidence that we are accurately estimating the

total cluster light.

Thomas Connor acknowledges support from a fellowship from the Michigan State Unver-

sity College of Natural Science. This research has made use of the NASA/IPAC Extragalactic

Database (NED) which is operated by the Jet Propulsion Laboratory, California Institute of

Technology, under contract with the National Aeronautics and Space Administration. We

used the cosmological calculator presented in Wright (2006) in this work.

Facilities: Hubble Space Telescope/ACS, Hubble Space Telescope/WFC3,

103

Chapter 4

Galaxy Properties, Membership, and Red Sequence Evolution in CLASH

Clusters

4.1 Introduction

Clusters of galaxies, including their associated dark matter halos and hot baryonic gas, are the largest gravitationally bound systems in the Universe, and therefore are an important tool for studying cosmology, structure formation, and the evolution of the Universe (Voit, 2005; Giodini et al., 2013; Reiprich et al., 2013). Bulk properties of clusters, measured through X-ray observations of the hot, ionized intracluster gas, show self-similar scaling from low to high-mass systems, with minimal evolution with redshift (Maughan, 2007; Sun et al., 2009; Mahdavi et al., 2013; Connor et al., 2014). Cluster galaxies are sensitive to their environment (Delaye et al., 2014; Darvish et al., 2016), and they therefore provide an opportunity to study the differences between clusters across mass (Weinmann et al., 2006) and redshift space (Erfanianfar et al., 2014; Andreon et al., 2016; Nantais et al., 2016).

In particular, cluster galaxies have been observed to follow a linear relationship in color-

 $^{^{1}}$ Self-similar scaling means that small clusters are effectively just scaled-down versions of larger clusters.

magnitude space (Baum, 1959; Visvanathan & Sandage, 1977), wherein cluster galaxies appear as a tight bunching in color that is distinct from the general population of field galaxies. This relationship, called the red sequence or color-magnitude relation, is found in clusters out to at least $z\approx 1.5$ - 2.0 (Blakeslee et al., 2003; De Lucia et al., 2007; Lemaux et al., 2012; Rudnick et al., 2012; Andreon et al., 2014). The red sequence is also used as an efficient means for blindly detecting galaxy clusters (Annis et al., 1999; Gladders & Yee, 2000; Gladders et al., 2007; Hao et al., 2010; Murphy et al., 2012) and for estimating their photometric redshifts (Koester et al., 2007a; Gal et al., 2009; Thanjavur et al., 2009; Rykoff et al., 2014).

One important parameter of the red sequence is its slope on a color-magnitude diagram for galaxies, which manifests as lower luminosity galaxies being bluer than brighter galaxies. It is believed the slope is determined by a mass-metallicity relation, such that less massive objects are less metal-rich than more massive objects (Kodama & Arimoto, 1997; Stanford et al., 1998; Ferreras et al., 1999; Gallazzi et al., 2006). Due to metal lines blanketing the bluest parts of stellar spectra and metal opacity increasing the physical sizes of stars, more metal rich stars (and, by extension, galaxies) are redder than metal-poor galaxies (e.g., Bruzual & Charlot, 2003; Maraston, 2005). More metal-rich galaxies appear redder (Faber, 1973; Worthey, 1994), so the red sequence slopes toward the more massive galaxies being redder. A qualitative origin for the mass-metallicity relation is that, in less massive galaxies, supernova-driven wind is more effective at ejecting gas due to the smaller potential well of the galaxy (Larson, 1974; Arimoto & Yoshii, 1987; Matteucci & Tornambe, 1987; Lilly et al., 2013; Voit et al., 2015); by driving out metal-rich gas, less-massive galaxies are therefore more metal-poor than their larger neighbors (Tremonti et al., 2004). While this

is a compelling model, detailed numerical simulations have had difficulty reproducing the mass-metallicity relation without fine-tuning (e.g., De Lucia et al., 2004a; de Rossi et al., 2007; Mouhcine et al., 2008).

Alternatively, age may have an effect on the properties of the red sequence. Galaxy colors are subject to an age-metallicity degeneracy; changes in either can make galaxies redder (Worthey, 1994, 1999). One way to break this entanglement is to observe the evolution of the red sequence; since it exists beyond even moderate redshifts ($z \approx 0.3$), the red sequence must be a consequence of the mass-metallicity relation (Kodama & Arimoto, 1997; Kauffmann & Charlot, 1998; Kodama et al., 1998). Were it driven by age, the passive evolution in that redshift range would cause significant evolution in the slope as bluer galaxies would have significantly younger populations at earlier redshifts. However, others have argued that age effects still affect the observed red sequence slope (Ferreras et al., 1999; Terlevich et al., 1999; Trager et al., 2000; Poggianti et al., 2001; Rakos & Schombert, 2004).

Another way for age to impact the observed color-magnitude relation is by adjusting the scatter about the relation. A population with a nearly identical formation time has a larger scatter at early times, when the small differences in formation time have relative significance, but this scatter reduces as the population ages. Early observations of the relation showed a tight scatter, implying that cluster galaxies formed at the same time and early on (Bower et al., 1992; Ellis et al., 1997; Stanford et al., 1998; Bower et al., 1998; Andreon, 2003; McIntosh et al., 2005). Recent works have shown that the measured scatter of the red sequence evolves with time (Hilton et al., 2009; Papovich et al., 2010; Foltz et al., 2015) and increases at the fainter end of the red sequence (Conselice et al., 2002; Gallazzi et al., 2006). This

observed tight scatter implies a long-lived, quiescent population, while the scatter increasing with age is evidence that the scatter is the result of age.

It is also important to consider the evolution of the slope of the red sequence itself. Clusters are not static objects; they are constantly growing and accreting new galaxies (e.g., Ichinohe et al., 2015). Porter et al. (2008) found a sudden enhancement in star formation for galaxies just outside the cluster's virial radius that are falling into a cluster via a supercluster filament. Previous works have found evidence for infalling galaxies having their star formation shut-off in the hostile cluster environment and merging onto the red sequence (De Lucia et al., 2007; Stott et al., 2007; Smith et al., 2008; Stott et al., 2009). In this context, the evolution of the red sequence – particularly at the faint end – is a sensitive marker of cluster evolution. In contrast, others (Andreon, 2008; Crawford et al., 2009) find no evolution in the slope. Stott et al. (2009) have argued that this discrepancy is caused by k-correction, which, if inaccurate, can bias slope measurements.

Recent work on red sequence research has focused on the extensive coverage provided by the Sloan Digital Sky Survey (SDSS) and other large survey programs (Hogg et al., 2004; Bernardi et al., 2005; Cool et al., 2006; Hao et al., 2009; Rykoff et al., 2014; Oguri, 2014). These studies have provided an excellent opportunity to study the properties of the red sequence for a large number of clusters, but they are inherently limited to only study clusters at a shallow depth. Breaking the age/metallicity degeneracy for the interpretation of indi-

²A k-correction is a correction from observed magnitudes to rest frame magnitudes, accounting for the dual effects of filters sampling bluer regions of the rest frame spectrum at higher redshift and of the relative spectral width of the rest frame spectrum being sampled in smaller increments with increasing redshift. K-corrections are informed by assumed spectral properties of a galaxy; this is why it is important we sample the spectra of our galaxies continuously across a wide range of wavelengths in this work.

vidual galaxy colors requires photometric coverage beyond optical images alone. Models of the red sequence predict changes at the faint end, which these surveys cannot well sample beyond the local Universe. In order to properly understand what shapes the red sequence, it is apparent we need a sample of cluster galaxies that 1) spans a range of redshift, 2) includes faint $(M^* + 4)$ members, 3) has age and metallicity information, and 4) can be placed on the same photometric system.

In this work, we exploit 16-filter, multi-wavelength coverage with the Hubble Space Telescope (HST) of 25 massive galaxy clusters at redshifts z=0.187 to z=0.890 to examine the red sequence in great detail. In particular, we optimize our photometric analysis to recover the faint population of galaxies embedded in the light profiles of massive galaxies. We use spectral energy distribution (SED)-fitting to constrain the properties of red sequence members, which we use to study the effects of age, metallicity, and star-formation histories on the growth, evolution, and scatter in the observed cluster red sequence across cosmic time. We exploit the 16 bandpasses and SED fitting to obtain the highly robust estimates of k-corrections, based on interpolations of the photometry of overlapping filters.

4.2 Data

The data used in this work are described in Chapter 3, but we briefly describe them here. We used mode-filtered images to detect galaxies throughout the 25 cluster fields of the Cluster Lensing and Supernova survey with Hubble (CLASH, Postman et al., 2012b). Objects were detected in at least 4 filters; in total, we had 16 filters of data for each cluster covering the

Table 4.1. CLASH Redshifted Filter Analogs

Cluster Name	Redshift	u	g	r	Y	J	m – M
Abell 383	0.189	F435W	F625W	F775W	F125W	F160W	39.82
Abell 209	0.206	F435W	F625W	F775W	F125W	F160W	40.03
Abell 1423	0.213	F435W	F625W	F775W	F125W	F160W	40.11
Abell 2261	0.224	F435W	F625W	F775W	F125W	F160W	40.23
RXJ 2129	0.234	F435W	F625W	F775W	F125W	F160W	40.34
Abell 611	0.288	F435W	F606W	F775W	F140W	F160W	40.85
MS 2137	0.313	F475W	F625W	F814W	F140W	F160W	41.06
RXJ 1532	0.345	F475W	F625W	F814W	F140W	F160W	41.31
RXJ 2248	0.348	F475W	F625W	F814W	F140W	F160W	41.33
MACS 1115	0.352	F475W	F625W	F814W	F140W	F160W	41.36
MACS 1931	0.352	F475W	F625W	F814W	F140W	F160W	41.36
MACS 1720	0.391	F475W	F625W	F814W	F140W	F160W	41.63
MACS 0416	0.396	F475W	F625W	F814W	F140W	F160W	41.66
MACS 0429	0.399	F475W	F625W	F814W	F140W	F160W	41.68
MACS 1206	0.440	F475W	F625W	F814W	F140W	F160W	41.93
MACS~0329	0.450	F475W	F625W	F814W	F140W	F160W	41.99
RXJ 1347	0.451	F475W	F625W	F814W	F140W	F160W	41.99
MACS 1311	0.494	F475W	F775W	F105W	F140W	F160W	42.23
MACS 1149	0.544	F555W	F775W	F105W	F140W	F160W	42.48
MACS 1423	0.545	F555W	F775W	F105W	F140W	F160W	42.49
MACS 0717	0.548	F555W	F775W	F105W	F140W	F160W	42.50
MACS 2129	0.570	F555W	F775W	F105W	F140W	F160W	42.60
MACS 0647	0.584	F555W	F775W	F105W	F140W	F160W	42.67
MACS 0744	0.686	F555W	F814W	F105W	F140W	F160W	43.09
$\mathrm{CLJ}\ 1226$	0.890	F625W	F814W	F125W	F140W	F160W	43.79

ultraviolet to infrared bands. For each galaxy, background subtraction was performed using a mode-based estimate of the local light. Photometry for each galaxy was performed in the same aperture for all filters. As the point spread function (PSF) full width at half maximum (FWHM) is $\sim 0.07'' - 0.15''$ (Ford et al., 2003; Sirianni et al., 2003), which is smaller than our apertures, we do not include a PSF correction.

All 25 clusters used in this work are listed in Table 4.1 in order of ascending redshift. To compare these clusters to other works and each other, we define a set of five filters for each cluster that act as analogs to the u, g, r, Y, and J filters. HST filters named in Table 4.1 were chosen to best sample the rest-frame bandpasses of these five filters while also avoiding an HST filter being classified as the analog for two adjacent ground-based filters for the same cluster (a potential problem for clusters at the high redshift end of our sample).

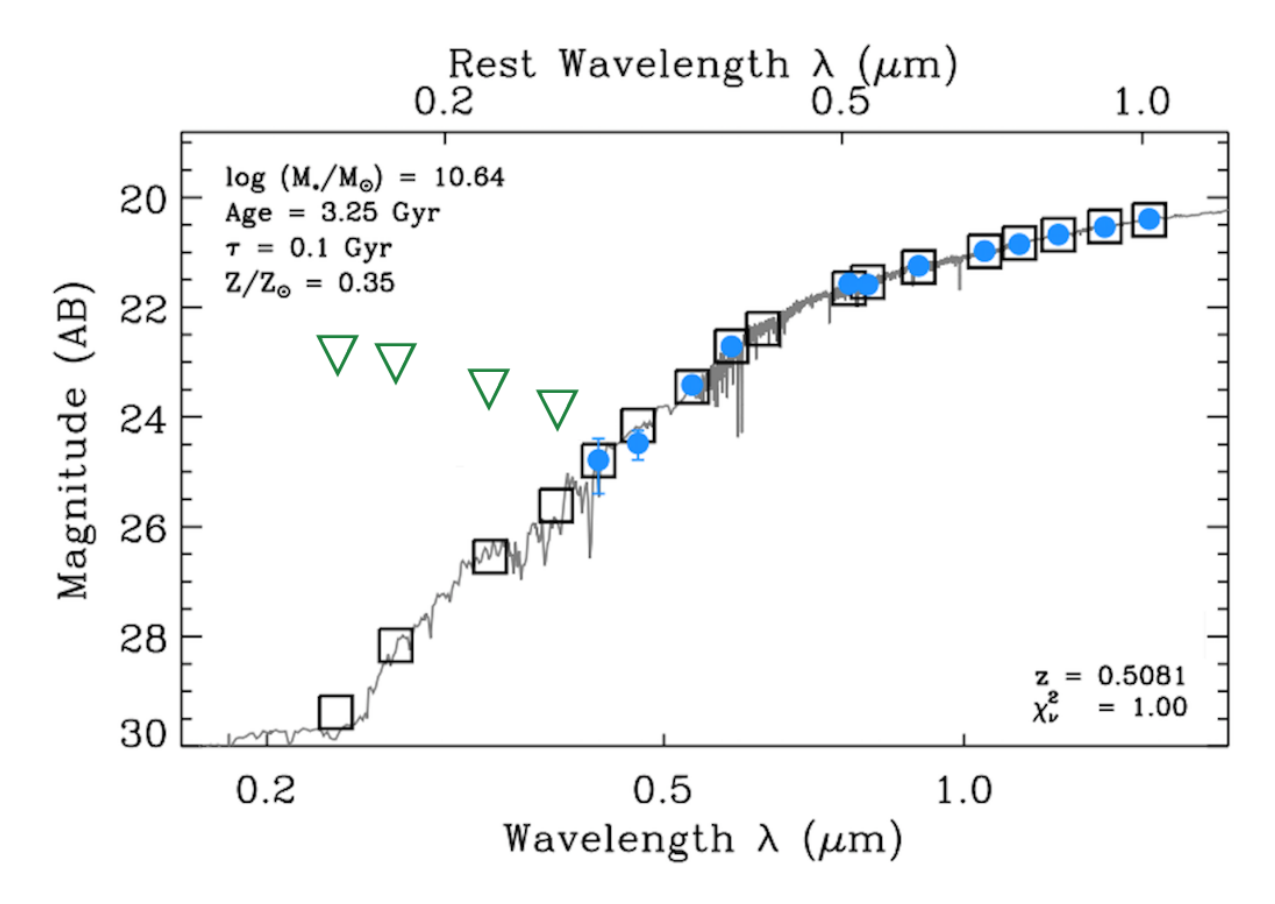


Figure 4.1 Modeled SED fit to a galaxy in the field of MACS1423 (z=0.545). In this particular run, the redshift was allowed to vary. Upper limits are marked with downward pointing arrows. The empty box corresponds to the F555W filter; no data were taken using that filter for this cluster. The parameters of the shown best-fit spectrum are listed on the left.

4.2.1 SED Fitting

We fit SEDs to every galaxy in our catalog with AB Mag m < 25.5 in the F814W filter, or, for those galaxies outside of the F814W field of view, the apparent magnitude in the closest available filter. To accomplish these fits, we used iSEDfit (Moustakas et al., 2013), an IDL-based Bayesian inference routine for extracting physical parameters from broadband photometry. iSEDfit is a widely-used code for estimating galaxy properties at all redshifts (e.g., Zitrin et al., 2012a; Aird et al., 2013; Brodwin et al., 2013; Zeimann et al., 2013; Fogarty et al., 2015). While the methods used, as well as systematic issues caused by prior selection,

are detailed in Moustakas et al. (2013), we briefly explain the technique here.

iSEDfit computes an integrated SED of a galaxy using the convolution integral

$$C(\lambda, t, Z) = \int_0^t \psi(t - t') \ S(\lambda, t', Z) \ 10^{-0.4} \ A(\lambda, t') dt'. \tag{4.1}$$

Here, λ is the wavelength, $S(\lambda, t', Z)$ is the spectral evolution of a simple stellar population of metallicity Z, and $A(\lambda, t')$ is the wavelength-dependent dust attenuation. $\psi(t - t')$, the star formation history (SFH), here takes the form a delayed τ -model,

$$\psi(t) = \frac{M_{\odot}}{\tau^2} t e^{-t/\tau}. \tag{4.2}$$

characterized by τ , the characteristic time for star formation, and normalized to M_{\odot} . Both t and τ are in units of years, so that $\psi(t)$ is in units of Solar masses per year. This form of the SFH allows for a linear rise and an exponential cutoff.

Each galaxy is input into iSEDfit as having broadband fluxes F_i , flux uncertainties σ_i , and redshift z. iSEDfit computes a posterior probability distribution function

$$p(\mathcal{Q}|F_i, z) = p(\mathcal{Q}) \times p(F_i, z|\mathcal{Q}), \tag{4.3}$$

where Q are the model parameters and p(Q) is the parameters's prior probabilities. The likelihood of the model given the data is

$$p(F_i, z|Q) = \mathcal{L} \propto \exp(-\chi^2(F_i, z|Q)/2), \tag{4.4}$$

where χ^2 is computed as

$$\chi^{2}(F_{i}, z|\mathcal{Q}) = \sum_{i}^{N} \frac{[F_{i} - \mathcal{AC}_{i}(\mathcal{Q}, z)]^{2}}{\sigma_{i}^{2}}.$$
(4.5)

Here \mathcal{A} is a normalization factor and $\mathcal{C}_i(\mathcal{Q}, z)$ are the broadband fluxes from each model with parameters \mathcal{Q} at redshift z. Values of a parameter are derived by randomly drawing values with probability given by the probability distribution (Equation 4.3). Errors are found by taking 1/4 of the range covered by the 2.3-97.7 percentiles, which reduces to 1σ for a Gaussian distribution.

We performed an analysis with iSEDfit with the redshift fixed at the redshift of the cluster each galaxy was near. For a simple stellar population model, we used Flexible Stellar Population Synthesis models (v. 2.4; Conroy et al., 2009; Conroy & Gunn, 2010) based on the MILES stellar library (Sánchez-Blázquez et al., 2006). We assumed a Salpeter (Salpeter, 1955) initial mass function and a time-dependent attenuation curve of Charlot & Fall (2000). Our priors included stellar metallicity $Z \in [0.005, 0.03]$ (defined such that $Z_{\odot} \equiv 0.019$), star formation timescale $\tau \in [0.0, 5.0]$ Gyr, and galaxy age $t \in [1.0, 11.5]$ Gyr. An example of a well-fit galaxy is shown in Figure 4.1.

For galaxies not detected in some filters, we used the measured 3σ flux upper-limit in that aperture as an upper limit for fitting the SEDs. However, for those galaxies not observed in a given filter, we did not include that filter in our fit, although we required good photometry in at least three bands in order to fit the galaxy. Due to the uncertainties in the HST zero points (Bohlin et al., 2014; Bohlin, 2016), we add a 0.02 magnitude error in quadrature with

our measured photometry errors before fitting. This systematic uncertainty is particularly important for bright galaxies in the infrared, which have tiny statistical photometric errors.

One of the important parameters we derive from these fits is the star-formation rate (SFR)-weighted age. For a star formation history, $\psi(t')$, the SFR-weighted age is defined as

$$\langle t \rangle_{\rm SFR} \equiv \frac{\int_0^t \psi(t')(t-t')dt'}{\int_0^t \psi(t')dt'},\tag{4.6}$$

where t is the age of the galaxy at which $\langle t \rangle_{\rm SFR}$ is being evaluated. Effectively, this term provides a measure of a characteristic age of the stellar population of the galaxy. For a star formation history consisting of a single burst at time t_0 ($\psi(t') = \delta(t' - t_0)$), the numerator of Equation 4.6 is an integral over a delta function, and the SFR-weighted age is the elapsed time since that burst occurred, $t - t_0$. For constant star formation ($\psi(t') = c \times t'$), Equation 4.6 integrates to $\langle t \rangle_{\rm SFR} = t/3$ – that is, the SFR-weighted age is one-third of the total age of the galaxy. Finally, for an exponentially-decaying star-formation history ($\psi(t') = \tau^{-1} \exp^{-t/\tau}$), after the exponential term has decayed toward 0, $\langle t \rangle_{\rm SFR} \lesssim t - \tau$.

We show in Figure 4.2 the distribution of best-fit values for metallicity, t_{form} (described below), total mass (including, but not limited to, stellar mass), and best-fit χ^2_{ν} , as well as the uncertainties on metallicity and t_{form} , for galaxies we classify as members (in Section 4.3). These values are from the run of iSEDfit assuming the cluster redshift. As can be seen, the errors are non-negligible, particularly for metallicity. We therefore caution against drawing conclusions from individual values; in this work, we only consider the aggregate properties of large samples, particularly in the case of metallicity.

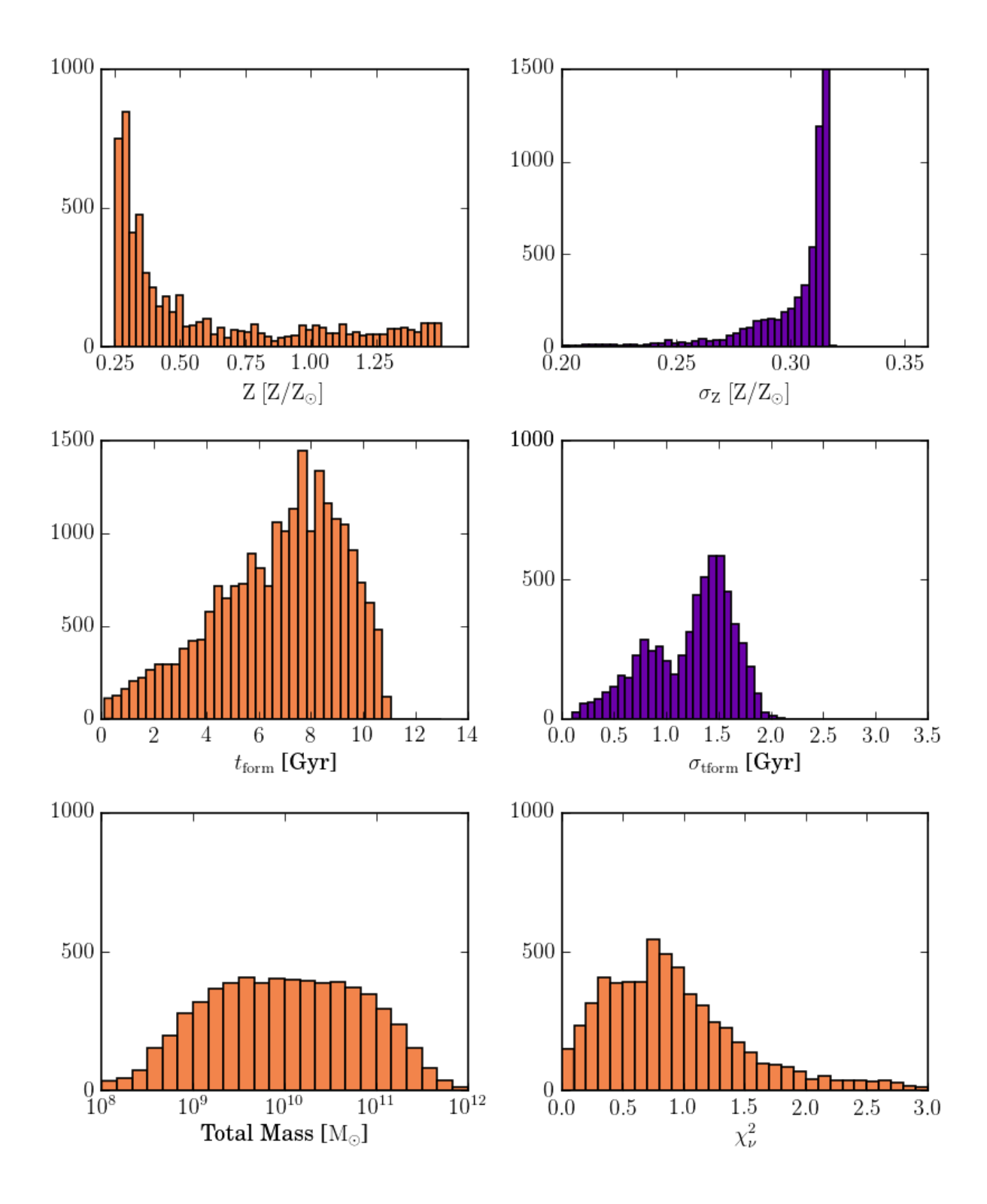


Figure 4.2 Best fit parameters (orange) and uncertainties (purple) from our SED fits. $t_{\rm form}$ is the age of the Universe at the cluster's redshift minus the SFR-weighted age. Only galaxies classified as cluster members are shown here. Derivation of these parameters is explained in the text.

As part of the SED fitting routine, we also obtained k-corrected u, g, r, i, and z magnitudes for every object. To derive these values, **iSEDfit** begins by determining the closest matched filter to each target filter at the redshift of the galaxy. It then computes a magnitude offset based on the best-fit SED and returns the original photometry corrected by that offset. This procedure retains the photometric errors on the original filter. For galaxies lacking photometry in the best-matched filter, the code will synthesize a magnitude from the SED fit but will not return a photometric error, as those are limited to observed errors. Synthetic magnitudes are needed when galaxies are outside of the field of view of certain filters and therefore are not observed in the closest-matched filter.

4.3 Cluster Membership

Having assembled a catalog of photometry and SED fits for a large sample of galaxies around 25 galaxy clusters, we next determined cluster membership. Along with the SED fits, we also used spectral redshift catalogs and previously-determined photometric redshift probabilities (both of which are described in Section 3.3.2). We compare the results of our selection to the results of an alternative technique: red sequence member selection.

Here we consider only those galaxies with SED fits; that is, we again exclude galaxies with F814W magnitude $m_{\rm F814W} > 25.5$. We combine the photometry, photometric redshift parameters, SED fit values, k-corrected magnitudes, and spectroscopic redshift measurements for all of these galaxies into one catalog. For each galaxy, we use the discrete probabil-

ity distributions produced by BPZ to determine a total probability of that galaxy being within some redshift range of the nominal cluster redshift. Here, we consider $|\Delta_z| < 0.03$, $|\Delta_z| < 0.05$, $|\Delta_z|/(1+z_c) < 0.03$, and $|\Delta_z|/(1+z_c) < 0.05$; we label the summed probabilities within those ranges P_{03} , P_{05} , P_{103} , and P_{105} , respectively.

For each galaxy in this catalog, we first consider spectroscopic redshifts. Any galaxy with $|\Delta_z|/(1+z_c) < 0.03$ is considered a cluster member; those with $|\Delta_z|/(1+z_c) > 0.10$ are considered non-members. The rest of the galaxies – either those with indeterminate spectroscopic redshifts or no spectroscopic redshifts – are then characterized by their photometric redshift probabilities. As a first pass, those galaxies with total probability $P_{03} > 0.8$ are assigned as members, while those with $P_{105} < 0.1$ are classified as non-members.

We next considered two possible ways to identify cluster members: a well-fit SED or a best-fit photometric redshift solution. Galaxies with $\chi^2 < 1.5$ and $\chi^2 > 0.7$ (to avoid selecting galaxies with poorly-constrained fits through this cut) in the SED fit at the cluster redshift were classified as cluster members, as were those with a most likely or best redshift determination from BPZ within $|\Delta_z|/(1+z_c) < 0.05$. For the remaining objects, we examined the distributions of P_{03} , P_{05} , P_{103} , and P_{105} ; we only classify those remaining galaxies with $P_{103} > 0.2$ and $P_{105} > 0.6$ as members, while the rest are classified as non-members. Our catalog contains all of the information used to make this decision, so alternative cuts can be tested.

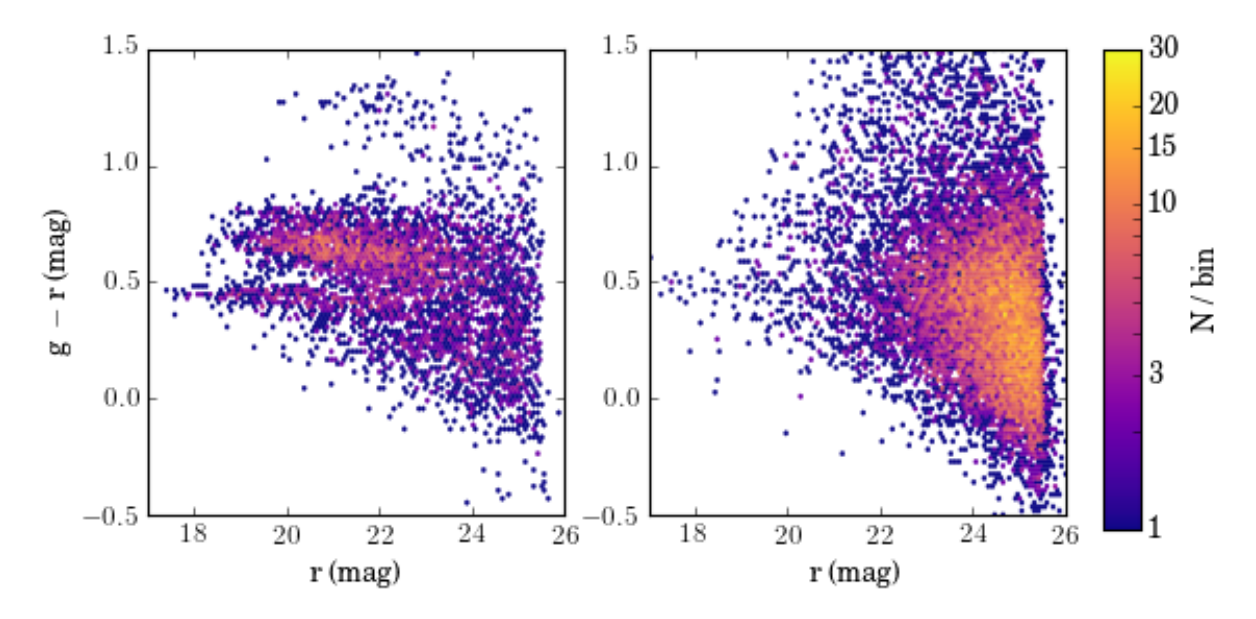


Figure 4.3 The analog filter g - r CMD for all 25 clusters. Shown on the left are those galaxies we call members, while those classified as non-members are plotted on the right. Hex bins are scaled logarithmically with the number of galaxies contained inside.

4.3.1 Alternative Selections

Selecting cluster members from the red sequence is a common task in cluster science (e.g., Koester et al., 2007b; Hao et al., 2009; Rykoff et al., 2014, 2016, among many others). As this project leverages over 500 hours of HST observations and a coordinated spectroscopic followup campaign to determine cluster galaxy properties, our cluster member catalogs can greatly surpass those using only ground-based, few-color observations. To better enable the science from those observations, we quantify the effects of red sequence selection on our more rigorously compiled membership determinations.

Shown in Figure 4.3 is a plot of g - r analog colors vs. r magnitude using the filter analogs listed in Table 4.1. On the left panel is shown those galaxies classified as members; on the right are those classified as non-members. Readily apparent in this image is a second

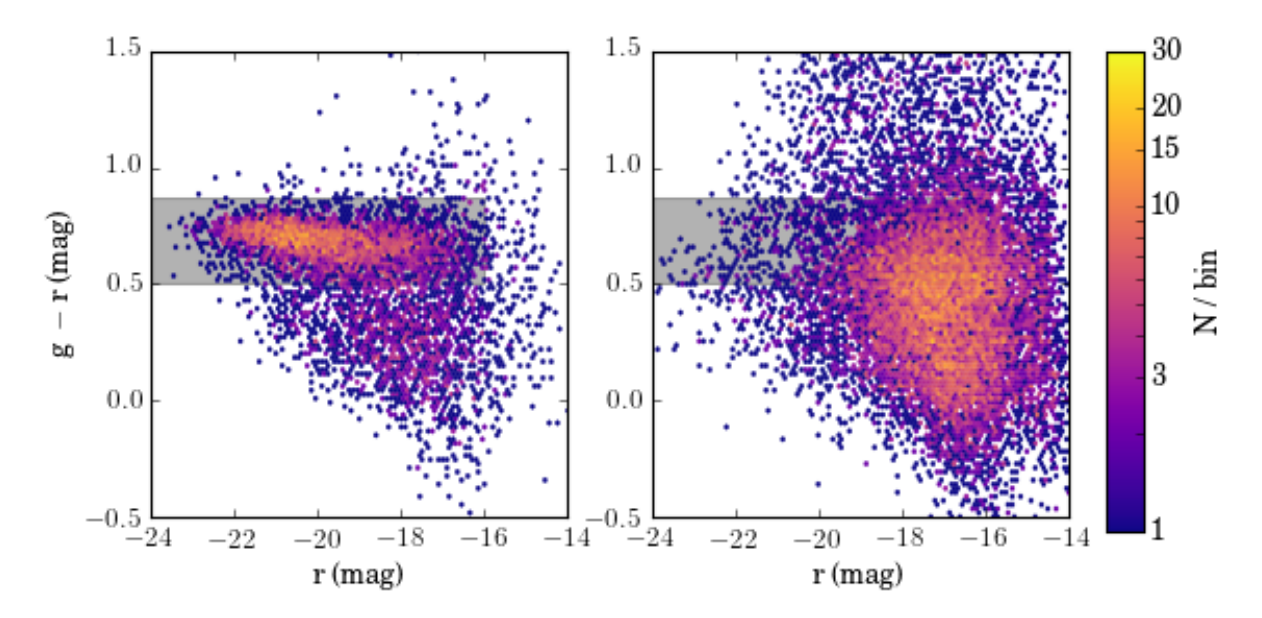


Figure 4.4 The k-corrected g-r CMD for all 25 clusters. Shown on the left are those galaxies we call members, while those classified as non-members are plotted on the right. A potential red sequence selection region is shown as a shaded box. Hex bins are scaled logarithmically with the number of galaxies contained inside.

red sequence. This is an effect of the analog filters not exactly matching the rest-frame bandpasses from cluster to cluster. Thus, several jumps are visible between clusters, and we caution against using even best-matched filter analogs in lieu of k-corrected magnitudes. Nevertheless, we further examine the effects of red sequence fitting for "best-matched filters" in Section 4.4.

Similarly, in Figure 4.4 we show a plot of g-r colors, this time using k-corrected magnitudes. By mitigating the effects of offset filters (that is, interpolating to a uniform set of rest-frame magnitudes), we see the red sequences are all at similar locations. Here, we define a selection region, counting those galaxies with 0.5 < g-r < 0.875. For galaxies brighter than r < -16, 67.0% of cluster members are inside this color region, but so is an additional population of non-members with size equal to 68.3% of the total member population above

that brightness threshold. Increasing the magnitude cut to r < -16, 89.9% of members fall within that color region, while the contaminant population is only equal to 18.1% of the total cluster population in that luminosity range. Based on these results, selecting galaxies using the red sequence is well suited for selecting galaxies at the tip of the relation. However, this selection not only fails to account for the entire cluster population at fainter magnitudes, it also becomes significantly affected by contamination.

4.4 Red Sequence Fitting

Numerous studies have examined the red sequence across redshift, making use of a number of ground- and space-based observatories. Here, we have access to 16 filters with which to select a color and magnitude component. To best match our results with those of the Sloan Digital Sky Survey (SDSS), we select g-r colors, using both k-corrected magnitudes and the HST filter analogs that best match the rest frame characteristics of those two ugriz filters. The filters chosen to accomplish this are specified in Table 4.1.

As the data we are fitting a slope to have errors on both variables, we fit a linear slope to our photometry using a python BCES (Akritas & Bershady, 1996) routine used in Nemmen et al. (2012). Here, we used the orthogonal estimator, although we obtained similar results with the y|x estimator. Our fit was to the relation

$$g - r = A \times (r + 20) + B. \tag{4.7}$$

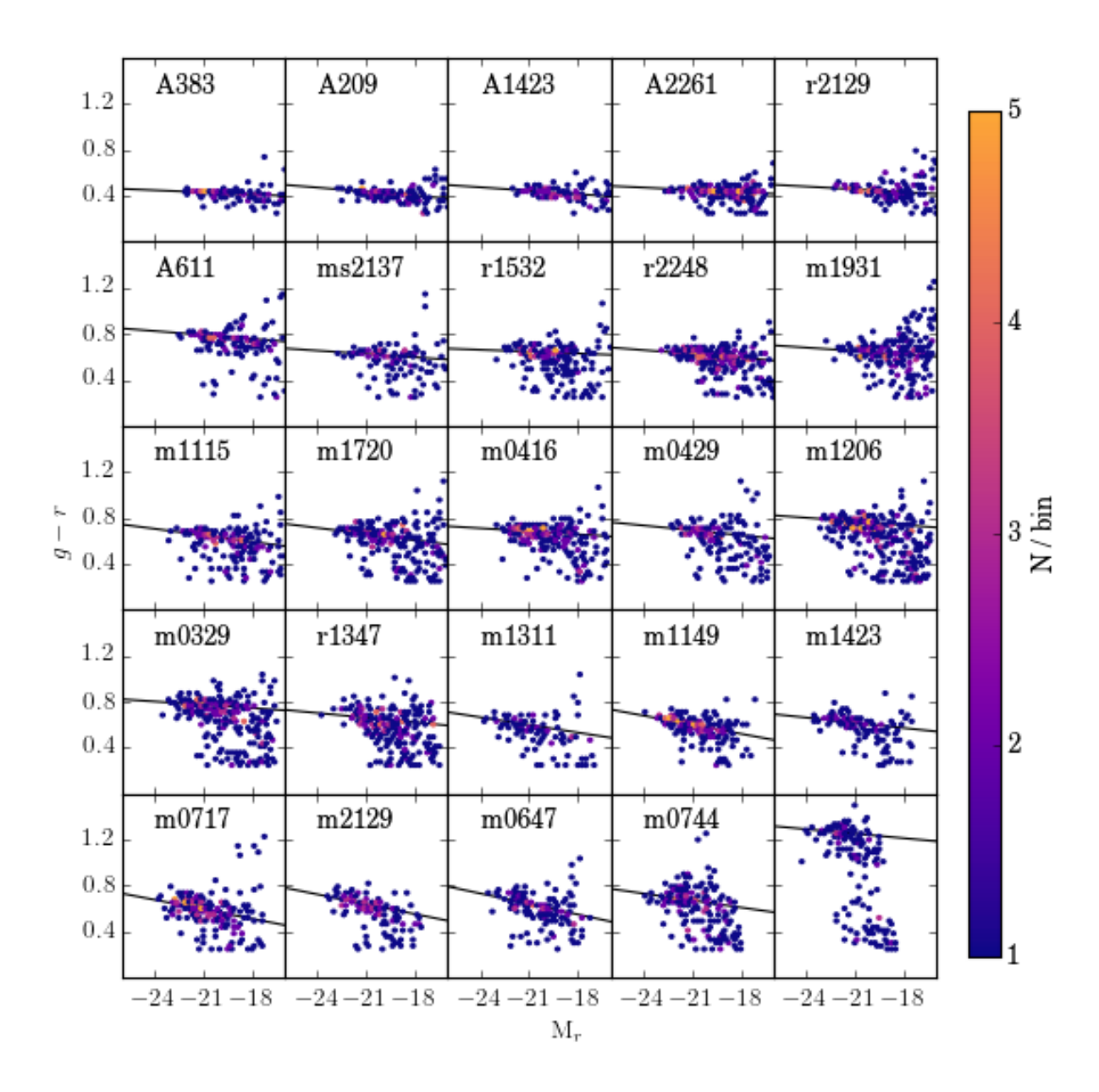


Figure 4.5 The g-r vs. r color magnitude diagrams for galaxies classified as color members using analog filter magnitudes identified in Table 4.1. Clusters are plotted in increasing redshift order, starting in the upper left and finishing in the lower right; the second-lowest-redshift cluster is the second frame in the top row. Cluster names for all clusters except CLJ1226.9+3332 are displayed following the convention in Table 1.1.

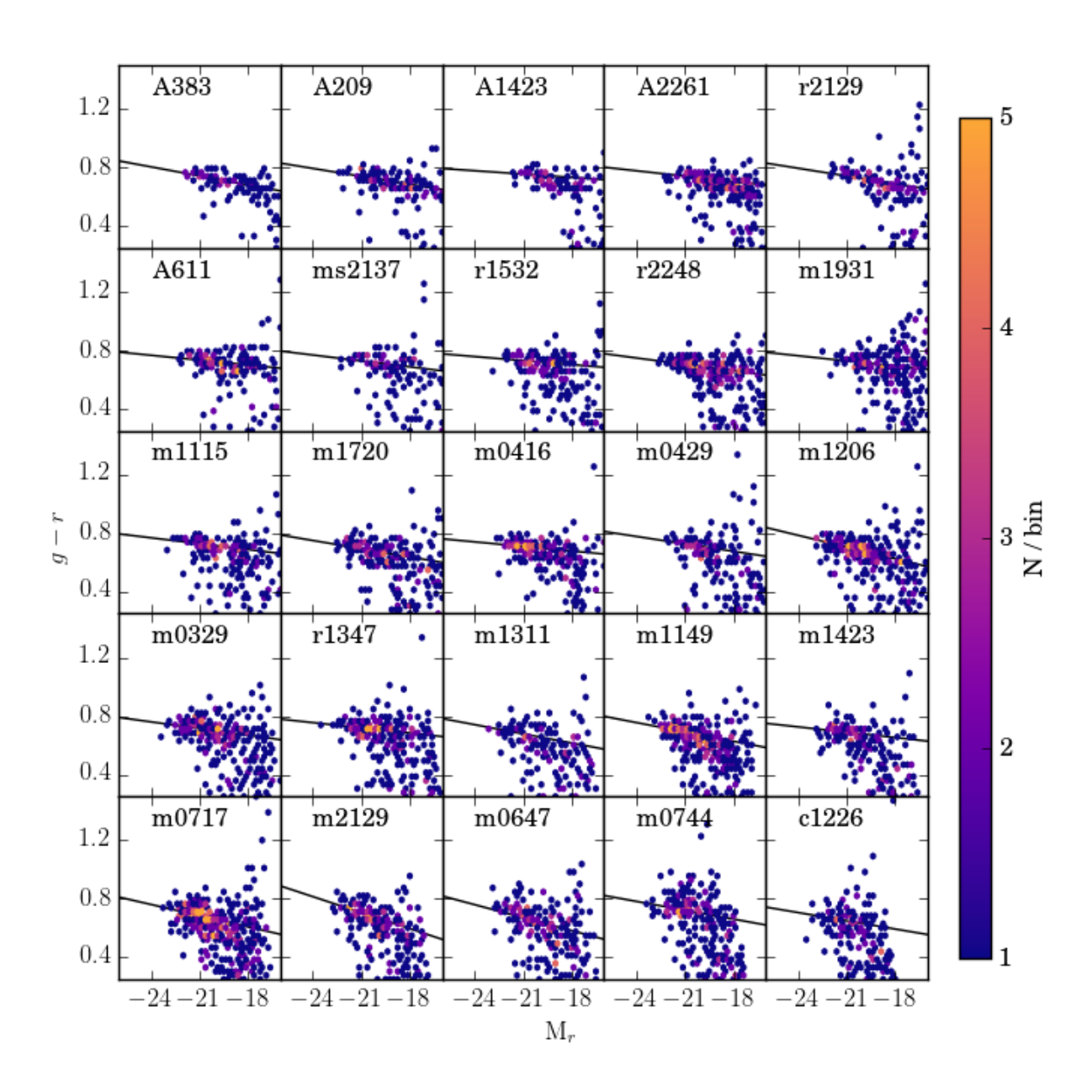


Figure 4.6 The g-r vs. r color magnitude diagrams for galaxies classified as color members using k-corrected magnitudes. The details of this plot are otherwise the same as for Figure 4.5.

Table 4.2. Red Sequence Fits

	Analog	Filter ^a	K-corr		
Cluster Name	A × 100	В	$A \times 100$	В	$\sigma_{ m int}$
Abell 383	-0.610 ± 0.131	0.425 ± 0.003	-2.053 ± 0.209	0.723 ± 0.005	0.008
Abell 209	-1.180 ± 0.094	0.426 ± 0.002	-1.808 ± 0.240	0.722 ± 0.005	0.016
Abell 1423	-0.989 ± 0.150	0.436 ± 0.003	-0.759 ± 0.315	0.748 ± 0.006	b
Abell 2261	-0.687 ± 0.129	0.446 ± 0.003	-1.218 ± 0.186	0.729 ± 0.004	b
RXJ 2129	-0.801 ± 0.246	0.450 ± 0.005	-1.768 ± 0.317	0.724 ± 0.007	0.010
Abell 611	-1.132 ± 0.181	0.780 ± 0.002	-1.102 ± 0.297	0.722 ± 0.005	0.018
MS 2137	-0.972 ± 0.301	0.616 ± 0.004	-1.352 ± 0.324	0.714 ± 0.006	ь
RXJ 1532	-0.538 ± 0.318	0.640 ± 0.004	-0.919 ± 0.323	0.721 ± 0.005	b
RXJ 2248	-1.138 ± 0.202	0.614 ± 0.004	-1.460 ± 0.176	0.690 ± 0.003	ь
MACS 1115	-0.969 ± 0.250	0.642 ± 0.005	-1.172 ± 0.240	0.716 ± 0.005	ь
MACS 1931	-1.877 ± 0.255	0.630 ± 0.003	-1.337 ± 0.231	0.715 ± 0.003	b
MACS 1720	-1.794 ± 0.227	0.641 ± 0.004	-1.876 ± 0.252	0.675 ± 0.004	0.011
MACS 0416	-0.884 ± 0.196	0.675 ± 0.003	-1.038 ± 0.282	0.699 ± 0.003	ь
MACS 0429	-1.416 ± 0.239	0.678 ± 0.003	-1.695 ± 0.419	0.710 ± 0.004	ь
MACS 1206	-1.053 ± 0.221	0.759 ± 0.003	-2.674 ± 0.202	0.679 ± 0.003	b
MACS 0329	-0.965 ± 0.209	0.765 ± 0.003	-1.522 ± 0.256	0.699 ± 0.004	0.021
RXJ 1347	-1.357 ± 0.284	0.649 ± 0.005	-1.191 ± 0.209	0.708 ± 0.003	b
MACS 1311	-2.224 ± 0.482	0.577 ± 0.006	-2.091 ± 0.320	0.658 ± 0.005	b
MACS 1149	-2.642 ± 0.310	0.575 ± 0.004	-2.132 ± 0.239	0.670 ± 0.003	b
MACS 1423	-1.509 ± 0.402	0.603 ± 0.005	-1.217 ± 0.301	0.677 ± 0.004	b
MACS 0717	-2.756 ± 0.341	0.568 ± 0.005	-2.550 ± 0.271	0.660 ± 0.003	0.028
MACS 2129	-2.864 ± 0.325	0.611 ± 0.006	-3.651 ± 0.297	0.670 ± 0.004	b
MACS 0647	-3.050 ± 0.474	0.612 ± 0.006	-2.959 ± 0.394	0.642 ± 0.005	0.034
MACS 0744	-2.034 ± 0.362	0.652 ± 0.006	-2.018 ± 0.327	0.702 ± 0.004	0.024
CLJ 1226	-1.314 ± 0.360	1.240 ± 0.007	-1.877 ± 0.533	0.631 ± 0.007	ь

Note. — For ease of understanding, A is scaled up by a factor of 100 in this table.

 $^{^{\}rm a}$ Best-fit values of $g-r~=~{\rm A}~\times (r-20)~+B$

 $^{^{\}rm b}$ χ^2 value of best fit below 1.

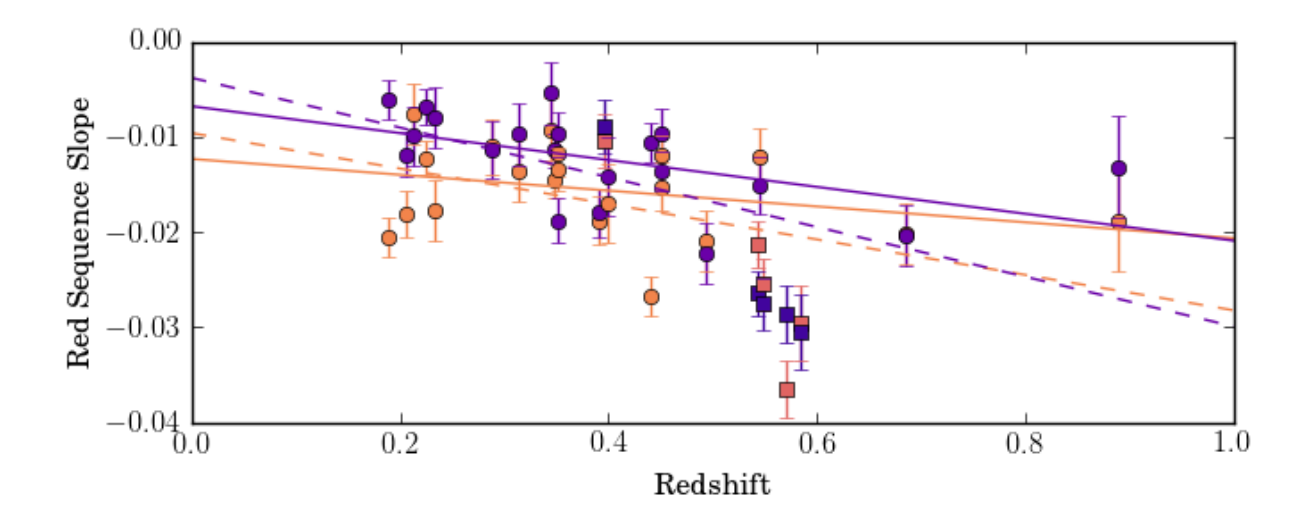


Figure 4.7 Measured red sequence slopes for the 25 CLASH clusters as a function of redshift. K-corrected values are shown in orange; observed values are in purple. The five clusters chosen for their magnification properties are marked with boxes, while the 20 X-ray selected clusters are denoted with circles. A best-fit of just the X-ray selected clusters for both sets of magnitudes is shown with solid lines; those same fits when including the strong lens sources are shown by dashed lines.

To avoid misfitting, we applied a cut in color-magnitude space to exclude galaxies well off of the red sequence for each cluster. We report the results of our best fits for all 25 clusters in Table 4.2 and show them in Figure 4.5. Additionally, we consider the k-corrected values of this relationship for each cluster. After again applying a selection cut, we fit the red sequence for q and r at z=0; these fits are also shown in Table 4.2 and shown in Figure 4.6.

Our best-fit slopes are shown in Figure 4.7. We again used BCES with the y|x estimator to perform a linear fit to $A_{rs} \propto m \times z$, where m is the change in the slope of the red sequence, as a function of redshift. For the k-corrected values, $m = (-18.64 \pm 8.17) \times 10^{-3}$, while for the not k-corrected values, $m = (-26.15 \pm 11.08) \times 10^{-3}$. However, these slopes are significantly affected by the slopes of the red sequences in the five CLASH clusters chosen due to their strong magnification potential. Selecting only the 20 X-ray selected clusters, these slopes

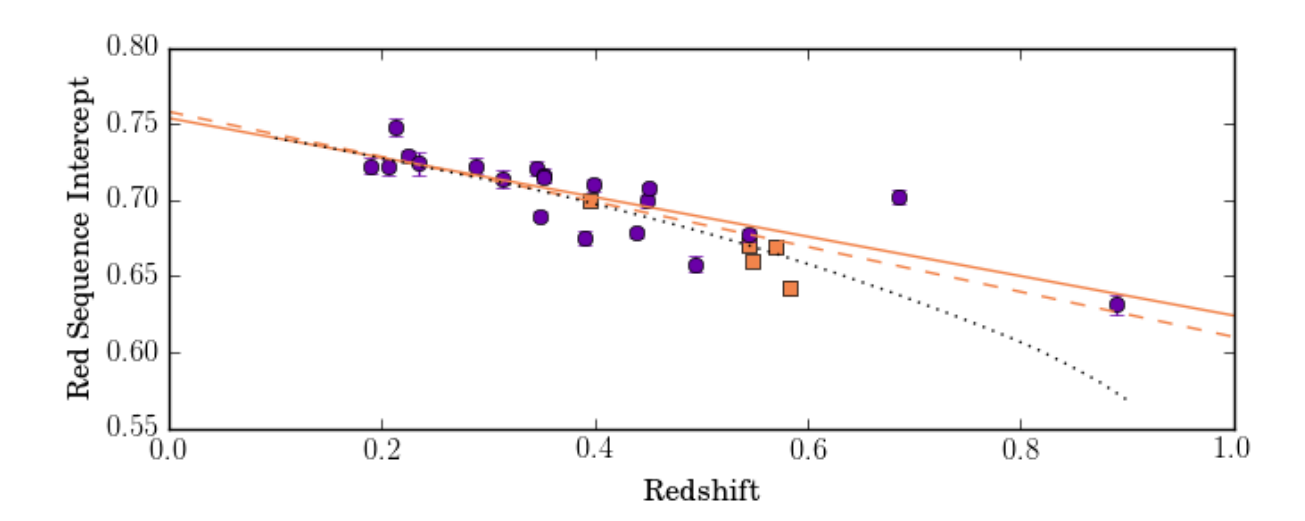


Figure 4.8 Measured red sequence intercepts for the 25 CLASH clusters as a function of redshift. The five clusters chosen for their magnification properties are marked with orange boxes, while the 20 X-ray selected clusters are denoted with purple circles. A best fit of just the X-ray selected clusters is shown with a solid line; the same fit when including the strong lensing sources is shown by a dashed line. The expected behavior of a population with metallicity $Z \approx 0.5Z_{\odot}$ formed at z=2 is shown by the dotted black line.

become $m = (-8.33 \pm 4.37) \times 10^{-3}$ with the k-correction and $m = (-14.14 \pm 6.38) \times 10^{-3}$ without. In all four methods, we see an evolution in the red sequence slope on the order of 2σ , but the importance of accurate k-correction is clearly shown by the decrease in the magnitude of the evolution.

Although we ignore the intercept of the red sequence for observed colors (as it is inherently biased by filter choices), we show the evolution of the intercept with k-corrected magnitudes in Figure 4.8. Again, we use BCES to fit a line to these values with redshift. Here, the best fit slope is -0.13 ± 0.02 when including only 20 clusters and -0.15 ± 0.02 with all 25. These results are clear evidence that the red sequence gets redder with age. While this result is not surprising (reddening would be a natural consequence of passive evolution; cf. field galaxies, Brown et al., 2007), we do further populate the limited sample of rest-frame

measurements of red sequence intercepts (e.g., Foltz et al., 2015, who reported no intercept values below z=0.8). We show an expected track for a stellar population formed at z=2.0 with metallicity $Z\approx 0.5Z_{\odot}$ and an exponential burst star formation history with decay time $\tau=0.5$ Gyr. These models were generated with EzGal (Mancone & Gonzalez, 2012) using the models of Conroy et al. (2009) and Conroy & Gunn (2010), assuming a Kroupa (2001) initial mass function.

We also consider the intrinsic scatter about the red sequence for these clusters. We attempt to fit a term, σ_{int} to the red sequence galaxies such that, for a cluster,

$$\chi_{\nu}^{2} = \frac{1}{n-2} \sum_{i} \frac{((g_{i} - r_{i}) - (A \times (r_{i} + 20) + B))^{2}}{\sigma_{g-r}^{2} + \sigma_{\text{int}}^{2}} = 1.$$
 (4.8)

However, for 16 clusters when using k-corrected magnitudes, χ^2_{ν} was already below 1 without any intrinsic scatter, implying that the measurement errors were too large to measure any intrinsic scatter. For the remaining 9, our measured intrinsic scatter is given in Table 4.2.

4.5 Individual Galaxies

While photometric analysis of the CLASH clusters is obviously important, we also have the ability to consider the physical properties of individual galaxies along the red sequence. Two properties of particular interest are the metallicity and age of galaxies, as we predict they will influence the slope and scatter of the red sequence, respectively. To that end, we use the full results of our SED fits to consider the aggregate behavior of cluster galaxies.

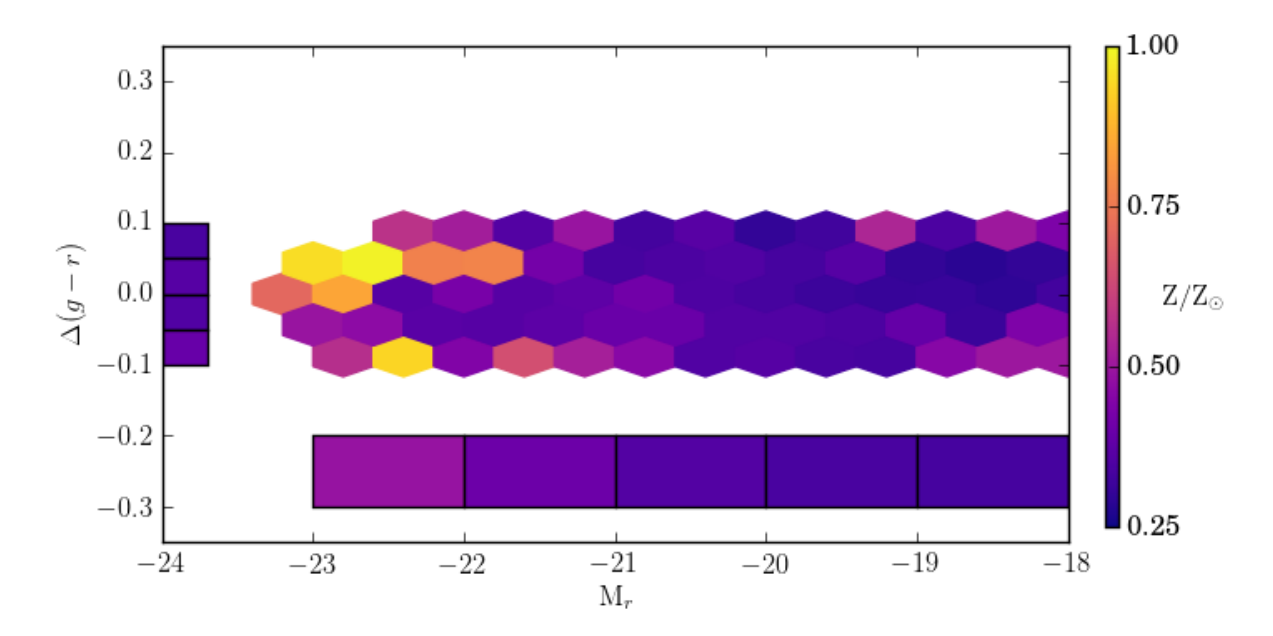


Figure 4.9 The metallicity function of cluster members, given by offset from and position along the red sequence. Hex bins are colored according to their median metallicity, as indicated by the colorbar. For legibility, only those bins with at least two counts are shown. g and r magnitudes are k-corrected. The median metallicity in one magnitude-wide bins is shown at the bottom of the plot, while the median metallicity in 0.05 magnitude-wide color bins is shown on the left.

First, we examined the relationship between metallicity and absolute magnitude for the galaxies in our sample. Using k-corrected magnitudes, we considered only those galaxies with g-r color within 0.1 mags of the measured red sequence. We show the results of this sample cut in Figure 4.9. To maximize the statistical power of our sample, we only show hex bins with at least two galaxies, and the metallicity for each bin is the median metallicity.

Strikingly, an increase in median metallicity as red sequence brightness increases is visible in Figure 4.9. To verify this, we consider the median metallicity value for galaxies in one-magnitude-wide bins, starting with $-23 < M_r < -22$ and decreasing to $-19 < M_r < -18$, ignoring those galaxies with g - r colors offset from the red sequence by more than 0.1

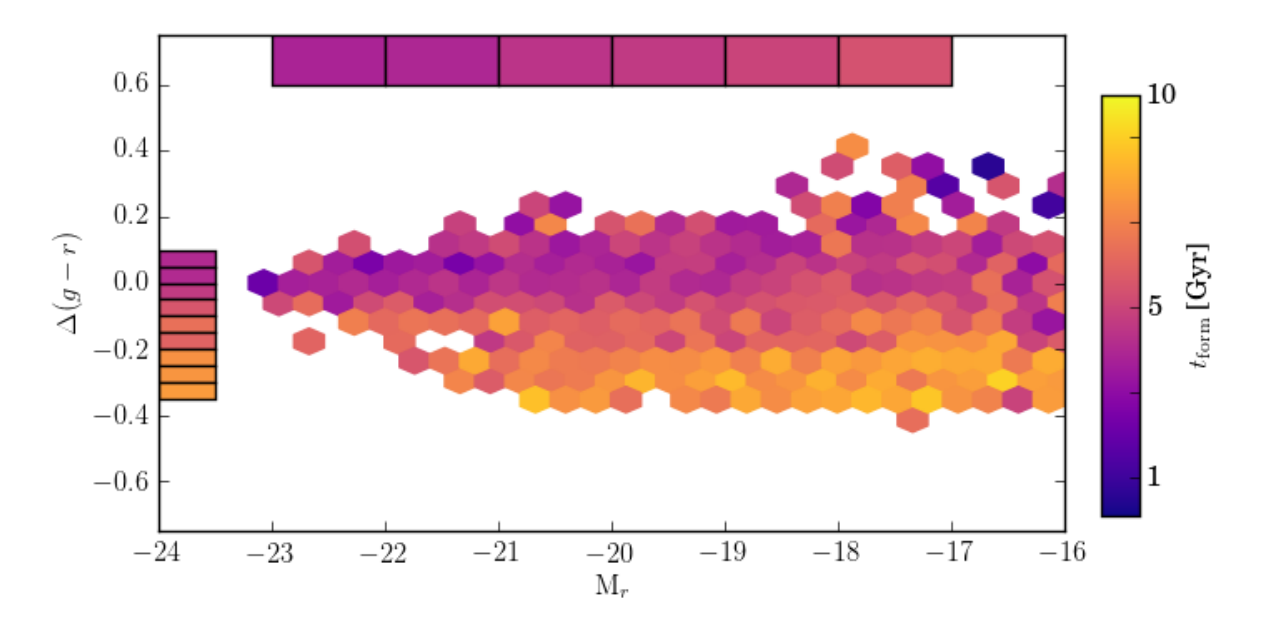


Figure 4.10 The SFR-weighted formation age function of cluster members. Hex bins are colored according to their median t_{form} , which is described in the text, as indicated by the colorbar. For legibility, only those bins with at least two counts are shown. g and r magnitudes are k-corrected. The median age in 9 color bands are shown on the left of the figure and in 6 magnitude bins at the top.

magnitudes. The median metallicity in these bins (with sample size in parenthesis) are $0.487 \pm 0.032 \ Z_{\odot}$ (164), $0.404 \pm 0.018 \ Z_{\odot}$ (556), $0.357 \pm 0.015 \ Z_{\odot}$ (851), $0.340 \pm 0.016 \ Z_{\odot}$ (698), and $0.332 \pm 0.018 \ Z_{\odot}$ (535), respectively. This trend is shown in Figure 4.9 as the bar on the bottom.

In addition to metallicity's influence on the slope of the red sequence, our SED fits also provide information on how galaxy ages determine the properties of the red sequence. To investigate this trend, we consider the SFR-weighted ages derived from the SED best fits. By subtracting from these ages the age of the Universe at each cluster redshift (calculated using Wright, 2006), we compute a parameter, $t_{\rm form}$, that describes the age of the Universe at which each galaxy's stellar component was formed.

As we expect that age's primary effect on the red sequence is to place galaxies above or below the measured line, we also calculated an offset color, $\Delta(g-r)$, of how far offset from the red sequence of its host cluster each galaxy was. This metric was defined so that positive values are redder than the measured red sequence slope. We then plotted our results as before, with hexes showing the median t_{form} value for all galaxies contained inside of it, and only hexes with at least two galaxies being shown. This result is shown in Figure 4.10.

We see a gradient along the color offset axis, whereby objects redder than the red sequence formed earlier than those bluer than the red sequence. This result is seen at all magnitude ranges. As a check, we compute the median $t_{\rm form}$ values in $\Delta(g-r)$ bins of 0.05 magnitudes, beginning at $\Delta(g-r)=0.1$ and working down to $\Delta(g-r)=-0.35$ for those galaxies brighter than r<-17; the $t_{\rm form}$ values in each bin are $4.1\pm0.1, 4.1\pm0.1, 4.6\pm0.1, 5.6\pm0.1, 6.4\pm0.1, 6.0\pm0.1, 7.4\pm0.2, 7.6\pm0.1,$ and 7.7 ± 0.2 Gyr, respectively. We note that this minimum value of $t_{\rm form}$ reached is consistent with cluster formation beginning at around $z\sim1.5$.

We also consider the two orthogonal gradients – changes in metallicity with color offset and changes in $t_{\rm form}$ with absolute magnitude. To measure metallicity, we used four 0.05 magnitude-wide bins from $\Delta(g-r)=0.1$ to $\Delta(g-r)=-0.1$ extending to r<-19, and found median metallicities of $0.341\pm0.025~{\rm Z}_{\odot}$ (268), $0.370\pm0.015~{\rm Z}_{\odot}$ (827), $0.362\pm0.015~{\rm Z}_{\odot}$ (818), and $0.384\pm0.022~{\rm Z}_{\odot}$ (367). This is shown on the left-hand side of Figure 4.9. We also look at age variation by finding the median ages in 1 magnitude-wide bins containing all galaxies within $\Delta(g-r)=0.1$ to $\Delta(g-r)=-0.1$. Here, we find $t_{\rm form}$ values of 3.8 ± 0.2 , 3.9 ± 0.1 , 4.4 ± 0.1 , 4.6 ± 0.1 , 4.9 ± 0.1 , and 5.4 ± 0.1 Gyr, respectively. These results are shown on the top of Figure 4.10.

4.6 Mass-to-Light Ratios

We used our k-corrected photometry and SED mass estimates to derive mass-to-light values for the galaxies in our sample. Using k-corrected i-band magnitudes, we calculated luminosities using

$$L/L_{\odot} = 10^{0.4(M_{\odot}, i-M_i)},$$
 (4.9)

where $M_{\odot,i}$ is the absolute magnitude of the Sun in *i*-band. We used a value of $M_{\odot,i} = 4.57$; this is taken from the SDSS online documentation³, but it also agrees with reported values from Blanton et al. (2003), although that work used a solar model redshifted to z=0.1.

In Figure 4.11 we show the distribution of stellar mass to *i*-band luminosity ratios for all of the cluster members in our sample. We see two populations in this figure: a grouping of higher mass-to-light ratio galaxies that extends from bright to faint galaxies and a low mass-to-light clump limited to fainter galaxies. When we select only those galaxies near the red sequence, we see that these populations trace red sequence and blue cloud populations, respectively. For those galaxies with g-r colors within 0.05 magnitudes of the red sequence, the mean mass-to-light value is $\log\left((\frac{M_*}{M_{\odot}})/(\frac{L}{L_{\odot}})\right) = 0.41 \pm 0.18$. When only considering those galaxies with $L/L_{\odot} > 10$, this becomes $\log\left((\frac{M_*}{M_{\odot}})/(\frac{L}{L_{\odot}})\right) = 0.48 \pm 0.12$.

³http://www.sdss.org/dr13/algorithms/ugrizVegaSun/

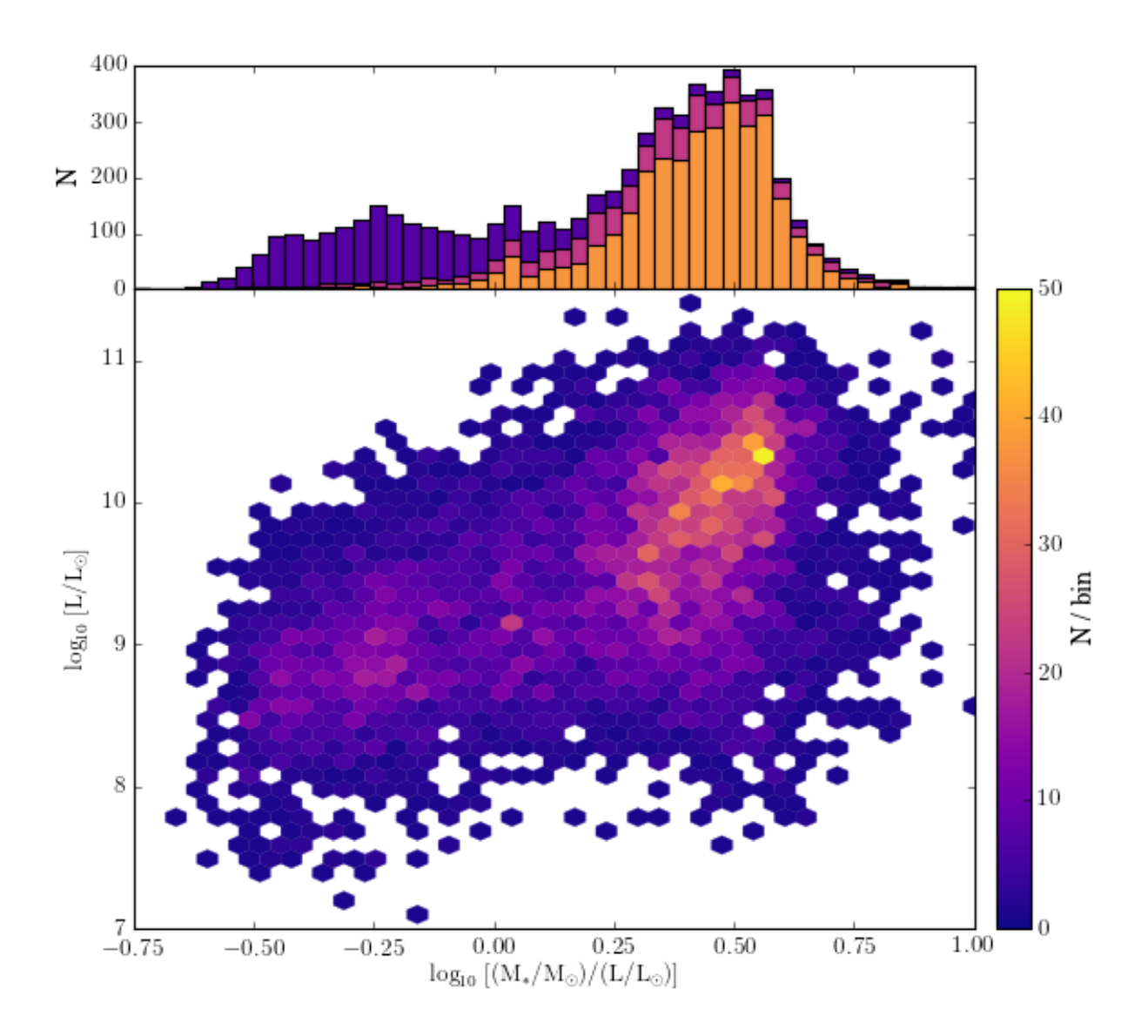


Figure 4.11 Stellar mass to *i*-band light ratios for all cluster members. In the bottom panel, we show the distribution of mass-to-light ratios with respect to overall luminosity, in Solar units. Only hex bins with at least one count are shown. In the upper panel, we show the distribution of mass-to-light ratios; purple is all galaxies, fuchsia is those galaxies g-r colors within 0.1 magnitudes of the red sequence, and orange is those galaxies with g-r colors within 0.05 magnitudes of the red sequence. The distribution of low mass-to-light ratio galaxies is dominated by low-luminosity galaxies off of the red sequence.

4.7 Discussion

In this work, we have characterized the red sequence properties for 25 massive galaxy clusters covering a redshift range of $z\approx 0.2$ to $z\approx 0.9$. We find little ($<2\sigma$) evidence for an evolution in the slope with redshift out to redshift z=0.89; the magnitude of this evolution is reduced when excluding the 5 high-magnification clusters in the CLASH sample. We observe the reddening of the red sequence gets redder with age, here presented in rest-frame colors. And, while limited by the scale of photometric errors, we see an increase in the intrinsic scatter about the red sequence for increasing redshift. In combination with these, we use SED fitting to study the properties of red sequence galaxies. We find a trend of increasing metallicity with increasing brightness as well as a tendency for galaxies bluer than the red sequence value to have formed later; however, we also find a faint age gradient along the red sequence itself. Here, we consider how these results factor into our understanding of cluster evolution.

Cerulo et al. (2016) find little evolution in the red sequence slope from z = 1.5 to $z \sim 0$, a picture supported by numerous other works (e.g., Lidman et al., 2004; Ascaso et al., 2008; Lidman et al., 2008; Mei et al., 2009; Snyder et al., 2012). In contrast, Stott et al. (2009) find a slope evolution from z = 0.5 to $z \sim 0.1$. Others, such as Hao et al. (2009) find evidence of a small amount of slope evolution, comparable to this work. Constraining this evolution is critical for uncovering the origin of the red sequence (Kodama & Arimoto, 1997).

Determining the exact formation epoch of the red sequence is an ongoing challenge. While proto-clusters have been discovered beyond z > 3 (Dey et al., 2016), detection of the

red sequence itself is tougher. Kato et al. (2016) identify an enhancement of star-formation density around $2 \lesssim z \lesssim 3$ protoclusters. Franck et al. (2015) identified a red sequence precursor in a galaxy cluster at z=1.83, although the red sequence was not well developed. Andreon et al. (2014) observed a Coma progenitor at z=1.803 with a mass function similar to low-redshift clusters. However, Eisenhardt et al. (2008) find a drop-off in the population of color-magnitude identified clusters at around $z\approx 1.5$, despite these being within the limit of their survey.

The origin of metals in galaxies across cosmological timescales has been previously studied. Davé & Oppenheimer (2007) used cosmological simulations to show that galaxies have metals early on – at $z\sim 6$, stars already have mean metallicities of 0.1 $\rm Z_{\odot}$. Similarly, Hopkins & Beacom (2006) found that the metal mass build-up rate peaks between 1< z< 3. Yuan et al. (2013) found only a 0.35 dex metallicity deficit from z=2.07 to a local sample. For clusters in particular, De Lucia et al. (2004a) found that 35 - 60% of the current ICM metal value was in place by z=2. A formation epoch of the red sequence in the regime of $z\approx 1.5-2$ would imply that metal accumulation has already occurred, and cluster galaxies could show metallicity deviations according to their mass.

Andreon et al. (2014) find an age gradient among cluster galaxies in a cluster at $z \sim 1.8$, whereby less massive galaxies are younger at the rate of 650 Myr per order of magnitude decrease in mass. We also consider the results of Tanaka et al. (2005), who presented a "down-sizing" hypothesis that larger galaxies finish their star formation before smaller galaxies, and this result propagates downward. Similarly, De Lucia et al. (2004b) find evidence for ongoing evolution of low luminosity cluster galaxies. Likewise, De Lucia et al. (2007) argue that high

redshift clusters still have galaxies transitioning onto the red sequence. Evidence for this is seen by Lemaux et al. (2012), who found not only a deficit of low-luminosity red-sequence galaxies in the Cl1604 ($z \sim 0.9$) supercluster but also evidence that the average cluster galaxy in this field has the spectrum of a star-forming galaxy.

One of the main arguments for a build up of the red sequence comes from the deficit of the faint-end slope in the cluster luminosity function for red sequence members (e.g., Rudnick et al., 2009). Strazzullo et al. (2010) and Mancone et al. (2012) did not limit their sample to red sequence selected members only, and they report flat luminosity functions at $z \sim 1.4$. These results, in tandem, imply that cluster galaxies were in place at the formation of the red sequence, but faint galaxies did not immediately occupy the relation.

In this context, we consider our results. To first order, our finding of a gradient in metallicity down the red sequence, minimal age evolution from bright to faint red galaxies, and only a weak evidence of evolution in the slope of the red sequence supports the well-defended paradigm that the red sequence is itself a consequence of a metallicity gradient between large and small galaxies. However, our secondary indicators – a small age gradient from bright to faint members, the aforementioned small yet present evolution of the slope, the growth of intrinsic scatter with increasing age, and the increase in galaxy age for bluer galaxies off the main relation – offer tantalizing evidence of the ongoing growth and evolution of smaller cluster members onto the main relation.

We show two toy models of red sequence slope evolution in Figure 4.12. In pink, we show a slope caused by two galaxies spaced three magnitudes apart, in which the brighter object

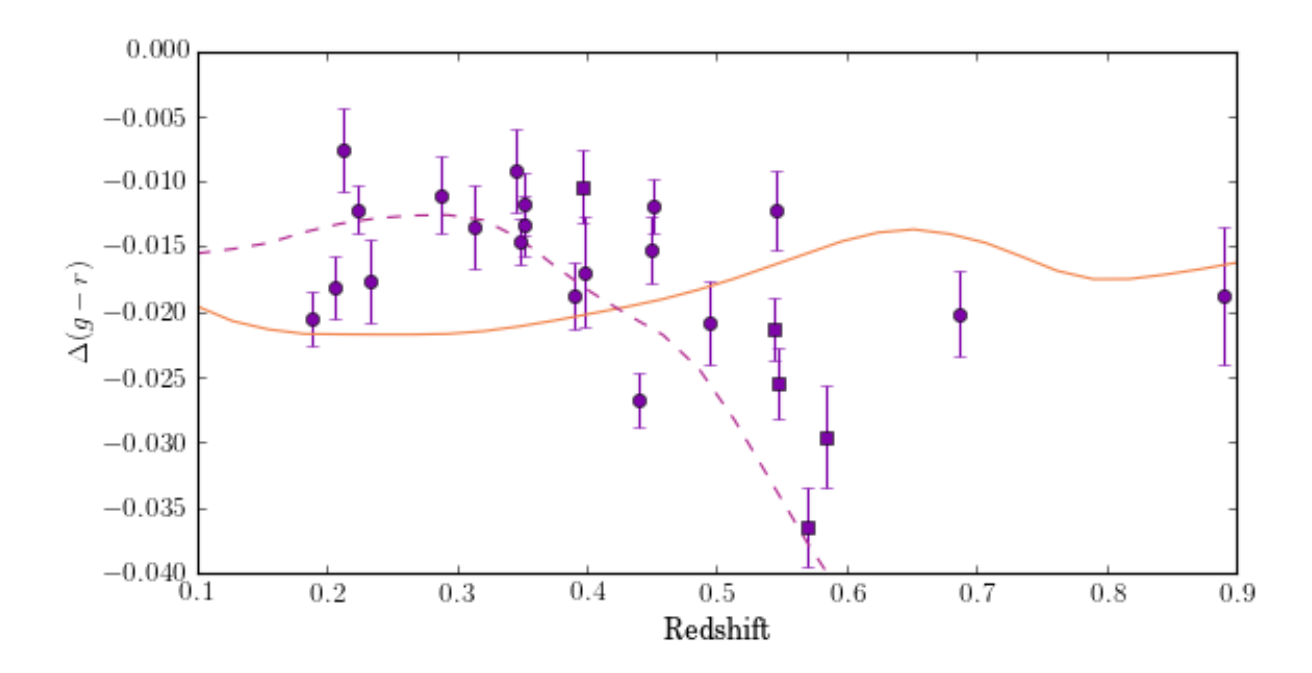


Figure 4.12 Measured slopes of the g-r red sequence for the 25 CLASH clusters as a function of redshift. Measured slopes are shown in purple. We show two toy models: a metal-driven slope model (orange) and an age-driven slope model (pink), both of which are described in the text. Neither is able to completely model the behavior of the red sequence.

formed at z=2.25 and the fainter galaxy formed at z=1.0. In orange, we show the slope caused by these two galaxies both forming at z=1.8, but with the brighter galaxy having a metallicity $Z \sim 0.5Z_{\odot}$ and the fainter galaxy having a metallicity $Z \sim 0.3Z_{\odot}$. These models were generated with EzGal (Mancone & Gonzalez, 2012) using the models of Conroy et al. (2009) and Conroy & Gunn (2010), assuming a Kroupa (2001) initial mass function, assuming an exponentially decaying star-formation profile with characteristic time scale $\tau = 0.1$ Gyr. Neither model describes the red sequence slope evolution, meaning that the red sequence formation mechanism is more complex than just metallicity offsets.

In Section 4.6 we found a connection between mass-to-light ratios and the red sequence, with the red sequence on the color-magnitude diagram having the same membership as a

mass-to-light sequence when compared to stellar masses. Previous studies have noted a connection between red galaxies having higher mass-to-light ratios (Bell & de Jong, 2001; Bell et al., 2003; Zibetti et al., 2009; Taylor et al., 2011). Here, we quantify the value of the relation specifically for red sequence cluster galaxies, which evolve in denser environments than field galaxies and may therefore be subject to different evolution.

We also consider the concern of circularity in our fits. Finding a gradient of metallicity along the red sequence, as well as an age gradient off of the red sequence, could both be consequences of iSEDfit making red galaxies more metal-enriched and older. However, while we have only discussed the red sequence as it applies in one color, our SED fits leverage significantly more colors, with spectral coverage from the ultraviolet to the infrared.

Figure 4.13 shows tracks of constant age and metallicity for galaxy populations, as seen in three color sets. These data were taken from the MILES stellar library (Sánchez-Blázquez et al., 2006; Vazdekis et al., 2010) using Padova isochrones (Girardi et al., 2000) and a revised Kroupa (2001) initial mass function. These tracks cover ages from ~ 0.01 to ~ 15 Gyr and metallicities of [M/H] ~ -2.2 to [M/H] ~ -0.2 .

Although single-color measurements do not have the ability to differentiate between age and metallicity tracks, color-color measurements do. And, while some regions show pile-up (such as $V - R \approx 0.2$ when compared with U-B), a third color can break that degeneracy. For that reason, while the red sequence may be defined in this work as a g - r color, our SED fits can utilize all of the other available data to make a determination of metallicity and age. Our findings of the properties in one color are not circularly based on that one color.

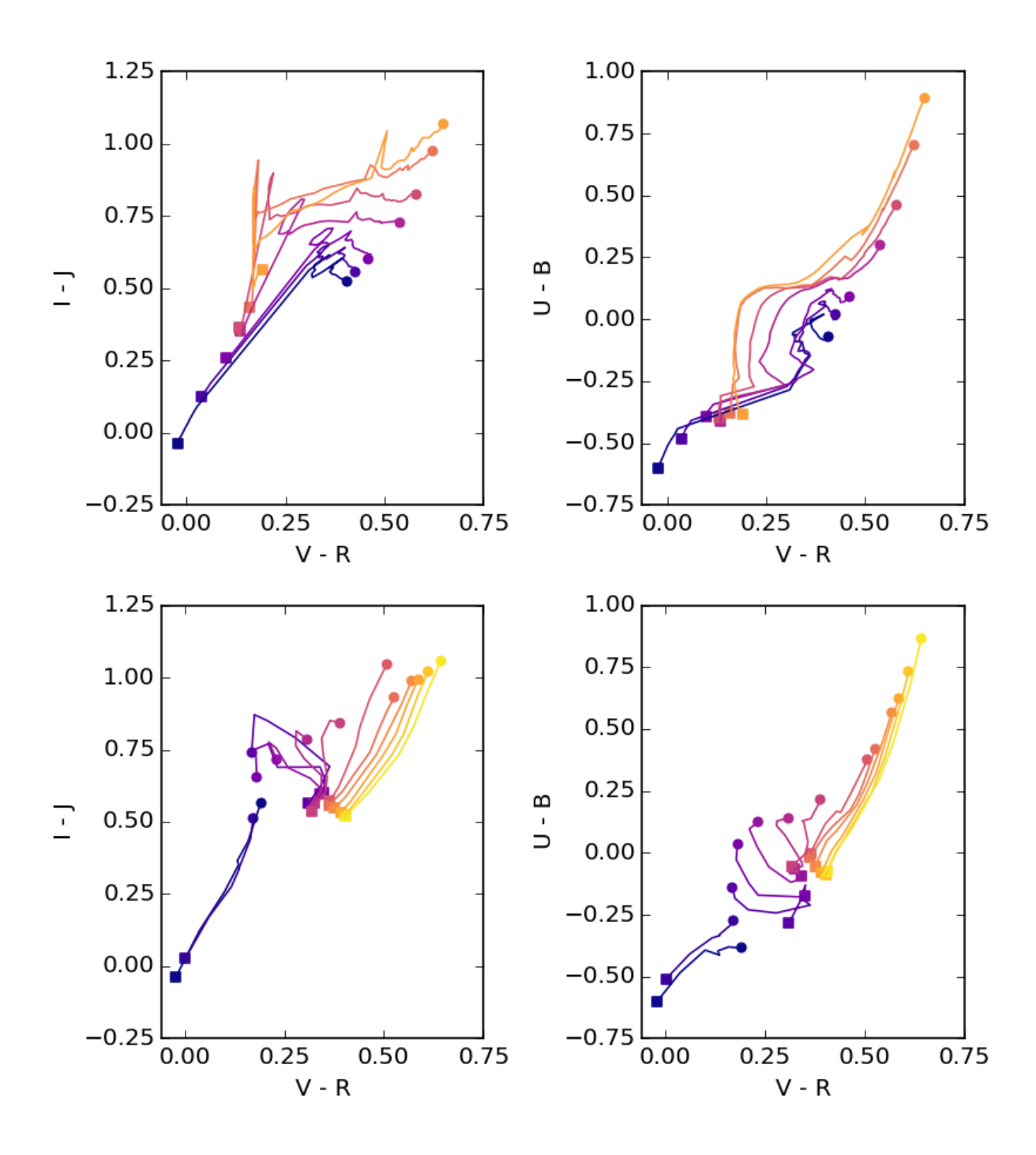


Figure 4.13 Color-color plots showing how galaxies of different metallicities and ages occupy similar spaces in color-color plots that can be broken apart by further photometric information. In the top panel, tracks show lines of constant metallicity, while the bottom panel shows isochrones. Colors are from Johnson/Cousin filters. In the top (bottom) panel, lines are colored by increasing metallicity (age), with the bluest lines being the most metal-poor (youngest). Squares denote the youngest (most metal-poor) part of each track, while circles denote the oldest (most metal-rich). These tracks are taken from the MILES stellar library.

4.8 Summary

We expand upon the photometric catalog produced in Chapter 3 by integrating galactic parameters from SED fitting and determining cluster membership. We use these expanded catalogs to fit the red sequences of the CLASH sample. Additionally, we exploit our SED fit parameters to compare the properties of cluster galaxies at different parts of the red sequence. Our results are summarized below.

- 1. We use all available redshift information to derive membership probabilities for the 22,557 galaxies in our photometric catalog. We find 6,185 (27%) of the galaxies in our catalog are cluster members. Using these determinations and galaxy photometry, we measure the impact of red sequence selection alone in classifying cluster galaxies. We find significant contamination (on the order of the extracted cluster population) for selections well below M*, but when only selecting the tip of the red sequence, cluster purity is at the order of 80%. Additionally, k-corrected magnitudes, if available, perform better at cluster galaxy selection than observed magnitudes for determinations across multiple clusters.
- 2. We measure the slope and intercepts of the red sequence for all 25 CLASH clusters in both observed and k-corrected bands. While we see weak evidence for an increase in the red sequence slope with redshift for observed magnitudes, this is reduced both by using k-corrected values and excluding the 5 CLASH clusters not in the X-ray selected sample. However, we do measure a decrease in the red sequence intercept with increasing magnitude;

this entails that the red sequence itself gets redder with age.

3. Using metallicity measurements for our cluster galaxies in aggregate, we measure the

total metallicity as a function of position along the red sequence. We find that brighter

galaxies are more metal-rich than their fainter counterparts.

4. In a similar fashion, we determine the SFR-weighted ages for galaxies in all 25 clusters,

and use the age of the Universe at the cluster redshift to estimate a formation time. By

comparing these values to the color offsets from our measured red sequence slopes, we find

not only that cluster members bluer than the red sequence preferentially formed after those

galaxies on the red sequence itself, but that a gradient exists in the cluster itself, such that

fainter red sequence members are slightly younger than their bright counterparts.

5. We investigate the stellar mass-to-light ratios of galaxies identified as cluster mem-

bers. We find that galaxies fall into two populations, which align with their association with

the red sequence. Red sequence members show a greater ratio of stellar mass to light, fit

by $\log\left((\frac{M_*}{M_{\odot}})/(\frac{L}{L_{\odot}})\right)=0.48\pm0.12$ at the bright end. In contrast, cluster members not

associated with the red sequence are more luminous for their stellar mass.

Thomas Connor acknowledges support from a fellowship from the Michigan State Un-

versity College of Natural Science. We used the cosmological calculator presented in Wright

(2006) in this work.

Facilities: Hubble Space Telescope/ACS, Hubble Space Telescope/WFC3,

138

Chapter 5

Summary

The body of this dissertation has studied the evolution of galaxy cluster properties across mass and redshift using high-quality space-based observations. In Chapter 2, we used new and archival XMM imaging to re-examine a sample of moderate-luminosity, intermediate-redshift galaxy clusters with well fit weak lensing masses. Our measurements of the scaling relations between mass, luminosity, and temperature pushed to the limit of the group/cluster boundary, where we saw no evidence for a break in scaling relation properties. In Chapter 3, we detailed a novel new technique for detecting and photometering galaxies well beyond M* in clusters of galaxies. Our consistency measurements with similar datasets verify the accuracy of our technique, the utility of which we demonstrated with a measurement of cluster luminosity functions. In Chapter 4, we used SED fitting in conjunction with photometric redshifts to classify the members from our new cluster galaxy sample. We used these SED-derived parameters to investigate the properties of the red sequence, which showed evidence of a delayed onset for faint luminosity galaxies to join the color-magnitude relation. We conclude this work with a brief discussion on the future steps of this research.

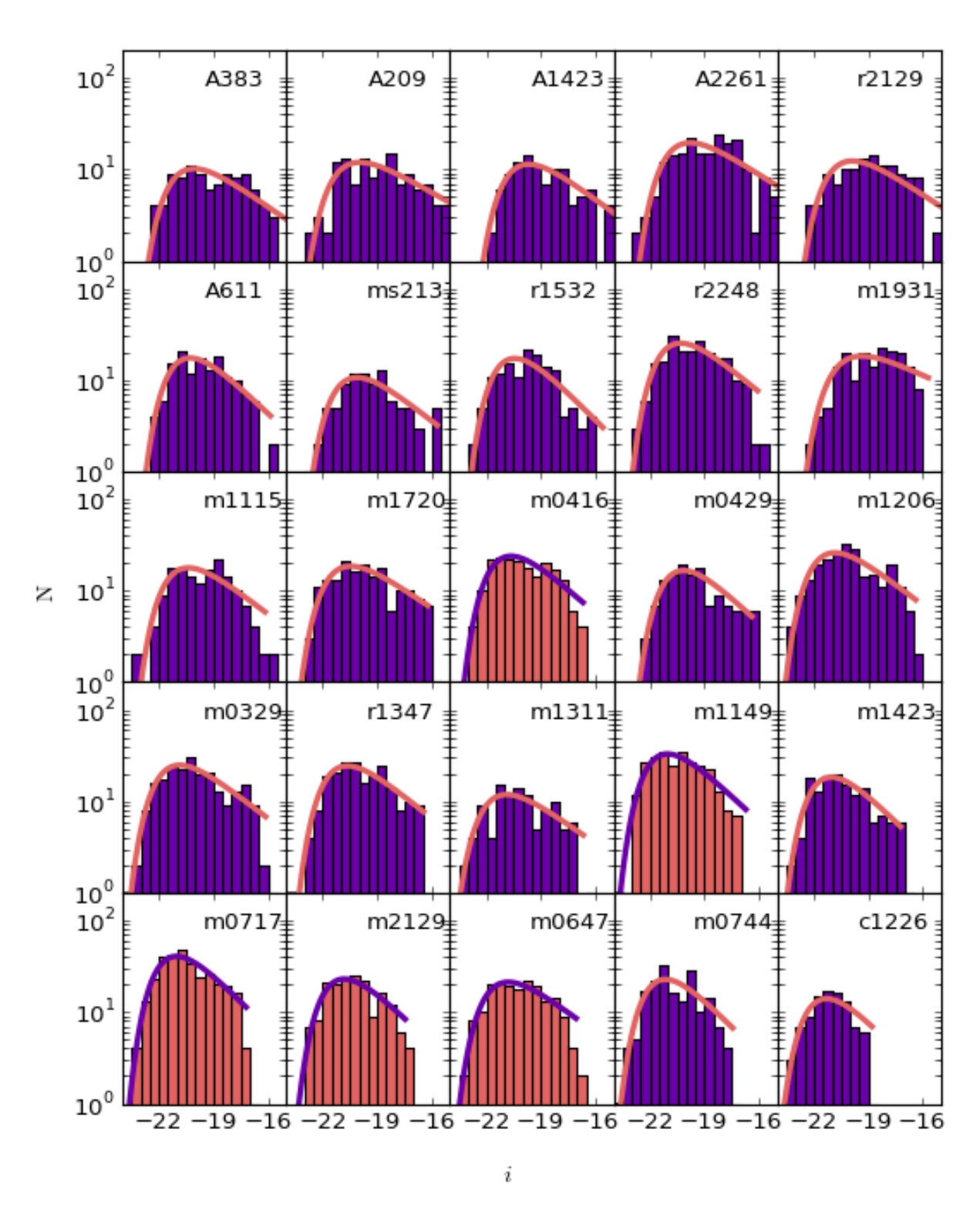


Figure 5.1 Luminosity functions for the 25 CLASH cluster galaxies, taking only those within $|\Delta(g-r)| < 0.2$ of the measured red sequence. This figure is otherwise the same as Figure 3.11.

5.1 Revisiting the Luminosity Function

In Chapter 3, we briefly discussed the results of fitting a Schechter luminosity function to the CLASH cluster galaxies. However, these data offer an unprecedented laboratory to delve even deeper. As a starting point, we consider the luminosity function only for red sequence members. While our measured values of α are consistent with $\alpha \sim -0.8$, implying only a minimum amount of drop-off in cluster population, fitting only those galaxies with red sequence colors within $|\Delta(g-r)| < 0.2$, we find a sharp decline in α . This is shown in Figure 5.1.

In the context of a cluster color-magnitude relation, fainter galaxies are believed to arrive later in time. This is evidenced by deficiencies in faint, red-sequence objects at greater redshifts relative to lower redshifts. As we are able to sample approximately 5 magnitudes below M*, we will be able to measure the magnitude of this effect from $z \sim 0.2$ to $z \sim 0.9$ with our cluster sample.

Additionally, we have well-constrained k-corrected colors across a large magnitude range and a large expanse of redshift. We will be able to study the evolution of M* at multiple wavelengths. Although interesting in its own right, we will be able to provide a uniform standard with which to compare cluster galaxies across a host of photometric systems and redshifts, facilitating further investigation of cluster luminosity functions by ourselves and others.

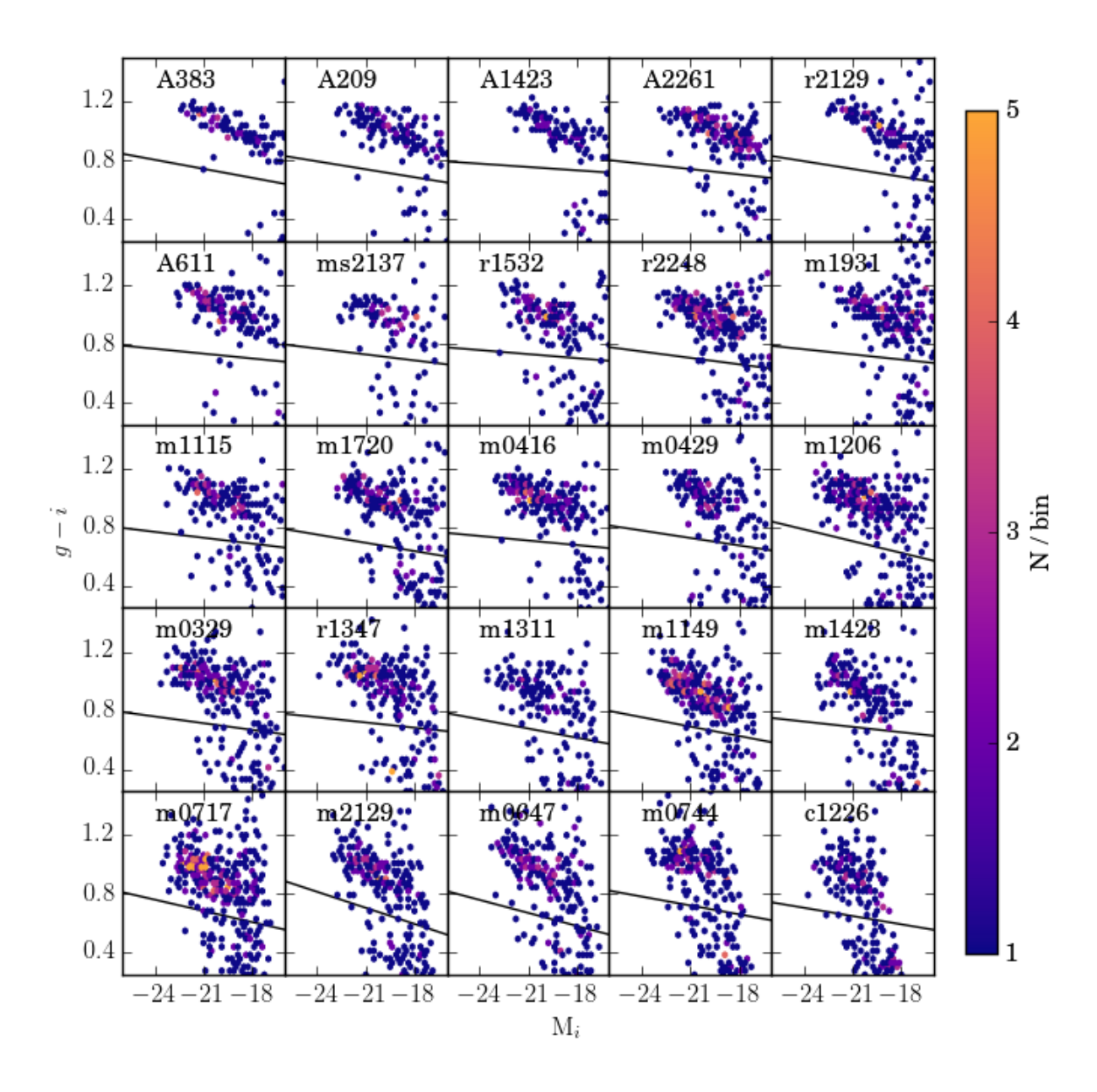


Figure 5.2 The g-i vs. i color magnitude diagrams for galaxies classified as color members using k-corrected magnitudes. The details of this plot are otherwise the same as for Figure 4.6. The value of the g-r slope is still shown to illustrate the change between filter sets.

5.2 Which Red Sequence

In this work, we only considered the red sequence using g-r colors. However, we have multiple other filters to chose from. Constraining the evolution of the red sequence in one filter set provides a pivot arm with which to investigate cluster evolution. Constraining the evolution in many filter sets sets a path through which cluster galaxy evolution must travel, as opposed to simply defining a region it must avoid.

We show an example of how the red sequence measurements change with regard to filter choices in Figure 5.2. As well as being defined by different values of the slope and intercept of the red sequence, the additional color term allows us to even more finely select cluster members to define as "red sequence members." Iterative passes of fitting in multiple filter sets can be used to more accurately characterize the intrinsic scatter for each cluster, while also minimizing contamination from galaxies with photometry that only partially follows the color ridgeline.

One further product of more complete red sequence measurements will be models of galaxy evolution. Previous works have fit evolutionary tracks using their measured red sequences to set mandatory photometric values at certain redshifts. However, we can take this one step further, by utilizing our age and metallicity constraints from SED fitting to require galaxies with certain physical parameters to have certain photometry at a given redshift. As shown in Figure 4.13, age tracks are apparent when utilizing multiple colors.

5.3 Bring the Background to the Foreground

Throughout this work, we have made full use of our photometry for galaxies in the cluster fields. However, one advantage of our photometric technique not currently utilized is the ability to account for all light in a cluster field, not just that of galaxies. Our residual light maps contain information on ICL, cluster substructure, non-detected lensed background sources, and the under-detected wings of extended sources.

An obvious step is to consider the ICL in these clusters. While previous studies have been released of the CLASH ICL, we can leverage dual fits to ICL properties and the faint galaxy population. Additionally, CLASH is not the last HST observation of galaxy clusters, and the Frontier Fields are still ripe for exploration. We intend to further utilize our techniques to push deep into the cluster light profile.

5.4 Public Release

As a final note, we consider our plans for public release of the data we have presented here. We intend to release our detection catalogs through two sources: VizieR¹ and the Mikulski Archive for Space Telescopes (MAST)². Both will allow us to host our catalog for convenient access to the astronomical community. We intend to release the complete photometric catalog. This entails the spatial and geometric parameters of each ellipse aperture, the measured CLASH photometry, photometric and spectroscopic redshift determinations, SED best fit

¹http://vizier.u-strasbg.fr/

²https://archive.stsci.edu/hst/

parameters, and the k-corrected and analog magnitudes used in Chapter 4. A full description of our catalog is provided in Appendix B.

APPENDICES

Appendix A

Appendices for Chapter 2¹

Conversion of ROSAT fluxes to $f_{300\,\mathrm{kpc}}$

In this appendix, we discuss how we converted the fluxes reported by Vikhlinin et al. (1998) into aperture fluxes. As the original fluxes were found by integrating a β -model to infinity, we derived a means of obtaining the normalization from a given flux. We then integrated the β -model to a desired angular aperture using this normalization.

The flux of a β -model is found by integrating the intensity

$$f = \int I_0 \left(1 + \left(\frac{\theta}{\theta_c} \right)^2 \right)^{-3\beta + 0.5} 2\pi \theta d\theta. \tag{A.1}$$

Substituting $x=-3\beta+0.5,$ this is an analytic integral with solution

$$f = 2\pi I_0 \frac{(\theta_c^2 + \theta^2)(\theta^2/\theta_c^2 + 1)^x}{2(x+1)} + c$$
(A.2)

When evaluating this as $\theta \to \infty$ for any x < 1, the upper part of the fraction will go to 0. When evaluating at $\theta = 0$, this becomes

$$f(\theta = 0) = 2\pi I_0 \frac{\theta_c^2}{2(x+1)}. (A.3)$$

¹These appendices are taken mostly word-for-word from Connor et al. (2014), as published in the Astrophysical Journal

As Vikhlinin et al. (1998) reported their fluxes as the average of the fluxes found with $\beta = 0.6$ and $\beta = 0.7$, we can determine their normalization, I_0 , by inserting the appropriate values of x and rearranging Equation (A.3). We use $x_{0.6}$ and $x_{0.7}$ to denote the values of x found with $\beta = 0.6$ and $\beta = 0.7$, respectively, and include a factor of 1/2 to account for averaging, so that we have

$$I_0 = \frac{-2f_{ROSAT}}{\pi\theta_c^2} \left(\frac{1}{x_{0.6} + 1} + \frac{1}{x_{0.7} + 1} \right)^{-1}.$$
 (A.4)

We note the leading negative sign is a consequence of our definition of x, which will be negative for all $\beta > 1/6$. From this, the total flux that would be measured inside a aperture of radius θ can be computed for a given value of β using

$$f_x(\theta) = \frac{-2f_{ROSAT}}{\theta_c^2(x+1)} \left(\frac{1}{x_{0.6}+1} + \frac{1}{x_{0.7}+1} \right)^{-1} \left[(\theta_c^2 + \theta^2) \left(\frac{\theta^2}{\theta_c^2} + 1 \right)^x - \theta_c^2 \right]. \tag{A.5}$$

To compare the *ROSAT* fluxes to our own, we solve this for the angle equivalent to 300 kpc for $\beta = 0.6$ and $\beta = 0.7$, averaging the two results.

Replication of Previous XMM Analyses

RXJ0110.3+1938

Bruch et al. (2010) first analyzed this cluster with the same observation used in this paper. While their analysis followed a similar path to our own, their reported results are not the same as ours. Our reported bolometric luminosity is similar to theirs $(2.19^{+0.12}_{-0.14})$ and $2.08^{+0.22}_{-0.22}$ × 10^{43} erg s⁻¹, respectively), but their reported temperature is noticeably lower than our own $(1.46^{+0.26}_{-0.19})$ keV compared to $2.95^{+0.72}_{-0.62}$ keV). The difference in the result may arise from

their less stringent cut for selecting good time intervals, their grouping of their data into energy bins, their use of a smaller aperture, and their lack of pn observations, which supply around 50% of the counts but were often problematic to calibrate 5 years ago. If we also make these choices, we measure a new temperature of $1.27^{+0.06}_{-0.11}$ keV, which agrees with the earlier result.

However, when we reduce our aperture size and bin the spectral data, we find an even lower luminosity; our new bolometric luminosity is $0.79^{+0.04}_{-0.05} \times 10^{43}$ erg s⁻¹. After private communication with S. Bruch, we discovered that the same spectral fitting results were obtained but not published for an aperture of 0.5 Mpc. Using the 4.647 kpc arcsec⁻¹ scale provided in the refereed paper, we extract spectra from a 107.60" aperture. When letting the abundance vary, we find $T_X = 1.50^{+0.45}_{-0.32}$ keV and $L_{\text{bolo}} = 1.83^{+0.10}_{-0.19} \times 10^{43}$ erg s⁻¹. In addition, we find 252 and 219 net counts for MOS1 and MOS2, respectively. These results are in agreement with the earlier result, which found 231 and 205 counts for the two cameras. We therefore conclude that their reported X-ray aperture radius of 32" is incorrectly reported, and the actual aperture used was 0.5 Mpc. Using this aperture, we obtain similar results.

RXJ0847.1+3449

Lumb et al. (2004) originally looked at RXJ0847.1+3449 using XMM-Newton observation 0107860501. They reported higher values for flux and bolometric luminosity, but a cooler temperature. One source of this difference may be the larger spectral extraction area they used – it was 120", while ours was ≈ 70 ". Therefore we attempted to reproduce their results by using the same aperture and masks, as that work included images of where point sources were excluded.

Bolometric luminosities reported by Lumb et al. (2004) are not for the 120'' apertures.

Rather, they are for apertures scaled to the entire virial radius, as found by using the fitted temperatures and the $T-r_v$ relation of Evrard et al. (1996). In addition, they increased the estimated photon count rate to account for lack of spatial coverage due to chip gaps or masked point sources. We find a comparable luminosity by fitting a MEKAL model to the parameters specified in Table 5 of Lumb et al. (2004). Unlike the reported luminosity, these parameters are for the best fit of the spectrum within 120" and are the best measure of what a similar aperture luminosity would be from that work. In order to allow for changes in MEKAL over the past ten years, we let the abundance vary but match the flux reported in the original work.

When fitting to data from the larger aperture, our temperature estimate changes from $4.16^{+0.58}_{-0.39}$ keV to $3.72^{+0.51}_{-0.41}$ keV, which agrees with the reported value of $3.62^{+0.58}_{-0.51}$ keV. Similarly, our flux estimate changes from $5.20^{+0.12}_{-0.14} \times 10^{-14}$ erg s⁻¹ cm⁻² to $6.77^{+0.14}_{-0.12} \times 10^{-14}$ erg s⁻¹ cm⁻², in agreement with the predicted $7.04 \pm 0.3 \times 10^{-14}$ erg s⁻¹ cm⁻². For bolometric luminosity, our value within r_{2500} is $1.31^{+0.04}_{-0.03} \times 10^{44} h_{70}^{-2}$ erg s⁻¹, while inside a 120'' aperture it is $1.70^{+0.06}_{-0.05} \times 10^{44} h_{70}^{-2}$ erg s⁻¹. The expected luminosity inside that aperture is $1.75 \times 10^{44} h_{70}^{-2}$ erg s⁻¹.

RXJ1354.2-0221

RXJ1354.2—0221 was also originally investigated by Lumb et al. (2004), and, as before, they find a higher flux, higher luminosity, and a lower temperature than we do. As with RXJ0847.1+3449, their technique deviated in aperture size, binning, and definition of luminosity. Additionally, we filtered this data for intervals of flaring differently than they did, which we adjust for in our reanalysis.

We again find a drop in temperature, which changes from $7.60^{+1.92}_{-1.22}$ keV to $3.88^{+0.93}_{-0.59}$

keV when expanding the aperture, in comparison to the originally reported value of $3.66^{+0.6}_{-0.5}$ keV. Likewise, the flux increases from $6.90^{+0.15}_{-0.19} \times 10^{-14}$ erg s⁻¹ cm⁻² to $10.17^{+0.18}_{-0.22} \times 10^{-14}$ erg s⁻¹ cm⁻², which matches the earlier result of $9.8 \pm 0.5 \times 10^{-14}$ erg s⁻¹ cm⁻². Finally, our luminosity rises from $2.11^{+0.10}_{-0.12} \times 10^{44} \, h_{70}^{-2}$ erg s⁻¹ to $2.47^{+0.09}_{-0.06} \times 10^{44} \, h_{70}^{-2}$ erg s⁻¹, which agrees with the predicted expectation of $2.41 \times 10^{44} \, h_{70}^{-2}$ erg s⁻¹. As before, we are able to reproduce the earlier results.

RXJ1117.4+0743

Carrasco et al. (2007) used the same observations analyzed here to look at RXJ1117.4+0743. Their reported temperature $(3.3^{+0.7}_{-0.6} \text{ keV})$ is slightly lower than our own $(4.30^{+0.70}_{-0.38} \text{ keV})$, but they find larger luminosities from 0.5-2.0 keV (4.19 \pm 0.35 to our 1.84 $^{+0.03}_{-0.03}$, in units of $10^{43}~{\rm erg~s^{-1}}$) and in a bolometric band (11.8 \pm 0.9 to our 5.27 $^{+0.08}_{-0.16}$ in units of $10^{43}~{\rm erg~s^{-1}}$). There are a few differences in our analysis that can bring those results into closer alignment. Along with using a larger aperture -66'' to our choice of 47'' – the previous work binned its data to a minimum of 12 counts per energy bin. Making those adjustments is not enough to match the previous work, however, without also using a different background. In the initial paper, the background was described only as "a larger extraction region near the detector border without any visible sources." To that end, we used a background centered around $\alpha_{2000} = 11^{\rm h}17^{\rm m}40^{\rm s}, \ \delta_{2000} = +07^{\circ}55^{\rm m}10^{\rm s}$ that was 72'' in size. With this background, we recover similar results to the original reporting: $T_X = 3.13^{+0.30}_{-0.29} \text{ keV}, F_{[0.5-2.0 \text{ keV}]} =$ $8.90^{+0.47}_{-0.37} \times 10^{43} \text{ erg s}^{-1}$. Even without knowing their exact background region, we reproduce the results of Carrasco et al. (2007).

Appendix B

Appendices for Chapters 3 and 4

Description of parameters in Photometry Table

The following parameters are to be included in our catalog upon public release:

- 1. **GALID** A unique identifier for each galaxy
- 2. α_{2000} The right ascension in J2000 coordinates
- 3. δ_{2000} The declination in J2000 coordinates
- 4. X X pixel location on CLASH mosaiced images
- 5. Y Y pixel location on CLASH mosaiced images
- 6. a Semi-major axis of photometric ellipse, in pixels (0.065"/pix)
- 7. b Semi-minor axis of photometric ellipse, in pixels (0.065"/pix)
- 8. PA Position angle, measured east of north, in degrees

For the following magnitudes, values of -99 indicate that the object was not observed in that filter, while values of 99 indicate it was not detected above error values

- 9. m_{F225W} AB apparent magnitude in F225W filter, after extinction correction
- 10. m_{F275W} AB apparent magnitude in F275W filter, after extinction correction

- 11. m_{F336W} AB apparent magnitude in F336W filter, after extinction correction
- 12. m_{F390W} AB apparent magnitude in F390W filter, after extinction correction
- 13. m_{F435W} AB apparent magnitude in F435W filter, after extinction correction
- 14. m_{F475W} AB apparent magnitude in F475W filter, after extinction correction
- 15. m_{F555W} AB apparent magnitude in F555W filter, after extinction correction
- 16. m_{F606W} AB apparent magnitude in F606W filter, after extinction correction
- 17. m_{F625W} AB apparent magnitude in F625W filter, after extinction correction
- 18. m_{F775W} AB apparent magnitude in F775W filter, after extinction correction
- 19. m_{F814W} AB apparent magnitude in F814W filter, after extinction correction
- 20. m_{F850LP} AB apparent magnitude in F850LP filter, after extinction correction
- 21. $\rm m_{F105W}-AB$ apparent magnitude in F105W filter, after extinction correction
- 22. m_{F110W} AB apparent magnitude in F110W filter, after extinction correction
- 23. m_{F125W} AB apparent magnitude in F125W filter, after extinction correction
- 24. m_{F140W} AB apparent magnitude in F140W filter, after extinction correction
- 25. m_{F160W} AB apparent magnitude in F160W filter, after extinction correction
- 26. zb BPZ most likely redshift
- 27. zb_{\min} BPZ 95% lower limit on best redshift
- 28. zb_{max} BPZ 95% upper limit on best redshift

- 29. tb BPZ best spectral type
- 30. $\chi^2_{\rm BPZ}$ BPZ goodness-of-fit
- 31. M_0 Primary magnitude used by BPZ
- 32. z_s Spectroscopic magnitude; =-1 if no match
- 33. $u_{\rm analog}$ AB apparent magnitude in u-analog filter
- 34. $u_{\rm analog}$ AB apparent magnitude in g-analog filter
- 35. $u_{\rm analog}$ AB apparent magnitude in r-analog filter
- 36. Y_{analog} AB apparent magnitude in Y-analog filter
- 37. K_{analog} AB apparent magnitude in K-analog filter
- 38. $u_{\rm k}$ K-corrected absolute magnitude in u filter
- 39. $g_{\mathbf{k}}$ K-corrected absolute magnitude in g filter
- 40. $r_{\rm k}$ K-corrected absolute magnitude in r filter
- 41. $i_{\rm k}$ K-corrected absolute magnitude in i filter
- 42. $z_{\rm k}$ K-corrected absolute magnitude in z filter
- 43. P_{03} Integrated photometric redshift probability with $-0.03 < z z_c < 0.03$
- 44. P₀₅ Integrated photometric redshift probability with $-0.05 < z z_c < 0.05$
- 45. P₁₀₃ Integrated photometric redshift probability with $-0.03 < (z-z_c)/(1+z_c) < 0.03$
- 46. P₁₀₅ Integrated photometric redshift probability with $-0.05 < (z-z_c)/(1+z_c) < 0.05$

- 47. Age SED best-fit age, in Gyr
- 48. SFRAge SED best-fit star-formation-weighted age, in Gyr
- 49. $\rm Z_{metal}-SED$ best-fit absolute metallicity
- 50. $\rm M_{tot}-SED$ best-fit total mass, in $\rm M_{\odot}$
- 51. M_* SED best-fit stellar mass, in M_{\odot}
- 52. $\chi^2_{\rm SED}$ SED goodness-of-fit
- 53. Cluster Galaxy cluster field galaxy is associated with
- 54. m-M Distance modulus magnitude correction, in magnitudes
- 55. Member Binary value; 1 if classified as a cluster member, 0 if not.

Extended Tables

Table B.1: ACS Data Properties – Exposure time (s), Zeropoint (AB Mag), and A_{λ} (Mag)

Cluster	F435W	F475W	F555W	F606W	F625W	F775W	F814W	F850LP
Abell 209	4136	4128		4096	4066	4126	8080	8236
	25.666	26.056		26.493	25.900	25.662	25.947	24.857
	0.070	0.063		0.048	0.043	0.032	0.030	0.024
Abell 383	4250	4128		4210	4128	4084	8486	8428
	25.658	26.059		26.491	25.907	25.665	25.943	24.842
	0.112	0.101		0.077	0.069	0.051	0.047	0.039
Abell 611	4118	4160		4320		4128	8092	8216
	25.666	26.059		26.511		25.665	25.947	24.842
	0.205	0.186		0.140		0.093	0.087	0.071
Abell 1423	3890	3928		3850	3928	4238	8480	8062
	25.666	26.056		26.493	25.900	25.662	25.947	24.857
	0.072	0.065		0.050	0.044	0.033	0.031	0.025
Abell 2261	4154	4128		4114	4128	4144	8198	11868
	25.658	26.059		26.491	25.907	25.665	25.943	24.842
	0.156	0.142	• • •	0.107	0.096	0.071	0.066	0.054
CLJ 1226	4372	4396	• • •	32000	4428	4418	44720	8488
	25.666	26.056	• • •	26.510	25.900	25.662	25.956	24.857
	0.069	0.062	• • •	0.047	0.042	0.031	0.029	0.024
MACS 0329	4144	4128	• • •	4104	4128	4134	8168	8266
	25.658	26.059	• • •	26.491	25.907	25.665	25.943	24.842
	0.218	0.197	• • •	0.149	0.134	0.098	0.092	0.075
MACS 0416	4104	4128	• • •	4036	4034	4062	8074	8172
	25.666	26.056	• • •	26.493	25.900	25.662	25.947	24.857
	0.148	0.134	• • •	0.101	0.091	0.067	0.062	0.051
MACS 0429	3952	3728	• • •	3938	3728	3942	8016	8090
	25.666	26.056	• • •	26.493	25.900	25.662	25.947	24.857
	0.218	0.197	• • •	0.149	0.134	0.098	0.092	0.075
MACS 0647	4248	4496	15480	4128	4262	4324	25520	8650

Table B.1 (cont'd)

Cluster	F435W	F475W	F555W	F606W	F625W	F775W	F814W	F850LP
	25.658	26.059	25.735	26.491	25.907	25.665	25.959	24.842
	0.402	0.364	0.311	0.275	0.247	0.181	0.170	0.138
MACS 0717	4052	4064	8940	7920	4128	4092	25826	8200
	25.658	26.059	25.735	26.505	25.907	25.665	25.959	24.842
	0.277	0.251	0.214	0.190	0.170	0.125	0.117	0.095
MACS 0744	4034	4022	8940	4128		4110	17786	8214
	25.658	26.059	25.735	26.491	• • •	25.665	25.959	24.842
	0.208	0.189	0.161	0.143	• • •	0.094	0.088	0.072
MACS 1115	3828	3728	• • •	3870	3728	3900	7998	7784
	25.658	26.059	• • •	26.491	25.907	25.665	25.943	24.842
	0.140	0.127	• • •	0.096	0.086	0.063	0.059	0.048
MACS 1149	3976	4136	9000	4128	4094	4094	13548	8280
	25.658	26.059	25.735	26.491	25.907	25.665	25.959	24.842
	0.083	0.075	0.064	0.057	0.051	0.037	0.035	0.029
MACS 1206	4248	4128	• • •	6608	4128	4238	8480	8578
	25.658	26.059	• • •	26.505	25.907	25.665	25.943	24.842
	0.227	0.206	• • •	0.156	0.140	0.103	0.096	0.078
MACS 1311	4172	3928	• • •	4158	3728	4176	8252	8300
	25.666	26.056	• • •	26.493	25.900	25.662	25.947	24.857
	0.112	0.101	• • •	0.077	0.069	0.050	0.047	0.038
MACS 1423	4196	4368	9000	4240	• • •	4128	13548	8464
	25.666	26.056	25.727	26.493	• • •	25.662	25.952	24.857
	0.112	0.102	0.087	0.077	• • •	0.051	0.048	0.039
MACS 1720	4080	4128	• • •	4040	4128	4070	7976	8074
	25.666	26.056	• • •	26.493	25.900	25.662	25.947	24.857
	0.136	0.123	• • •	0.093	0.084	0.061	0.058	0.047
MACS 1931	4030	4042	• • •	3850	3928	4002	7846	7838
	25.666	26.056	• • •	26.493	25.900	25.662	25.947	24.857
	0.399	0.362		0.273	0.245	0.180	0.169	0.138

Table B.1 (cont'd)

Cluster	F435W	F475W	F555W	F606W	F625W	F775W	F814W	F850LP
MACS 2129	3728	4040	8880	3728	3846	4048	13396	7808
	25.658	26.059	25.735	26.491	25.907	25.665	25.959	24.842
	0.274	0.248	0.212	0.188	0.168	0.124	0.116	0.094
MS 2137	4026	4060		17920	4128	4000	8132	8902
	25.658	26.059	• • •	26.505	25.907	25.665	25.943	24.867
	0.183	0.166		0.125	0.113	0.083	0.077	0.063
RXJ 1347	4068	10560		3878	3848	4096	14680	10560
	25.658	26.081		26.491	25.907	25.665	25.959	24.867
	0.223	0.202	• • •	0.153	0.137	0.101	0.094	0.077
RXJ 1532	4100	4128		4060	4128	4090	8036	8134
	25.666	26.059	• • •	26.491	25.907	25.665	25.943	24.842
	0.107	0.097		0.073	0.066	0.048	0.045	0.037
RXJ 2129	3910	3728	• • •	3870	3728	7792	7866	15084
	25.666	26.056	• • •	26.493	25.900	25.662	25.947	24.857
	0.146	0.132	• • •	0.100	0.090	0.066	0.062	0.050
RXJ 2248	4102	4128		3976	4128	4058	11972	
	25.666	26.056		26.493	25.900	25.662	25.947	
	0.044	0.040		0.030	0.027	0.020	0.019	

Table B.2: WFC3 (UVIS/IR) Data Properties – Exposure time (s), Zeropoint (AB Mag), and A_{λ} (Mag)

Cluster	F225W	F275W	F336W	F390W	F105W	F110W	F125W	F140W	F160W
Abell 209	7316	7464	4752	4894	2815	2515	2515	2312	5029
	24.097	24.174	24.645	25.371	26.269	26.822	26.230	26.452	25.946
	0.135	0.106	0.086	0.075	0.019	0.017	0.014	0.012	0.010
Abell 383	7343	7344	4868	4868	3621	2515	3321	2412	5935
	24.097	24.174	24.645	25.371	26.271	26.825	26.247	26.464	25.956

Table B.2 (cont'd)

Cluster	F225W	F275W	F336W	F390W	F105W	F110W	F125W	F140W	F160W
	0.217	0.170	0.138	0.121	0.030	0.027	0.023	0.019	0.016
Abell 611	7290	7446	4782	4866	2815	2515	2515	2312	5029
	24.097	24.174	24.645	25.371	26.271	26.825	26.247	26.452	25.956
	0.397	0.312	0.253	0.221	0.055	0.050	0.041	0.035	0.029
Abell 1423	7342	7506	4890	4918	2815	2515	2515	2412	5029
	24.097	24.174	24.645	25.371	26.269	26.822	26.230	26.452	25.946
	0.140	0.110	0.089	0.078	0.019	0.018	0.015	0.012	0.010
Abell 2261	7343	7490	4817	4912	2815	2515	2515	2412	5029
	24.097	24.174	24.645	25.371	26.271	26.825	26.247	26.464	25.956
	0.303	0.238	0.193	0.169	0.042	0.038	0.031	0.027	0.022
CLJ 1226	7636	7554	4504	5000	2815	2415	2515	2312	5129
	24.097	24.174	24.645	25.371	26.269	26.822	26.230	26.452	25.946
	0.134	0.105	0.085	0.074	0.019	0.017	0.014	0.012	0.010
MACS 0329	7328	7476	4808	4902	2815	2515	2515	2412	5029
	24.097	24.174	24.645	25.371	26.271	26.825	26.247	26.464	25.956
	0.421	0.331	0.268	0.235	0.058	0.053	0.044	0.037	0.031
MACS 0416	7268	7368	4720	4814	2815	2515	2515	2312	5029
	24.097	24.174	24.645	25.371	26.269	26.822	26.230	26.452	25.946
	0.286	0.224	0.182	0.159	0.040	0.036	0.030	0.025	0.021
MACS 0429	6968	7216	4568	4562	2715	2415	2415	2312	4829
	24.097	24.174	24.645	25.371	26.269	26.822	26.230	26.452	25.946
	0.422	0.331	0.269	0.235	0.058	0.053	0.044	0.037	0.031
MACS 0647	7610	7758	4996	5090	2915	2615	2615	2412	5229
	24.097	24.174	24.645	25.371	26.271	26.825	26.247	26.464	25.956
	0.778	0.611	0.496	0.434	0.108	0.098	0.081	0.068	0.057
MACS 0717	7289	7446	4781	4866	2815	2515	2515	2312	5029
	24.097	24.174	24.645	25.371	26.271	26.825	26.247	26.464	25.956
	0.536	0.421	0.342	0.299	0.074	0.068	0.056	0.047	0.039
MACS 0744	7288	7446	4780	4866	3521	2515	2515	3118	5029

Table B.2 (cont'd)

Cluster	F225W	F275W	F336W	F390W	F105W	F110W	F125W	F140W	F160W
	24.097	24.174	24.645	25.371	26.271	26.825	26.247	26.464	25.956
	0.403	0.317	0.257	0.225	0.056	0.051	0.042	0.035	0.030
MACS 1115	6978	7238	4574	4554	2515	2315	2315	2012	4929
	24.097	24.174	24.645	25.371	26.271	26.825	26.247	26.464	25.956
	0.271	0.213	0.173	0.151	0.038	0.034	0.028	0.024	0.020
MACS 1149	7112	7216	4781	4781	2815	2415	2515	2312	5029
	24.097	24.174	24.645	25.371	26.271	26.825	26.247	26.464	25.956
	0.160	0.126	0.102	0.089	0.022	0.020	0.017	0.014	0.012
MACS 1206	7386	7538	4912	4959	2815	2515	2515	2412	5029
	24.097	24.174	24.645	25.371	26.271	26.825	26.247	26.464	25.956
	0.440	0.345	0.280	0.245	0.061	0.055	0.046	0.039	0.032
MACS 1311	7298	7446	4788	4882	2815	2415	2415	2412	5029
	24.097	24.174	24.645	25.371	26.269	26.822	26.230	26.452	25.946
	0.216	0.170	0.138	0.121	0.030	0.027	0.022	0.019	0.016
MACS 1423	7184	7360	4712	4778	2815	2515	2515	2312	5029
	24.097	24.174	24.645	25.371	26.269	26.822	26.230	26.452	25.946
	0.218	0.171	0.139	0.121	0.030	0.027	0.023	0.019	0.016
MACS 1720	7232	7408	4744	4810	2715	2415	2415	2312	4829
	24.097	24.174	24.645	25.371	26.269	26.822	26.230	26.452	25.946
	0.263	0.207	0.168	0.147	0.037	0.033	0.027	0.023	0.019
MACS 1931	7256	7210	4546	4620	2715	2515	2315	2312	4829
	24.097	24.174	24.645	25.371	26.269	26.822	26.230	26.452	25.946
	0.773	0.607	0.493	0.431	0.107	0.097	0.080	0.068	0.057
MACS 2129	6934	7243	4580	4563	2415	2415	2415	2312	5029
	24.097	24.174	24.645	25.371	26.271	26.825	26.247	26.464	25.956
	0.530	0.416	0.338	0.296	0.074	0.067	0.055	0.047	0.039
MS 2137	7250	7419	4756	4827	2815	2515	2515	2312	7294
	24.097	24.174	24.645	25.371	26.271	26.825	26.247	26.464	25.956
	0.355	0.279	0.226	0.198	0.049	0.045	0.037	0.031	0.026

Table B.2 (cont'd)

Cluster	F225W	F275W	F336W	F390W	F105W	F110W	F125W	F140W	F160W
RXJ 1347	7243	7354	4781	4820	2515	5026	2415	2312	7741
	24.097	24.174	24.645	25.371	26.271	26.825	26.247	26.464	25.956
	0.432	0.339	0.275	0.241	0.060	0.054	0.045	0.038	0.032
RXJ 1532	7262	7428	4764	4840	2815	2515	2515	2312	5029
	24.097	24.174	24.645	25.371	26.269	26.825	26.247	26.452	25.956
	0.206	0.162	0.132	0.115	0.029	0.026	0.021	0.018	0.015
RXJ 2129	6978	7238	4574	4554	2615	2415	3421	2312	6238
	24.097	24.174	24.645	25.371	26.269	26.822	26.230	26.452	25.946
	0.282	0.221	0.180	0.157	0.039	0.036	0.029	0.025	0.021
RXJ 2248	7148	7274	4718	4740	2815	2515	2515	2312	5029
	24.097	24.174	24.645	25.371	26.269	26.822	26.230	26.452	25.946
	0.085	0.067	0.054	0.048	0.012	0.011	0.009	0.007	0.006

Table B.3: Masked Stars in CLASH fields (R >2'')

$=$ α_{2000}	δ_{2000}	radius	Cluster field
		(")	
1:31:53.938	-13:35:58.12	2.467	Abell 209
1:31:47.744	-13:37:24.03	2.048	Abell 209
2:48:05.482	-3:30:58.99	2.223	Abell 383
2:48:00.143	-3:31:34.71	2.004	Abell 383
2:47:58.373	-3:31:46.08	2.173	Abell 383
2:47:59.301	-3:30:57.46	2.245	Abell 383
8:00:55.966	+36:03:55.39	2.218	Abell 611
8:01:01.746	+36:03:31.90	2.019	Abell 611
8:00:53.077	+36:05:21.71	2.712	Abell 611
8:00:59.310	+36:04:49.79	2.128	Abell 611
8:01:05.045	+36:04:25.20	2.394	Abell 611
8:01:02.811	+36:04:08.19	2.742	Abell 611
8:01:04.748	+36:04:00.51	3.112	Abell 611
8:01:03.745	+36:03:44.43	2.461	Abell 611
8:01:00.700	+36:02:12.82	2.239	Abell 611
11:57:25.503	+33:36:52.94	2.816	Abell 1423
11:57:14.500	+33:35:13.27	2.824	Abell 1423
17:22:26.566	+32:08:51.68	2.351	Abell 2261
17:22:30.646	+32:08:50.85	2.496	Abell 2261
17:22:23.255	+32:08:37.20	2.302	Abell 2261
17:22:28.732	+32:08:34.29	2.418	Abell 2261
17:22:26.414	+32:07:44.61	2.292	Abell 2261
17:22:31.752	+32:07:42.20	2.756	Abell 2261
17:22:22.004	+32:07:39.36	2.388	Abell 2261
17:22:22.702	+32:07:18.10	2.366	Abell 2261
17:22:26.461	+32:07:15.10	2.270	Abell 2261
17:22:28.701	+32:07:02.65	2.432	Abell 2261
17:22:29.668	+32:06:54.04	2.657	Abell 2261
17:22:26.000	+32:06:50.59	2.240	Abell 2261
17:22:26.715	+32:06:49.76	2.058	Abell 2261
17:22:24.348	+32:09:43.62	2.137	Abell 2261
17:22:34.834	+32:08:53.88	2.602	Abell 2261
17:22:34.272	+32:07:11.32	2.513	Abell 2261
17:22:23.040	+32:06:17.22	2.256	Abell 2261
17:22:22.437	+32:06:06.14	2.859	Abell 2261
12:26:59.747	+33:33:31.34	2.010	CLJ1226
12:26:58.996	+33:33:12.47	3.096	CLJ1226
12:26:56.518	+33:33:12.10	2.023	CLJ1226
12:26:58.195	+33:31:49.79	2.779	CLJ1226
3:29:40.192	-2:11:58.00	2.502	MACS 0329

Table B.3 (cont'd)

α_{2000}	δ_{2000}	radius	Cluster field
		(")	
			351000
3:29:44.866	-2:10:19.27	2.918	MACS 0329
3:29:45.807	-2:10:27.06	2.076	MACS 0329
3:29:48.030	-2:12:37.46	3.408	MACS 0329
3:29:47.153	-2:13:14.59	2.841	MACS 0329
3:29:38.482	-2:13:25.04	3.002	MACS 0329
4:16:10.089	-24:05:10.08	4.046	MACS 0416
4:16:03.772	-24:02:58.02	2.576	MACS 0416
4:16:15.565	-24:03:43.22	3.554	MACS 0416
4:16:06.967	-24:05:42.51	2.025	MACS 0416
4:29:36.659	-2:51:50.59	2.542	MACS 0429
4:29:39.676	-2:52:53.13	2.479	MACS 0429
4:29:38.960	-2:53:03.39	2.372	MACS 0429
4:29:40.023	-2:53:26.19	2.806	MACS 0429
4:29:32.624	-2:53:43.72	2.799	MACS 0429
4:29:33.989	-2:53:52.35	2.586	MACS 0429
4:29:37.282	-2:54:06.14	2.353	MACS 0429
4:29:35.863	-2:51:26.50	2.683	MACS 0429
4:29:33.347	-2:51:52.81	2.059	MACS 0429
4:29:42.013	-2:53:06.82	2.570	MACS 0429
4:29:37.370	-2:54:21.08	2.347	MACS 0429
6:47:38.640	+70:14:48.92	2.172	MACS 0647
6:47:39.959	+70:14:48.60	2.180	MACS 0647
6:47:46.323	+70:14:25.94	2.720	MACS 0647
6:47:39.875	+70:14:29.95	2.189	MACS 0647
6:47:51.066	+70:13:45.62	2.014	MACS 0647
6:47:44.684	+70:12:49.74	2.650	MACS 0647
6:47:57.864	+70:16:30.59	2.174	MACS 0647
6:47:42.894	+70:16:27.08	2.651	MACS 0647
6:48:01.146	+70:16:21.20	2.714	MACS 0647
6:48:01.227	+70:13:59.01	2.145	MACS 0647
7:17:25.932	+37:45:18.77	2.421	MACS 0717
7:17:37.044	+37:45:01.74	2.030	MACS 0717
7:17:34.425	+37:44:14.91	2.328	MACS 0717
7:17:33.642	+37:43:46.66	2.125	MACS 0717
7:17:34.634	+37:46:40.44	2.714	MACS 0717
7:17:40.790	+37:46:16.30	2.736	MACS 0717
7:17:42.875	+37:44:15.92	2.944	MACS 0717
7:17:26.522	+37:44:11.74	3.032	MACS 0717
7:17:28.085	+37:43:13.56	2.921	MACS 0717
7:44:50.660	+39:28:41.72	2.449	MACS 0744

Table B.3 (cont'd)

α_{2000}	δ_{2000}	radius (")	Cluster field
7:44:55.141	+39:28:29.71	2.255	MACS 0744
7:44:55.204	+39:28:14.08	2.029	MACS 0744
7:44:59.384	+39:27:57.19	2.882	MACS 0744
7:44:49.728	+39:27:52.02	2.397	MACS 0744
7:44:55.316	+39:27:45.62	2.748	MACS 0744
7:44:57.299	+39:27:26.17	2.546	MACS 0744
7:44:53.177	+39:26:12.32	2.323	MACS 0744
7:44:58.033	+39:28:23.15	2.789	MACS 0744
7:44:51.012	+39:28:52.43	3.014	MACS 0744
7:44:56.250	+39:28:36.72	4.060	MACS 0744
7:44:48.332	+39:25:49.14	2.727	MACS 0744
7:44:52.036	+39:25:43.71	2.469	MACS 0744
11:15:52.740	+1:30:11.05	2.921	MACS 1115
11:15:52.895	+1:29:18.37	2.276	MACS 1115
11:15:47.699	+1:29:06.37	2.896	MACS 1115
11:15:57.631	+1:28:16.35	2.422	MACS 1115
11:49:38.832	+22:24:23.38	2.934	MACS 1149
11:49:32.707	+22:24:08.69	2.534	MACS 1149
11:49:35.330	+22:23:37.46	2.953	MACS 1149
11:49:40.629	+22:23:35.88	2.414	MACS 1149
11:49:32.156	+22:23:26.96	2.681	MACS 1149
11:49:39.579	+22:23:21.85	2.624	MACS 1149
11:49:42.479	+22:25:38.87	2.659	MACS 1149
11:49:45.077	+22:24:15.89	2.687	MACS 1149
11:49:30.635	+22:22:41.76	2.200	MACS 1149
11:49:35.910	+22:22:12.66	2.654	MACS 1149
12:06:06.232	-8:46:24.87	2.336	MACS 1206
12:06:05.031	-8:48:01.42	2.066	MACS 1206
12:06:05.136			MACS 1206
13:11:03.609	-3:09:48.51	2.803	MACS 1311
13:11:01.906	-3:09:56.02	2.346	MACS 1311
13:10:58.724	-3:10:27.50	2.362	MACS 1311
13:11:02.523	-3:10:30.65	2.206	MACS 1311
13:11:00.729	-3:08:49.57	3.003	MACS 1311
13:11:04.761	-3:09:21.51	2.562	MACS 1311
13:11:06.025	-3:09:32.10	2.306	MACS 1311
13:11:03.823	-3:12:09.35	2.555	MACS 1311
14:23:46.627	+24:05:18.89		MACS 1423
14:23:50.123			
14:23:45.444	+24:03:43.63	2.593	MACS 1423

Table B.3 (cont'd)

	,		
α_{2000}	δ_{2000}	radius	Cluster field
		(")	
14:23:55.542	+24:03:43.47	2.298	MACS 1423
17:20:19.823	+35:37:32.34	2.298 2.531	MACS 1423 MACS 1720
17:20:13.823	+35.37.32.34 +35.37.29.07	2.909	MACS 1720 MACS 1720
17:20:12:333	+35.37.23.07 +35.37.02.74	2.046	MACS 1720 MACS 1720
17:20:13.036	+35:36:32.46	2.040	MACS 1720 MACS 1720
17:20:13:030	+35:35:48.28	3.094	MACS 1720 MACS 1720
17:20:12:522	+35.35.48.67	2.337	MACS 1720 MACS 1720
17:20:19.769	+35.35.25.68	2.598	MACS 1720 MACS 1720
17:20:17.492	+35:35:18.17	2.530 2.510	MACS 1720 MACS 1720
17:20:17:432	+35:35:15.18	2.495	MACS 1720 MACS 1720
17:20:15.102	+35:38:37.48	2.736	MACS 1720 MACS 1720
17:20:13:102	+35:38:14.21	2.438	MACS 1720 MACS 1720
17:20:24.181	+35:36:48.83	2.853	MACS 1720
17:20:26.990	+35:36:27.75	2.030	MACS 1720
17:20:27.567	+35:36:06.68	3.295	MACS 1720
17:20:08.116	+35:35:56.13	2.547	MACS 1720
17:20:25.281	+35:35:42.04	2.252	MACS 1720
19:31:53.021	-26:33:37.02	2.500	MACS 1931
19:31:54.476	-26:33:48.41	2.118	MACS 1931
19:31:44.427	-26:34:25.83	2.820	MACS 1931
19:31:52.496	-26:34:33.91	2.302	MACS 1931
19:31:44.440	-26:34:40.64	2.510	MACS 1931
19:31:49.075	-26:34:44.27	2.092	MACS 1931
19:31:49.161	-26:34:47.61	2.140	MACS 1931
19:31:46.201	-26:34:43.46	2.274	MACS 1931
19:31:46.391	-26:34:56.83	2.357	MACS 1931
19:31:47.359	-26:34:58.84	2.649	MACS 1931
19:31:53.706	-26:35:05.89	2.878	MACS 1931
19:31:46.249	-26:35:05.48	2.151	MACS 1931
19:31:52.953	-26:35:18.13	2.657	MACS 1931
19:31:52.630	-26:35:27.88	2.092	MACS 1931
19:31:48.850	-26:35:48.51	2.078	MACS 1931
19:31:51.263	-26:32:50.27	4.281	MACS 1931
19:31:54.879	-26:33:23.67	2.653	MACS 1931
19:31:56.886	-26:33:29.27	2.110	MACS 1931
19:31:54.527	-26:33:39.22	2.521	MACS 1931
19:31:57.454	-26:33:41.18	2.261	MACS 1931
19:31:57.717	-26:33:45.08	2.110	MACS 1931
19:31:55.965	-26:33:49.73	2.094	MACS 1931
19:31:43.941	-26:33:57.25	2.514	MACS 1931

Table B.3 (cont'd)

α_{2000}	δ_{2000}	radius (")	Cluster field
19:31:43.982	-26:34:10.33	2.538	MACS 1931
19:31:43.255	-26:34:37.15	2.030	MACS 1931
19:31:56.659	-26:34:51.65	2.166	MACS 1931
19:31:55.991	-26:34:52.11	2.780	MACS 1931
19:31:55.074	-26:35:09.38	2.906	MACS 1931
19:31:43.908	-26:35:15.42	2.334	MACS 1931
19:31:58.446	-26:35:20.60	2.508	MACS 1931
19:31:55.150	-26:35:22.42	2.779	MACS 1931
19:31:53.941	-26:35:28.20	2.326	MACS 1931
19:31:45.744	-26:35:36.27	2.084	MACS 1931
19:31:57.344	-26:35:49.85	2.353	MACS 1931
19:31:55.475	-26:35:52.67	2.322	MACS 1931
19:31:42.393	-26:35:56.22	2.532	MACS 1931
19:31:49.650	-26:36:03.56	2.831	MACS 1931
19:31:54.493	-26:36:02.53	2.450	MACS 1931
19:31:45.645	-26:36:18.69	2.483	MACS 1931
21:29:27.213	-7:40:31.32	2.859	MACS 2129
21:29:22.338	-7:40:55.86	2.638	MACS 2129
21:29:29.118	-7:41:13.54	2.212	MACS 2129
21:29:27.712	-7:41:18.71	2.464	MACS 2129
21:29:23.572	-7:41:43.73	2.705	MACS 2129
21:29:28.434	-7:42:28.14	2.276	MACS 2129
21:29:27.703	-7:39:08.91	2.098	MACS 2129
21:29:27.070	-7:39:44.66	2.621	MACS 2129
21:29:20.697	-7:40:47.17	2.442	MACS 2129
21:29:21.333	-7:40:55.36	2.555	MACS 2129
21:29:31.184	-7:42:20.05	2.502	MACS 2129
21:29:30.485	-7:42:36.60	2.507	MACS 2129
21:29:33.191	-7:42:38.06	2.565	MACS 2129
21:29:23.636	-7:42:49.54	2.285	MACS 2129
21:29:30.730	-7:42:54.60	2.913	MACS 2129
21:29:23.007	-7:43:11.32	2.310	MACS 2129
21:40:17.670	-23:38:59.26	2.996	MS 2137
21:40:14.094	-23:39:59.62	2.367	MS 2137
21:40:17.522	-23:40:33.32	2.622	MS 2137
21:40:07.770	-23:39:07.19	2.918	MS 2137
21:40:20.674	-23:39:48.82	2.028	MS 2137
21:40:15.278	-23:41:29.03	3.024	MS 2137
21:40:17.614	-23:41:31.90	2.709	MS 2137
13:47:34.344	-11:44:30.07	2.916	RXJ 1347

Table B.3 (cont'd)

α_{2000}	δ_{2000}	radius	Cluster field
		(")	
13:47:27.362	-11:45:08.45	2.133	RXJ 1347
13:47:28.584	-11:45:36.97	2.831	RXJ 1347
13:47:32.518	-11:46:01.79	2.245	RXJ 1347
13:47:27.808	-11:43:52.03	2.944	RXJ 1347
13:47:34.858	-11:44:01.04	2.186	RXJ 1347
13:47:33.412	-11:46:53.16	2.607	RXJ 1347
15:32:59.519	+30:20:50.70	2.515	RXJ 1532
15:32:48.512	+30:20:44.25	2.523	RXJ 1532
15:32:56.525	+30:22:59.46	2.327	RXJ 1532
15:32:58.078	+30:19:52.87	2.293	RXJ 1532
21:29:36.235	+0.06:18.15	2.230	RXJ 2129
21:29:44.089	+0.05.59.02	2.215	RXJ 2129
21:29:44.792	+0.05.55.15	2.385	RXJ 2129
21:29:42.193	+0.05.15.15	4.314	RXJ 2129
21:29:43.597	+0.05.04.82	2.440	RXJ 2129
21:29:40.542	+0.04:42.77	2.012	RXJ 2129
21:29:39.536	+0.04:32.55	2.976	RXJ 2129
21:29:44.260	+0.06:47.85	2.895	RXJ 2129
21:29:46.893	+0.06:07.20	2.403	RXJ 2129
21:29:33.738	+0.05.28.13	2.842	RXJ 2129
21:29:34.948	+0.04:42.23	2.440	RXJ 2129
21:29:34.857	+0.04:32.27	2.342	RXJ 2129
22:48:44.045	-44:30:47.96	2.978	RXJ 2248

REFERENCES

REFERENCES

Abell, G. O. 1958, ApJS, 3, 211

Abell, G. O., Corwin, Jr., H. G., & Olowin, R. P. 1989, ApJS, 70, 1

Agulli, I., Aguerri, J. A. L., Sánchez-Janssen, R., et al. 2016, MNRAS, 458, 1590

Aird, J., Coil, A. L., Moustakas, J., et al. 2013, ApJ, 775, 41

Akritas, M. G., & Bershady, M. A. 1996, ApJ, 470, 706

Allen, S. W., Evrard, A. E., & Mantz, A. B. 2011, ARA&A, 49, 409

Allen, S. W., Rapetti, D. A., Schmidt, R. W., et al. 2008, MNRAS, 383, 879

Anders, E., & Grevesse, N. 1989, Geochim. Cosmochim. Acta, 53, 197

Anderson, J., & Bedin, L. R. 2010, PASP, 122, 1035

Andreon, S. 2003, A&A, 409, 37

Andreon, S. 2008, MNRAS, 386, 1045

Andreon, S., Dong, H., & Raichoor, A. 2016, ArXiv e-prints, arXiv:1606.03996

Andreon, S., Newman, A. B., Trinchieri, G., et al. 2014, A&A, 565, A120

Annis, J., Kent, S., Castander, F., et al. 1999, in Bulletin of the American Astronomical Society, Vol. 31, American Astronomical Society Meeting Abstracts, 1391

Annunziatella, M., Biviano, A., Mercurio, A., et al. 2014, A&A, 571, A80

Arimoto, N., & Yoshii, Y. 1987, A&A, 173, 23

Arnaud, M., Pointecouteau, E., & Pratt, G. W. 2005, A&A, 441, 893

Arnaud, M., Pointecouteau, E., & Pratt, G. W. 2007, A&A, 474, L37

Ascaso, B., Moles, M., Aguerri, J. A. L., Sánchez-Janssen, R., & Varela, J. 2008, A&A, 487, 453

Bahcall, N. A., & Fan, X. 1998, ApJ, 504, 1

Bahé, Y. M., McCarthy, I. G., Balogh, M. L., & Font, A. S. 2013, MNRAS, 430, 3017

Baldry, I. K., Glazebrook, K., Brinkmann, J., et al. 2004, ApJ, 600, 681

Balestra, I., Mercurio, A., Sartoris, B., et al. 2016, ApJS, 224, 33

Balogh, M. L., Babul, A., & Patton, D. R. 1999, MNRAS, 307, 463

Balogh, M. L., Baldry, I. K., Nichol, R., et al. 2004, ApJ, 615, L101

Baum, W. A. 1959, PASP, 71, 106

Bell, E. F., & de Jong, R. S. 2001, ApJ, 550, 212

Bell, E. F., McIntosh, D. H., Katz, N., & Weinberg, M. D. 2003, ApJS, 149, 289

Bell, E. F., Wolf, C., Meisenheimer, K., et al. 2004, ApJ, 608, 752

Belsole, E., Sauvageot, J.-L., Pratt, G. W., & Bourdin, H. 2005, A&A, 430, 385

Benítez, N. 2000, ApJ, 536, 571

Benítez, N., Ford, H., Bouwens, R., et al. 2004, ApJS, 150, 1

Bernardi, M., Sheth, R. K., Nichol, R. C., Schneider, D. P., & Brinkmann, J. 2005, AJ, 129, 61

Berrier, J. C., Stewart, K. R., Bullock, J. S., et al. 2009, ApJ, 690, 1292

Bertin, E., & Arnouts, S. 1996, A&AS, 117, 393

Bhattacharya, S., Heitmann, K., White, M., et al. 2011, ApJ, 732, 122

Biviano, A., Rosati, P., Balestra, I., et al. 2013, A&A, 558, A1

Blakeslee, J. P., Franx, M., Postman, M., et al. 2003, ApJ, 596, L143

Blanton, M. R., Hogg, D. W., Bahcall, N. A., et al. 2003, ApJ, 592, 819

Bohlin, R. C. 2016, ArXiv e-prints, arXiv:1606.01838 [astro-ph.IM]

Bohlin, R. C., Gordon, K. D., & Tremblay, P.-E. 2014, PASP, 126, 711

Böhringer, H., & Chon, G. 2015, A&A, 574, L8

Böhringer, H., Chon, G., Collins, C. A., et al. 2013, A&A, 555, A30

Bouwens, R. J., Bradley, L., Zitrin, A., et al. 2014, ApJ, 795, 126

Bower, R. G. 1997, MNRAS, 288, 355

Bower, R. G., Benson, A. J., Lacey, C. G., et al. 2001, MNRAS, 325, 497

Bower, R. G., Kodama, T., & Terlevich, A. 1998, MNRAS, 299, 1193

Bower, R. G., Lucey, J. R., & Ellis, R. S. 1992, MNRAS, 254, 601

Boylan-Kolchin, M., Springel, V., White, S. D. M., Jenkins, A., & Lemson, G. 2009, MNRAS, 398, 1150

Bradley, L. D., Zitrin, A., Coe, D., et al. 2014, ApJ, 792, 76

Brent, R. P. 1973, Algorithms for Minimization Without Derivatives (Prentice Hall)

Brodwin, M., Stanford, S. A., Gonzalez, A. H., et al. 2013, ApJ, 779, 138

Brown, M. J. I., Dey, A., Jannuzi, B. T., et al. 2007, ApJ, 654, 858

Bruch, S., Donahue, M., Voit, G. M., Sun, M., & Conselice, C. J. 2010, ApJ, 724, 608

Bruzual, G., & Charlot, S. 2003, MNRAS, 344, 1000

Bryan, G. L. 2000, ApJ, 544, L1

Bryan, G. L., & Norman, M. L. 1998, ApJ, 495, 80

Butcher, H., & Oemler, Jr., A. 1978, ApJ, 219, 18

Carrasco, E. R., Cypriano, E. S., Neto, G. B. L., et al. 2007, ApJ, 664, 777

Cash, W. 1979, ApJ, 228, 939

Castellano, M., Amorín, R., Merlin, E., et al. 2016, A&A, 590, A31

Cavaliere, A., & Fusco-Femiano, R. 1976, A&A, 49, 137

Cerulo, P., Couch, W. J., Lidman, C., et al. 2016, MNRAS, 457, 2209

Chandrasekhar, S. 1935, MNRAS, 96, 21

Charlot, S., & Fall, S. M. 2000, ApJ, 539, 718

Coe, D., Benítez, N., Sánchez, S. F., et al. 2006, AJ, 132, 926

Coe, D., Bradley, L., & Zitrin, A. 2015, ApJ, 800, 84

Coe, D., Umetsu, K., Zitrin, A., et al. 2012, ApJ, 757, 22

Coe, D., Zitrin, A., Carrasco, M., et al. 2013, ApJ, 762, 32

Cohen, J. G., & Kneib, J.-P. 2002, ApJ, 573, 524

Connor, T., Donahue, M., Sun, M., et al. 2014, ApJ, 794, 48

Conroy, C. 2013, ARA&A, 51, 393

Conroy, C., & Gunn, J. E. 2010, ApJ, 712, 833

Conroy, C., Gunn, J. E., & White, M. 2009, ApJ, 699, 486

Conselice, C. J., Gallagher, III, J. S., & Wyse, R. F. G. 2002, AJ, 123, 2246

Cool, R. J., Eisenstein, D. J., Johnston, D., et al. 2006, AJ, 131, 736

Crawford, S. M., Bershady, M. A., & Hoessel, J. G. 2009, ApJ, 690, 1158

Da Rocha, C., & Mendes de Oliveira, C. 2005, MNRAS, 364, 1069

Darvish, B., Mobasher, B., Sobral, D., et al. 2016, ApJ, 825, 113

Davé, R., & Oppenheimer, B. D. 2007, MNRAS, 374, 427

David, L. P., Slyz, A., Jones, C., et al. 1993, ApJ, 412, 479

De Lucia, G., Kauffmann, G., & White, S. D. M. 2004a, MNRAS, 349, 1101

De Lucia, G., Poggianti, B. M., Aragón-Salamanca, A., et al. 2004b, ApJ, 610, L77

De Lucia, G., Poggianti, B. M., Aragón-Salamanca, A., et al. 2007, MNRAS, 374, 809

De Propris, R., Phillipps, S., & Bremer, M. N. 2013, MNRAS, 434, 3469

de Rossi, M. E., Tissera, P. B., & Scannapieco, C. 2007, MNRAS, 374, 323

Delaye, L., Huertas-Company, M., Mei, S., et al. 2014, MNRAS, 441, 203

DeMaio, T., Gonzalez, A. H., Zabludoff, A., Zaritsky, D., & Bradač, M. 2015, MNRAS, 448, 1162

Dey, A., Lee, K.-S., Reddy, N., et al. 2016, ApJ, 823, 11

Donahue, M., & Voit, G. M. 1999, ApJ, 523, L137

Donahue, M., Voit, G. M., Mahdavi, A., et al. 2014, ApJ, 794, 136

Donahue, M., Connor, T., Fogarty, K., et al. 2015, ApJ, 805, 177

Donahue, M., Ettori, S., Rasia, E., et al. 2016, ApJ, 819, 36

Dressler, A. 1980, ApJ, 236, 351

Ebeling, H., Barrett, E., Donovan, D., et al. 2007, ApJ, 661, L33

Ebeling, H., Edge, A. C., & Henry, J. P. 2001, ApJ, 553, 668

Ebeling, H., Edge, A. C., Mantz, A., et al. 2010, MNRAS, 407, 83

Ebeling, H., Ma, C.-J., & Barrett, E. 2014, ApJS, 211, 21

Eckmiller, H. J., Hudson, D. S., & Reiprich, T. H. 2011, A&A, 535, A105

Edge, A. C., & Stewart, G. C. 1991, MNRAS, 252, 414

Edwards, L. O. V., & Fadda, D. 2011, AJ, 142, 148

Eisenhardt, P. R. M., Brodwin, M., Gonzalez, A. H., et al. 2008, ApJ, 684, 905

Eke, V. R., Cole, S., & Frenk, C. S. 1996, MNRAS, 282, 263

Ellis, R. S., Smail, I., Dressler, A., et al. 1997, ApJ, 483, 582

Erfanianfar, G., Popesso, P., Finoguenov, A., et al. 2014, MNRAS, 445, 2725

Ettori, S., & Brighenti, F. 2008, MNRAS, 387, 631

Ettori, S., Tozzi, P., Borgani, S., & Rosati, P. 2004, A&A, 417, 13

Evrard, A. E., & Henry, J. P. 1991, ApJ, 383, 95

Evrard, A. E., Metzler, C. A., & Navarro, J. F. 1996, ApJ, 469, 494

Faber, S. M. 1973, ApJ, 179, 731

Fabjan, D., Borgani, S., Tornatore, L., et al. 2010, MNRAS, 401, 1670

Ferrarese, L., Côté, P., Sánchez-Janssen, R., et al. 2016, ApJ, 824, 10

Ferreras, I., Charlot, S., & Silk, J. 1999, ApJ, 521, 81

Fitzpatrick, E. L. 1999, PASP, 111, 63

Fogarty, K., Postman, M., Connor, T., Donahue, M., & Moustakas, J. 2015, ApJ, 813, 117

Foltz, R., Rettura, A., Wilson, G., et al. 2015, ApJ, 812, 138

Ford, H. C., Clampin, M., Hartig, G. F., et al. 2003, in Proc. SPIE, Vol. 4854, Future EUV/UV and Visible Space Astrophysics Missions and Instrumentation., ed. J. C. Blades & O. H. W. Siegmund, 81

Fotopoulou, S., Buchner, J., Georgantopoulos, I., et al. 2016, A&A, 587, A142

Franck, J. R., McGaugh, S. S., & Schombert, J. M. 2015, AJ, 150, 46

Fruchter, A. S., & Hook, R. N. 2002, PASP, 114, 144

Gal, R. R., Lopes, P. A. A., de Carvalho, R. R., et al. 2009, AJ, 137, 2981

Gallazzi, A., Charlot, S., Brinchmann, J., & White, S. D. M. 2006, MNRAS, 370, 1106

Gaspari, M., Brighenti, F., Temi, P., & Ettori, S. 2014, ApJ, 783, L10

Geller, M. J., Diaferio, A., Kurtz, M. J., Dell'Antonio, I. P., & Fabricant, D. G. 2012, AJ, 143, 102

Georgakakis, A., Aird, J., Buchner, J., et al. 2015, MNRAS, 453, 1946

Giodini, S., Lovisari, L., Pointecouteau, E., et al. 2013, Space Sci. Rev., 177, 247

Girardi, L., Bressan, A., Bertelli, G., & Chiosi, C. 2000, A&AS, 141, 371

Girardi, M., Mercurio, A., Balestra, I., et al. 2015, A&A, 579, A4

Gladders, M. D., & Yee, H. K. C. 2000, AJ, 120, 2148

Gladders, M. D., Yee, H. K. C., Majumdar, S., et al. 2007, ApJ, 655, 128

Gómez, P. L., Valkonen, L. E., Romer, A. K., et al. 2012, AJ, 144, 79

Gonzalez, A. H., Sivanandam, S., Zabludoff, A. I., & Zaritsky, D. 2013, ApJ, 778, 14

Graham, A. W., & Driver, S. P. 2005, PASA, 22, 118

Grogin, N. A., Kocevski, D. D., Faber, S. M., et al. 2011, ApJS, 197, 35

Grossi, M., Dolag, K., Branchini, E., Matarrese, S., & Moscardini, L. 2007, MNRAS, 382, 1261

Gruen, D., Brimioulle, F., Seitz, S., et al. 2013, MNRAS, 432, 1455

Guzzo, L., Schuecker, P., Böhringer, H., et al. 2009, A&A, 499, 357

Haines, C. P., Pereira, M. J., Smith, G. P., et al. 2015, ApJ, 806, 101

Hansen, C. J., Kawaler, S. D., & Trimble, V. 2004, Stellar interiors: physical principles, structure, and evolution

Hao, J., Koester, B. P., Mckay, T. A., et al. 2009, ApJ, 702, 745

Hao, J., McKay, T. A., Koester, B. P., et al. 2010, ApJS, 191, 254

Helsdon, S. F., & Ponman, T. J. 2000, MNRAS, 319, 933

Hicks, A. K., Pratt, G. W., Donahue, M., et al. 2013, MNRAS, 431, 2542

Hilton, M., Stanford, S. A., Stott, J. P., et al. 2009, ApJ, 697, 436

Hoekstra, H., Bartelmann, M., Dahle, H., et al. 2013, Space Sci. Rev., 177, 75

Hoekstra, H., Donahue, M., Conselice, C. J., McNamara, B. R., & Voit, G. M. 2011, ApJ, 726, 48

Hoekstra, H., Mahdavi, A., Babul, A., & Bildfell, C. 2012, MNRAS, 427, 1298

Hogg, D. W., Blanton, M. R., Brinchmann, J., et al. 2004, ApJ, 601, L29

Holden, B. P., Franx, M., Illingworth, G. D., et al. 2009, ApJ, 693, 617

Holder, G., Haiman, Z., & Mohr, J. J. 2001, ApJ, 560, L111

Hopkins, A. M., & Beacom, J. F. 2006, ApJ, 651, 142

Hubble, E., & Humason, M. L. 1931, ApJ, 74, 43

Humphrey, P. J., Liu, W., & Buote, D. A. 2009, ApJ, 693, 822

Ichinohe, Y., Werner, N., Simionescu, A., et al. 2015, MNRAS, 448, 2971

Jenkins, A., Frenk, C. S., White, S. D. M., et al. 2001, MNRAS, 321, 372

Jouvel, S., Host, O., Lahav, O., et al. 2014, A&A, 562, A86

Kaiser, N. 1986, MNRAS, 222, 323

Kaiser, N. 1991, ApJ, 383, 104

Kalberla, P. M. W., Burton, W. B., Hartmann, D., et al. 2005, A&A, 440, 775

Kato, Y., Matsuda, Y., Smail, I., et al. 2016, MNRAS, arXiv:1605.07370

Kauffmann, G., & Charlot, S. 1998, MNRAS, 294, 705

Kay, S. T. 2004, MNRAS, 347, L13

Kettula, K., Finoguenov, A., Massey, R., et al. 2013, ApJ, 778, 74

Klypin, A. A., Trujillo-Gomez, S., & Primack, J. 2011, ApJ, 740, 102

Kodama, T., & Arimoto, N. 1997, A&A, 320, 41

Kodama, T., Arimoto, N., Barger, A. J., & Arag'on-Salamanca, A. 1998, A&A, 334, 99

Koekemoer, A. M., Fruchter, A. S., Hook, R. N., & Hack, W. 2003, in HST Calibration Workshop: Hubble after the Installation of the ACS and the NICMOS Cooling System, ed. S. Arribas, A. Koekemoer, & B. Whitmore, 337

Koekemoer, A. M., Faber, S. M., Ferguson, H. C., et al. 2011, ApJS, 197, 36

Koester, B. P., McKay, T. A., Annis, J., et al. 2007a, ApJ, 660, 239

Koester, B. P., McKay, T. A., Annis, J., et al. 2007b, ApJ, 660, 221

Kotov, O., & Vikhlinin, A. 2005, ApJ, 633, 781

Kravtsov, A. V., & Borgani, S. 2012, ARA&A, 50, 353

Krick, J. E., Bernstein, R. A., & Pimbblet, K. A. 2006, AJ, 131, 168

Kron, R. G. 1980, ApJS, 43, 305

Kroupa, P. 2001, MNRAS, 322, 231

Lampton, M., Margon, B., & Bowyer, S. 1976, ApJ, 208, 177

Lan, T.-W., Ménard, B., & Mo, H. 2016, MNRAS, 459, 3998

LaRoque, S. J., Bonamente, M., Carlstrom, J. E., et al. 2006, ApJ, 652, 917

Larson, R. B. 1974, MNRAS, 166, 585

Lemaux, B. C., Gal, R. R., Lubin, L. M., et al. 2012, ApJ, 745, 106

Lidman, C., Rosati, P., Demarco, R., et al. 2004, A&A, 416, 829

Lidman, C., Rosati, P., Tanaka, M., et al. 2008, A&A, 489, 981

Lilly, S. J., Carollo, C. M., Pipino, A., Renzini, A., & Peng, Y. 2013, ApJ, 772, 119

Limousin, M., Ebeling, H., Richard, J., et al. 2012, A&A, 544, A71

Lin, Y.-T., Stanford, S. A., Eisenhardt, P. R. M., et al. 2012, ApJ, 745, L3

Lintott, C. J., Schawinski, K., Slosar, A., et al. 2008, MNRAS, 389, 1179

Liu, S.-F., Yuan, Q.-R., Yang, Y.-B., et al. 2011, AJ, 141, 99

Loewenstein, M. 2000, ApJ, 532, 17

Loveday, J., Norberg, P., Baldry, I. K., et al. 2012, MNRAS, 420, 1239

Lu, T., Gilbank, D. G., Balogh, M. L., & Bognat, A. 2009, MNRAS, 399, 1858

Lumb, D. H., Bartlett, J. G., Romer, A. K., et al. 2004, A&A, 420, 853

Mahdavi, A., Hoekstra, H., Babul, A., et al. 2013, ApJ, 767, 116

Mahdavi, A., Hoekstra, H., Babul, A., et al. 2014, ApJ, in press

Mahdavi, A., Hoekstra, H., Babul, A., & Henry, J. P. 2008, MNRAS, 384, 1567

Mancone, C. L., & Gonzalez, A. H. 2012, PASP, 124, 606

Mancone, C. L., Baker, T., Gonzalez, A. H., et al. 2012, ApJ, 761, 141

Mantz, A., Allen, S. W., Ebeling, H., Rapetti, D., & Drlica-Wagner, A. 2010a, MNRAS, 406, 1773

Mantz, A., Allen, S. W., Rapetti, D., & Ebeling, H. 2010b, MNRAS, 406, 1759

Maraston, C. 2005, MNRAS, 362, 799

Markevitch, M. 1998, ApJ, 504, 27

Marshall, H. L., Tananbaum, H., Avni, Y., & Zamorani, G. 1983, ApJ, 269, 35

Martinet, N., Durret, F., Guennou, L., et al. 2015, A&A, 575, A116

Matsushita, K., Böhringer, H., Takahashi, I., & Ikebe, Y. 2007, A&A, 462, 953

Matteucci, F., & Tornambe, A. 1987, A&A, 185, 51

Maughan, B. J. 2007, ApJ, 668, 772

Maughan, B. J., Giles, P. A., Randall, S. W., Jones, C., & Forman, W. R. 2012, MNRAS, 421, 1583

McCarthy, I. G., Schaye, J., Ponman, T. J., et al. 2010, MNRAS, 406, 822

McIntosh, D. H., Zabludoff, A. I., Rix, H.-W., & Caldwell, N. 2005, ApJ, 619, 193

McLeod, D. J., McLure, R. J., & Dunlop, J. S. 2016, MNRAS, 459, 3812

Medezinski, E., Umetsu, K., Nonino, M., et al. 2013, ApJ, 777, 43

Mei, S., Holden, B. P., Blakeslee, J. P., et al. 2009, ApJ, 690, 42

Meneghetti, M., Rasia, E., Vega, J., et al. 2014, ApJ, 797, 34

Mercurio, A., La Barbera, F., Haines, C. P., et al. 2008, MNRAS, 387, 1374

Merlin, E., Amorín, R., Castellano, M., et al. 2016, A&A, 590, A30

Merten, J., Meneghetti, M., Postman, M., et al. 2015, ApJ, 806, 4

Mihos, J. C., Harding, P., Feldmeier, J., & Morrison, H. 2005, ApJ, 631, L41

Milne, E. A. 1928, The Observatory, 51, 88

Monna, A., Seitz, S., Balestra, I., et al. 2016, ArXiv e-prints, arXiv:1605.08784

Morgan, W. W. 1961, Proceedings of the National Academy of Science, 47, 905

Mouhcine, M., Gibson, B. K., Renda, A., & Kawata, D. 2008, A&A, 486, 711

Moustakas, J., Coil, A. L., Aird, J., et al. 2013, ApJ, 767, 50

Muanwong, O., Kay, S. T., & Thomas, P. A. 2006, ApJ, 649, 640

Mulchaey, J. S. 2000, ARA&A, 38, 289

Mullis, C. R., McNamara, B. R., Quintana, H., et al. 2003, ApJ, 594, 154

Murphy, D. N. A., Geach, J. E., & Bower, R. G. 2012, MNRAS, 420, 1861

Mushotzky, R. F. 1984, Physica Scripta Volume T, 7, 157

Muzzin, A., Wilson, G., Demarco, R., et al. 2013, ApJ, 767, 39

Nantais, J. B., van der Burg, R. F. J., Lidman, C., et al. 2016, ArXiv e-prints, arXiv:1606.07832

Nastasi, A., Böhringer, H., Fassbender, R., et al. 2014, A&A, 564, A17

Navarro, J. F., Frenk, C. S., & White, S. D. M. 1997, ApJ, 490, 493

Nemmen, R. S., Georganopoulos, M., Guiriec, S., et al. 2012, Science, 338, 1445

Nousek, J. A., & Shue, D. R. 1989, ApJ, 342, 1207

Oguri, M. 2014, MNRAS, 444, 147

O'Hara, T. B., Mohr, J. J., Bialek, J. J., & Evrard, A. E. 2006, ApJ, 639, 64

Osmond, J. P. F., & Ponman, T. J. 2004, MNRAS, 350, 1511

Pacaud, F., Pierre, M., Adami, C., et al. 2007, MNRAS, 382, 1289

Papovich, C., Momcheva, I., Willmer, C. N. A., et al. 2010, ApJ, 716, 1503

Pearson, K. 1895, Philosophical Transactions of the Royal Society of London A: Mathematical, Physical and Engineering Sciences, 186, 343, pertinent material on page 375

Poggianti, B. M., Bridges, T. J., Mobasher, B., et al. 2001, ApJ, 562, 689

Ponman, T. J., Bourner, P. D. J., Ebeling, H., & Böhringer, H. 1996, MNRAS, 283, 690

Ponman, T. J., Cannon, D. B., & Navarro, J. F. 1999, Nature, 397, 135

Porter, S. C., Raychaudhury, S., Pimbblet, K. A., & Drinkwater, M. J. 2008, MNRAS, 388, 1152

Postman, M., Lauer, T. R., Donahue, M., et al. 2012a, ApJ, 756, 159

Postman, M., Coe, D., Benítez, N., et al. 2012b, ApJS, 199, 25

Pratt, G. W., Croston, J. H., Arnaud, M., & Böhringer, H. 2009, A&A, 498, 361

Puchwein, E., Sijacki, D., & Springel, V. 2008, ApJ, 687, L53

Rakos, K., & Schombert, J. 2004, AJ, 127, 1502

Reichert, A., Böhringer, H., Fassbender, R., & Mühlegger, M. 2011, A&A, 535, A4

Reiprich, T. H., Basu, K., Ettori, S., et al. 2013, Space Sci. Rev., 177, 195

Reiprich, T. H., & Böhringer, H. 2002, ApJ, 567, 716

Richard, J., Smith, G. P., Kneib, J.-P., et al. 2010, MNRAS, 404, 325

Rines, K., Geller, M. J., Diaferio, A., & Kurtz, M. J. 2013, ApJ, 767, 15

Rosati, P., Borgani, S., & Norman, C. 2002, ARA&A, 40, 539

Rozo, E., Wechsler, R. H., Rykoff, E. S., et al. 2010, ApJ, 708, 645

Rudick, C. S., Mihos, J. C., Harding, P., et al. 2010, ApJ, 720, 569

Rudnick, G., von der Linden, A., Pelló, R., et al. 2009, ApJ, 700, 1559

Rudnick, G. H., Tran, K.-V., Papovich, C., Momcheva, I., & Willmer, C. 2012, ApJ, 755, 14

Rykoff, E. S., Evrard, A. E., McKay, T. A., et al. 2008, MNRAS, 387, L28

Rykoff, E. S., Rozo, E., Busha, M. T., et al. 2014, ApJ, 785, 104

Rykoff, E. S., Rozo, E., Hollowood, D., et al. 2016, ApJS, 224, 1

Salpeter, E. E. 1955, ApJ, 121, 161

Sánchez-Blázquez, P., Peletier, R. F., Jiménez-Vicente, J., et al. 2006, MNRAS, 371, 703

Sánchez-Janssen, R., Aguerri, J. A. L., & Muñoz-Tuñón, C. 2008, ApJ, 679, L77

Sandage, A. R., & Eggen, O. J. 1959, MNRAS, 119, 278

Schechter, P. 1976, ApJ, 203, 297

Schiminovich, D., Wyder, T. K., Martin, D. C., et al. 2007, ApJS, 173, 315

Schlafly, E. F., & Finkbeiner, D. P. 2011, ApJ, 737, 103

Schlegel, D. J., Finkbeiner, D. P., & Davis, M. 1998, ApJ, 500, 525

Schmidt, K. B., Treu, T., Brammer, G. B., et al. 2014, ApJ, 782, L36

Sereno, M., Giocoli, C., Ettori, S., & Moscardini, L. 2015, MNRAS, 449, 2024

Sirianni, M., De Marchi, G., Gilliland, R., et al. 2003, in Bulletin of the American Astronomical Society, Vol. 35, American Astronomical Society Meeting Abstracts #202, 722

Smith, R. J., Marzke, R. O., Hornschemeier, A. E., et al. 2008, MNRAS, 386, L96

Snyder, G. F., Brodwin, M., Mancone, C. M., et al. 2012, ApJ, 756, 114

Spitzer, Jr., L., & Baade, W. 1951, ApJ, 113, 413

Springel, V., White, S. D. M., Jenkins, A., et al. 2005, Nature, 435, 629

Stanford, S. A., Eisenhardt, P. R., & Dickinson, M. 1998, ApJ, 492, 461

Stern, D., Jimenez, R., Verde, L., Stanford, S. A., & Kamionkowski, M. 2010, ApJS, 188, 280

Stott, J. P., Pimbblet, K. A., Edge, A. C., Smith, G. P., & Wardlow, J. L. 2009, MNRAS, 394, 2098

Stott, J. P., Smail, I., Edge, A. C., et al. 2007, ApJ, 661, 95

Stott, J. P., Hickox, R. C., Edge, A. C., et al. 2012, MNRAS, 422, 2213

Strateva, I., Ivezić, Z., Knapp, G. R., et al. 2001, AJ, 122, 1861

Strazzullo, V., Rosati, P., Pannella, M., et al. 2010, A&A, 524, A17

Strüder, L., Briel, U., Dennerl, K., et al. 2001, A&A, 365, L18

Sun, M., Voit, G. M., Donahue, M., et al. 2009, ApJ, 693, 1142

Tanaka, M., Kodama, T., Arimoto, N., et al. 2005, MNRAS, 362, 268

Taylor, E. N., Hopkins, A. M., Baldry, I. K., et al. 2011, MNRAS, 418, 1587

Terlevich, A. I., Kuntschner, H., Bower, R. G., Caldwell, N., & Sharples, R. M. 1999, MNRAS, 310, 445

Thanjavur, K., Willis, J., & Crampton, D. 2009, ApJ, 706, 571

Tian, J.-T., Yuan, Q.-R., Zhou, X., et al. 2012, Research in Astronomy and Astrophysics, 12, 1381

Tinker, J., Kravtsov, A. V., Klypin, A., et al. 2008, ApJ, 688, 709

Tozzi, P., & Norman, C. 2001, ApJ, 546, 63

Tozzi, P., Gilli, R., Mainieri, V., et al. 2006, A&A, 451, 457

Trager, S. C., Faber, S. M., Worthey, G., & González, J. J. 2000, AJ, 120, 165

Tremonti, C. A., Heckman, T. M., Kauffmann, G., et al. 2004, ApJ, 613, 898

Turner, M. J. L., Abbey, A., Arnaud, M., et al. 2001, A&A, 365, L27

Umetsu, K., Zitrin, A., Gruen, D., et al. 2016, ApJ, 821, 116

Umetsu, K., Medezinski, E., Nonino, M., et al. 2012, ApJ, 755, 56

Umetsu, K., Medezinski, E., Nonino, M., et al. 2014, ApJ, 795, 163

van der Burg, R. F. J., Aussel, H., Pratt, G. W., et al. 2016, A&A, 587, A23

Vazdekis, A., Sánchez-Blázquez, P., Falcón-Barroso, J., et al. 2010, MNRAS, 404, 1639

Vikhlinin, A., McNamara, B. R., Forman, W., et al. 1998, ApJ, 502, 558

Vikhlinin, A., Burenin, R. A., Ebeling, H., et al. 2009, ApJ, 692, 1033

Vílchez-Gómez, R. 1999, in Astronomical Society of the Pacific Conference Series, Vol. 170, The Low Surface Brightness Universe, ed. J. I. Davies, C. Impey, & S. Phillips, 349

Visvanathan, N., & Sandage, A. 1977, ApJ, 216, 214

Voit, G. M. 2005, Reviews of Modern Physics, 77, 207

Voit, G. M., & Bryan, G. L. 2001, Nature, 414, 425

Voit, G. M., Bryan, G. L., Balogh, M. L., & Bower, R. G. 2002, ApJ, 576, 601

Voit, G. M., Bryan, G. L., O'Shea, B. W., & Donahue, M. 2015, ApJ, 808, L30

von der Linden, A., Best, P. N., Kauffmann, G., & White, S. D. M. 2007, MNRAS, 379, 867

Wachter, K., Leach, R., & Kellogg, E. 1979, ApJ, 230, 274

Wall, J. V., & Jenkins, C. R. 2012, Practical Statistics for Astronomers

Weinmann, S. M., van den Bosch, F. C., Yang, X., & Mo, H. J. 2006, MNRAS, 366, 2

Williams, B. F., Ciardullo, R., Durrell, P. R., et al. 2007, ApJ, 656, 756

Worthey, G. 1994, ApJS, 95, 107

Worthey, G. 1999, in Astronomical Society of the Pacific Conference Series, Vol. 192, Spectrophotometric Dating of Stars and Galaxies, ed. I. Hubeny, S. Heap, & R. Cornett, 283

Wright, E. L. 2006, PASP, 118, 1711

Wu, X.-P., Xue, Y.-J., & Fang, L.-Z. 1999, ApJ, 524, 22

Wyder, T. K., Martin, D. C., Schiminovich, D., et al. 2007, ApJS, 173, 293

Xia, L., Zhou, X., Yang, Y., Ma, J., & Jiang, Z. 2006, ApJ, 652, 249

Xue, Y.-J., & Wu, X.-P. 2000, ApJ, 538, 65

Yang, H.-Y. K., Ricker, P. M., & Sutter, P. M. 2009, ApJ, 699, 315

Yuan, T.-T., Kewley, L. J., & Richard, J. 2013, ApJ, 763, 9

Zeimann, G. R., Stanford, S. A., Brodwin, M., et al. 2013, ApJ, 779, 137

Zhang, L., Yuan, Q., Yang, Q., et al. 2011, PASJ, 63, 585

Zibetti, S., Charlot, S., & Rix, H.-W. 2009, MNRAS, 400, 1181

Zibetti, S., White, S. D. M., Schneider, D. P., & Brinkmann, J. 2005, MNRAS, 358, 949

Zitrin, A., Broadhurst, T., Coe, D., et al. 2011, ApJ, 742, 117

Zitrin, A., Moustakas, J., Bradley, L., et al. 2012a, ApJ, 747, L9

Zitrin, A., Rosati, P., Nonino, M., et al. 2012b, ApJ, 749, 97

Zitrin, A., Meneghetti, M., Umetsu, K., et al. 2013, ApJ, 762, L30

Zitrin, A., Fabris, A., Merten, J., et al. 2015, ApJ, 801, 44